TACKLING TAXONOMIC AND TAPHONOMIC BIASES IN THE TRIASSIC FOSSIL FISH RECORD

by

IACOPO CAVICCHINI

A thesis submitted to the University of Birmingham for the degree of

DOCTOR OF PHILOSOPHY

Department of Earth Sciences
School of Geography, Earth and Environmental Sciences
College of Life and Environmental Sciences
University of Birmingham

September 2024

UNIVERSITY OF
BIRMINGHAM

University of Birmingham Research Archive

e-theses repository

This unpublished thesis/dissertation is copyright of the author and/or third parties. The intellectual property rights of the author or third parties in respect of this work are as defined by The Copyright Designs and Patents Act 1988 or as modified by any successor legislation.

Any use made of information contained in this thesis/dissertation must be in accordance with that legislation and must be properly acknowledged. Further distribution or reproduction in any format is prohibited without the permission of the copyright holder.

Abstract

Actinopterygians survived four of the Phanerozoic main extinctions, including the Permo-Triassic mass extinction (PTME), 252 million years ago. Neopterygians, a clade including most extant fish, appeared in the late Permian and became widespread in the Triassic, thus surviving the PTME. However, definitive estimations of the impact the extinction had on fish are lacking, despite thousands of exquisite 3D fossils from the Early Triassic. This uncertainty is due to weak phylogenetic hypotheses pertaining to late Permian-Early Triassic actinopterygian evolution, and limited knowledge of the taphonomic biases potentially affecting the Early Triassic fossil record of the clade. In this thesis, micro-computed tomography (XCT scanning) is the main tool used to obtain new taxonomic data and develop new taphonomic methods to help reduce the uncertainties. For taxonomy, a poorly known but well-preserved species from the Early Triassic, *Pteronisculus gunnari*, is redescribed from tomograms. The results add to our knowledge of the anatomical diversity and ontogeny of non-neopterygian fish, as well as suggesting some Early Triassic fish are the youngest representatives of Carboniferous radiations. In taphonomy, XCT scanning is tested as a data collection method in decay experiments. The results show that it is possible to gather data from carcasses under sediment, even visualising the internal anatomy if aided by staining agents, but additional work is required to conduct an entire experiment non-destructively. Together, the results highlight how applying novel approaches to old specimens and established procedures, can

improve our knowledge and contribute to solving uncertain aspects of Early Triassic actinopterygian evolution and preservation.

Acknowledgements

Supervision and mentoring (academic): SG1, TC, IS, ZJ, SL

Humane supervision and mentoring (academic) even in the face of a pandemic: SG1, TC

Money, training courses, UKRI internship and more: Central England NERC Training Alliance (CENTA) PhD scholarship via grant NE/S007350/1

Em dash knowledge and usage: SG1, TC

Hate of semicolons: TC

Fish (fossil): SG1

Fish (recently deceased): TC, PJ

Software (reasonably new): PM, JA, SG1, RD

Software (from a forgotten time before recorded history): SG1

Fear of God-lab practices: TC

Fear of God-notions and anatomy: SG1

Fear of God-collection visits: SG1, TC

Guidance-X rays: SG1, PW, LM

Supervision (non-academic, mostly humane): JA, LS

Guidance-other (software, university practices, posters, general knowledge): JA, LS, LM, KM, GB, PM, RD, TC, ED, SG1

Mischief: LS, LM, SF, PM,

Friendship: JA, LS, LM, KM, EH, GB, MM, JPC, SF, HK, AJ, BW, PV, MA, RD, AH1, BI, JFS, JB, MC, PM, SG2, AH2, SH, DF

Procrastination and fun (including but not limited to: game nights, arts and crafts, wine and cheese nights, lunchtime pints, karaoke nights, improvised weapons fights, gossiping, illegal corridor races, food reallocation, Friday pints): JA, LS, LM, KM, EH, GB, MM, JPC, SF, HK, AJ, BW, PV, MA, RD, AH1, BI, JFS, JB, MC, PM, SG2, AH2, SH, DF

Food (store-bought): JA, LS, LM, KM, EH, GB, MM, JPC, SF, HK, AJ, BW, PV, MA, RD, AH, BI, JFS, JB, MC, PM, SG2, AH2, DF

Food (homemade): SG2, LS, PV

Coffee: LM, JPC, KM, GB

Mugging (as in, mugs): JA, LS, LM

Wisdom, kilts and Dorset Knobs: LM

Annoying dice rolls, plastic projectiles and precise organisation: LS

Shared fish burden, neighbouring and Lego: JA

Fighting the system, wine and chatting: KM

Doggos and cruises: EH

Weather forecasts and travel: GB

Scottish culture: MM

Wholesome chaos: JPC

PBDB, energy drinks and style: SF

Tier lists and horses: HK

Collections and Eurovision: AJ

Words, Minesweeper and plant caring: BW

Games and cheese: PV

News, lunch conversations and laminations: MA

Mug conjuring and hidden middle fingers: RD

Nando's history: AH1

Volcanoes and Hot Wheels: AH2

Repeated, fortuitous ending up working in the same places: JFS

Fish and style: BI

Teeth and accents: JB

Boundless knowledge, wholesomeness and Rat Kings: PM

Baking and science: SG2

Self-confidence and hard work: MC

Dungeons: JA, LS, LM, HK, SF, AJ, PV, BW, TC

Dragons: TC, BW, PV, AJ, SF, HK, LM, LS, JA

Trains (they know what they did): JA

Showing me it is possible to finish a PhD project: BW, LS, LM, JPC, AH1, AH2, EH, JA, SH

Showing me it is possible to finish a PhD project and keep one's sanity: SH

(Barely) organised travel-conferences: JA, LS, LM, SF, PM, JB, RD, JFS, SH

(Barely) organised travel-field trips: LS, MM, GB, HK,

Remote support-friends: SP, GQ, SQ, FP, GP, ES, MA

Remote support-family: RP, AC, SC1, SC2

All the above, and much much more: CDD

I thank my arms, for always being at my side.

I thank my fingers, for I could always count on them.

I thank my hips, for always telling the truth.

I thank my feet, for carrying me around.

So long, and thank you for all the fish.

Table of Contents

1 | Introduction 1

1.1.1 Palaeogeography and climate during the PTME 8

1.1.2 Biotic crises 10

1.1.3 Biotic recovery after the extinction 14

1.2 The actinopterygian fossil record 16

1.2.1 Late Permian 16

1.2.2 Early Triassic 19

1.3 Taphonomy and preservation of Early Triassic actinopterygians 24

1.3.1 Taphonomy of fossil fish 24

1.3.2 Modes of preservation for actinopterygians in the Early Triassic 27

1.4 Aims and thesis outline 30

2 | A Portrait of a Young Fish: Redescription of Pteronisculus gunnari (Nielsen, 1942) from a juvenile specimen from the Early Triassic of East Greenland, with implications for ontogenetic development in early actinopterygians 34

2.1 Introduction 36

2.2 Materials and methods 40

2.3 Systematic palaeontology 46

2.4 Results 49

2.4.1 Description 49

2.4.2 Phylogenetic analysis 104

2.5 Discussion 108

2.5.1 Updates to previous descriptions 108

2.5.2 Phylogenetic affinity of Pteronisculus 117

2.5.3 Juvenile features and comparative anatomy 122

2.6 Conclusion 131

3 | Investigating the impact of X-rays on decay: X-ray computed tomography as a non-invasive visualisation

technique for sediment-based decay experiments 132

3.1 Introduction 134

3.2 Materials and methods 137

3.2.1 Control (CTRL) and sediment matrix (SNDCTRL) experiments 138

3.2.2 Computed tomography experiment 139

3.2.3 3D model mesh comparison 142

3.3 Results 144

3.3.1 A chronological report of the control experiment: D. rerio carcasses decaying in water (CTRL) 144

3.3.2 A chronological report of carcasses decaying within a sand matrix (SNDCTRL) 147

3.3.3 Comparison between the control experiment (CTRL) and carcasses decaying in sediment (SNDCTRL) 150

3.3.4 Cataloguing the morphological decay of carcasses using XCT scanning 152

3.3.5 Comparison between the carcasses decaying in sediment (SNDCTRL) and the XCT scanned carcasses 158

3.3.6 Carcass orientation within substrate and 3D model mesh comparison 160

3.4 Discussion 163

3.4.1 The impact of XCT scanning on carcasses in decay experiments 166

3.4.2 Burial orientation and stabilisation: the role of sediment visualised by XCT 170

3.5 Conclusion 173

4 | Dicing with decay: diceCT scanning as a visualisation tool to aid decay experiments 175

4.1 Introduction 176

4.2 Materials and methods 180

4.2.1 Specimens and decay assessment 180

4.2.2 Experimental protocols 182

4.3 Results 188

4.3.1 Preliminary experimental trial (W-diceCT experiment). 188

4.3.2 Main experiment (S-diceCT experiment) 200

4.3.3 Accuracy of diceCT in decay experiments 206

4.4 Discussion 208

4.4.1. Assessment of using diceCT in decay experiments. 208

4.4.2. The logistical cost of diceCT in decay experiments. 216

4.4.3. Experiments demonstrate that decay in a restricted space is a proxy for sediment 217

4.5 Conclusion 219

5 | Summary and future directions 220

5.1 Summary 220

5.2 Future directions 223

Appendices 286

A | A Portrait of a Young Fish: Redescription of Pteronisculus gunnari (Nielsen, 1942) from a juvenile specimen from the Early Triassic of East Greenland, with implications for ontogenetic development in early actinopterygians 286

A.1 Phylogenetic matrix and analysis 286

A.2 Additional characters and taxa of the phylogenetic analysis 287

A.3 Characters list 289

A.4 Taxon list for phylogenetic analyses 366

A.5 Figures and Tables 370

B | Investigating the impact of X-rays on decay: X-ray computed tomography as a non-invasive visualisation technique for sediment-based decay experiments 374

B.1 Character matrix and decay data 374

B.2 Figures and Tables 374

C | Dicing with decay: diceCT scanning as a visualisation tool to aid decay experiments 378

C.1 Preliminary experiments 378

C.2 Character matrix and decay data 379

List of Figures

1.1 Stratigraphic ranges of selected marine actinopterygian taxa between the Late Permian and the Early Triassic 3

1.2 Estimates of disparity, number of lineages, origination and extinction rates across the PTME from the literature 5

1.3 Distribution of the principal Changsingian and Early Triassic fossiliferous sites on palaeomaps. 15

1.4 Distribution of the principal Early Triassic fossiliferous sites on a present-day map of the world. 19

1.5 Examples of concretionary preservation of actinopterygian fossils from the Early Triassic. 25

2.1 Pictures and line drawings of *Pteronisculus gunnari* NHMD 73588. 37

2.2 Renders of dermal and endoskeletal anatomy of *Pteronisculus gunnari* NHMD–75388. 42

2.3 Renders of the snout and skull roof bones of *Pteronisculus gunnari* NHMD 73588. 44

2.4 Renders of the skull roof, cheek and infraorbital bones of *Pteronisculus gunnari* NHMD–75388. 47

2.5 Renders of the hyoid arch and jaw of *Pteronisculus gunnari* NHMD–75388. 50

2.6 Renders of the upper jaw and palate of *Pteronisculus gunnari* NHMD–75388. 53

2.7 Synchrotron renders of the parasphenoid, left jaws and parotic toothplates of *Pteronisculus gunnari* NHMD–73588. 55

2.8 Renders of the palate, parasphenoid and accessory vomers of *Pteronisculus gunnari* NHMD–75388. 57
2.9 Renders of the lower jaw of *Pteronisculus gunnari* NHMD 73588. 61
2.10 Renders of the braincase of *Pteronisculus gunnari* NHMD–75388. 66
2.11 Renders of the ethmoids, parasphenoid, sclerotic rings, and parotic toothplates of *Pteronisculus gunnari* NHMD–75388. 69
2.12 Renders of the endocast of *Pteronisculus gunnari* NHMD–75388. 75
2.13 Renders of the gill skeleton of *Pteronisculus gunnari* NHMD–75388. 79
2.14 Distribution of toothplates and gill rays in *Pteronisculus gunnari* NHMD-73588. 84
2.15 Renders of the shoulder girdle and pectoral fin endoskeleton of *Pteronisculus gunnari* NHMD–75388. 87
2.16 Renders of the pectoral fin of *Pteronisculus gunnari* NHMD–75388. 89
2.17 Renders of the axial skeleton of *Pteronisculus gunnari* NHMD–75388. 92
2.18 Strict consensus tree of 10752 most parsimonious trees, equal weights analysis with outgroup topology constrained. 95
2.19 Composite reconstructions of the skeleton of *Pteronisculus gunnari* NHMD–73588. 98
3.1 Sequence of anatomical character loss in zebrafish decaying in water (CTRL; A) and quartz sand substrate (SNDCTRL; B). 128
3.2 Decay rates of zebrafish in water (CTRL) and in a quartz sand substrate (SNDCTRL). 131
3.3 3D XCT models of zebrafish in various stages of decay in right-lateral view. 136
3.4 Comparison of carcass volume change during decay. 144

3.5 A comparative schematic showing variance in appearance and anatomical character coding of a decaying zebrafish in quartz sand substrate on day 50. 151
4.1 Graphical representation of the protocol of the W-diceCT experiment (A-E) and the S-diceCT experiment for specimen C (F). 163
4.2 3D models of the external morphology of specimens from the W-diceCT experiment. 171
4.3 3D models of the internal anatomy of diceCT scanned specimens from the W-diceCT experiment. 173
4.4 Bar graphs comparing the 4-states character coding for the specimens in the W-diceCT experiment through different assessment methods. 180
4.5 3D models of diceCT scanned specimens from the S-diceCT experiment. 182
4.6 Comparison of the amount of decay between selected specimens and different assessment methods. 186
A.1 Strict consensus tree of 135 most parsimonious trees, implied weights analysis (K=100) with outgroup topology constrained. 314
A.2 Strict consensus tree of 9 most parsimonious trees, implied weights analysis (K=8) with outgroup topology constrained. 314
B.1 Bar graph comparison between 4 states percentages of the CTRL and SNDCTRL. 317
B.2 Line graphs of the abundance of each character state in the CTRL and SNDCTRL. 318

List of Tables

3.1 Summary of comparisons and Spearman's rank analysis using presence/absence data from dissection. 142
3.2 Summary of comparisons and Spearman's rank analysis using combined presence/absence data from dissections and tomograms. . . 143
B.1 Scoring and rankings of the Spearman's rank analysis between characters of the CTRL and SNDCTRL. 316

1 | Introduction

Actinopterygii (ray-finned fishes) have survived, with varying effects, four of the “big five” Phanerozoic mass extinctions (Friedman and Sallan 2012; Sallan 2014; Alfaro et al. 2018; Smithwick and Stubbs 2018) and the subsequent recovery phases, reaching a number of living species comparable with that of all other extant vertebrates combined (Nelson et al. 2016). Despite being of vast scientific and ecological importance, the early evolutionary history of actinopterygians is far from clear. The main causes of this imbalance are a poor and geographically biased fossil record (Friedman and Sallan 2012; Tintori et al. 2014a; Smithwick and Stubbs 2018; Romano 2021; Henderson et al. 2022), a taxonomy in need of review (Sallan 2014; Betancur-R et al. 2015; Friedman 2015; Nelson, et al. 2016) and contrasting signals between genomic and fossil data regarding the tempo of major lineage differentiation events (Hurley et al. 2007; Faircloth et al. 2013; Redmond et al. 2023). These knowledge gaps hinder a full understanding of phylogenetic relationships among Actinopterygii and could obscure the origin of modern-day clades (Hurley, et al. 2007; Sallan 2014; Friedman 2015; Redmond, et al. 2023).

One of the periods requiring further investigation is the latest Palaeozoic-earliest Mesozoic, which encompasses the Permo-Triassic mass extinction (PTME; ~251.9 Ma). The PTME was the worst of all the Phanerozoic biological crises, with different estimation methods suggesting that between 70 to 90% of all species were wiped out (Erwin et

al. 2002; Chen and Benton 2012; Payne and Clapham 2012). The effects on the biosphere were severe, with numerous investigations focusing on the impact of this event on tetrapod clades
(Ward et al. 2005; Sidor et al. 2013; Shishkin and Novikov 2017; Ezcurra and Butler 2018; Allen et al. 2020; Romano et al. 2020), invertebrates (Fraiser and Bottjer 2005; Fraiser et al. 2005; Pruss and Bottjer 2005; Chen et al. 2009; Brayard et al. 2011; Payne and Clapham 2012) and plants (Visscher et al. 1996; Looy et al. 2001; Wignall 2008).

In contrast with the wealth of information concerning these clades, comparatively few studies have investigated the effects of the PTME on ray-finned fishes. Evaluations of diversity loss within the clade vary, since there are gaps in our understanding of if and/or how the extinction affected actinopterygians (Friedman 2015; Puttick et al. 2017; Smithwick and Stubbs 2018), mainly caused by an imbalance between the taxonomic data available from the late Permian and from the Early Triassic. In fact, for the Wuchiapingian genera and species counts are relatively high for the Palaeozoic, particularly because of the presence of two important Lagerstätten: the Marl Slate, UK, and the Kupferschiefer, Germany (Romano et al. 2016; Henderson et al. 2023). Faunas are characterised by abundant fusiform "palaeopterygians" (e.g. *Plegmolepis*, *Acropholis*, *Boreolepis, Pygopterus*), and rarer putative early neopterygians like the deep-bodied *Dorypterus* and *Acentrophorus* (Aldinger 1937; Westoll 1941; Benton et al. 2015; Friedman 2015). However, our understanding of actinopterygian diversity in this period is partially obscured by common

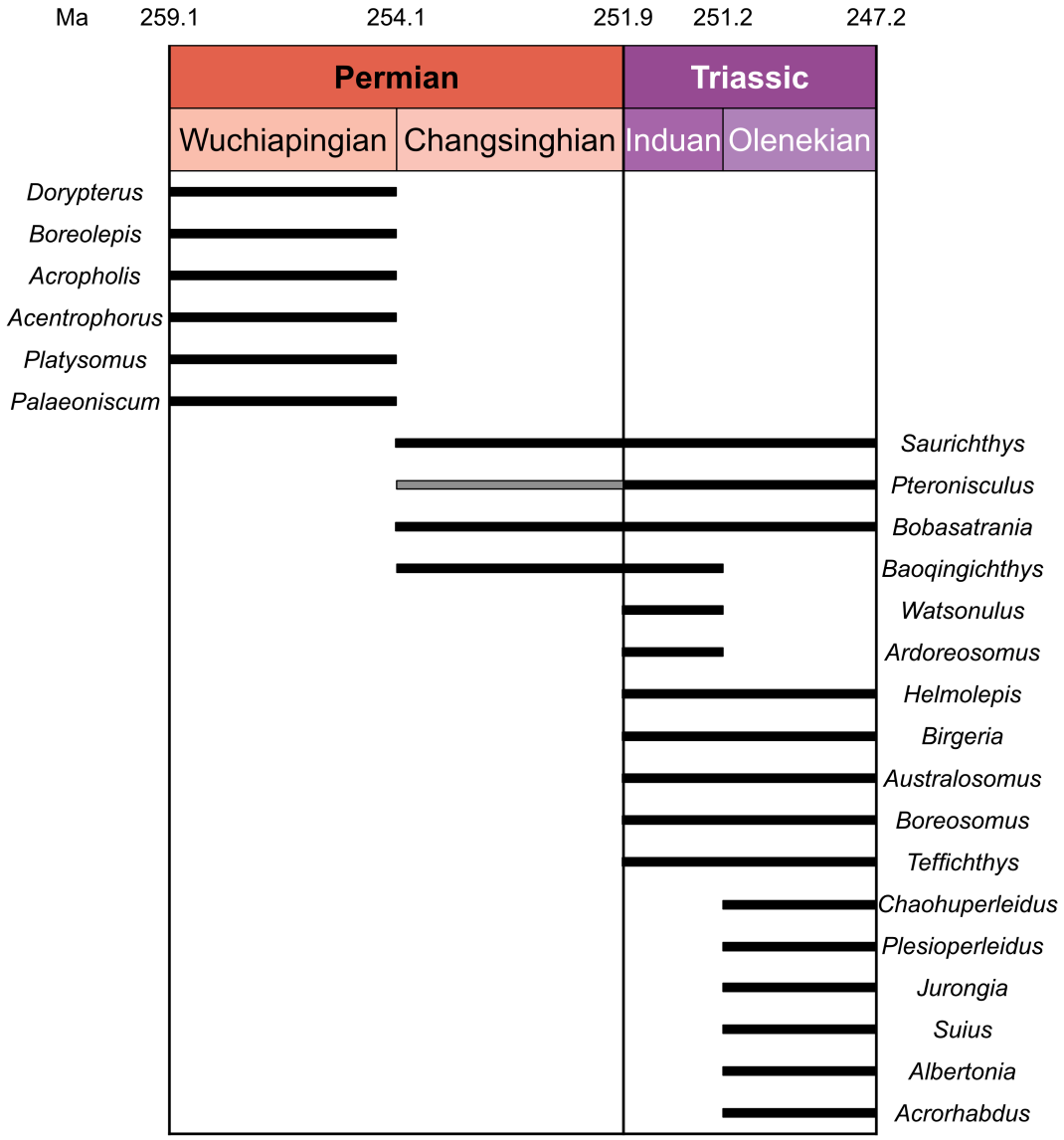


Fig. 1.1: Stratigraphic ranges of selected marine actinopterygian taxa between the Late Permian and the Early Triassic. Dubious ranges are in grey.

occurrences of "wastebasket taxa" (mostly *Palaeoniscum*, *Platysomus*, "*Elonichthys*"), which originate in part from historical imprecise taxonomic practices and weak genus diagnoses (Friedman and Sallan 2012; Henderson, et al. 2023). In addition, three-dimensional preservation is uncommon for Lopingian actinopterygians, which are more commonly found flattened along bedding planes. Consequently, despite high numbers of specimens, many phylogenetically informative characters (e.g.

details of the braincase, morphology of the endochondral ossifications) are poorly known (King 1850; Aldinger 1937; Phuoc 1980; Campbell and Phuoc 1983; Schaumberg 1989; Diedrich 2009).

In the Changsingian, on the other hand, proximate to the P-T boundary, actinopterygian occurrences are altogether rare, making considerations on faunal changes difficult. There are just a handful of genera that appear to cross into the Triassic (Fig. 1.1): *Bobasatrania*, *Saurichthys*, *Baoqingichthys*, and possibly *Pteronisculus* (Gardiner and Jubb 1975; Benton et al. 2013; Tintori, et al. 2014a). Some authors have attributed this poor fossil record to a reduction in suitable outcrop record during this time period, related to the formation of Pangaea (McGowan and Smith 2008; Friedman and Sallan 2012). However, standardisation metrics that use equal-length time bins consider the entire Lopingian (late Permian) as one bin, and suggest that it is very diverse, implying different potential reasons for the late Palaeozoic-early Mesozoic imbalance, e.g. sampling biases (Henderson, et al. 2023).

Irrespective of the underlying reason, this lack of data has led to debates and different interpretations of the actinopterygian fossil record across the PTME (Fig. 1.2). The few studies that investigate actinopterygians and their response to the extinction variably: report the severity of the extinction event for Actinopterygii (Blieck 2011; Friedman and Sallan 2012; Puttick, et al. 2017; Vázquez and Clapham 2017); find profound changes in marine communities at the P-T boundary and during the Early Triassic, with a peak of osteichthyan diversity in the Middle Triassic (Scheyer et al.

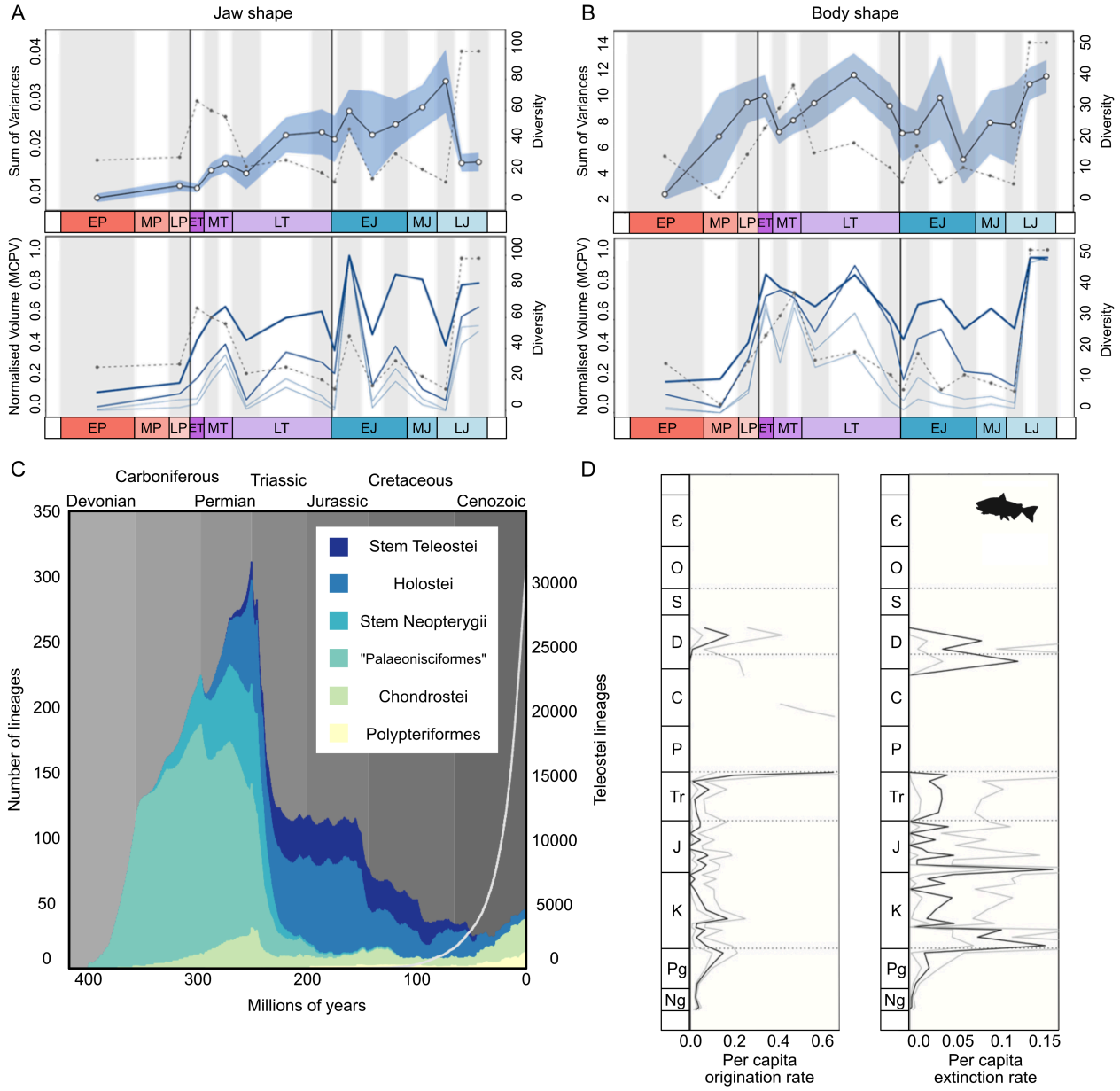


Fig. 1.2: Estimates of disparity, number of lineages, origination and extinction rates across the PTME from the literature. A-B, disparity (top graphs) and normalised morphospace volume (bottom graphs) time series for jaw shape (A) and body shape (B) in actinopterygians. Dotted line: diversity. Blue area: 95% confidence interval for disparity. Blue lines weight indicates the number of PC axes represented (heaviest: 2; lightest: 5). From Smithwick and Stubbs, 2018. C, actinopterygian lineages through time, from Puttick et al., 2017. D, per capita origination (left plot) and extinction rates (right plot) for actinopterygians in the Phanerozoic, from Friedman and Sallan, 2012. Abbreviations: EJ, Early Jurassic; EP, Early Permian; ET, Early Triassic; LJ, Late Jurassic; LP, Late Permian; LT, Late Triassic; MJ, Middle Jurassic; MP, Middle Permian; MT, Middle Triassic; Є, Cambrian; C, Carboniferous; D, Devonian; J, Jurassic; K, Cretaceous; Ng, Neogene; O, Ordovician; P, Permian; Pg, Palaeogene; S, Silurian; Tr, Triassic.

2014; Tintori, et al. 2014a; Romano et al. 2016); or find no trends with respect to morphological or body size changes correlated to the P-T transition (Puttick, et al. 2017; Smithwick and Stubbs 2018).

The Early Triassic represents an important epoch for Actinopterygii, encompassing a wide variety of forms with a better fossil record compared to the latest Permian (Brinkmann et al. 2010; Tintori, et al. 2014a; Romano 2021). Some genera, such as *Saurichthys*, *Birgeria*, *Bobasatrania*, *Boreosomus*, *Australosomus*, and *Pteronisculus* are common, known from many fossils in great detail and with a Pangaea-wide distribution, prompting the creation of the term TEFF (Triassic Early Fish Fauna) to encompass them (Schaeffer and Mangus 1976; Brinkmann, et al. 2010; Friedman and Sallan 2012; Friedman 2015; Tintori, et al. 2014a). Others, such as *Helmolepis*, *Albertonia*, and *Watsonulus* appear to have a restricted geographical range or to be endemic to a particular locality or environment (Olsen 1984; Neuman and Mutter 2005; Neuman 2015). These Early Triassic environments were home to ancestors of modern clades (stem holosteans, like the parasemionotids,; but, critically, no known stem teleosts) as well as less derived taxa, the latter often wrongly grouped together in the past as the "palaeoniscoids" or "palaeonisciformes" (Gardiner and Schaeffer 1989; Sallan 2014; Friedman and Giles 2016; López-Arbarello and Sferco 2018). Despite an abundance of fossils, phylogenetic relationships among these taxa are unclear, and decades of work have seen the rise of numerous, often conflicting hypotheses (Gardiner and Schaeffer 1989; Gardiner et al. 2005; Friedman

and Sallan 2012; Arratia 2013; Nelson, et al. 2016; Giles et al. 2017). The vast majority of TEFF fossils come from a handful of sites, potentially inducing geographical bias and "Lagerstätten-effect" in their fossil record (Seilacher et al. 1985; Romano, et al. 2016). Combined with a poor fossil record in the latest Permian, which includes many "wastebasket" occurrences and is itself in need of review (Friedman and Sallan 2012; Henderson, et al. 2023), it is unclear whether the varied and speciose fossil record of Early Triassic actinopterygians represents a quick recovery and diversification event following the PTME, or is an artefact induced by the lack of Changsingian occurrences.

An often-overlooked source of additional data, particularly relevant for fishes in the Early Triassic epoch, is taphonomy; more specifically, the peculiar modes of preservation for actinopterygians. A number of Early Triassic marine sites, including the East Greenland, Madagascar and Spitsbergen (Svalbard) Lagerstätten, as well as localities in China and the US, in fact, share a similar mode of preservation: the famous fossil-bearing concretions (e.g. Stensiö 1921b, 1932; Nielsen 1935; Lehman 1952; Beltan 1996; Benton, et al. 2013; Romano et al. 2017; Romano et al. 2019; Qiu et al. 2019). Although two-dimensionally preserved fossils are also known from the Early Triassic (e.g. Schaeffer and Mangus 1976; Benton, et al. 2013; Romano, et al. 2019), concretions have yielded many 3D-preserved specimens in high degrees of completeness and articulation that represent the main source of anatomical data about the TEFF

(Stensiö 1921b, 1932; Stensio 1925b; Lehman 1952; Beltan 1996; Qiu, et al. 2019).

On the other hand, since most of the data we have for the TEFF comes from such 3D specimens, this could suppress our knowledge of taxa not known from these deposits, or palaeoenvironments unfavourable for concretionary preservation (Beltan 1996; Romano et al. 2012; Romano, et al. 2017; Kogan and Romano 2016). The few existing works on Early Triassic taphonomy have been either focused on faunas from single sites, quality of preservation and palaeoenvironment determination (Beltan 1996; Anderson et al. 2013) or have targeted invertebrate clades (Iniesto et al. 2019). This way, it is unsure whether the fossil record accurately portrays the palaeogeographical distribution of the TEFF and the actual faunal composition, but also whether differences in ecology or anatomy can lead to differential preservation.

1.1 The end of the Palaeozoic era

1.1.1 Palaeogeography and climate during the PTME

In the latest Permian and Early Triassic, extensional tectonics had just started to break apart the supercontinent of Pangaea, which formed earlier in the Palaeozoic from the collision of Laurussia and Gondwana (Ziegler et al. 1982; Parrish 1993; Zharkov and Chumakov 2001; Woods 2005; Preto et al. 2010). Thus, major palaeogeographic features remained stable at the start of the Mesozoic: a single landmass, extending from pole to pole and roughly symmetrical with respect to the

equator, surrounded by the main oceanic basins of Panthalassa and Tethys (divided into Palaeotethys and Neotethys) (Parrish 1993; Ziegler et al. 2003; Woods 2005).

Early Triassic climatic conditions were also very similar to those of the late Palaeozoic: the rise of atmospheric temperatures continued, peaking around the PTME and staying above modern averages for the whole epoch (Retallack 1999; Kidder and Worsley 2004; Horacek et al. 2010; Korte et al. 2010; Sun et al. 2012; Chen et al. 2015). As a result, the polar regions had no permanent ice cover, exhibiting instead a cold temperate climate, and wide deserts extended around the tropics (Ziegler, et al. 2003; Woods 2005; Preto, et al. 2010; Montenegro et al. 2011). Atmospheric circulation was dominated by a so-called “mega-monsoon”, enhanced by the high temperatures and continental conformation; as a result, precipitation was strongly seasonal (Parrish 1993; Preto, et al. 2010).

The seas could have been an even more inhospitable habitat: seawater temperatures rose in the late Palaeozoic, in a similar trend to the atmosphere (Kidder and Worsley 2004; Montenegro, et al. 2011; Brand et al. 2012; Sun, et al. 2012; Romano et al. 2013), causing stratification of the water column and a reduction in oceanic current strength (Kidder and Worsley 2004; Montenegro, et al. 2011; Shen et al. 2015). In addition, geochemical data from sedimentary sections worldwide show signs of anoxic, euxinic and possibly hypercapnic waters not just during the PTME, but in multiple, variably extended periods of time between the late Permian

and across the whole Early Triassic (Isozaki 1997; Wignall and Twitchett 2002; Cao et al. 2009; Algeo et al. 2011; Payne and Clapham 2012; Li et al. 2019). The altered and deteriorated conditions of marine environments caused crises in the organic factories of carbonate and silica, leaving traces in the sedimentary record with the occasional deposition of unusual calcimicrobial facies, a strong reduction in metazoan-built reefs (Pruss and Bottjer 2005; Baud et al. 2007; Brayard, et al. 2011; Payne and Clapham 2012), and a reduction in the abundance of chert deposits in the Early Triassic (the so called “chert gap”), although its hypothesised global nature has been questioned (Kakuwa 1996; Beauchamp and Baud 2002; Wignall and Newton 2003; Sperling and Ingle Jr 2006; Muto et al. 2020).

There is still debate about how widespread and long-lasting these unfavourable conditions were and how great their contribution was to the PTME as a killing mechanism (Bond and Wignall 2010; Algeo, et al. 2011; Brand, et al. 2012; Payne and Clapham 2012; Clarkson et al. 2016). Certainly, the persistence (or successive pulses) of such conditions in the Early Triassic negatively affected the recovery of marine clades in different ways (Payne et al. 2004; Fraiser and Bottjer 2005; Knoll et al. 2007; Retallack et al. 2011; Feng and Algeo 2014).

1.1.2 Biotic crises

The PTME was the most severe biotic crisis of the Phanerozoic. It played a fundamental role in reshaping ecosystems, and has been suggested to mark the passage from the Palaeozoic evolutionary fauna to the Modern evolutionary fauna (Erwin, et al. 2002; Fraiser and Bottjer

2005; Fraiser, et al. 2005; Knoll, et al. 2007; Song et al. 2011; Chen and Benton 2012; Payne and Clapham 2012; Hofmann 2016; Vázquez and Clapham 2017; Dineen et al. 2019). Estimates of the duration of the extinction event vary from almost 1 My (million years) to 60-200 ky (thousand years) (Huang et al. 2011; Shen et al. 2011a; Shen et al. 2019; Burgess et al. 2014; Wang et al. 2014) and multiple pulses of extinction have been detected in some sections (Song et al. 2013). In the past, many causes have been proposed for the biotic crisis, but recent consensus has centred around intense late Permian-Early Triassic volcanism of the Siberian Traps as being the major driver (Erwin, et al. 2002; Lo et al. 2002; Racki and Wignall 2005; Isozaki et al. 2007; Isozaki 2009; Metcalfe and Isozaki 2009; Saunders and Reichow 2009; Korte, et al. 2010; Konstantinov et al. 2014; Luppo et al. 2018). An alternative hypothesis, an impact event at the PT boundary, has now lost consensus (Becker et al. 2001; Becker et al. 2004; Kaiho et al. 2001; Erwin, et al. 2002; Erwin 2003; Koeberl et al. 2004).

The palaeoenvironmental consequences were multiple and disruptive: perturbations in the geochemical cycles and isotopic ratios of C, S, Sr and Hg have been detected, both in terrestrial and marine sediments in the Late Permian and Early Triassic (Retallack 1999; Krull and Retallack 2000; Erwin, et al. 2002; Payne, et al. 2004; Payne and Clapham 2012; Racki and Wignall 2005; Isozaki 2009; Korte, et al. 2010; Shen et al. 2011b; Shen, et al. 2019; Burgess, et al. 2014); injection of CO_2 and CH_4 from various sources in the atmosphere and a

corresponding increase of CO_2 in seawater caused hypercapnia, acidic rain, dramatic temperature and climate disruption (Retallack 1999; Krull and Retallack 2000; Erwin, et al. 2002; Kidder and Worsley 2004; Hochuli et al. 2010; Brand, et al. 2012; Kaiho et al. 2012; Payne and Clapham 2012; Sun, et al. 2012; Romano, et al. 2013; Chen, et al. 2015); and widespread anoxic and euxinic conditions were present in the water column, possibly reaching the photic zone (Erwin, et al. 2002; Wignall and Newton 2003; Bond and Wignall 2010; Chen and Benton 2012; Song et al. 2012). On land, various plant groups went extinct, increasing runoff of sediments and nutrients to sedimentary basins and causing the so-called “coal gap” in the Early and Middle Triassic (Retallack et al. 1996; Retallack 1999; Erwin, et al. 2002; Racki and Wignall 2005; Newell et al. 2010).

Terrestrial and marine ecosystems were affected by the harsh environmental conditions, albeit to different extents (Erwin, et al. 2002), and there is discussion about the conditions of ecosystems prior to the PTME (Clapham et al. 2009; Wang, et al. 2014). Diversity in the biosphere had been in decline since the Middle Permian, with a distinct, selective extinction event at the end of the Capitanian, ~257-260 Ma (Erwin, et al. 2002; Zhou et al. 2002; Clapham, et al. 2009; Zhang et al. 2015); the effects of the end-Permian crisis surely aggravated the loss, calculated at around 90% of the total number of species (Erwin, et al. 2002; Payne and Clapham 2012; Song, et al. 2013). Land plants were heavily impacted, as testified by the loss of the Permian *Glossopteris* flora and a spike in fungal activity at the PTME (Retallack, et al. 1996; Visscher, et al. 1996).

Tetrapods suffered a loss of diversity in all the sites spanning the PTME, although it has been suggested that this represented a gradual decline rather than a sharp extinction pulse (Sennikov and Golubev 2005, 2012; Ward, et al. 2005; Allen, et al. 2020; Romano, et al. 2020). In the marine realm, trilobites, rugose and tabulate corals went extinct and large portions of echinoid, ammonoid, brachiopod and foraminifera diversity were lost (Erwin, et al. 2002; Knoll, et al. 2007; Payne and Clapham 2012; Song, et al. 2013; Chen, et al. 2015). Common Palaeozoic reef builders disappeared and their place was taken by microbes or sponge-serpulid associations (Pruss and Bottjer 2005; Brayard, et al. 2011; Zatoń et al. 2018) until a new rise in the diversity and radiation of scleractinian corals in the Middle Triassic (Pruss and Bottjer 2005).

Fishes and marine vertebrates appear to have been less affected than invertebrates and terrestrial tetrapods in terms of diversity loss, although studies suffer from a lack of bulk statistical data (Erwin, et al. 2002; Blieck 2011; Friedman and Sallan 2012; Puttick, et al. 2017; Vázquez and Clapham 2017; Song et al. 2018). A qualitative reading of the fossil record indicates that a number of chondrichthyan and osteichthyan lineages disappear at the end of the Permian, including durophagous holocephalans, stethacantid and petalodontiform chondrichthyans, and multiple actinopterygian genera (e.g. *Palaeoniscum*, *Dorypterus*, *Acentrophorus*, *Platysomus*) although “palaeopterygian”, "sub-holostean" and stem neopterygian lineages cross the P-T boundary (Friedman and Sallan 2012; Vázquez and Clapham 2017; López-Arbarello

and Sferco 2018). However, the patchy Late Permian fossil record brings uncertainty to any considerations (Friedman and Sallan 2012; Vázquez and Clapham 2017; Smithwick and Stubbs 2018).

1.1.3 Biotic recovery after the extinction

Patterns and timings of the recovery from the PTME vary, depending on the palaeoecology of the groups considered (Pruss and Bottjer 2005; Song, et al. 2018; Dineen, et al. 2019), the palaeogeographic position (Pruss and Bottjer 2004; Fraiser, et al. 2005; Song, et al. 2011; Brayard et al. 2017) and the persistence of unfavourable environmental conditions in the Early Triassic (Retallack 1999; Knoll, et al. 2007; Sun, et al. 2012; Romano, et al. 2013; Song et al. 2020). Ecosystems did not stably regain high levels of trophic and ecological complexity until the Middle Triassic, which saw the rise and diversification of new marine and terrestrial clades (Irmis and Whiteside 2012; Scheyer, et al. 2014; Ezcurra and Butler 2018; Dineen, et al. 2019; Pietsch et al. 2019; Romano, et al. 2020), although there are a handful of complex ecosystems known from the Dienerian (Dai et al. 2023) and the Olenekian (Brayard et al. 2017). Some marine clades, with high origination and metabolic rates, recovered and even radiated within less than 1 My of the PTME (Metcalfe and Isozaki 2009; Song, et al. 2011; Chen and Benton 2012; Pietsch, et al. 2019): ammonoids and conodonts show quick cycles of radiations and extinction for all the Early Triassic (Wignall 2008; Stanley 2009; Goudemand et al. 2019), while benthic communities, including ichnoassemblages, experienced a longer recovery interval, stably

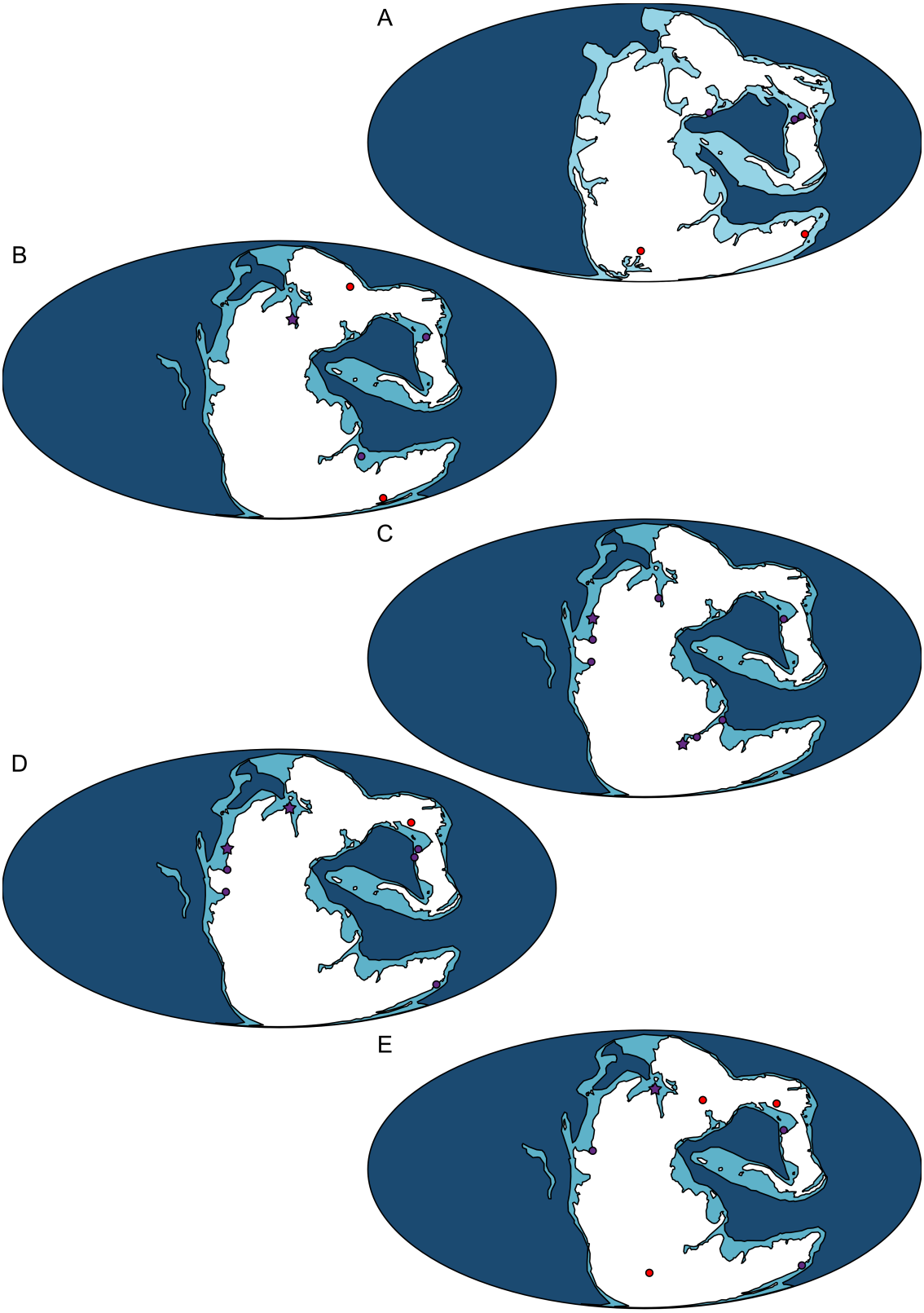


Fig. 1.3: Distribution of the principal Changsingian and Early Triassic fossiliferous sites on palaeomaps. A, Locations of principal fossiliferous sites on a palaeomap of the Changsingian; B-E, Locations of principal fossiliferous sites on palaeomaps of the the Griesbachian (B), Dienerian (C), Smithian (D) and Spathian (E). Legend: purple, marine site; red, freshwater site; circle, non-lagerstatten site; star, lagerstatten site.

regaining their lost diversity only in the Middle Triassic (Fraiser and Bottjer 2005; Fraiser, et al. 2005; Hofmann 2016; Song, et al. 2018). Finally, fishes and other marine vertebrates already occupied high and varied trophic levels within ~1 My of the extinction event, with multiple genera and species that have their first occurrence in the Griesbachian (Scheyer, et al. 2014; Romano, et al. 2016). The unconstrained impact of the PTME on Actinopterygii, mostly due to a poor late Changsingian fossil record, makes it uncertain whether this represents a fast recovery or a new diversification event unrelated to the PTME (Hurley, et al. 2007; Friedman 2015).

1.2 The actinopterygian fossil record

1.2.1 Late Permian

Fossils of ray-fins are more abundant during the Wuchiapingian, which has some of the highest genera and species raw counts in the Palaeozoic, than during the Changhsingian (Romano, et al. 2016; Henderson, et al. 2023). The only occurrences of genera known to cross the P-T boundary from the Wuchiapingian are *Australosomus*, reported from East Greenland, and *Pygopterus,* from Svalbard (Stensiö 1921a, 1932; Nielsen 1932). In addition, the putative lineage of platysomids and bobasatraniids has representatives in the late Palaeozoic and the Mesozoic (Campbell and Phuoc 1983; Zidek 1992; Wilson et al. 2021). However, a considerable percentage of all the Wuchiapingian actinopterygian occurrences come from taxa now known to be wastebasket taxa (mostly

Palaeoniscum and *Platysomus*), confusing the picture of taxonomic diversity, while the presence of the Marl Slate and Kupferschiefer Lagerstätten introduces bias by over-representing taxa from these deposits (Romano, et al. 2016; Wilson, et al. 2021; Henderson, et al. 2022; Henderson, et al. 2023).

For the Changsinghian, available data on diversity and distribution of actinopterygians is scarce, as are sections that span the P-T boundary (Fig. 1.3A). Sedimentary sections spanning the P-T transition are known from the Tethyan realm (Krystyn et al. 2003; Szurlies et al. 2003; Groves et al. 2005; Lehrmann et al. 2006; Wang et al. 2007; Chen, et al. 2009; Chen, et al. 2015; Hampe et al. 2013), the Boreal realm (Stemmerik et al. 2001; Bjerager et al. 2006; Zuchuat et al. 2020), and Panthalassa (Kakuwa 1996; Henderson 1997; Sperling and Ingle Jr 2006), as well as from non-marine basins in South Africa (Retallack et al. 2003; Ward, et al. 2005) and Russia (Benton et al. 2004; Sennikov and Golubev 2012). The most intensely studied are located in China, where the GSSP for the P-T boundary is located (Jin et al. 2000; Chen, et al. 2009; Chen, et al. 2015).

A bare handful of marine actinopterygians are known from this stage: *Archaeolepidotus* and *Bobasatrania* are reported from the Changsinghian of northern Italy (Prinoth and Posenato 2007), indeterminate actinopterygian microfossils are present in the latest Palaeozoic Hambast Formation of Iran but absent from the Early Triassic of the same region (Hampe, et al. 2013), and a species of *Pteronisculus* has been described from the Late Permian of South Africa, although this attribution is dubious



Fig. 1.4: Distribution of the principal Early Triassic fossiliferous sites on a present-day map of the world. Legend: purple, marine site; red, freshwater site; circle, non-lagerstatten site; star, lagerstatten site.

(Gardiner and Jubb 1975). In the Zhejiang and Jiangxi localities (China), where latest Changsingian-earliest Griesbachian marine fossil fish have been found, just two Permian actinopterygians (*Baoqingichthys microdontus*, known only from isolated teeth, and *Saurichthys*) are known from both the late Permian and the Early Triassic (Liu and Wei 1988; Benton, et al. 2013). In contrast, several new genera and species, many of which are endemic to Chinese localities like *Jurongia*, *Qingshania*, *Suius*, *Plesioperleidus*, have their first occurence in the Early Triassic (Wang, et al. 2007; Benton, et al. 2013; Qiu, et al. 2019). The fossil record of Late Permian freshwater actinopterygians is more abundant, with multiple genera described from the *Datpocephalus* Zone of the Beaufort Group of South Africa (Viglietti 2020), the Sokolki and Vyazniki faunal assemblage

in central-eastern Russia (Sennikov et al. 2003; Sennikov and Golubev 2006) and the Blackwater Group in western Australia (Campbell and Phuoc 1983). Almost none of these taxa are present in the Early Triassic, either because there is a lack of actinopterygian fossils of this age (South Africa), or because of faunal changes (central-eastern Russia, western Australia), with the exception of *Saurichthys* from central Russia (Sennikov, et al. 2003; Sennikov and Golubev 2006)

The abundance of sedimentary rock exposures of any given age is typically correlated with the abundance of fossils and, by extension, to the perceived level of palaeodiversity for the time interval (Raup 1976; Smith 2001; Smith and McGowan 2011; Vilhena and Smith 2013; Henderson, et al. 2022, but see Benton, 2015). The rock record and abundance of ray-finned fishes in the Changsinghian are both very low but apparently decoupled, a situation that seems to confirm what was previously reported for the fossil record of actinopterygians from the United Kingdom (Lloyd and Friedman 2013). More data will be needed to clarify actual actinopterygian richness, diversity and abundance in the Changsinghian and thus the real entity of the impact of the PTME on the clade.

1.2.2 Early Triassic

The Early Triassic (251.9-247.2 Ma) actinopterygian fossil record benefits from the presence of a number of highly fossiliferous localities (Fig. 1.3B-E) with research history approximating or exceeding 100 years: East Greenland (Stensiö 1932; Nielsen 1936, 1942), the sites in northern and southern Madagascar (Priem 1924; Piveteau 1929; Piveteau 1935;

Lehman 1952), Spitzbergen in the Svalbard Isles (Stensiö 1921b; Stensio 1925a) and British Columbia, Canada (Lambe 1914, 1916; Warren 1936; Schaeffer and Mangus 1976). These sites can be considered Lagerstätten due to the high number of specimens that were recovered and described, and are invaluable as the source of much of our current knowledge of the TEFF genera (Brinkmann, et al. 2010; Romano, et al. 2016). However, the imbalance between the huge amount of data collected from these sites and the data from the rest of the world could skew our perception of the richness of the period by over-representing the taxa found in such deposits and inducing artefact diversity peaks by the so-called Lagerstätten-effect (Seilacher, et al. 1985; Benson and Butler 2011; Romano, et al. 2016; Flannery Sutherland et al. 2019; Walker et al. 2020). Early Triassic actinopterygians are also known, in lower numbers and richness, from the Karoo Group of southern Africa (Murray 2000; Bender and Hancox 2004), the Siberian and Caspian region in Russia (Minikh and Minikh 1997; Ivanov and Klets 2007), Australia (Dickins and McTavish 1963; Northwood 1999; Haig et al. 2015; Berrell et al. 2020), Tasmania (Johnston and Morton 1889, 1890; Dziewa 1980; Bender 2008), central-western USA (Romano, et al. 2012; Romano, et al. 2017; Romano, et al. 2019), India and Nepal (Beltan and Janvier 1978; Mishra et al. 1990; Gupta 2009; Romano et al. 2016c), Croatia (Herak et al. 1983) and several locations in eastern and northern China (Jin 2006; Tong et al. 2006; Wang, et al. 2007; Li 2009; Xu and Gao 2011; Xu et al. 2015; Benton, et al. 2013; Sun et al. 2013; Tintori et al. 2014b). The high level of

cosmopolitanism in the Early Triassic actinopterygian fossil record makes the Lagerstätten-effect less pronounced (Romano, et al. 2016), although novel analytical techniques and new data could challenge this view in the future (see below).

Most localities, including those considered Lagerstätten, are clustered at mid- and high-palaeolatitudes (Fig. 1.3B-E), with the exception of a few sites such as Nevada and Idaho, USA (Romano, et al. 2017; Romano, et al. 2019). As a consequence, when considering raw counts of genera and species in the palaeogeographic context, low palaeolatitudes appear to be the least diverse areas of the Early Triassic for actinopterygians. This departure from the standard global diversity gradient, with the richest regions being around the equator, is restricted to the Early Triassic (Jablonski et al. 2006; Mittelbach et al. 2007). The inversion of the diversity gradient could be linked to the extremely warm Early Triassic climate, generating unfavourable conditions for life in the equatorial region, both on land and in the sea (Sun, et al. 2012; Romano, et al. 2020), but it is equally possible that it derives from a collection bias, since most of the sites are concentrated in the modern-day northern hemisphere (Fig. 1.4). Geographical unevenness and anthropogenic collection biases can influence our perception of palaeodiversity sampling: in particular, Europe and North America are the most intensely sampled areas of the world, not only for actinopterygians or in the Early Triassic (Close et al. 2020; Henderson, et al. 2023). The Madagascar Lagerstätten and other global sites only mitigate this issue to a certain degree, and geographical

sampling for the Early Triassic is strongly uneven (Fig. 1.3B-E) (Romano, et al. 2016), to the point that existing data pertaining to the latitudinal diversity gradient may not be accurate.

A commonly associated group of genera, comprising *Australosomus*, *Boreosomus*, *Birgeria*, *Bobasatrania*, *Pteronisculus*, *Saurichthys* and *Teffichthys* (formerly *Perleidus madagascariensis, P. lehmani, P. lutoensis, P. stoschiensis, P. woodwardi*, see Marramà *et al*., 2017), characterises marine sites in Europe and Madagascar, alongside small numbers of endemic taxa, from the earliest Triassic until the Smithian (White 1932; Cox and Smith 1973; Schaeffer and Mangus 1976; Brinkmann, et al. 2010; Tintori, et al. 2014a; Romano 2021). Coeval Eastern Tethys sites, on the other hand, have a distinct actinopterygian fauna, characterised by common occurrences of the genera *Plesioperleidus*, *Jurongia* (Perleididae), *Suius* and *Qingshania* (Parasemionotidae) and the omnipresent *Saurichthys* (Jin 2006; Benton, et al. 2013; Qiu, et al. 2019). The Spathian (late Olenekian) appears to deviate from this pattern (Fig. 1.2E): despite being the longest stage of the Early Triassic, it is almost devoid of actinopterygian fossils with just a handful of occurrences from China, United States, Poland and Svalbard (Sun, et al. 2013; Tintori, et al. 2014b; Kogan and Romano 2016; Romano, et al. 2017; Brayard, et al. 2017). It has been hypothesised that this gap could have been caused by a lower frequency of anoxic oceanic events, compared with the rest of the Early Triassic (Romano 2021).

Early Triassic freshwater faunas are more common in Gondwana than in Laurasia (Fig. 1.3B-E) and are fewer in number when compared to the Middle and Late Triassic (Murray 2000; López-Arbarello 2004; Jin 2006; Berrell, et al. 2020). Genera like *Acrolepis*, *Apateolepis*, *Cleithrolepis*, "*Elonichthys"* and *Myriolepis* are commonly found in Australia and southern Africa (Murray 2000; López-Arbarello 2004; Berrell, et al. 2020). Actinopterygians known from freshwater deposits in Laurasia are fewer and no genus, apart from *Saurichthys*, has a wide distribution (Minikh and Minikh 1997; López-Arbarello 2004; Brinkmann, et al. 2010). The genus *Saurichthys*, in fact, is a truly cosmopolite taxon, having colonised freshwater and marine environments all around Pangaea (Dziewa 1980; Minikh and Minikh 1997; Bender and Hancox 2004; Mutter et al. 2008; Romano, et al. 2012; Kogan and Romano 2016a, b). When coupled with long geological timescales, wide geographical distribution can be typical of wastebasket taxa e.g., "*Elonichthys*", *Rhadinichthys*, *Palaeoniscum*; (Henderson, et al. 2023). However, in the case of the Early Triassic, it may be a sign of "disaster taxa": genera that thrive in perturbed post-extinction environments (Kauffman and Harries 1996). While none of the TEFF genera have particularly long-spanning occurrences that might be indicative of wastebasket taxa or prevalence in deposits typical of "disaster taxa" (Romano, et al. 2016), the geographically wide distribution of some genera hints at a more complex diversification patterns that novel research approaches, like non-invasive imaging, could help disentangle.

1.3 Taphonomy and preservation of Early Triassic actinopterygians

1.3.1 Taphonomy of fossil fish

Taphonomy fundamentally underpins palaeontology, because it investigates the interplay of the *post mortem* processes a carcass undergoes – in particular how organic material is lost to decay or is transferred to the lithosphere by fossilisation processes (e.g. Brett and Baird 1986; Briggs 1995; Behrensmeyer et al. 2000; Purnell et al. 2018; Gabbott et al. 2021). Taphonomic investigations on fossils are concerned not only with inferences on ecology, mode of death of organisms and/or the palaeoenvironmental conditions at the time of death using parameters like mode of preservation, completeness and mineralisation (e.g. Brett and Baird 1986; Greenwood and Donovan 1991; Fernández-Jalvo et al. 2011; Fernández et al. 2017), but also on the pathways of preservation of organic material and the biases that may prevent or influence the preservation of organisms, thus assisting our interpretations of the fossil record (Briggs and Kear 1993b; Briggs and Kear 1993a; Sansom et al. 2010; Sansom et al. 2011).

When considering the fossil record of fish, it is common to find only microremains of both chondrichtyans and osteichthyans (e.g. teeth, scales, isolated bones) (e.g. Burrow et al. 2013; Cavicchini et al. 2018; Szabó et al. 2019), due to the fact that fish carcasses tend to disarticulate after death, limiting the amount of information available (Mancuso 2003; Orr et al. 2016). The presence of complete or partially articulated fish

fossils (sometimes in statistically relevant quantities) can allow the reconstruction of some palaeoenvironmental variables, based upon the interpretation of features of the skeletons and the overall preservation (Elder and Smith 1988; Tintori 1992; Chellouche et al. 2012; Malenda et al. 2012; Pan et al. 2019). The degree of disarticulation of the fish skeleton can give an estimate of the time elapsed between deposition on the water-sediment interface and burial, although it is unclear whether disarticulation proceeds from the head towards the tail (Mancuso 2003; Chellouche, et al. 2012), or if it starts from the fins (Clements et al. 2022; this study). Complete but locally scattered carcasses indicate a reduced or absent floatation period before deposition on the water-sediment interface, or some degree of binding by microbial mats (Chellouche, et al. 2012; Pan et al. 2015; Pan, et al. 2019; Orr, et al. 2016); iso-orientation of carcasses or disarticulated remains can hint at the presence of bottom currents (Diedrich 2009; Pan, et al. 2019); and finally, fin, mouth and/or vertebral column tetany are potential indicators of low oxygen levels in the water at the time of death (Faux and Padian 2007; Anderson, et al. 2013).

Many previous studies have regarded the taphonomy of freshwater fossil fish assemblages (e.g. Wilson and Barton 1996; Mancuso 2003; Malenda, et al. 2012), and time periods other than the latest Palaeozoic or earliest Mesozoic (e.g. Smith et al. 1988; Wilson and Barton 1996; Pan, et al. 2019). Studies on latest Permian fish are lacking altogether, and only one taphonomic investigation has focussed on Early Triassic fish fossils (Anderson, et al. 2013). This study used the fossils of four of the most

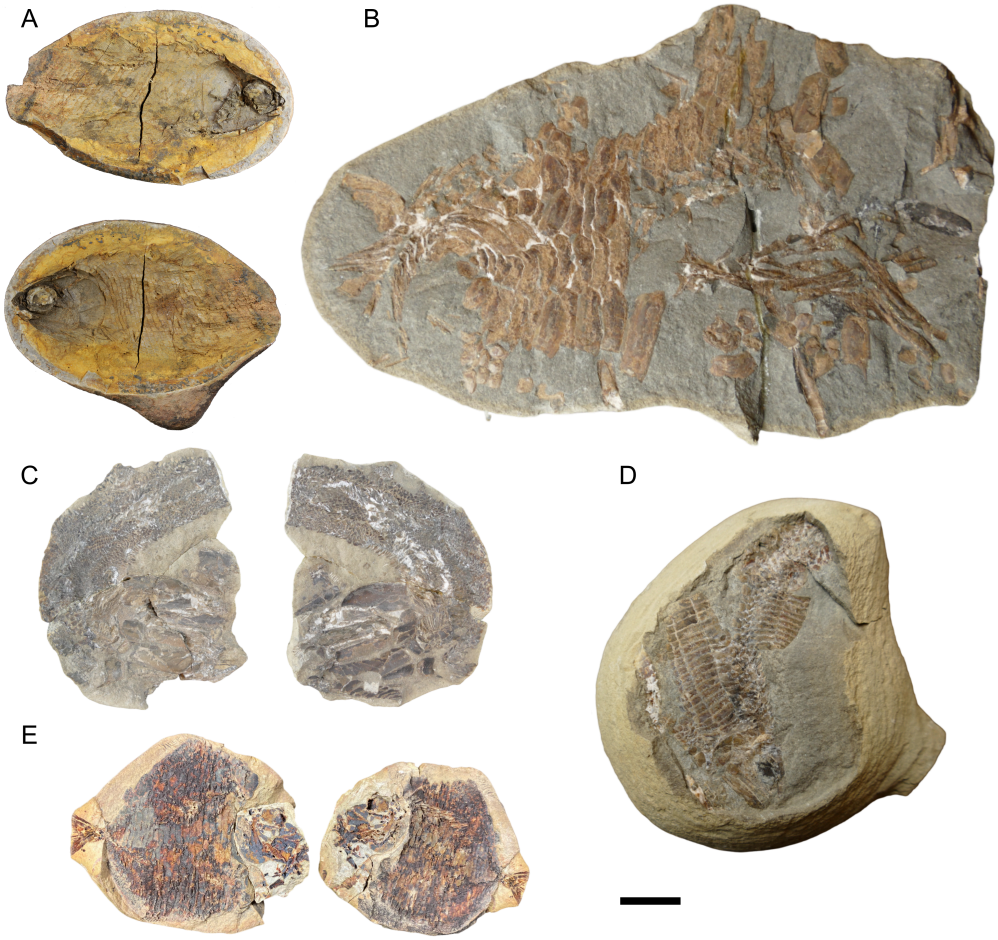


Fig. 1.5: Examples of concretionary preservation of actinopterygian fossils from the Early Triassic. A, *Boreosomus gillioti*, specimen NHMUK PV P19814-5 from the Early Triassic of Madagascar; B, *Bobasatrania* sp., specimen NHMD–159153 from the Early Triassic of Greenland; C, *Pteronisculus gunnari*, specimen NHMD–157507 from the Early Triassic of Greenland; D, *Australosomus kochi*, specimen NHMD–157312 from the Early Triassic of Greenland; E, *Bobasatrania mahavavica*, specimen NHMUK PV P17090-1 from the Early Triassic of Madagascar. Specimens A, E are part of the Natural History Museum collection (London, UK); specimens B-D are part of the Natural History Museum of Denmark collection (Copenhagen, Denmark). Scale bar is 2 cm.

abundant osteichthyan genera from the Wapiti Lake area (British Columbia, Canada) to extrapolate palaeoenvironmental conditions (anoxic bottom waters) and considerations on the ecology of the genera. Two of those (*Bobasatrania*, interpreted as a deep-water slow swimmer, and *Boreosomus*, a shallow-water fast swimmer) are traditionally included in

the TEFF. We lack, however, wider-spectrum investigations on whether ecology or anatomy influenced the preservation potential of fish. Many different ecologies are represented among Early Triassic actinopterygians, from fast-swimming carnivores (e.g., *Birgeria*, *Saurichthys*), to slow-swimming durophagous fish (e.g. *Bobasatrania*) (Schaeffer and Mangus 1976; Beltan 1996), and from small, fusiform, generalist "palaeopterygians" with heavily mineralised scales (e.g., *Pteronisculus*, *Boreosomus*) to genera that lacked scales altogether (*Birgeria*, *Saurichthys*) (Stensio 1925a; Nielsen 1949; Schaeffer and Mangus 1976). In addition, the majority of the most fossiliferous Early Triassic localities are from proximal marine palaeoenvironments, with variable but predominant siliciclastic influx (e.g. Boast and Nairn 1982; Mørk et al. 1999; Neuman 2015; Surlyk et al. 2017; Qiu, et al. 2019). Our picture of Early Triassic actinopterygian diversity may therefore be heavily biased towards continental shelf-dwelling fish, missing a portion of the actual diversity that, without additional data, is hard to quantify.

1.3.2 Modes of preservation for actinopterygians in the Early Triassic

Microremains (e.g., isolated teeth or scales) and body fossils flattened along bedding planes are common modes of preservation for marine actinopterygians from the Early Triassic (e.g. Schaeffer and Mangus 1976; Tong, et al. 2006; Neuman 2015; Dai, et al. 2023), but the most striking specimens are preserved in concretions (Fig. 1.5) (Nielsen 1942; Beltan 1996; Tintori, et al. 2014a; Kogan and Romano 2016a; Romano 2021; Qiu, et al. 2019). Concretions form and grow by

precipitation of cement around a nucleation point in a localised volume of sediment, both in freshwater and marine settings, and organisms can fossilise within the concretions (McCoy 2014; Mccoy et al. 2015a). The supersaturated conditions necessary to start the precipitation of cement may be induced by the interplay between the presence of microorganisms, organic material and the creation of a microenvironment with limited fluid exchange with the surroundings, but the actual triggering mechanisms are still poorly understood (Raiswell 1976; Mccoy, et al. 2015a; Yoshida et al. 2018).

Concretions are known to preserve fossils in 3D and with soft tissues (e.g. McCoy et al. 2015b; Clements et al. 2019; Figueroa et al. 2023). Concretionary preservation is not restricted to the Early Triassic and is also not particularly common in this epoch, when compared to the rest of the Mesozoic (McCoy 2014), but concretions represent an important source of data. As previously stated, the TEFF genera typically known from concretionary preservation, such as *Saurichthys*, *Pteronisculus*, *Australosomus*, *Boreosomus*, *Birgeria*, are known in great detail (Stensio 1925a; Nielsen 1942, 1949; Lehman 1952; Argyriou et al. 2018). This fact is important and could hide a composite bias: the most intensely sampled Early Triassic Lagerstätten are those that yielded hundreds of fossil-bearing concretions, and the genera preserved in this way (e.g. *Pteronisculus*, *Bobasatrania*, *Boreosomus*, *Australosomus*, *Birgeria*, *Saurichthys*) have been the subject of seminal, highly detailed descriptive works that still constitute the basis of our knowledge of the TEFF (Stensio

1925a; Nielsen 1942, 1949; Lehman 1952). On the other hand, a number of genera (critically, many of which appear to be endemic to specific sites), irrespective of preservation mode, are not known in similar levels of detail (Schaeffer and Mangus 1976; Beltan 1996; Tong, et al. 2006). Our knowledge could, therefore, be heavily biased towards the genera more common in Lagerstätten because of uneven geographical sampling, collection bias towards concretions, or even because some genera are more likely to fossilise inside a concretion. However, taphonomic studies on preservation within Early Triassic concretions are still lacking, despite a growing awareness of the preservational and taphonomic biases that can obscure our understanding of palaeofaunas (Fraiser et al. 2011; Henderson, et al. 2023).

This knowledge gap about potential biases compounded by concretionary preservation could be bridged with the help of decay experiments, which represent valid mechanisms to answer questions about the processes involved in fossilisation and in the formation of exceptional fossils (Iniesto et al. 2013; Sansom 2014; Butler et al. 2015; Briggs and McMahon 2016; Purnell, et al. 2018). Sediment can in fact be used in the context of a decay experiment, burying carcasses in different granulometries/ mineralogies to test and quantify the effects (if any) of the sediment on the decay process over time (e.g. Wilson and Butterfield 2014; McCoy, et al. 2015b; Naimark et al. 2016; Naimark et al. 2018b; Newman et al. 2017). However, complications are introduced by the use of sediment in a decay experiment: the operations of exhumation and dissection, needed for data

collection, can artificially damage the carcasses and distort the experimental results (Wilson and Butterfield 2014; Naimark et al. 2018a). Novel approaches for *in situ* non-destructive data collection, involving the use of micro-computed tomography (XCT scanning), have been implemented in recent investigations with the aim of collecting more truthful decay data from carcasses in sediment (Selly and Schiffbauer 2021; Waskom et al. 2023). In theory, non-destructive imaging of carcasses *in situ* under sediment can circumvent the issues related to exhumation and dissection by making these operations unnecessary, elevating the accuracy of experimental decay data and potentially bringing about a radical change in the way decay experiments are designed. However, thus far these pioneering investigations have not tested the actual accuracy of *in situ* imaging against a control, and some variables in their experimental designs (e.g., presence of unquantified and unidentified bacteria, lack of a true experimental control, use of non-standardised sediment) make results hard to generalise and build upon with further investigations. In order to improve the understanding of fossilisation inside concretions, a foundation of clear, repeatable decay experiments using XCT scanning *in* situ would be sorely needed.

1.4 Aims and thesis outline

The need for data to disentangle early actinopterygian phylogeny has been underlined in numerous studies (Friedman and Sallan 2012; Friedman 2022; Romano 2021). The application of novel techniques, like

XCT scanning, has proven to be an effective way to improve our knowledge of early actinopterygian anatomy and phylogeny, even in the case of museum specimens previously described with more traditional approaches (Argyriou, et al. 2018; Argyriou et al. 2022; Coates and Tietjen 2018; Giles et al. 2023; Caron et al. 2023). The aim of this thesis, as it was originally designed, was to analyse the Early Triassic fossil record of actinopterygians, looking for potential preservational or taxonomic biases that may hinder our understanding of a key period for actinopterygian evolution. Museum visits were going to be a key activity in order to find suitable specimens for (re)description, potentially using XCT scanning, and to build a database of taphonomic data about preservation styles from key localities and taxa (e.g. skeletal completeness). Experimental work on specific taxa with conservative anatomical elements (e.g., *Polypterus*, with its heavily mineralised scales) was meant to complement the datasets from museum collections, to improve the understanding of early actinopterygian preservation patterns.

However, the original plan for this thesis was severely impacted by the global Covid-19 pandemic. The difficulties to travel to access collections and specimens, which persisted for over a year, forced a reorganisation of the activities. The expected number of museum visits was scaled down, relying mostly on specimens already acquired for taxonomic descriptions, while taphonomy experiments were given more space, but focusing on a different taxon (zebrafish) for ease of acquisition, and on the implementation of new methodologies rather than on the preservational

biases. The focus of the thesis therefore moved to the use of XCT scanning in taxonomy and taphonomy, with the following overarching aims:

- Obtain novel anatomical and taxonomical data on Early Triassic actinopterygians, using tomographic datasets and segmentation to obtain 3D models of internal anatomical structures otherwise impossible to describe.
- Design and conduct decay experiments testing the use of XCT scanning as an innovative way to collect decay data non-destructively.

In chapter 2 I focus on the redescription of a specimen of Early Triassic actinopterygian previously described in the 1940's and belonging to a speciose genus. The new description is based on datasets acquired using XCT scanning and synchrotron tomography, which allowed me to completely resolve the internal anatomy, preserved in 3D and in striking detail. Using the new data, I tested the hypothesis that hidden morphological diversity confuses the taxonomy of Early Triassic actinopterygians, while collecting useful data on the ontogeny of "palaeopterygians".

In chapter 3 I explore the use of XCT scanning in decay experiments. This methodology is not commonly employed in experimental taphonomy, so this investigation is a proof-of-concept to clarify the basic aspects of conducting decay experiments using non-destructive imaging to collect data. In particular, I tested the hypothesis that exposure to X-rays during XCT scanning does not impact decay, making it a viable methodology.

Finally, in chapter 4 I investigate the use of diffusible contrast-enhanced computed tomography (diceCT scanning) in the context of a decay experiment. Partially building upon the results of the previous chapter, in this proof-of-concept study I test the hypothesis that with diceCT scanning it is possible to collect decay data from a carcass *in situ* under sediment, including information on the internal anatomy.

2 | A Portrait of a Young Fish: Redescription of *Pteronisculus gunnari* (Nielsen, 1942) from a juvenile specimen from the Early Triassic of East Greenland, with implications for ontogenetic development in early actinopterygians

Iacopo Cavicchini[1*], Thodoris Argyriou[2,3,4,5], Vincent Fernandez[6,7], Katheen Dollman[7], Sam Giles[1,8]

[1]Earth Sciences, University of Birmingham, Edgbaston, B152TT, Birmingham, UK.

[2]Paleontological Institute and Museum, University of Zurich, Karl-Schmid-Strasse 4, 8006, Zurich, Switzerland.

[3]CR2P, MNHN-CNRS-Sorbonne Universitée, Muséum National d'Histoire Naturelle, 57 Rue Cuvier, 75005, Paris, France.

[4]Department of Earth and Environmental Sciences, Paleontology & Geobiology, Ludwig-Maximilians-Universität München, Richard-Wagner-Str. 10, 80333, München, Germany.

[5]GeoBio-Center, Ludwig-Maximilians-Universität München, Richard-Wagner-Str. 10, 80333, München, Germany.

[6]Imaging and Analysis Centre, The Natural History Museum, Cromwell Road, SW7 5BD, London, United Kingdom.

[7]European Synchrotron Radiation Facility, 71 Avenue des Martyrs, CS-40220 38043 Grenoble, France

[8]The Natural History Museum, Cromwell Road, SW7 5BD, London, United Kingdom

My contribution to this chapter involved most of the data analysis (including segmentation and phylogenetic analyses), interpretation of results and production of the manuscript, including the figures. Sam Giles cured the tomography of the specimen. Vincent Fernandez, Kathleen Dollman and Sam Giles cured the synchrotron analysis of the specimen. Thodoris Argyriou and Sam Giles contributed to the data collection and data analysis (segmentation). All coauthors gave feedback on the analysis, interpretation of results and on the drafts of the manuscript.

This chapter was submitted and is currently under review in the Journal of Systematic Palaeontology. A preprint was published through the Biorxiv repository and is available at: https://doi.org/10.1101/2024.07.06.598961.

2.1 Introduction

During the Early Triassic (252-247 Ma) a group of ray-finned fish taxa attained a wide distribution and left a plentiful—and often exceptionally preserved—fossil record (Brinkmann, et al. 2010). The coherence of this fauna first became apparent in the 1970s (Schaeffer and Mangus 1976), prompting the naming of the Triassic Early Fish Fauna (TEFF) (Tintori, et al. 2014a; Romano 2021). The TEFF includes taxa with debated phylogenetic placements: taxa generally considered non-neopterygians (e.g., *Saurichthys*, *Birgeria*, *Australosomus, Boreosomus, Pteronisculus*), possible stem neopterygians (*Bobasatrania*) and crown group neopterygians (e.g., *Watsonulus*) (Olsen 1984; Gardiner, et al. 2005; Brinkmann, et al. 2010; Romano 2021; Tintori, et al. 2014a; Xu et al. 2014a; Friedman 2015; Argyriou, et al. 2018; López-Arbarello and Sferco 2018). Surprisingly, given the phylogenetic uncertainties, many of the boreal TEFF taxa are among the best known fossil actinopterygians, due to detailed monographic descriptions (Stensiö 1921a, 1932; Stensio 1925a; Nielsen 1949). This cosmopolitan and diverse fauna appears to thrive in the immediate aftermath of the Permo-Triassic mass extinction (PTME), a catastrophe that wiped out up to 96% of all species (Erwin, et al. 2002; Chen and Benton 2012), but how this event has affected actinopterygians is still unclear. The abrupt rise and diversification of the TEFF could represent a genuine recovery fauna, or an artefact related to the very poor late Permian actinopterygian fossil record (Friedman and Sallan 2012; Vázquez and Clapham 2017; Smithwick and Stubbs 2018;

but see Henderson, et al. 2022; and Henderson, et al. 2023). Some TEFF genera, like *Bobasatrania*, *Saurichthys* and possibly *Pteronisculus*, are indeed known from the late Permian (Gardiner and Jubb 1975; Tintori, et al. 2014a), but broader macroevolutionary patterns are the subject of ongoing debate (Friedman 2015; Romano, et al. 2016; Romano 2021; Smithwick and Stubbs 2018).

The genus *Pteronisculus* was originally erected by White (1933), who described two new species of actinopterygians from the Early Triassic of north-eastern Madagascar (*P. macropterus* and *P. cicatrosus*, the latter being the type species). A few years later, *Glaucolepis* (Stensiö 1921a), initially erected to contain incomplete fossil fish material from the Early Triassic of Svalbard, was synonymized with *Pteronisculus* (White and Moy-Thomas 1940). The temporal and geographical range of this genus grew with successive descriptions of new species from the Early Triassic of east Greenland (Nielsen 1942), north-western Madagascar (Lehman 1952), Nevada, USA (Romano, et al. 2019) and the Middle Triassic of Luoping, China (Xu et al. 2014b; Ren and Xu 2021). Fragmentary material has also been referred to the genus from the late Permian of South Africa (Gardiner and Jubb 1975) and the Early Triassic of Alberta and British Columbia, Canada (Lambe 1916; Schaeffer and Mangus 1976). The anatomy of *Pteronisculus* is known in great detail, especially from five species from the Early Triassic of East Greenland (Nielsen 1942) and four from north-western Madagascar (Lehman 1952). This taxon was originally considered a member of the ‘Palaeonisciformes’, an assemblage of taxa

which was thought to be a genuine clade united by a conservative skeletal morphology, but is now known to be paraphyletic (Gardiner & Schaeffer, 1989); in this work we use the term "palaeopterygian" to avoid historical associations of monophyly (see Friedman and Giles 2016 and references therein). *Pteronisculus* is routinely included in phylogenetic analyses of crown neopterygians, either as a formal outgroup or as a representative of non-neopterygian morphology more generally (Olsen 1984; Gardiner, et al. 2005; Hurley, et al. 2007; Xu, et al. 2014a; López-Arbarello and Sferco 2018). In more targeted investigations of early actinopterygian relationships, *Pteronisculus* has fluctuated between the actinopterygian and neopterygian stem (e.g., Lund, Poplin & McCarty, 1995; Cloutier & Arratia, 2004 and references therein; Hurley et al., 2007; Xu, Gao & Finarelli, 2014, etc.). More recently, it has been consistently recovered as a stem actinopterygian (but see Figueroa et al. 2019), although with limited agreement as to its immediate sister taxa or position relative to the actinopterygian crown node: as sister taxon to the Carboniferous *Cosmoptychius* and Bear Gulch actinopterygians (Giles, et al. 2017); in a clade with *Cyranorhis*, which is resolved as the sister taxon to a clade comprising the Triassic *Boreosomus*, *Cosmoptychius*, *Mesopoma* and a subset of Bear Gulch taxa (Ren and Xu 2021), or as sister to *Beagiascus* and a heterogeneous group of Carboniferous (*Cosmoptychius*, *Kansasiella*, *Coccocephalichthys*, *Lawrenciella*), Permian (*Luederia*), and Early Triassic (*Boreosomus*) genera (~~*Boreosomus*~~) (Argyriou, et al. 2022).

Although 13 species of *Pteronisculus* are described in the literature (plus two to three more dubious attributions; see e.g., Gardiner and Jubb 1975; Schaeffer and Mangus 1976; Romano, et al. 2019), only Ren & Xu (2021) and Caron et al. (2023) have included more than one taxon in a phylogenetic analyses, and the latter only consider neurocranial characters. In large part, this can be attributed to the uneven amount of information available for each taxon. *P. stensioi* and *P. magnus* from East Greenland have been described in great detail from 3D material (Nielsen 1942), and as are most commonly used in phylogenetic analyses. The dermal skeleton of the Malagasy species is well described, but due to preservational biases the braincase is only described in *P. cicatrosus* (Lehman 1952; Beltan 1996). The recently described Middle Triassic Chinese species *P. nielseni* and *P. changae*, and the Early Triassic *P. nevadanus* from Nevada, have been described based upon several complete but flattened specimens, with the result that the dermal skeleton is almost completely known but internal anatomy is lacking (Xu, et al. 2014b; Romano, et al. 2019; Ren and Xu 2021). *P. gyrolepidoides* is known from very fragmentary and incomplete remains (Stensiö 1921a). *P. arcticus*, *P. aldingeri*, and *P. gunnari* are also known from three-dimensional material and are referred to throughout Nielsen's (1942) monograph, but are rarely described in their own right, mostly relying on comparisons with *P. magnus* or *P. stensioi*.

Here, we use X-ray computed tomography (XCT) to reinvestigate the holotype of *P. gunnari*, previously only partially described by Nielsen

(1942). Its 3D preservation allows us to describe a wealth of morphological features previously unknown in the genus, including a small coronoid process formed by the dentary, medially-directed teeth on the palate, an intercalar, and a propterygium fused to the first lepidotrichium. We present an expanded phylogenetic analysis incorporating multiple species of *Pteronisculus*, confirming its monophyly. Its position nested deep within a clade with Carboniferous origins suggests it may be unsuitable for representing the morphology of generalized early actinopterygians.

2.2 Materials and methods

Fossil material and locality. NHMD–73588 (*ex*-MGUH VP.791), curated in the Natural History Museum of Denmark (Copenhagen), is a complete, articulated specimen including the skull, paired fins, median fins, body and caudal fin, lacking only the extreme tip of the dorsal lobe of the tail (Fig. 2.1). The cranium in particular is preserved in 3D and almost perfect articulation. The specimen was likely preserved within a concretion and has been extensively prepared to expose the skull in the round and the right side of the body and fins. It was found between 1932 and 1937 in the Kap Stosch area, West locality of the Spath Plateau, East Greenland (Nielsen 1942), in Griesbachian (Induan) strata of the Kap Stosch Formation (Surlyk, et al. 2017).

The fossil comes from Fish Zone III, one of five highly fossiliferous strata that were discovered and sampled intensively in the late 1920s and the 1930s (Nielsen 1942; Surlyk, et al. 2017). The Triassic ichthyofauna is rich

and includes actinopterygians (e.g., *Birgeria*, *Saurichthys*, *Australosomus*, *Boreosomus*, *Bobasatrania*), sarcopterygians (e.g., *Laugia*, *Sassenia*, *Whiteia*) and chondrichthyans (e.g., *Polyacrodus*, *Nemacanthus*) (Stensiö 1932; Brinkmann, et al. 2010). NHMD–73588 was described and chosen as the holotype of *Pteronisculus gunnari* by Nielsen (1942), who originally assigned it the specimen field number 18 and carried out mechanical preparation. The specimen itself does not figure in any plates in Nielsen's monograph, but the dermal bones of the skull roof, plus the rostral and nasals, are figured in a line drawing (Nielsen 1942: fig. 26A, p. 133).

X-ray Computed Tomography. The anterior portion of NHMD–73588, containing the three-dimensionally preserved cranium, was imaged using X-ray computed tomography at the XTM Facility, Palaeobiology Research Group, University of Bristol using a Nikon XT H 225 ST system. The parameters used are: 3140 projections, 224 kV, 191 μA, 1 mm copper filter, and a cone beam magnification resulting in an isotropic voxel size of 22.5 μm. The resulting images were processed using Mimics Materialise software (v.20-23, biomedical.materialise.com/mimics; Materialise, Leuven, Belgium) to create three-dimensional anatomical models. Most features are clearly visible in tomograms, although the smallest teeth (e.g. those on the oral surface of the palate, the vomers and the parasphenoid) appear to be on the limit of scan resolution. After segmentation, 3D models were exported in .ply format and processed in Blender, v. 3.4, for imaging and for digital reconstructions (https://www.blender.org/).

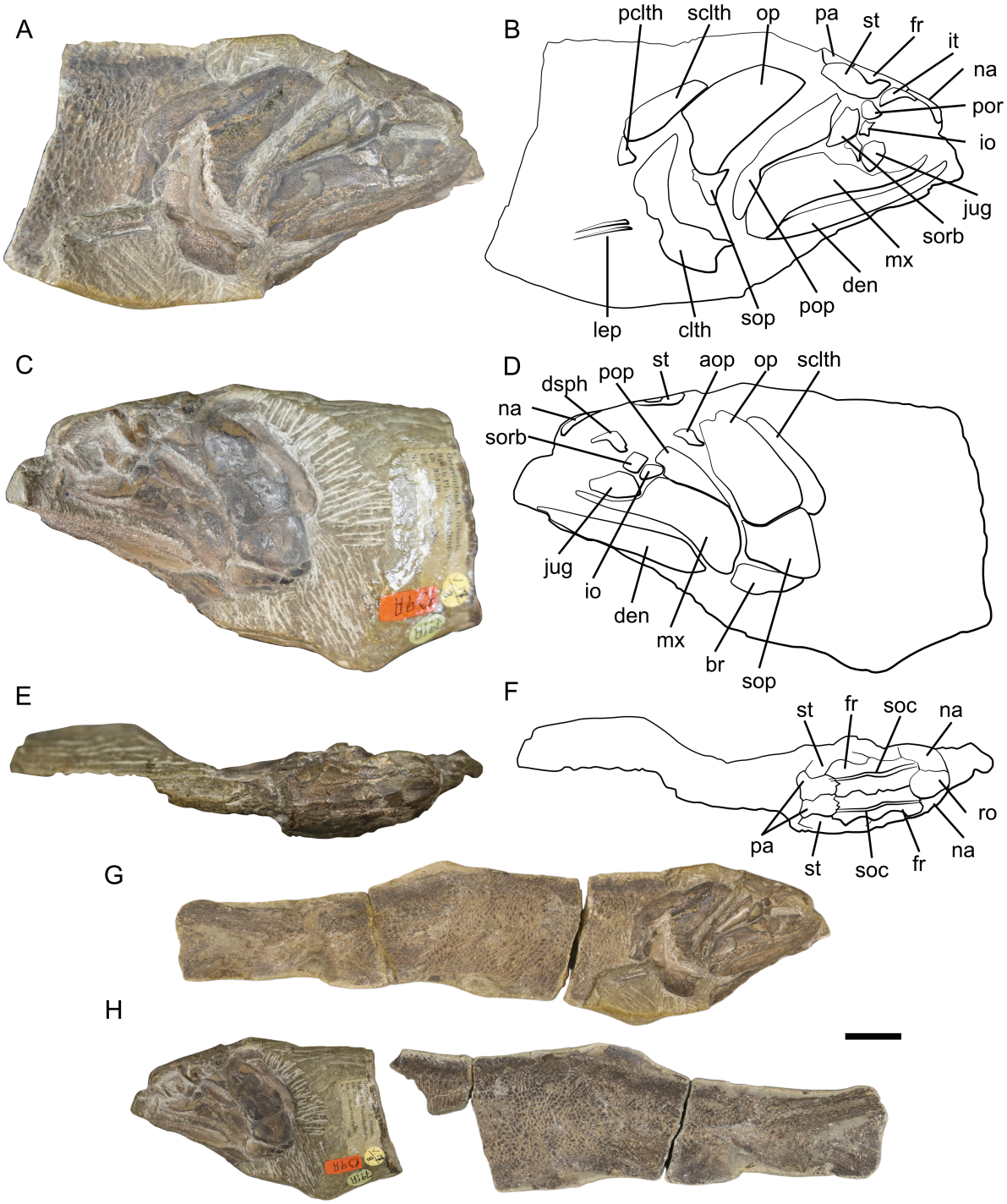


Figure 2.1: External photos and line drawings of *Pteronisculus gunnari* NHMD 73588, anterior half. Right lateral view (A) and interpretive line drawing (B). Left lateral view (C) and interpretive line drawing (D). Dorsal view (E) and interpretive line drawing (F). Entire specimen in right lateral (G) and left lateral view (H). Scale bar: 10 mm for A-F, 5 mm for G-H. Abbreviations: aop, accessory operculum; br, branchiostegal ray; clth, cleithrum; dsph, dermosphenotic; den, dentary; fr, frontal; io, infraorbital; it, intertemporal; jug, jugal; lep, lepidotrichia; mx, maxilla; na, nasal; op, operculum; pa, parietal; pclth, postcleithrum; pop, preoperculum; por, postorbital process; ro, rostral; sorb, suborbital; sclth, supracleithrum; soc, supraorbital canal; sop, suboperculum; st, supratemporal.

Synchrotron Tomography. The central region of the skull of NHMD–73588 was also imaged at the European Synchrotron Radiation Facility (ESRF) in Grenoble, France using propagation phase contrast synchrotron X-ray micro-Computed tomography at the BM05 beamline of the ESRF. The beam setup consisted of white beam from the 0.86 T 2-pole wiggler with fixed gap, filtered with 3.93 mm of Molybdenum, resulting in a total integrated detected energy of 133 keV. The acquisition setup consisted of an indirect detector, positioned 3.5 m downstream of the sample for propagation phase contrast, comprising a 2 mm thick LuAG ($Lu_3Al_5O_{12}$: Ce) scintillator with a visible light reflective layer; a 0.615x magnification from a Hasselblad macro 120 mm f/4 (Victor Hasselblad AB, Gothenburg, Sweden); and a sCMOS PCO.edge 4.2 (PCO, Kelheim, Germany). Measurements on recorded radiograph returned an isotropic pixel size of 10.14 µm. With this setup, the recorded field of view was 2048 x 304 pixels (horizontal x vertical), i.e., 20.77 x 3.08 mm (limited vertically by the size of the beam). To image the full specimen, 11 tomographic acquisitions were performed, moving the specimen by 2 mm along the vertical axis between each acquisition. To compensate for the limited horizontal field of view, the centre of rotation was shifted from the centre of the image by 900 pixels (9.13 mm), resulting in reconstructed tomograms of 3848 x 3848 pixels (39.02^2 mm^2). Each acquisition consisted of 5100 projections, each projection resulting from the accumulation of 5 frames of 10 msec exposure each (total integrated exposure of 50 msec), over a rotation of 360°. For each acquisition, 41 flatfield images (image without the

specimen) and 40 dark current images (image without beam) were recorded. Tomographic reconstruction was done with PyHST2 (Mirone et al. 2014) using the single distance phase retrieval approach (Paganin et al. 2002) with a δ/β = 1000 and an unsharp mask (sigma = 1.2, coefficient = 4). The resulting 32-bit float tomograms were converted to 16-bit integers by applying histogram windowing (value outside the 0.001% maximum and minimum percentiles were discarded). The post-processing also included ring correction (Lyckegaard et al. 2011; Matlab code for ring correction available at https://github.com/HiPCTProject/Tomo_Recon), normalisation of dense pyrite inclusions (the grey values of the inclusion are decreased to bring them closer to the values of the bones/sediment) (see Cau et al. 2017) and 3D cropping of the data.

Phylogenetic analysis. Our phylogenetic dataset is modified from that of Argyriou et al. (2022), in which the only species of *Pteronisculus* is *P. stensioi*. We added five additional species, coded from the literature: *P. gunnari*, *P. magnus* (Nielsen, 1942), *P. changae* (Ren & Xu, 2021), *P. nielseni* (Xu et al., 2014) and *P. cicatrosus* (Lehman, 1952); in addition, we coded NHMD–73588 as a different terminal from *P. gunnari*, separating the new information from the literature in order to investigate the impact of additional character information derived from XCT analysis on the topology of the genus *Pteronisculus*.

For the NHMD–73588 terminal, any characters describing skeletal morphology influenced by the juvenile/sub-adult condition of the individual at the time of death, were coded as '?' to reflect the missing adult

morphology (e.g., the anterior and mesocoracoid processes of the scapulocoracoid, the orbital and ethmoidal portions of the braincase).

We also added three characters from the character matrix of Ren & Xu (2021): lacrimal contributing to oral margin (absent/present); teeth on lacrimal (absent/present); position of dermosphenotic (dermosphenotic extending well below dermopterotic/dermosphenotic located at same horizontal level of dermopterotic). This brought the total to 303 characters. The following characters are ordered: 89, 91, 152, 173, 248, 258. Several character states for *Pteronisculus stensioi* were modified from those in Argyriou et al. (2022) to reflect the new information: char. 37: 1 to 0; char. 38: - to 0; char. 39: 0 to 1; char. 40: 1 to 0; char. 41: 0 to 1; char. 66: 0 to 1; char. 68: 0 to 1; char. 111: 1 to 0; char. 127: 1 to 0; char. 166: 0 to ?; char. 224: ? to 0; char. 225: ? to 1; char. 231: 0 to 1; char. 249: 0 to 1; char. 281: 1 to 0.

The equally weighted and implied weighted parsimony phylogenetic analyses were conducted in TNT (v. 1.6) (Goloboff et al. 2008; Goloboff and Morales 2023). The outgroup was constrained as follows for both analyses: (*Dicksonosteus arcticus* (*Entelognathus primordialis* ((*Acanthodes bronni* (*Cladodoides wildungensis Ozarcus mapesae*)) ("*Ligulalepis*" (*Dialipina salguerioensis*))). For the equally weighted analysis, the Consistency Index and Retention Index were calculated using the apposite TNT script (stats.run) on a random subset of 100 most parsimonious trees; Bremer support values were calculated using the built-in function of the software, performing a Tbr analysis on the 10752

most parsimonious trees, retaining trees that were suboptimal by up to 10 steps.

For the implied weights analysis, after some preliminary trials (k=8, see Appendix A5) we conducted the analysis with a very gentle concavity (K = 100) (Goloboff et al. 2018), recovering 135 best-fit trees and calculating a strict consensus tree.

2.3 Systematic palaeontology

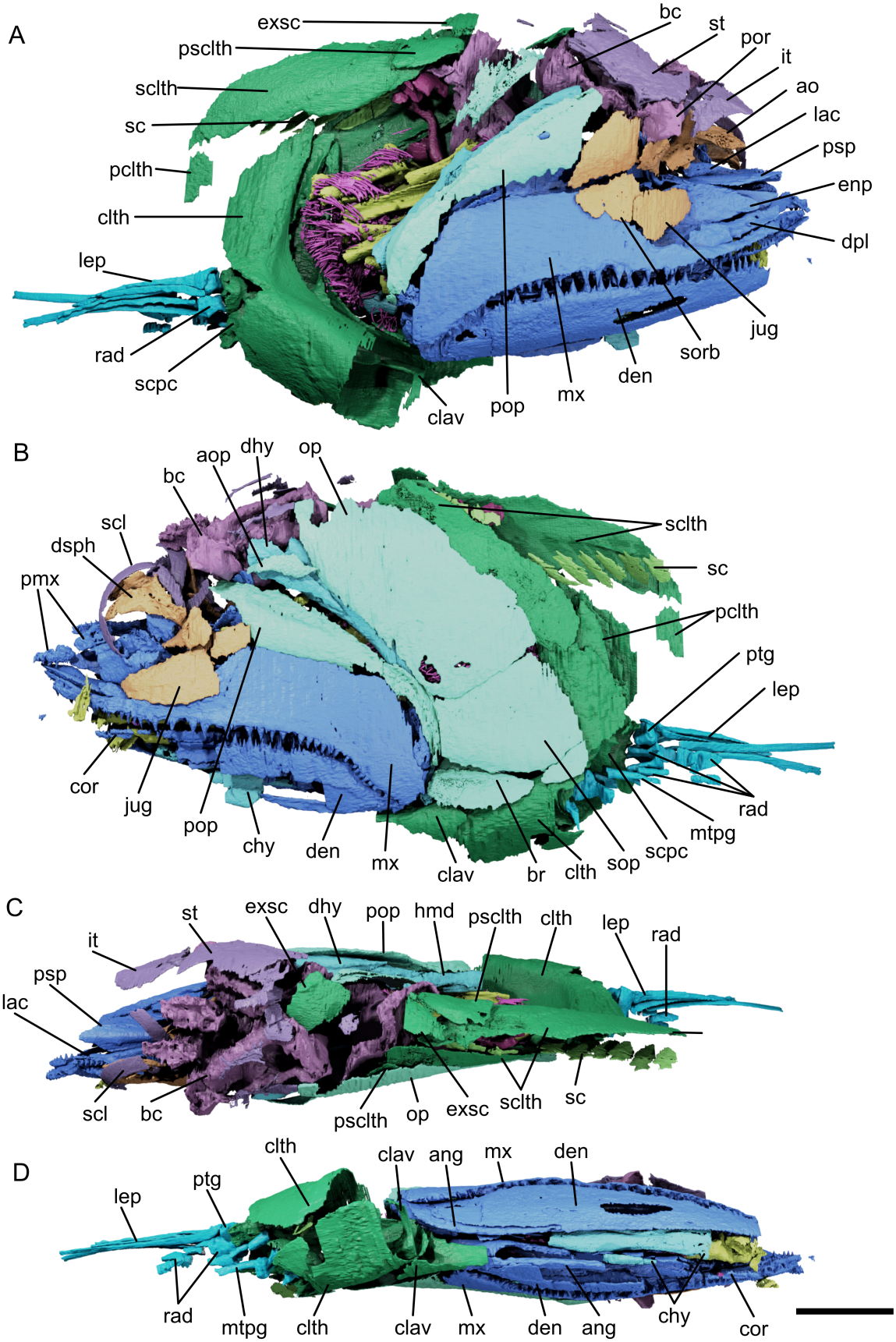
Superclass **Osteichthyes** Huxley, 1880

Class **Actinopterygii** sensu Goodrich, 1930

Genus Pteronisculus White, 1933

Species Pteronisculus gunnari Nielsen, 1942

Figure 2.2: Renders of external and internal anatomy of *Pteronisculus gunnari* NHMD–75388. Right lateral view (A), left lateral view (B), dorsal view (C) and ventral view (D). Some lepidotrichia and scales omitted. Scale bar: 10 mm. Colour coding of skeleton: orange, circumorbital; dark blue, jaws and palate; dark purple, skull roof and sclerotic ring; light purple, braincase; light blue, cheek and opercular series; turquoise, hyoid arch; yellow, branchial arches; magenta, gill rakers and toothplates; green, shoulder girdle; light green, scales; cyan, pectoral fin. Abbreviations: ang, angular**;** ao, antorbital**;** aop, accessory operculum**;** bc, braincase**;** br, branchiostegal ray**;** chy, ceratohyal**;** clth, cleithrum**;** clav, clavicle**;** cor, coronoid**;** dpl, dermopalatine**;** dsph, dermosphenotic**;** dhy, dermohyal; den, dentary**;** enp, entopterygoid**;** exsc, extrascapular**;** hmd, hyomandibula**;** it, intertemporal**;** jug, jugal**;** lac, lacrimal**;** lep, lepidotrichia; mtpg, metapterygium; mx, maxilla**;** op, operculum**;** pclth, postcleithrum**;** pmx, premaxilla**;** pop, preoperculum**;** por, postorbital process; psclth, presupracleithrum; psp, parasphenoid; ptg, propterygium**;** rad, radials**;** sc, scale**;** scl, sclerotic ring**;** sclth, supracleithrum**;** scpc, scapulocoracoid**;** sorb, suborbital**;** sop, suboperculum**;** st, supratemporal.


A
exsc
psclth
sclth
sc
pclth
clth
lep
rad
scpc
clav
pop
mx
den
sorb
jug
dpl
enp
psp
lac
ao
it
por
st
bc
B
aop
dhy
op
bc
scl
dsph
pmx
sclth
sc
pclth
ptg
lep
cor
jug
pop
chy
den
mx
clav
br
clth
sop
scpc
mtpg
rad
C
st
exsc
dhy
pop
hmd
psclth
clth
lep
rad
it
psp
lac
scl
bc
psclth
op
exsc
sclth
sc
D
clth
clav
ang
mx
den
lep
ptg
rad
mtpg
clth
clav
mx
den
ang
chy
cor

Revised genus diagnosis. Small actinopterygian characterised by the following autapomorphy: toothed lacrimal contributing to the orbit and the oral margin; in addition to the following combination of characters: separate intercalar ossification of the braincase; parasphenoid pierced by paired foramina for the internal carotids; tooth cover on anterior corpus of parasphenoid reduced to a median strip in anterior third; at least three pairs of parotic toothplates; absence of dermal basipterygoid processes; canals or cavities in premaxillae, maxillae, dermohyal and dermosphenotic that are not connected to the main lateral line network; anterior and posterior accessory vomers; medially oriented teeth on ectopterygoid and dermopalatines; paired premaxillae; additional prearticular plate on the medial side of the lower jaw; low process on the dorsal margin of the dentary; unperforated propterygium fused to the first lepidotrichium of the pectoral fin.

Revised species diagnosis: P. gunnari is differentiated from other species of *Pteronisculus* by: presence of a bony pedicel carrying the buccohypophyseal canal into the parasphenoid; unperforated ventral surface of the posterior myodome; presence of a single ceratohyal; uncinate processes on epibranchials I, II and III; wide entopterygoid process directed dorsolaterally; weak anterodorsal process on the suboperculum; course of the lateral line canal in the supracleithrum almost anteroposterior.

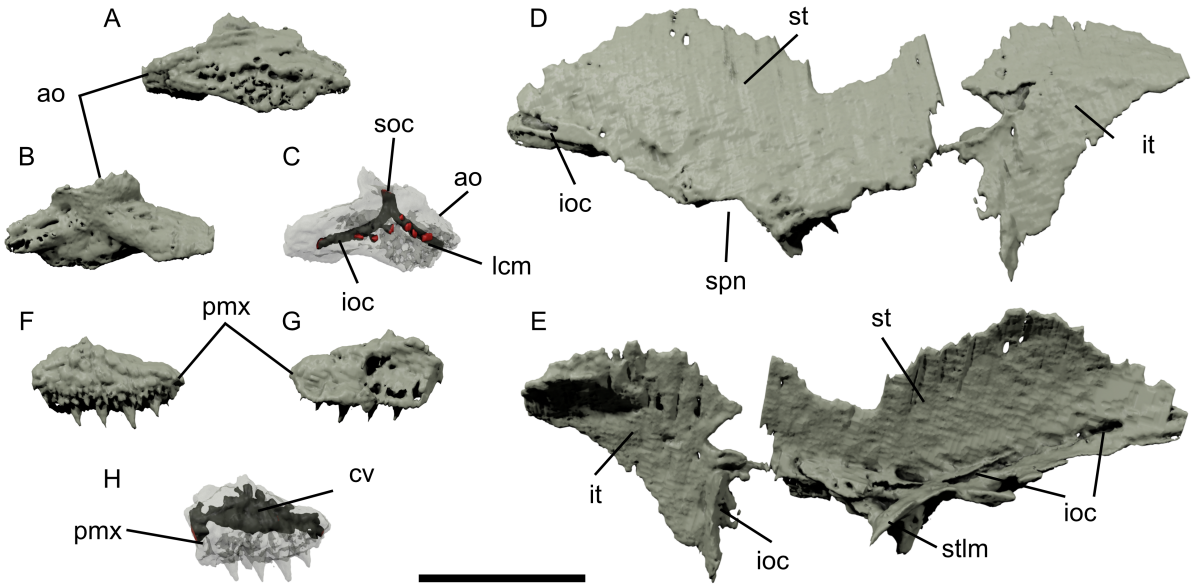


Figure 2.3: Renders of the snout and skull roof bones of *Pteronisculus gunnari* NHMD 73588. Right antorbital in anterior view (A), medial view (B) and partially transparent to show the internal ramifications of the infraorbital and supraorbital canals (C). Right supratemporal and intertemporal in lateral view (D) and medial view (E). Left premaxilla in external view (F), medial view (G) and partially transparent to show the infraorbital canal (H). Scale bar: 5 mm. Abbreviations: ao, antorbital; cv, cavity; ioc, infraorbital canal; it, intertemporal; lcm, lateral commissure; pmx, premaxilla; soc, supraorbital canal; spn, spiracular notch; st, supratemporal; stlm, supratemporal lamina.

2.4 Results

2.4.1 Description

External. The specimen has historically been mechanically prepared, removing the matrix to expose the skull roof, cheek, opercular series and shoulder girdle. As a result, most of the dermal bones in these areas remain as no more than impressions on the surface of the specimen (Fig. 2.1) and are not visible in tomograms. Parts of the skeleton and the matrix have been substituted by pyrite, particularly the anterior portion of the lower jaws, pectoral fins and scales, and sensory canals; these pyritized areas could not be segmented. The portion of the specimen that was imaged using XCT preserves most of the skull, the jaws, both pectoral

girdles and pectoral fins and a portion of the axial skeleton (Fig. 2.1A-F). It has been subject to a small amount of lateral compression, and some degree of shear in an anterolateral direction given the misalignment between the right and left halves of the specimen. Despite this, most of the bones of the skull and the pectoral girdle are undeformed and preserved in 3D, and range from articulated to loosely associated (Fig. 2.2A-D). The jaws and external dermal bones in particular are largely preserved in articulation.

Snout. The snout comprises the antorbital, premaxilla, rostral and nasal. The rostral and nasal are visible only as impressions on the surface of the specimen, in relative articulation (Fig. 2.1E-F). The right antorbital and premaxillae have been dislodged from life position.

Only the right antorbital is preserved (Fig. 2.2A; Fig. 2.3A-C, ao). It is roughly trapezoidal in lateral view. The dorsal margin of the bone bears an articulation surface for the nasal, and is pierced by a dorsally directed portion of the supraorbital canal. The medial surface is divided into a larger, ventrally directed articular surface and a smaller, dorsally directed one above and below the infraorbital canal. The external surface of the antorbital is ornamented with large tubercules, and is pierced by foramina that connect to the infraorbital canal and the ethmoidal commissure (Fig. 2.3A, C) The two have almost identical, vertically curved rami of canal (Fig. 2.3C, ioc, lcm) traverse the bone and converge in a triple junction with the shorter supraorbital canal (Fig. 2.3C, soc). The ethmoidal

commissure exits the antorbital medially, while the infraorbital canal enters through a smaller opening in the posterior margin from the lacrimal.

The premaxilla is small and triangular, with a tuberculate external surface (Fig. 2.1B; Fig. 2.3F-H, pmx). It has a straight, tooth-bearing ventral margin, with 4-5 principal teeth and numerous smaller ones; the tooth-bearing margin creates a small horizontal shelf lingually. The bone is deeper anteriorly, where it contacts its antimere. A cavity runs the length of the bone, entering from the lateral margin and without a clear exit on the medial side (Fig. 2.3H, cv).

The rostral is visible only as an impression on the surface of the specimen (Fig. 2.1F, ro). Its curved dorsal margin contacts both frontals, while the lateral margins contact the nasals. Nares are not visible. Similarly, the nasal is only visible as an impression (Fig. 2.1B, D, F, na). The groove for the supraorbital canal can be traced from the nasal into the frontal (Fig. 2.1F, soc).

Skull roof. The skull roof comprises frontals, parietals, intertemporals and supratemporals. They are present mostly as impressions on the dorsal surface of the specimen (Fig. 2.1A-F), and as such it is only possible to partially see their extent and the sutures between them. Some unidentifiable fragments were segmented below the surface of the specimen (Fig. 2.2A-C).

Only impressions and small patches of tuberculate ornamentation can be identified of the frontal (Fig. 2.1B, F, fr). It is also possible to follow the supraorbital canal, which has partially been infilled with pyrite (Fig. 2.1F,

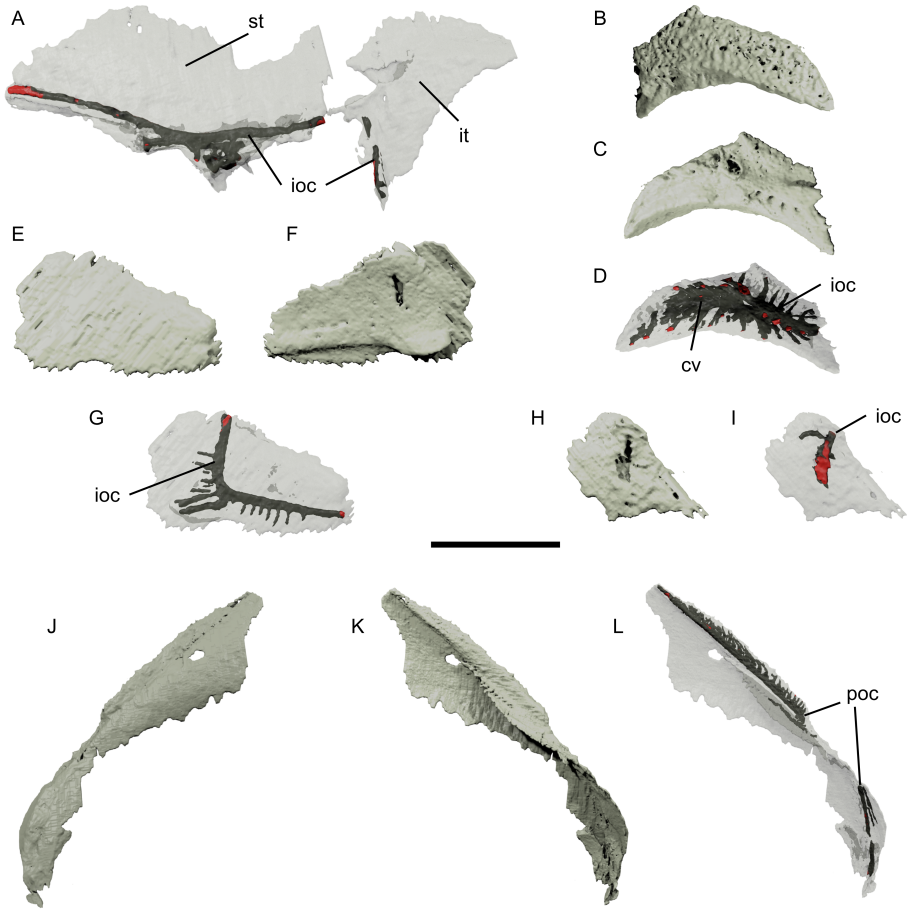


Figure 2.4: Renders of the skull roof, cheek and infraorbital bones of *Pteronisculus gunnari* NHMD–75388. Right supratemporal and intertemporal in lateral view, partially transparent to show the infraorbital canal (A). Right dermosphenotic in lateral view (B), medial view (C) and partially transparent to show the infraorbital canal and additional cavities (D). Right jugal in lateral view (E), medial view (F) and partially transparent to show the infraorbital canal (G). Left infraorbital in lateral view (H) and partially transparent to show the infraorbital canal (I). Right preoperculum in lateral view (J), medial view (K) and partially transparent to show the preopercular canal (L). Scale bar: 5 mm for A-I; 8 mm for J-L. Abbreviations: cv, cavity; ioc, infraorbital canal; it, intertemporal; poc, preopercular canal; st, supratemporal.

soc). The sutures between the frontals and between the frontals and the parietals are irregular, so much so that the left frontal is somewhat wider than the right. The parietal is preserved in a similar manner to the frontal

(Fig. 2.1A, F, pa). Its suture with the frontals is irregular, while that with the supratemporal is more linear.

Portions of the right intertemporal are partially preserved, but it is mostly reconstructed from impressions on the surface of the specimen. It is triangular in lateral view, and broadens posteriorly to meet the supratemporal (Fig. 2.1B; Fig. 2.2A, C; Fig. 2.3D-E; Fig. 2.4A, it); the suture between the two bones is incomplete, but they share the same mediolateral convexity. The infraorbital canal is continuous between the two ossifications and exits the intertemporal ventrally to enter the dermosphenotic, although the canal is incomplete (Fig. 2.3D-E; Fig. 2.4A, ioc). The anteroventral margin of the intertemporal is curved to accommodate the dermosphenotic. The medial margin is incomplete.

The supratemporal is mostly preserved as impression, although some portions of bone remain, particularly around the sensory canals and close to the braincase (Fig. 2.1B, D, F; Fig. 2.2A, C; Fig. 2.3D, E; Fig. 2.4A, st). As with other skull roof bones, the dermal ornament is tuberculate. Although the posterior, dorsal and anterior margins are incompletely preserved, the supratemporal is mediolaterally convex. Its lateral margin is produced as two lobes, separated by a distinct spiracular notch (Fig. 2.3D, spn). The infraorbital canal traverses the entire anteroposterior length, following the lateral margin of the supratemporal. A complex series of smaller canals and cavities depart from and join the infraorbital canal anterior to the supratemporal notch, opening on the ventral and medial surface of the bone (Fig. 2.3D-E; Fig. 2.4A, ioc). However, the canal does

not appear to exit through the lateral margin of the supratemporal towards the preoperculum. Multiple thin laminae descend from the sensory canal anteroventral and posteroventral to the spiracular notch (Fig. 2.3E, stlm); these likely correspond to the ventral lamina described by Nielsen (1942, pp. 119-120).

Cheek and infraorbitals. The cheek and infraorbital series consist of a dermosphenotic, jugal, third infraorbital, two suborbitals, accessory operculum, and preoperculum. Most of these bones are exposed on the surface of the specimen and as a result have been mechanically prepared to a greater or lesser extent (Fig. 2.1A-D); the suborbitals are completely reconstructed from surface impressions.

The dermosphenotic is roughly crescent-shaped in lateral view (Fig. 2.1D; Fig. 2.2B; Fig. 2.4B-D, dsph), with a curved ventral margin contributing to the orbit. It can be divided into smaller, ventrolateral and larger dorsolateral triangular surfaces, both bearing tubercular ornamentation. Its medial surface is pierced by multiple foramina (Fig. 2.4C). There appear to be two main cavities within the dermosphenotic, both connected to multiple branching rami, with little to no communication between the cavities. The smaller cavity hosts the infraorbital canal, traversing the bone dorsoventrally, entering from the medial surface and exiting from the ventral margin (Fig. 2.4F, ioc). Smaller vessels ramify from the canal in two rows, dorsally and ventro-medially. The second cavity is complex in shape, with many vessels branching posteriorly, posterodorsally and antero-dorsally, towards both the external and medial surface (Fig. 2.4F, cv).

The jugal is also partially preserved as an impression, and its margins cannot be fully reconstructed. It is wide and short, almost triangular in lateral view, and carries the infraorbital canal (Fig. 2.2A-B; Fig. 2.4E-G, jug). The dorsal margin contributes to the ventral margin of the orbit for the anterior half of its length, while the posterior half articulates dorsally with the third infraorbital. The infraorbital canal enters the bone from its dorsal margin and after a short distance bends anteriorly, running the length of the bone before exiting it into the lacrimal (Fig. 2.4G, ifc). Smaller branches emanate posteriorly and ventrally, but never towards the orbit. A low ridge on the medial surface traces the anterior arm of the canal, developing posteriorly into a small, ventromedially directed protrusion close to the posterior margin of the bone (Fig. 2.4E).

An additional, trapezoidal infraorbital, positioned dorsal to the jugal, is partially preserved (Fig. 2.1B, D; Fig. 2.4H-I, io). The infraorbital canal travels the bone dorsoventrally (Fig. 2.4I, ioc).

A total of three suborbitals are preserved as superficial impressions, two on the right side and one on the left (Fig. 2.1B, D; Fig. 2.2A, sorb). They are laminar, with convex external and concave internal faces, and are trapezoidal in lateral view. The dorsal suborbital is considerably bigger than the ventral.

As with other cheek bones, the preoperculum has been prepared, and its dorsal limb is partially reconstructed from its impression (Fig. 2.1B, D; Fig. 2.2A-C; Fig. 2.4J-L, pop). The dorsal limb is elongate and roughly triangular in lateral view, with an anterior margin that is recessed to

accommodate the suborbitals. The ventral limb of the bone is shorter and crescent shaped, although its anterior margin is probably not fully preserved. The preopercular canal travels the length of the preoperculum, close to its dorsal margin, with its path marked by a ridge on the medial surface of the bone (Fig. 2.4L, poc). The ridge becomes a ventromedially extending lamina for the posterior half of the dorsal limb (Fig. 2.4K), and is only faintly present on the ventral half. Within the dorsal triangular portion of the preoperculum, the canal has smaller, anteriorly directed branches that become curved more strongly dorsally further back along the limb (Fig. 2.4L, poc). The canal in the ventral limb of the preoperculum is directed ventrally and has a few long, ventrolaterally directed branches. The canal exits the ventralmost margin of the bone through a small, hooked process (Fig. 2.4L).

An accessory operculum is also present on the left side, although it can only be described from surface impressions (Fig. 2.1D; Fig. 2.2B, aop). It is small and triangular, tapering to a point anterodorsally and posteroventrally. It bears ridged ornament.

Hyoid Arch. The hyoid arch comprises the dermohyal, hyomandibula, symplectic and a single ceratohyal. Part of the left ceratohyal and both left and right hypohyals are obscured by pyrite.

The dermohyal is slender and triangular, tapering to a point posteroventrally (Fig. 2.2B, D; Fig. 2.5A-C, H, dhy). It is not fused to the hyomandibula, but lies along its dorsal margin, projecting some way dorsal to its anterior head. A raised triangular area on the external face is

ornamented with small tubercles; the rest of the dermohyal is smooth, and may have been overlapped by other bones. A distinct lamina is developed along much of the length of the dermohyal on its medial surface, somewhat posterior and ventral to the ridge of ornament. This lamina is developed as a hook-like process at the dorsal margin of the dermohyal and gradually tapers posteriorly. Unusually, the dermohyal carries a canal, which lies underneath the triangular ornamented area (Fig. 2.5C, cn). Small foramina open onto the dorsal margin between the two ridges.

The hyomandibula is elongate and almost straight, with a dorsal arm that is flattened in cross section and a ventral arm that is oval (Fig. 2.2C; Fig. 2.5A-C, H, hmd). A small opercular process is present halfway along the dorsal margin of the bone, marking its maximum curvature point (Fig. 2.5A-B, D, opc). The process is bilobed: the larger portion lies parallel to the hyomandibula, with a smaller, stumpy portion directed dorsomedially. The foramen for the hyomandibular nerve pierces the lateral face of the hyomandibula near the base of the process (Fig. 2.5D, hmc). In addition, two grooves are visible on the surface of the bone, more evident on the right hyomandibula: the first groove runs along the anteroventral margin of the dorsal arm, while the second runs on the lateral face of the ventral arm up to the opercular process (Fig. 2.5A-B). Each end of the hyomandibula is incompletely ossified. A small, conical symplectic lies anteroventral to the hyomandibula (Fig. 2.5F-H, sy). As previously described by Argyriou et al. (2022), the symplectic has a rounded dorsal face, tapers ventrally (Fig. 2.5F-G, vpsy), and bears a condyle and groove for the afferent mandibular

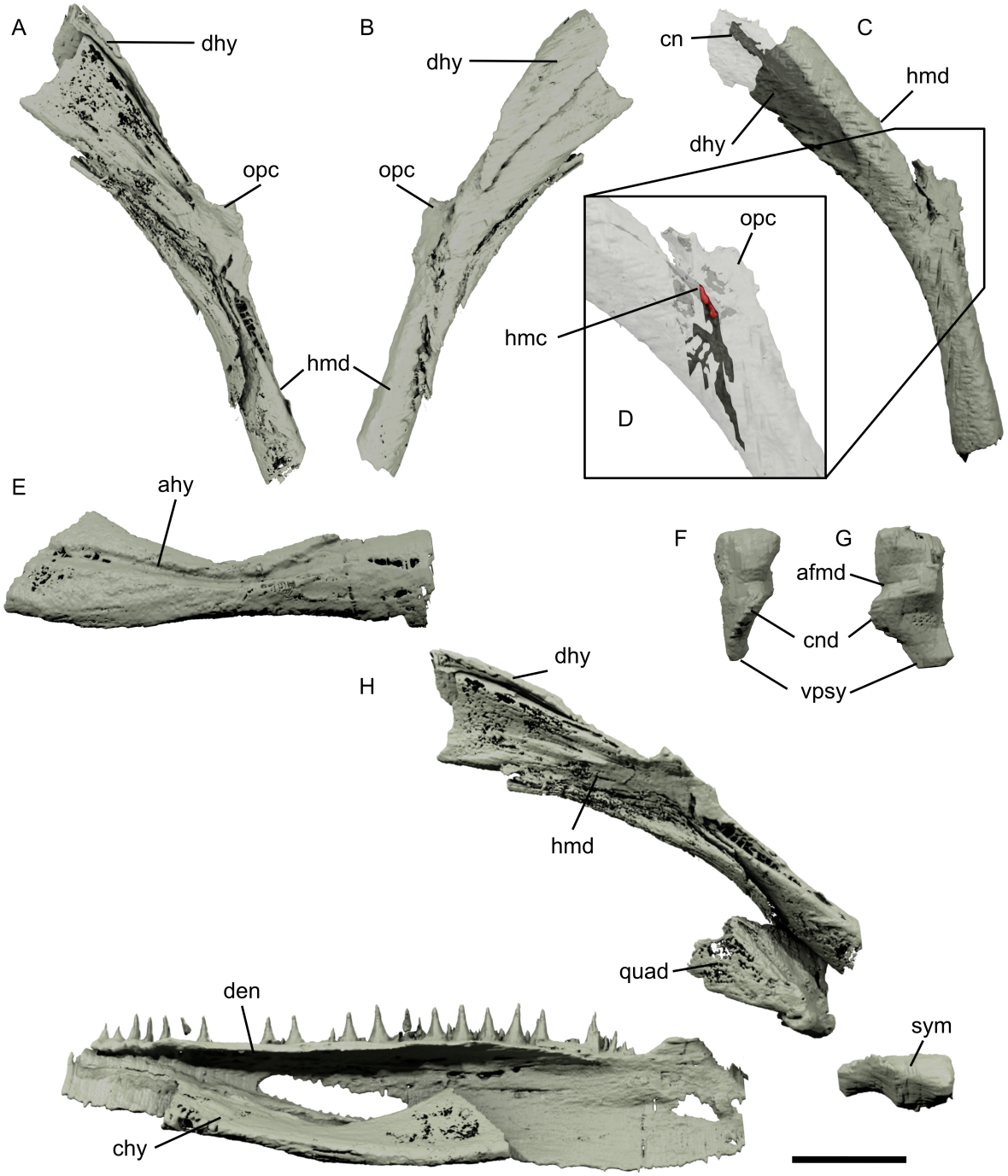


Figure 2.5: Renders of the hyoid arch and jaw of *Pteronisculus gunnari* NHMD–75388. Right hyomandibula and dermohyal in medial view (A), lateral view (B) and with the dermohyal partially transparent to show the canal (C). Close up of the middle portion of the hyomandibula, rendered partially transparent (D). Right ceratohyal in lateral view (E). Right symplectic in lateral view (F) and medial view (G). Right hyoid arch and selected jaw ossifications in medial view (H). Scale bar: 4 mm for A-C; 8 mm for D; 5.5 mm for E-G; 0.5 cm for H. Abbreviations: afmd, groove for afferent mandibular artery; chy, ceratohyal; ahy, groove for afferent hyoid artery; cn, canal; cnd, anterior condyle of symplectic; den, dentary; dhy, dermohyal; hmc, hyomandibular canal; hmd, hyomandibula; opc, opercular process; quad, quadrate; sym, symplectic; vpsy, ventral process of symplectic.

artery on its anterolateral face (Fig. 2.5F-G, afmd, cnd).

A single ceratohyal completes the preserved ossified components of the hyoid arch. It is laterally flattened and approximately half the length of the lower jaw, with a strongly curved dorsal margin and a gently curved ventral margin (Fig. 2.2B, D; Fig. 2.5E, H, chy). Its medial surface is slightly concave and external surface slightly convex, creating a narrow ellipsoidal cross section. A deep, sinuous groove for the afferent hyoid artery marks the lateral face (Fig. 2.5E, chyg).

Upper jaw and palate. The upper jaw and palate comprise external dermal bones (lacrimal, maxilla, quadratojugal), dermal palatal bones (dermometapterygoid, entopterygoid, ectopterygoid, anterior and posterior accessory vomer, dermopalatines) and endochondral palatoquadrate ossifications (autopalatine, metapterygoid, quadrate). Most components are well preserved, in relative life positions or closely associated, and essentially complete.

The tooth-bearing external dermal bones comprise the lacrimal and maxilla. The lacrimal is narrow, with a gently curved, posterior portion, and a triangular, tooth-bearing anterior portion (Fig. 2.2A, C; Fig. 2.6F-H, lac). The dorsal margin contributes to the ventral margin of the orbit for about ¾ of its length, indicated by a slim ridge. The ventral margin bears a similarly fragile ridge and a medial shelf. Both margins are slightly dorsoventrally curved. The anterior portion of the bone is wedge-shaped and has a ventral, toothed surface bearing 6-7 main teeth and numerous smaller lateral cusps. The infraorbital canal enters the bone from the posterior

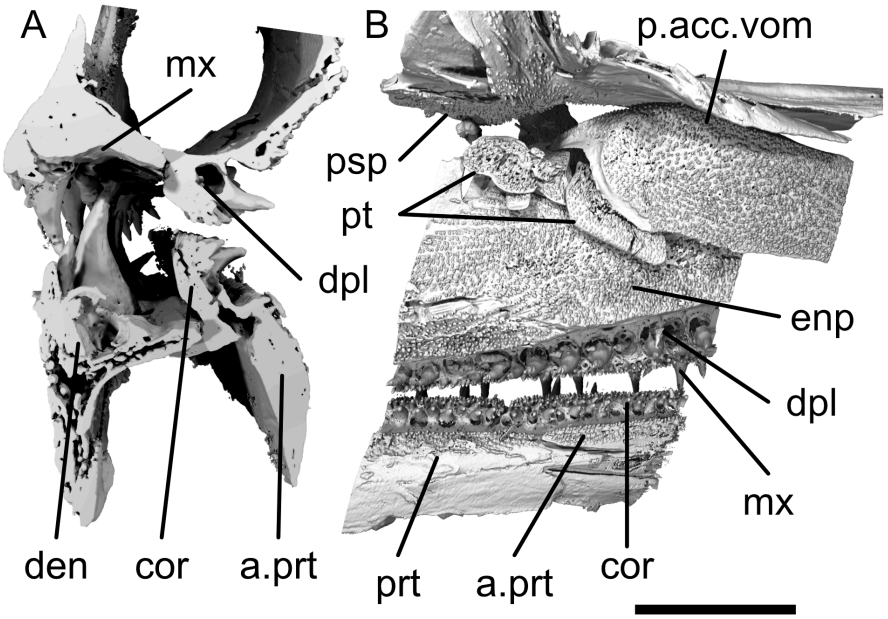


Figure 2.7: Synchrotron renders of the parasphenoid, left jaws and parotic toothplates of *Pteronisculus gunnari* NHMD–73588. Transverse section through right upper and lower jaws (A) and medial view of the left upper jaw, palate, and lower jaw (B). Scale bar: 5 mm for A; 2.5 mm for B. Abbreviations: a.prt, additional prearticular ossification; cor, coronoid; den, dentary; dpl, dermopalatine; enp, entopterygoid; mx, maxilla; p.acc.vom, posterior accessory vomer; prt, prearticular; psp, parasphenoid; pt, parotic toothplate.

margin and runs in an antero-posterior and slightly dorsal direction, extending above the teeth, exiting as the dorsal margin of the bone leaves the orbital margin (Fig. 2.6H, ioc).

The maxilla can be described in its entirety, although the anteriormost portion of the suborbital ramus is embedded in pyrite and the majority of the postorbital plate is moldic (Fig. 2.1B, D; Fig. 2.2A-B; Fig. 2.6A, C-E, mx). Overall, it has a slightly convex external surface. The suborbital ramus is narrow, forms about two fifths of the length of the maxilla, and curves slightly dorsally and medially. It consists of a narrow, medial horizontal lamina and a ventral tooth-bearing portion. The lamina extends some way anterior to the tooth-bearing portion of the maxilla, forming an overlap surface upon which the posterior ramus of the lacrimal rests (Fig.

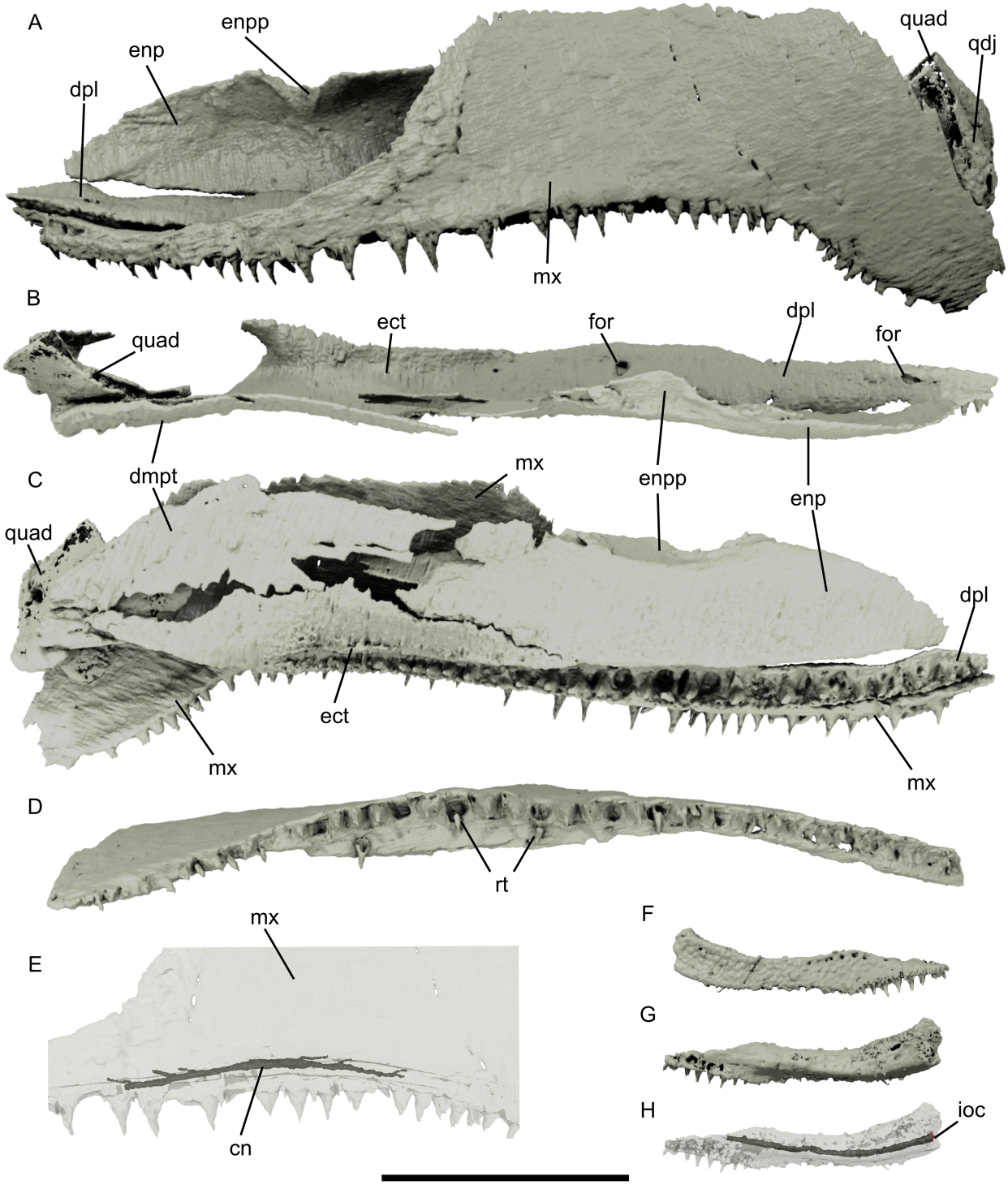


Figure 2.6: Renders of the upper jaw and palate of *Pteronisculus gunnari* NHMD–75388. Left upper jaw and dermal palate in lateral view (A); dorsal view with maxilla removed (B); and medial view (C). Right maxilla in ventral view (D). Close up of middle portion of maxilla in lateral view rendered partially transparent to show canal (E). Right lacrimal in lateral view (F), medial view (G) and partially transparent to show the infraorbital canal (H). Scale bar: 10 mm. Abbreviations: cn, canal; dpl, dermopalatine; dmpt, dermetapterygoid; ect, ectopterygoid; enp, entopterygoid; enpp, entopterygoid process; for, foramen; ioc, infraorbital canal; mx, maxilla; quad, quadrate; qdj, quadratojugal; rt, replacement tooth.

2.6A, C-D).

The postorbital plate of the maxilla is considerably higher: the anterodorsal margin rises in a curve following the posterior margin of the jugal, the dorsal margin is flat underlying the preoperculum, and the posterior margin falls sharply, descending some way past the quadratojugal (Fig. 2.6A). As a result, the posteroventral portion of the maxilla covers part of the mandible. A narrow strip along the anterodorsal margin of the maxilla is slightly depressed, forming an overlap surface for suborbital and infraorbitals. The horizontal lamina of the maxilla is thicker and wider below the postorbital plate. A canal runs anteroposteriorly along the maxilla lateral to the thickened portion of the lamina, just dorsal to the tooth row (Fig. 2.6E, cn); the canal also has small branches, directed posteriorly in the postorbital portion and anteriorly in the suborbital portion. As the maxilla deepens ventrally, the lamina gradually tapers out.

Teeth are borne along the entire ventral margin of the maxilla, which is sinusoidal, with the result that the small, posteriormost teeth point anteroventrally (Fig. 2.6A, C-D). Two kinds of teeth are present: at least 45 larger, pointed cusps, and numerous irregularly spaced smaller teeth lateral to the main tooth row (Fig 2.6-2.7, mx). In addition, around 11 empty sockets are present in each main tooth row, some with what appear to be small replacement teeth partially emplaced (Fig. 2.6D, rt). Each tooth is capped with acrodin: being a denser material than the rest of the teeth, this appears as a small, bright cone in tomograms.

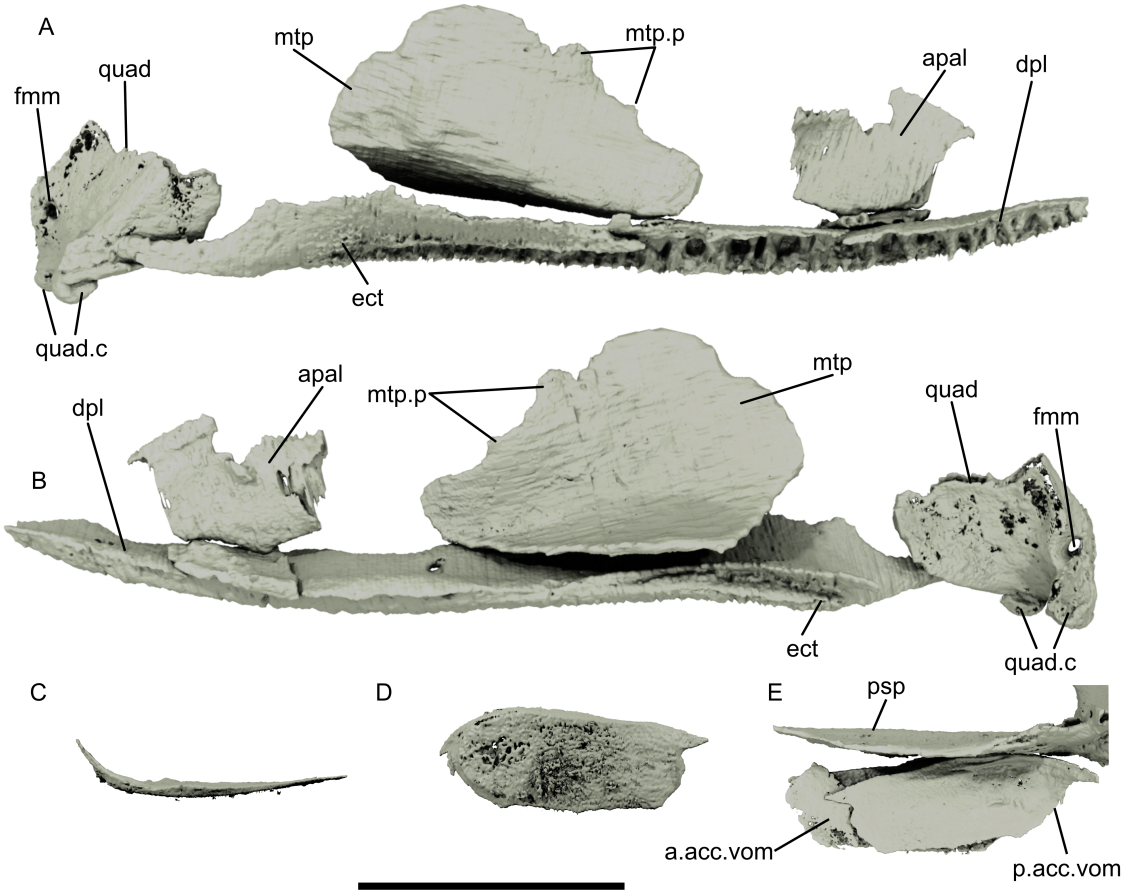


Figure 2.8: Renders of the palate, parasphenoid and accessory vomers of *Pteronisculus gunnari* NHMD–75388. Left palatal ossifications in medial view (A) and lateral view (B). Left posterior accessory vomer in medial view (C) and ventral view (D). Accessory vomers and parasphenoid in left lateral view (E). Scale bar: 10 mm. Abbreviations: a.acc.vom, anterior accessory vomer; apal, autopalatine; dpal, dermopalatine; ect, ectopterygoid; fmm, foramen for mandibular nerve; mpt, metapterygoid; mpt.p, metapterygoid processes; os, minor palatoquadrate ossification; p.acc.vom, posterior accessory vomer; psp, parasphenoid; quad, quadrate; quad.c, quadrate condyles.

The quadratojugal is very thin and triangular in lateral view, and appears to be incompletely preserved (Fig. 2.6A, qdj). It lies between the external surface of the quadrate and the medial surface of the preoperculum.

An ectopterygoid, dermopalatine series, entopterygoid and dermometapterygoid sheath the internal surface of the palate. A single, large trapezoidal dermometapterygoid, which thins and fragments

anteriorly, forms the posterodorsal margin of the dermal palate (Fig. 2.6B-C, dmp). It lies medial to both the quadrate and the metapterygoid, with its anteroventral margin contacting the ectopterygoid and the entopterygoid. A ridge on the lateral surface follows the posterodorsal and dorsal margin. The medial surface bears very diminutive teeth (Fig. 2.7A).

The ectopterygoid has a complex morphology, framing the adductor fossa posteriorly and tapering to a point anteriorly (Fig. 2.6B-C, ect; Fig. 2.8A-B, ect). It is continuous with the dermopalatines ventrally and anteriorly (Fig. 2.6A-C, dpl; Fig. 2.8 A-B, dpl). The medial face comprises a triangular, vertical lamina, bearing small teeth across almost its entire surface; these teeth are largest towards the ventral margin of the ectopterygoid. The dorsal margin of the lamina contacts the dermometapterygoid in its posterior half and the entopterygoid more anteriorly, before tapering out (Fig. 2.6C). The ectopterygoid contacts the maxilla via a laterally directed lamina, which is wider posteriorly (Fig. 2.6B). This lamina and the dorsolateral surface of the medial face are continuous and form a dorsally directed surface that is separated from the tooth row via a thickened ridge and, more ventrally, deep trough (Fig. 2.7B). Both the ridge and trough are continued by the entopterygoid and dermopalatine series anteriorly. The ectopterygoid tooth row is borne on a separate, ventral lamina. Its teeth are recurved and project medially, at right angles to those of the dentary.

The entopterygoid is elongate and ellipsoidal (Fig. 2.6A-C, enp). Its medial surface is almost entirely covered in minuscule teeth, except for a small strip parallel to the dorsal margin (Fig. 2.7A). About halfway along the

dorsal margin, just anterior to the metapterygoid, a stout triangular process projects dorsomedially. This may have articulated with the parasphenoid (Fig. 2.6A-C, enpp). The ventral margin of the entopterygoid is thickened into a ridge, continuous with the ectopterygoid posteriorly and dermopalatines ventrally, from which it is separated by a deep trough. The posterior margin contacts the dermometapterygoid. It is not possible to identify the boundary between the ectopterygoid and dermopalatine tooth, or the number of dermopalatines (der, Fig. 2.8A-B, dpl), but the teeth extend level to the anterior margin of the maxilla. The tooth-bearing lamina is thickened into a ridge, from which extends a thin lateral lamina, and there is a considerable, gap between the maxillary tooth row and the palatal tooth row (Fig. 2.7B). Numerous teeth are present on the dermopalatines: a main row dorsally, with a number of empty sockets, and numerous irregularly spaced smaller teeth ventrally. As with the ectopterygoid, the main teeth of the dermopalatine series recurved and project medially—and in some cases almost dorsally—at right angles to the maxillary teeth (Fig. 2.7A-B, dpl).

Dorsal to the tooth row, the dermopalatines extend as a thin flange towards the entopterygoid. This surface is pierced by two large foramina: a larger, more posterior opening, positioned approximately halfway along the length of the palate, which pierces the bone dorsoventrally and has a minor branch towards the medial side of the bone; and a second, more anterior foramen, which is smaller and opens on the dorsal and ventral

margins (Fig. 2.6B, for). The ventrolateral margin of the tooth-bearing lamina is pierced by numerous small foramina.

A large, posterior accessory vomer is present on each side of the skull. It is rectangular and gently concave in dorsal view, with a medial surface covered in minuscule teeth (Fig. 2.8E-G, p.vo). Both the anterodorsal and posterodorsal corners are developed as triangular projections; the posterodorsal projection is continuous with a thickened ridge on the lateral face of the posterior accessory vomer, which together taper to a narrow, dorsolaterally-directed point (Fig. 2.8E-G).

A flat, thin ossification bearing small teeth that lies between the posterior accessory vomers is interpreted as the anterior accessory vomer (Fig. 2.8E, a.vo).

Rather than being present as a single ossification, the palatoquadrate is ossified as a number of separate elements (Fig. 2.8A-B). The autopalatines are the most anterior, and are made of a triangular portion applied on the dorsal surface of the dermopalatines, and a vertical polygonal portion (Fig. 2.8A-B, apal). In the right autopalatine the two portions are continuous, while in the left autopalatine are discontinuous, probably as a result of post-mortem damage (Fig. 2.8A-B, apal).

The metapterygoid is the largest palatoquadrate ossification. It lies midway along the upper jaw and is strongly curved, with almost vertical and ventrolateral laminae (Fig. 2.8A-B, mtp). The anterodorsal margin of the vertical face bears two low, vertical processes, more evident on the left metapterygoid (Fig. 2.8A-B, mtp.n).

The quadrate is robustly ossified (Fig. 2.6A-C; 2.8A-B, quad). The posterior and medial surfaces are triangular and are divided by a low, anterodorsally directed ridge that originates from the internal condyle. The anterior face is concave, forming the medial and posterior margins of the adductor fossa, and the lateral surface is small and crescent-shaped; its ventral portion contacts the quadratojugal. The condyles are borne on the ventral surface near the posterior margin (Fig. 2.8A-B, quad.c). The lateral condyle is larger and somewhat medially-directed; the medial condyle is smaller and more rounded. The posterior margin of the quadrate forms a curved ridge, pierced by a large foramen for the internal mandibular branch of the facial nerve (Fig. 2.8A-B, fmm).

Lower jaw. The lower jaw is composed of external dermal bones (dentary, angular, surangular), endochondral ossifications (Meckel's cartilage) and internal dermal bones (prearticular, coronoids, accessory toothplates). The tooth-bearing portions of the right prearticular and coronoids are slightly flattened against the dentary and the prearticular and quadrate are displaced laterally, distorting the outline of the adductor fossa, but in general the mandible is largely articulated (Fig. 2.9C-D). The left mandible is preserved in life position, although the anterior half of the dentary is pyritized and cannot be segmented (Fig. 2.9A-B). Both symphyses are concealed within pyrite and thus the anteriormost morphology of the dentary and coronoids is unclear.

The dentary is stout, tapering only slightly anteriorly (Fig. 2.1B, D; Fig. 2.2A-B, D; Fig. 2.5H; Fig. 2.9A-E, den). Its lateral surface is convex and

ornamented with a combination of short ridges ventrally and tubercules dorsally. The dorsal margin bears small lateral teeth, although as they are exposed on the surface and have been partially prepared, many are lost. A main row of larger, conical teeth is present medially (Fig. 2.9). The right dentary preserves 23 cusps in this tooth row, with the tips covered by a cap of acrodin, and 5 empty sockets. The tooth row begins anterior to a rounded concavity on the external surface, which in life was overlapped by the ventralmost portion of the maxilla. Behind this depression, the dentary is the sole contributor to a low and thin "coronoid" process (Fig. 2.9B-C, cp).

A broad horizontal lamina of the dentary extends medially towards a corresponding lateral lamina of the prearticular and coronoids, such that a wide gap separates the dentary tooth row from that of the inner dentition (Fig. 2.7B; Fig. 2.9A). The dentary lamina is separated from the rim of the adductor fossa by a flange of the prearticular, but otherwise runs for the whole length of the tooth row.

The ventral margin of the mandible is formed by the angular and dentary. The mandibular canal closely follows this ventral margin while it is hosted by the angular, but as soon as the canal passes into the dentary it angles dorsally, probably to meet the tooth row at the anterior tip of the bone (Fig. 2.9E, mc).

The angular is roughly triangular, forming the posterolateral margin of the mandible and tapering anteriorly to almost the midpoint of the mandible, reaching roughly the end of the horizontal lamina of the prearticular (Fig.

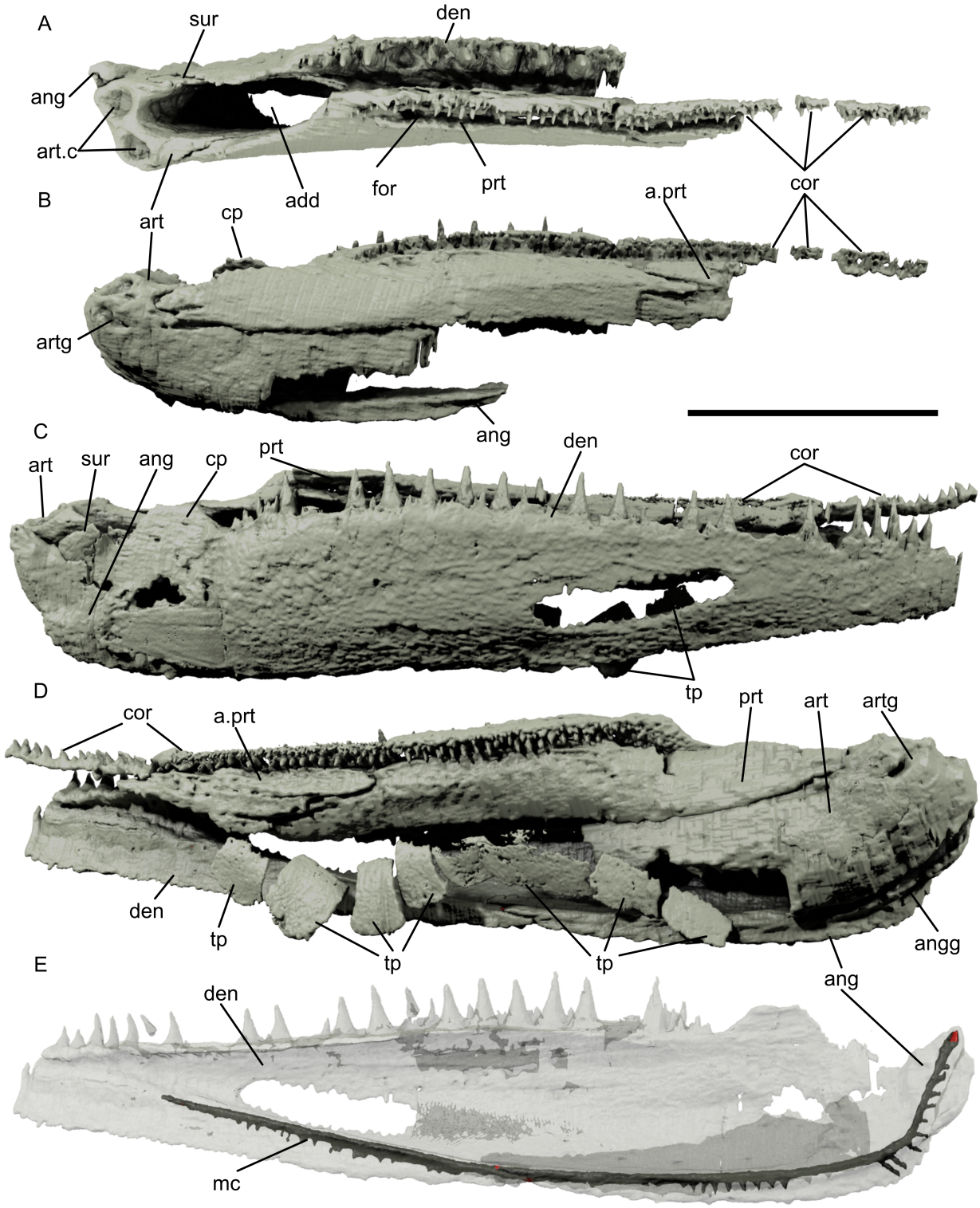


Figure 2.9: Renders of the lower jaw of *Pteronisculus gunnari* NHMD 73588. Left lower jaw in dorsal view (A) and medial view (B). Right lower jaw in lateral view (C) and medial view (D). Right dentary and angular in medial view, partially transparent to show the mandibular canal. Scale bar: 10 mm. Abbreviations: a.prt, additional prearticular ossification; add, adductor fossa; ang, angular; angg, groove on the angular; art, articular; art.c, articular cotyles; artg, groove on the articular; cor, coronoid; cp, coronoid process; den, dentary; for, foramen; mc, mandibular canal; prt, prearticular; sur, surangular; tp, toothplate.

2.9A, C-E, ang). It contacts the articular and surangular medially, contributes to the lateral side of the adductor fossa, and is largely covered by the dentary laterally. A dorsoventral groove runs down its posterior margin and part of the ventral margin (Fig. 2.9D, angg). A ridge runs along the entire length of the angular, hosting the mandibular canal (Fig. 2.9E, mc). The surangular lies dorsal and partially anterior to the angular, and forms the area of the mandible overlapped by the maxilla (Fig. 2.9A, C, sur). It contacts the horizontal lamina of the prearticular anteriorly, and contributes to the rim of the adductor fossa.

The articular is robust, with two rounded posterodorsal depressions corresponding to the condyles of the quadrate on its dorsal margin (Fig. 2.9A-D, art; Fig. 2.9A, qf). A faint ridge runs down the posterior and ventral margin of the articular, originating from the rim of the lateral condyle. Ventral to the condyles, the medial surface is covered in thin dermal bone. A groove runs along the medial surface of the articular, between it and the dermal sheathing bones (Fig. 2.9B, D, artg). The anterior surface of the articular frames the posterior margin of the adductor fossa, and a narrow lateral projection contacts the surangular. The Meckel's cartilage is ossified anterior to the articular for approximately a third of the length of the mandible. It becomes increasingly poorly ossified anteriorly, with the perichondral bone hardly developed near its anterior margin. As pyrite obscures the anterior portion of the lower jaws, it is not possible to say whether a mentomeckelian ossification was present.

The prearticular forms much of the medial surface of the lower jaw and the anteromedial margin of the adductor fossa (Fig. 2.9A-D, prt). Dorsally, it contributes to the internal tooth row for roughly one quarter of its length; Teeth of a variety of sizes are present but organisation into distinct rows is poor. The more ventral teeth are generally larger, with a number of smaller teeth positioned more dorsally; all are directed medially, at 90 degrees to those of the dentary, and have their roots in a dorsolaterally oriented lamina (Fig. 2.7B; Fig. 2.9A). A deep groove and ventral ridge separate the tooth row from the more ventral portion of the prearticular. These both fade posteriorly, and an elliptical foramen is present near the posterior termination (Fig. 2.9A, for). Minuscule teeth are present on the medial surface of the ridge, and this tooth covering extends down for about half of the width of the medial surface of the prearticular (Fig. 2.7A, prt). Ventrolaterally from the tooth row, the prearticular forms a lateral, horizontal lamina that contacts the dentary and frames the anterolateral rim of the adductor fossa (Fig. 2.9A, add). Anteriorly, the horizontal lamina of the prearticular tapers, and the groove between the dentary and the coronoids is floored by the lamina from the dentary. The tooth-bearing portion passes anteriorly into the coronoids. Ventral to the first coronoid, the prearticular interdigitates with a separate ossification with a similar, entirely dermal composition (Fig. 2.7; Fig. 2.9B, D, a.prt). Pyrite obscures the anterior extent of this additional bone. A similar bone was described by Lehman (1952) and Nielsen (1942, pp.163-164, figure 38), but wrongly assuming that it had an endochondral component.

At least 3 coronoids are present, sutured to, but distinct from, the prearticular (Fig. 2.9A-D, cor). The coronoids of the right jaw have rotated somewhat medially.

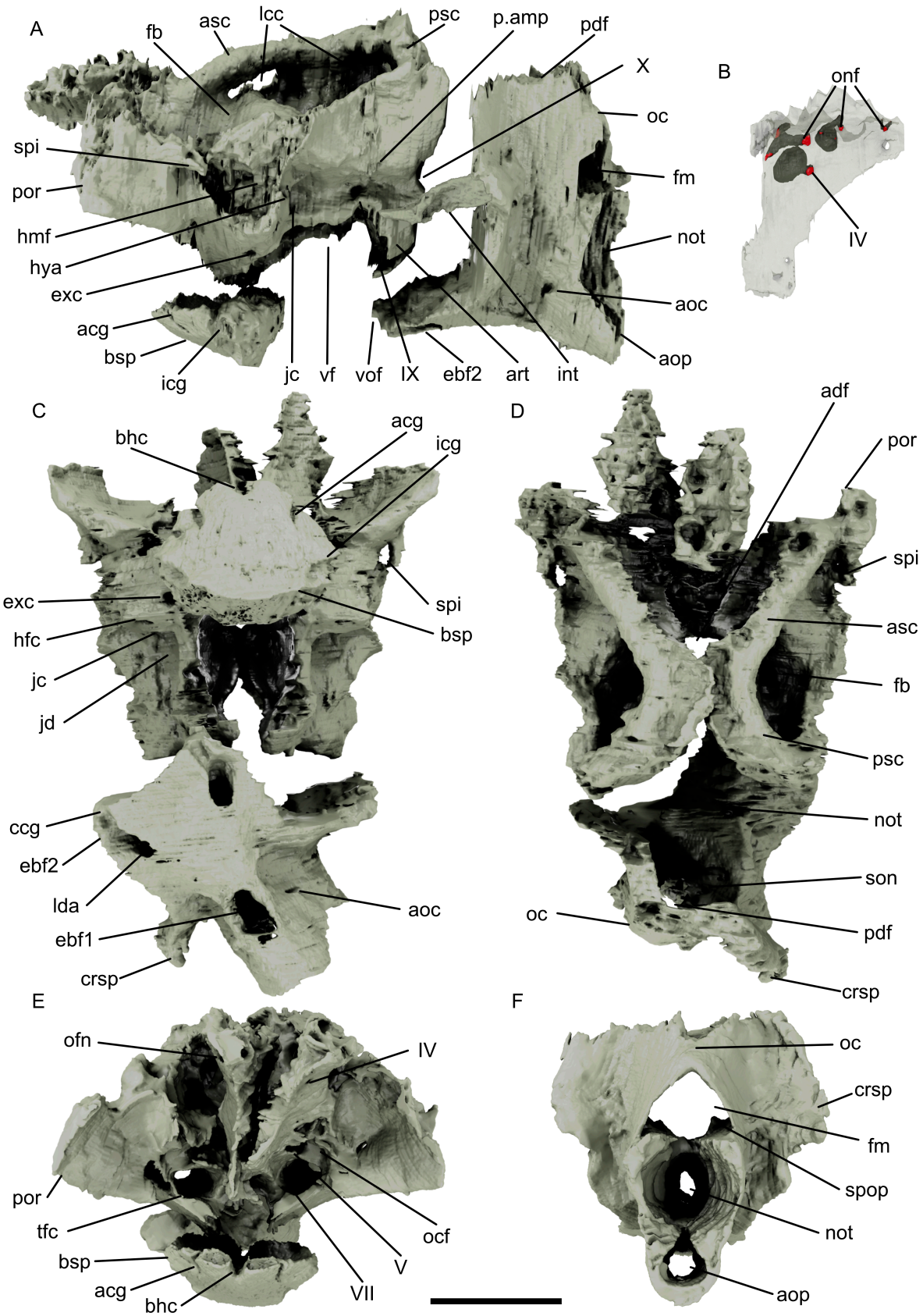
The dorsal portion of each coronoid is directed dorsomedially and surmounted by a low dorsolateral wall, covered in small, irregularly spaced teeth (Fig. 2.7B). Pyrite invasion means that details cannot be determined anteriorly.

A number of small laminar bones, sub-rectangular in lateral view, with a concave lateral surfaces and convex medial surfaces, lie medial to the lower jaws (Fig. 2.9D, tp). The dorsal margin is thicker than the ventral, and each plate bears minuscule teeth. Together, these form an elongate row. Some toothplates may be lost or displaced, as eight are associated with the right mandible and six with the left.

Braincase and parasphenoid. The braincase is incompletely ossified, lacking the ethmoidal and most of the orbitotemporal regions. It is ossified in six different pieces: median basisphenoid, median basiocciput, left and right intercalars, and left and right otic-orbitotemporal regions. Each is slightly displaced from their relative life positions. The areas between each of these ossifications, as well as the ethmoid region and the remainder of the orbitotemporal region, would have been filled with cartilage in life. Some areas of the braincase, particularly in the orbitotemporal region and the lateral face of the otic region, are incompletely ossified; this will be highlighted in the description.

The basioccipital portion of the braincase is almost completely ossified, and is composed of posterior, posterolateral, anterodorsal and ventral surfaces (Fig. 2.10A, C-D, F). The posterior surface has three openings: a ventral, ellipsoidal aortic canal; a central, rounded notochordal canal, and a dorsal, triangular foramen magnum (Fig. 2.10A, D, F, aop, nc, fm). The first two face posteriorly while the third faces posteroventrally. The floor and roof of the notochordal canal are incompletely ossified on the midline posteriorly, thus partially connecting the three openings. The dorsal margin of the occipital region is probably incompletely ossified in the specimen; the margin forms the “v” shaped posterior edge of the posterior dorsal fontanelle in the middle, which is the highest point of the occipital portion, then extends laterally to meet the posterolateral surfaces and the lateral margin (Fig. 2.10A, C, pdf).

Figure 2.10: Renders of the braincase of *Pteronisculus gunnari* NHMD–75388. Braincase in left lateral view (A). Right pterosphenoid in lateral view rendered partially transparent (B). Braincase in ventral view (C), dorsal view (D) and anterior view (D). Occiput in posterior view (F). Scale bar: 5 mm. Abbreviations: acg, anterior carotid groove; adf, anterior dorsal fontanelle; aoc, occipital artery canal; aop, posterior opening for the aorta; art, suprapharyngobranchial articulation; asc, anterior semicircular canal; bhc, buccohypophyseal canal; bsp, basisphenoid; ccg, common carotid groove; not, notochordal canal; co, occipital crest; crsp, craniospinal process; ebf1-2, efferent branchial artery foramen; exc, external carotid foramen; fb, fossa bridgei; fm, foramen magnum; hfc, foramen for the hyomandibular trunk of the facial nerve; hmf, hyomandibular facet; hya, foramen for the hyoid artery; icg, internal carotid groove; int, intercalar; jc, jugular canal; jd, jugular depression; lcc, lateral cranial canal; lda, lateral dorsal aorta; my, myodome; oc, occipital crest; ocf, otic canal foramen; onf, ophthalmic nerve foramen; p.amp, parampullary process; pdf, posterior dorsal fontanelle; por, postorbital process; psc, posterior semicircular canal; son, spinoccipital nerve; spi, spiracular canal; spop, spinoccipital process; vf, vestibular fontanelle; vof, ventral otic fissure; IV, trochlear nerve; V, trigeminal nerve; VII, facial nerve; IX, glossopharyngeal nerve; X, vagus nerve.



The aortic canal is enclosed for approximately two thirds of the length of

the basiocciput, and its floor is pierced by a median rectangular foramen for the first epibranchial artery (Fig. 2.10C, ebf1). Dorsal to this, two smaller, paired canals for the occipital arteries pierce the walls of the aortic canal and exit the posterolateral surface of the occipital region (Fig. 2.10A, C, aoc). The aortic canal bifurcates anterior to the epibranchial artery foramen, and the lateral dorsal aortae diverge from this point and run in an anterolateral direction (Fig. 2.10C; Fig. 2.11G, lda). These emerge into grooves approximately three quarters of the way along the ventral surface of the basiocciput, bifurcating again into anterior (for the common carotids) and dorsolateral (for the branchial efferent artery) grooves immediately before the ventral otic fissure (Fig. 2.10C; Fig. 2.11G, ccg, ebf2).

The notochordal canal is the largest opening on the posterior face of the braincase, but rapidly narrows anteriorly (Fig. 2.10A, D, F; Fig. 2.11A, not); the walls are not lined with perichondral bone. The notochordal canal opens into the anterior face of the occipital ossification (Fig. 2.10D, not). The foramen magnum expands almost immediately into the cranial cavity (Fig. 2.10A, F; Fig. 2.11F, fm). Its short ventral margin is pierced by two pairs of small foramina: the posterior pair host the spinoccipital nerves, while the anterior pair host branches of the occipital artery (Fig. 2.10D; Fig. 2.11F-G, son, oa). The occipital artery canals have secondary branches. Just posterior to the spinoccipital nerve foramina are two small processes, originating from the foramen magnum floor in dorsomedial direction (Fig. 2.10F, spop).

The posterolateral surfaces of the occipital region flare laterally around the three medial posterior openings and meet dorsally above the foramen magnum to form a blunt occipital crest (Fig. 2.10A, D, F, oc). The anterolateral margin of these posterolateral surfaces forms the posterior margin of the otoccipital fissure; the widest point of the occipital region is marked, on the lateral margins, by the posteriorly directed craniospinal process, more evident on the right side in this specimen (Fig. 2.10C-D, F, crsp). Ventral to the process, a notch in the margin marks the contact with the intercalar, while the likely exit for the vagus (X) nerve is anterior to the process (Fig. 2.10A, int, X). The otoccipital fissure becomes almost horizontal ventrally, marking the base of the vestibular fontanelle (Fig. 2.10A, vf). The ventral otic fissure (Fig. 2.10A, vof) constitutes the anterior margin of the occipital region, forming a concavity that matches a convexity on the posterior margin of the basisphenoid.

A small, elongate ossification corresponding to the intercalar of Pradel et al. (2016) is preserved in articulation with the braincase (Fig. 2.10A, int). In life, the intercalar would have been in contact with the occipital and otic regions, articulating just ventral to the craniospinal process and the vagus (X) nerve exit and extending partially into the jugular depression. It is pointed anteriorly, with a blunt posterior extremity. its dorsal and ventral margins are sigmoidal in lateral view and the bone has a relatively deep concavity on its lateral surface (Fig. 2.10A; Fig. 2.16D, int). The bone is pierced by small canals on the ventral and lateral surfaces.

The otic and orbitotemporal regions are co-ossified, although the left and right components are not preserved in continuity across the midline (Fig. 2.10D). Dorsally, the otic region is completely ossified only around the semicircular canals, and as such it is impossible to establish the extent of the anterior and posterior dorsal fontanelles. Lateral to the semicircular canals, the roof of the otic region is mostly complete, and the lateral faces are also completely mineralized to the level of the vestibular fontanelles, with the exception of the articulation surface for the hyomandibula (Fig. 2.10A, C-D). Ossification becomes poorer anteriorly, passing into the orbitotemporal region, except for the lateral portions of the postorbital processes (Fig. 2.10E).

The posterior margins of the otic region form the anterior margin of the otoccipital fissure laterally, and the margin of the posterior dorsal fontanelle dorsally. The vagus (X) nerve passed through a visible indentation in the posterolateral margin, giving it a sinuousoidal outline (Fig. 2.10A, X). The almost straight dorsal margin marks the lateral border of the fossa bridgei, although here too are signs of incomplete ossification towards the spiracular canal (Fig. 2.10A, C-D, spi). The fossae bridgei are formed of two deep depressions, connected by a triangular “saddle” above the ampulla of the horizontal semicircular canal (Fig. 2.10A, D, fb). The posterior depression is rhombic in dorsal view and occupies most of the volume between the posterior and horizontal semicircular canals, reaching its lowest point below the plane of the horizontal semicircular canal; the anterior depression is shallower, positioned lateral to the ampulla of the

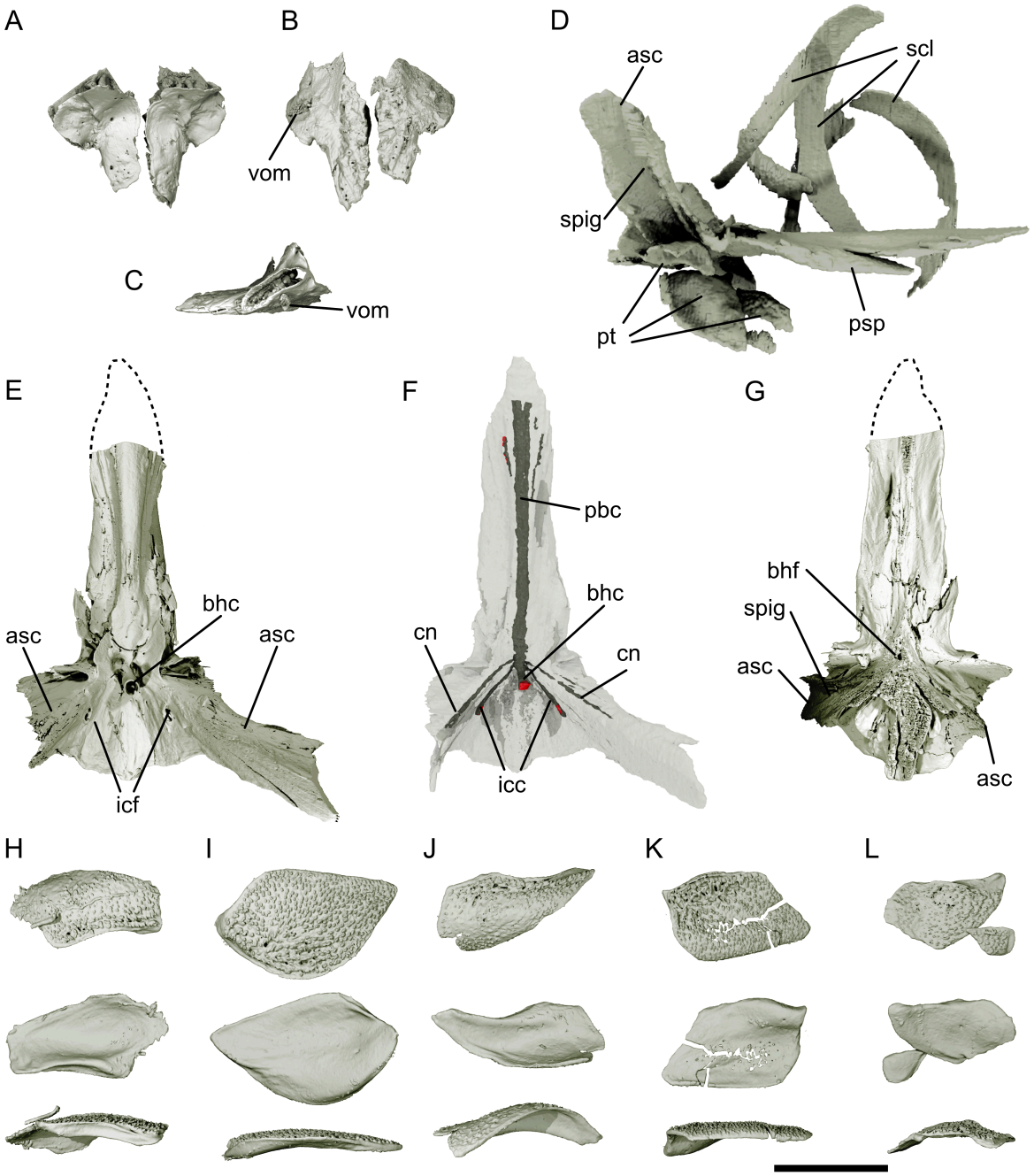


Figure 2.11: Renders of the ethmoids, parasphenoid, sclerotic rings, and parotic toothplates of *Pteronisculus gunnari* NHMD–75388. Ethmoids in dorsal view (A), ventral view (B) and right ethmoid in lateral view (C). Parasphenoid, sclerotic rings fragments and parotic toothplates in right lateral view (D). Parasphenoid in dorsal view (E), rendered partially transparent (F), and in ventral view (G). Parotic toothplates in ventral view (anterior to right, top row), dorsal view (anterior to left, middle row) and lateral view (anterior to right, bottom row) (H-L). A-C, E, G, H-L rendered from synchrotron data; D, F rendered from microCT data. Dashed lines in E and G indicate the anterior extent of the parasphenoid, as it was not part of the synchrotron data. Scale bar: 5 mm for A-G; 3.5 mm for H-L. Abbreviations: asc, ascending process; bhc, buccohypophyseal canal; bhf, buccohypophyseal foramen; cn, canal**;** icc, internal carotid canal**;** icf, internal carotid foramen; pbc, parabasal canal; psp, parasphenoid; pt, parotic toothplate; scl, sclerotic ossicle; spig, spiracular groove; vom, possible vomer**.**

anterior semicircular canal, and accommodated openings for the spiracular canal and the otic canal (Fig. 2.10A, C, fb). The lateral cranial canal exits the cranial cavity through a large, rounded canal in the loop on the posterior semicircular canal (Fig. 2.10A, lcc). It also reconnects with the cranial cavity through the loop of the anterior semicircular canal, lateral to the fossa bridgei (Fig. 2.10A, lcc), although this feature may be due to incomplete ossification relating to the juvenile nature of the specimen.

The ventral margin face of the otic region is developed into an ovoidal parampullary process (Fig. 2.10A, p.amp) somewhat posterior to the large vestibular fontanelle. The jugular depression runs just dorsal to the vestibular fontanelle, in a straight line from the posterior margin to the jugular canal (Fig. 2.10A, C, jd); the glossopharyngeal (IX) nerve exits the cerebral cavity about halfway through this depression via a small foramen (Fig. 2.10A, IX). The area around the articulation surface for the hyomandibula is incompletely ossified on both sides, extending to include both the spiracular canal and a portion of the postorbital process, and thus appears to cover a much larger area than it would in life (Fig. 2.10A, hmf). The area around the spiracular canal is incompletely ossified on both sides (Fig. 2.10A, C-D, spi). It is continuous ventrally with a short spiracular groove that in life would have passed onto the lateral face of the ascending process of the parasphenoid.

Three foramina pierce the postorbital process posterior to the hyomandibula facet: a large, anterior opening for the jugular vein, a ventrolateral opening for the hyomandibular trunk of the facial nerve, and a

lateral opening for the hyoid artery (Fig. 2.10A, C, jc, hfc, hya). The smaller two almost immediately join the main jugular canal, which runs in anterior and slightly ventral direction, to open into the trigeminofacialis chamber on the posterior wall of the orbit (Fig. 2.10E, tfc). Two additional small canals branch from the jugular canal before it enters the trigeminofacialis chamber: a ventral one for the external carotid, which pierces the lateral face of the braincase below the articulation with the hyomandibula (Fig. 2.10A,C, exc), and a small lateral one which does not appear to exit the braincase wall. The facial (VII) nerve canal enters the jugular canal just before it opens into the trigeminofacialis chamber, while the trigeminal (V) nerve exit foramen is just above the opening of the jugular canal, in a depression that also hosts the ventral foramen of the otic canal (Fig. 2.10E, V, VII, ocf).

The postorbital process marks the widest point of the braincase (Fig. 2.10A, C-E, por); it juts anterolaterally, almost in a plane with the anterior semicircular canal. Its dorsal margin, as well as the portion that connects it to the interorbital wall, are poorly ossified. The dorsal half of the posterior myodome and the, the area surrounding the internal carotids and the optic (II) nerve are completely unossified (Fig. 2.10E).

The orbitotemporal region is only partially ossified, preserving portions of the posterodorsal interorbital wall and areas surrounding the trochlear (IV) nerve and ophthalmic nerves (Fig. 2.10A, C-E). The right posterodorsal interorbital wall is separated from the rest of the right otic region. Ossification extends ventrally as far as the oculomotor (III) nerve foramen,

although it is too poor for this region to be segmented. The dorsalmost portion of the orbitotemporal region has various foramina preserved: five foramina for the ophthalmic nerves are present in a line, arching very close to the dorsal margin of the preserved interorbital wall (Fig. 2.10B, E, ofn), while the trochlear (IV) nerve is situated more ventrally (Fig. 2.10B, E, IV).

A separate basisphenoid cup is preserved ventral to the rest of the braincase, slightly disarticulated but still in association (Fig. 2.10A, C, E, bsp). It is roughly cup-shaped, with a deeply concave, elliptical dorsal surface, a wide, convex anteroventral surface and an almost vertical, convex posterior surface. The anterior and posterior surfaces meet ventrally at an acute angle, forming a transversal ridge; the posterior surface marks the anterior margin of the ventral otic fissure. Both the anterior and posterodorsal margins are notched on the midline (Fig. 2.10E). The anterior notch abutted the buccohypophyseal canal pedicle of the parasphenoid (Fig. 2.10C, E, bhc). A pair of grooves that mark the anterior portion of the basisphenoid housed the anterior carotids, and a more lateral pair housed the internal carotids (Fig. 2.10A, C, E, acg, icg). Both pairs of grooves are deep dorsally and fade ventrally.

The ethmoids are mineralized separately from the remainder of the braincase, and have been displaced to lie lateral and somewhat dorsal to the parasphenoid. They are roughly trapezoidal, with a straight medial margin and curved anterior margins (Fig. 2.11A-B). Laterally, the anterior portion is wider than the posterior portion, with these two regions

separated by a distinct notch for the autopalatine articulation facet. A large, ovoid articulation facet for articulation with the anterior portion of the palatoquadrate (autopalatine) occupies the entire anterolateral margin. Both the dorsal and ventral surfaces are pierced by small canals, and the ventral surface also bears a curved groove near its medial margin. A small toothplate applied to the anterolateral extremity of the ventral surface, may represent a vomer (Fig. 2.11B-C, vom).

Multiple fragments from both sclerotic rings are commingled within the orbit (Fig. 2.11C, scl). Each ring appears to be made up of at least three or four plates, each of which is very thin and has a medial margin slightly thicker than the lateral margin. The plates differ in dimensions, and it is difficult to tell how complete they are.

The parasphenoid is well preserved, extending to the ethmoid region and terminating anterior to the ventral otic fissure. The anterior corpus is long, with a longitudinal medial crest that gives this portion of the bone a triangular cross section. The right margin is slightly damaged in its posterior half (Fig. 2.11D-G, psp). Small teeth are borne on a narrow medial strip on the anterior third of the ventral surface of the anterior corpus, either side of which are large overlap areas that would have been covered by the accessory vomers (Fig. 2.11G). The anterior corpus gradually widens posteriorly towards the ascending processes. Dermal basipterygoid processes are absent. The ascending process is broad, bipartite, and in life would have covered most of the posterior face of the sphenotic (Fig. 2.11D-E, G, asc), with two faces separated by the

spiracular groove (Fig. 2.11D, G, spig): the anterior part of the process is short, rounded, and directed laterally, whereas the more posterior is tall and directed dorsally. Tiny teeth cover the base of the posterior face (Fig. 2.11G). Roughly half of the left ascending process is fragmented, although it is complete on the right side, reaching the level of the spiracular canal foramen. A deep spiracular groove incises the ascending processes, narrowing to a ventral point and almost meeting its antimere on the midline either side of the small buccohypophyseal foramen (Fig. 2.11G, bhf, spig).

The buccohypophyseal canal enters the dorsal margin of the parasphenoid via a substantially raised pedicel between the ascending processes (Fig. 2.11E-F, bhc), with only a small corresponding foramen on the ventral face of the bone (Fig. 2.11G, bhf). An enclosed midline parabasal canal runs for almost the full length of the parasphenoid, diverging and exiting close to its anterolateral tip (Fig. 2.11F, pbc). Two additional small canals are emitted from near the origin of the parabasal canal. The more posterior of these leaves the dorsal margin of the parasphenoid near the base of the ascending process, and likely accommodated the internal carotid (Fig. 2.11E-F, icf, icc), The more anterior runs through the anteriormost portion of the ascending processes and does not appear to exit the parasphenoid (Fig. 2.11F, cn).

Posterior to the buccohypophyseal foramen, the dorsal and ventral surfaces of the parasphenoid diverge. The dorsal surface is continuous laterally with the ascending processes and cups the basisphenoid ossification. In contrast, the ventral surface is reduced to a narrow,

multipartite pedicel covered in tiny teeth almost beyond the limit of the scan resolution. Deep concave embayments flank this pedicel (Fig. 2.11D, E). These embayments accommodate parotic toothplates, six of which are preserved in a disarticulated position ventral to the posterior corpus of the parasphenoid (Fig. 2.7A, 11H-L, pt). They are thin and vary from roughly rectangular to teardrop-shaped, with a deeply concave dorsal surface and a convex ventral surface bearing minuscule teeth. One margin of each plate is thickened into a ridge. In life, they appear to have formed pairs and were likely arrayed in two rows, posterior to the buccohypophyseal foramen.

Endocast. Limited ossification of the internal walls of the cranial cavity, combined with the presence of multiple separate and displaced braincase ossifications, make it difficult to reconstruct much of the endocast. The lateral faces of the mid- and hindbrain regions of the endocast and the labyrinth are best preserved. Of the forebrain region of the endocast, only the posterolateral limits of the optic lobes can be identified. The walls of the midbrain region are also mostly unossified: the anteriormost features that can be described are the anterior ampullae, the canal for the trigeminal (V) nerve and the cerebellar auricles (Fig. 2.12C-D).

The hindbrain region can be almost completely reconstructed (Fig. 2.12A-E). It is hourglass-shaped in dorsal view, but the relative displacement of the two halves of the orbitotemporal region must be taken into account when considering the endocast proportions in Figure 12(C-E). Its highest

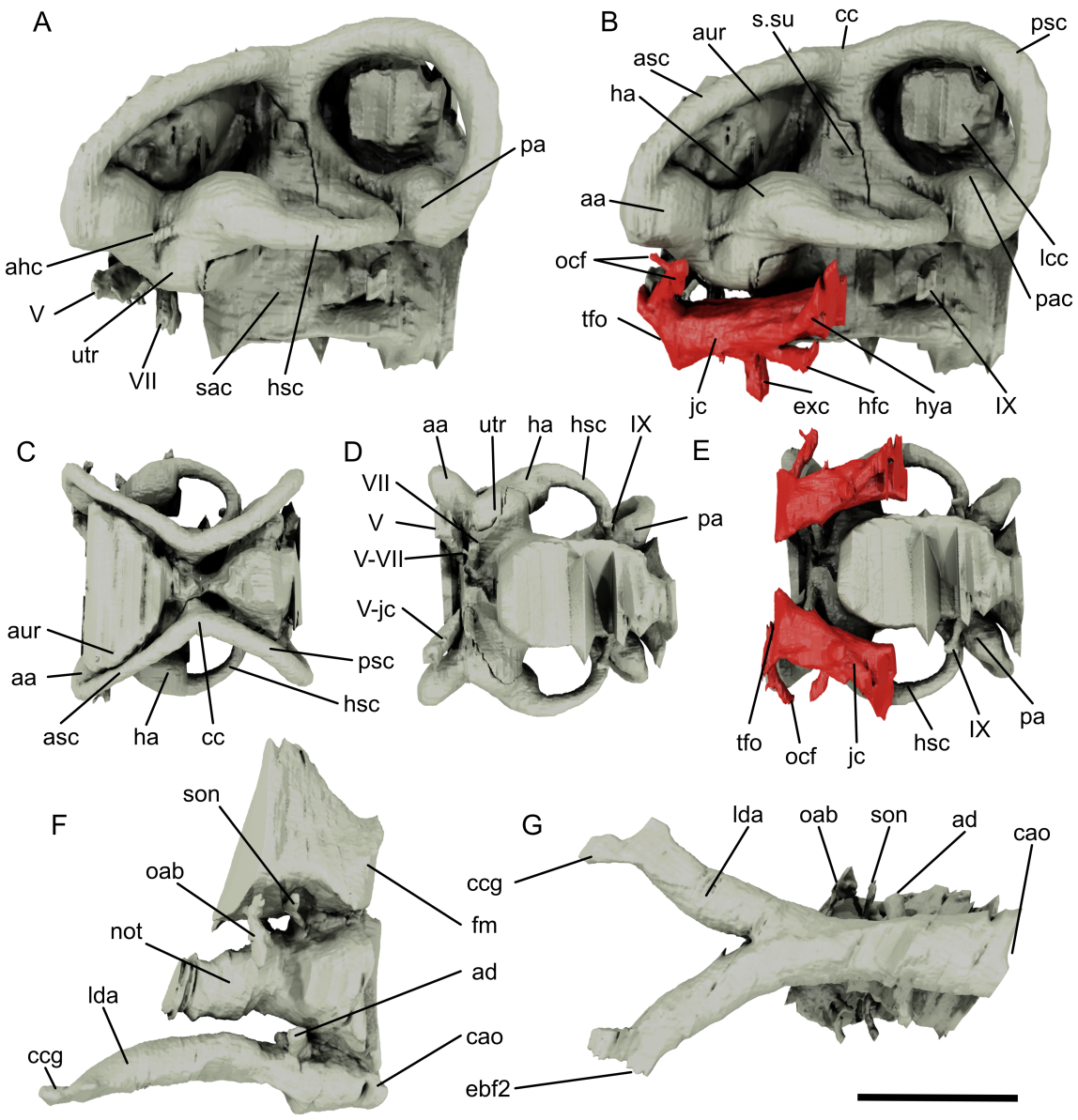


Figure 2.12: Renders of the endocast of *Pteronisculus gunnari* NHMD–75388. Endocast in left lateral view (A) and with the jugular canal in red (B). Endocast in dorsal view (C), ventral view (D) and with the jugular canal in red (E). Posterior portion of the endocast and basicranial circulation in left lateral view (F) and ventral view (G). Scale bar: 5 mm for A, B; 4 mm for C-E; 6 mm for F, G. Abbreviations: aa, anterior ampulla; ad, artery canal; ahc, connection between anterior and horizontal ampullae; asc, anterior semicircular canal; aur, cerebellar auricle; cao, canal for dorsal aorta; cc, crus commune; ccg, common carotid; ebf2, efferent branchial artery; exc, external carotid foramen; fm, foramen magnum; ha, horizontal ampulla; hfc, hyomandibular trunk of the facial nerve; hsc, horizontal semicircular canal; hya, hyoid artery canal; jc, jugular canal; lcc, lateral cranial canal; lda, lateral dorsal aorta; not, notocord; oab, occipital artery branch; ocf, otic canal; pa, posterior ampulla; pac, preampullary canal; psc, posterior semicircular canal; s.su, sinus superior; sac, saccular recess; son, spinoccipital nerve; tfo, trigeminofacialis opening; utr, utriculus; V, trigeminal nerve; V-jc, trigeminal-jugular canal connection; V-VII, trigeminal-facial nerve connection; VII, facial nerve; IX, glossopharyngeal nerve.

point is medial to the posterior semicircular canal. The cranial cavity, lateral cranial canal and fossa bridgei are continuous; the medial walls of the cranial cavity are incompletely ossified such that the lateral cranial canal has both an anterior and posterior connection through the loops of the corresponding semicircular canals (Fig. 9A; 12A-B, lcc). The cerebellar auricles are just visible as slight bulges medial to the anterior semicircular canals (Fig. 2.12B-C, aur). The cranial walls surrounding the midbrain and forebrain regions of the endocast are not ossified, and thus these portions cannot be described.

Unlike much of the rest of the endocast, the perichondral bone surrounding the bony labyrinth is almost completely preserved, permitting a full description. The sinus superior is roughly triangular in lateral view (Fig. 2.12B, ss) and is partially separated from the rest of the endocast by flaps of bone. The posterior semicircular canal is thicker than the others and describes an almost perfect circle, but the corresponding ampulla is the smallest (Fig. 2.12A-E, psc, pa). A short length of preampullary canal separates the posterior ampulla from the cranial cavity (Fig. 2.12A-B, pac). The anterior semicircular canal has a very slight curvature, is dorsoventrally compressed (Fig. 2.12A-E, asc) and enters its ampulla through its anterodorsal margin (Fig. 2.12A-E, aa).

The posterior and anterior canals meet at the crus commune at a roughly 120° angle in dorsal view, while in lateral view the dorsal margins of the two canals form almost a straight line (Fig. 2.12A-B, cc). The horizontal semicircular canal is the smallest, but its ampulla is the largest and

communicates with the anterior ampulla by means of a narrow canal (Fig. 2.12A, ahc). Both the posterior end of the horizontal semicircular canal and the preampullary portion of the posterior semicircular canal run parallel for a distance before entering the cranial cavity at the ventral limit of the sinus superior. The utriculus is about twice the size of any of the ampullae and communicates with the ventromedial side of the horizontal ampulla and the posteromedial side of the anterior ampulla (Fig. 2.12A-B, D, utr). The lateral margin of the saccular chamber is vertical, but its exact shape cannot be determined (Fig. 2.12A, sac). A short canal carries the glossopharyngeal (IX) nerve laterally into the jugular depression from a point anterior and ventral to the posterior ampulla (Fig. 9A, IX; Fig. 2.12A-B, D-E, IX). Very narrow canals connect the facial (VII) and the trigeminal (V) nerves and the trigeminal (V) nerve with the jugular canal, while the otic canal has a small branch in anterodorsal direction before exiting into the fossa bridgei posterodorsally (Fig. 2.12A-E, ocf, V, V-jc, V-VII, VII).

Operculogular Series. The operculogular series is partially preserved in the specimen and includes the opercular, subopercular and first branchiostegal ray of the left series. As these are mostly preserved on the surface of the specimen, ornamentation is almost completely lost. Other elements of the operculogular series are either prepared away or embedded in pyrite clusters.

The operculum is rectangular, with the shorter side about half the length of the long sides (Fig. 2.1B, D; Fig. 2.2B-C, op). The posteroventral margin is straight, while the dorsal and anteroventral margins are slightly curved,

and anterodorsally the bone tapers slightly. Much of the suboperculum can only be reconstructed from its impression on the surface, although a fragment of the right is preserved (Fig. 2.1B, D; Fig. 2.2B, sop). It is roughly trapezoidal, a little under half the height of the operculum, with an anterior margin shorter than the posterior margin. A small, thin anterodorsal process is present, although this, and the dorsal margin of the suboperculum, were overlapped by the operculum.

The sole undisputed branchiostegal is roughly triangular and somewhat wider than the suboperculum (Fig. 2.1D; Fig. 2.2B, br). It bears an anteroposteriorly directed low ridge parallel with its dorsal margin and traces of tubercular ornamentation on its lateral surface. Another thin and long ossification, tapering posteriorly to an asymmetrical tip and with a rounded anterior margin, could be another branchiostegal displaced between the cleithra.

Gill skeleton. The branchial skeleton is preserved almost in its entirety and largely in articulation. It comprises three incompletely ossified basibranchials, four hypobranchials, five ceratobranchials, four epibranchials, three infrapharyngobranchials and one suprapharyngobranchial. Hundreds of gill filaments and toothplates are also preserved all around the branchial skeleton.

Three basibranchials are present. They have limited internal endochondral ossification and their extremities are unfinished, typically appearing as open, concave surfaces (Fig. 2.13A-B, bbI-III). The dorsal surface of each is slightly convex, smooth and rectangular. The first basibranchial is

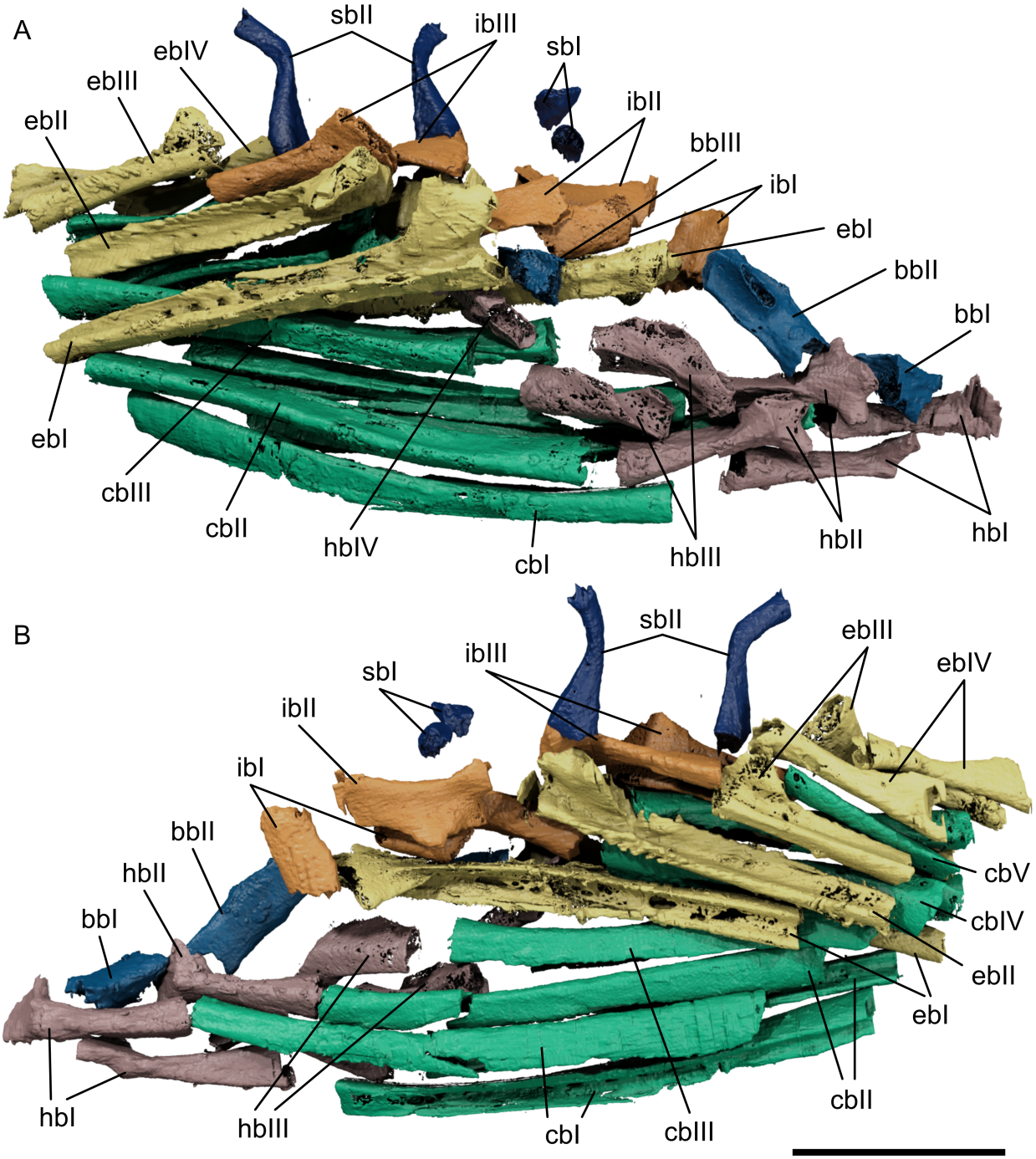


Figure 2.13: Renders of the gill skeleton of *Pteronisculus gunnari* NHMD–75388. Gill skeleton in right lateral view (A) and left lateral view (B). Scale bar: 10 mm. Colour coding: blue, basibranchials; light brown, hypobranchials; purple, ceratobranchials; green, epibranchials; magenta, infrapharyngobranchials; dark green, suprapharyngobranchials. Abbreviations: bbI-III, basibranchials; cbI-V, ceratobranchials; ebI-IV, epibranchials; hbI-IV, hypobranchials; ibI-III, infrapharyngobranchials; sbI-II, suprapharyngobranchials.

triangular in cross section, while the other two have a trapezoidal cross section, which becomes triangular ventrally. Basibranchial I has a convex anterior face, which likely articulated with the hypohyals. Basibranchial II is the most completely ossified element. Two pairs of rectangular depressions are present on its ventral side, one pair near the anterior margin and one pair either side of the ventral process, probably for articulation with the second and third pairs of hypobranchials (Fig. 2.13A, bbII). Basibranchial III, despite being poorly ossified, has a similar ventral process flanked by depressions (Fig. 2.13A, bbIII), likely for the fourth hypobranchials.

Hypobranchials are preserved in association with the first four gill arches. Hypobranchial I is straight and slender with a rectangular cross section, a triangular, medially directed head, and a slightly expended posterior end (Fig. 2.13A-B, hbI). Hypobranchial II is similar but slightly shorter, with a bigger, triradiate head (Fig. 2.13A-B, hbII). The articulation facets for the basibranchials would have been almost vertical in life position. The third hypobranchial is very different, being shorter and twisted. The anterior half of its ventral surface is deeply grooved, while the medial surface bears an anterior hook-like process that articulates with basibranchial II (Fig. 2.13A-B, hbIII). Hypobranchial IV is much smaller, with a grooved ventral surface giving it an n-shaped cross section, and a slightly flared posterior margin (Fig. 2.13A-B, hbIV).

Ceratobranchials I – IV are elongate, slightly curved ossifications that decrease in length from the first to the fourth and bear a ventral groove

(Fig. 2.13A-B, cbI-IV). Ceratobranchials I and II have a trapezoidal cross section anteriorly but develop a longitudinal groove on the ventral surface that runs the length of the bone, resulting in an n-shaped cross section posteriorly (Fig. 2.13A-B, cbI-II). The third ceratobranchial differs in bearing a ventral groove along its entire length, with a corresponding n-shaped cross section, and is slightly sinusoidal in dorsal view (Fig. 2.13A-B, cbIII). Ceratobranchial IV is also grooved along its entire ventral surface and sinusoidal in dorsal view. Additionally, it has an expanded anterior head with a ventromedially-directed process; the groove runs dorsal to this process (Fig. 2.13A-B, cbIV). The fifth ceratobranchial is short, thin, and rod-like, lacking a ventral groove (Fig. 2.13A-B, cbV).

Epibranchials I-III are rod-like, U-shaped in cross section, with a dorsally-directed uncinate process directed on their anterior heads, and a longitudinal groove on their dorsal surface (Fig. 2.13A-B, ebI-III). Both the total length and the size of the uncinate process decrease from epibranchial I to epibranchial III, but otherwise the bones are very similar. Epibranchial IV is markedly different, being more cylindrical, with anterior and posterior expanses at angles to each other (Fig. 2.13A-B, ebIV). It lacks both an uncinate process and ventral groove.

A single suprapharyngobranchial I is associated with the first gill arch. It is small and stubby, articulating between the uncinate process of epibranchial I and the parampullary process on the braincase (Fig. 2.13A-B, sbI). A much longer suprapharyngobranchial II is associated with the second gill arch. It is sinusoid, comprising two arms that meet at an obtuse

angle: the anteroventral arm is longer and flares at its base, giving it a conical appearance, while the dorsal arm is about half as long and does not flare at its extremity (Fig. 2.13A-B, sb II). Infrapharyngobranchial I is short, roughly rectangular in lateral view, and ellipsoidal in cross section (Fig. 2.13A-B, ibI). The second and third infrapharyngobranchials are larger than infrapharyngobranchial I and dorsoventrally flattened. Infrapharyngobranchial II has a concave dorsal margin, a small lateral process and a flared, bilobate posterior extremity where it contacts the anterior margin of the corresponding epibranchial (Fig. 2.13A-B, ibII). The third pair is the largest of the three, flares at both extremities and has a longitudinal twist between the anterior and posterior extremities of about 15° (Fig. 2.13A-B, ibIII).

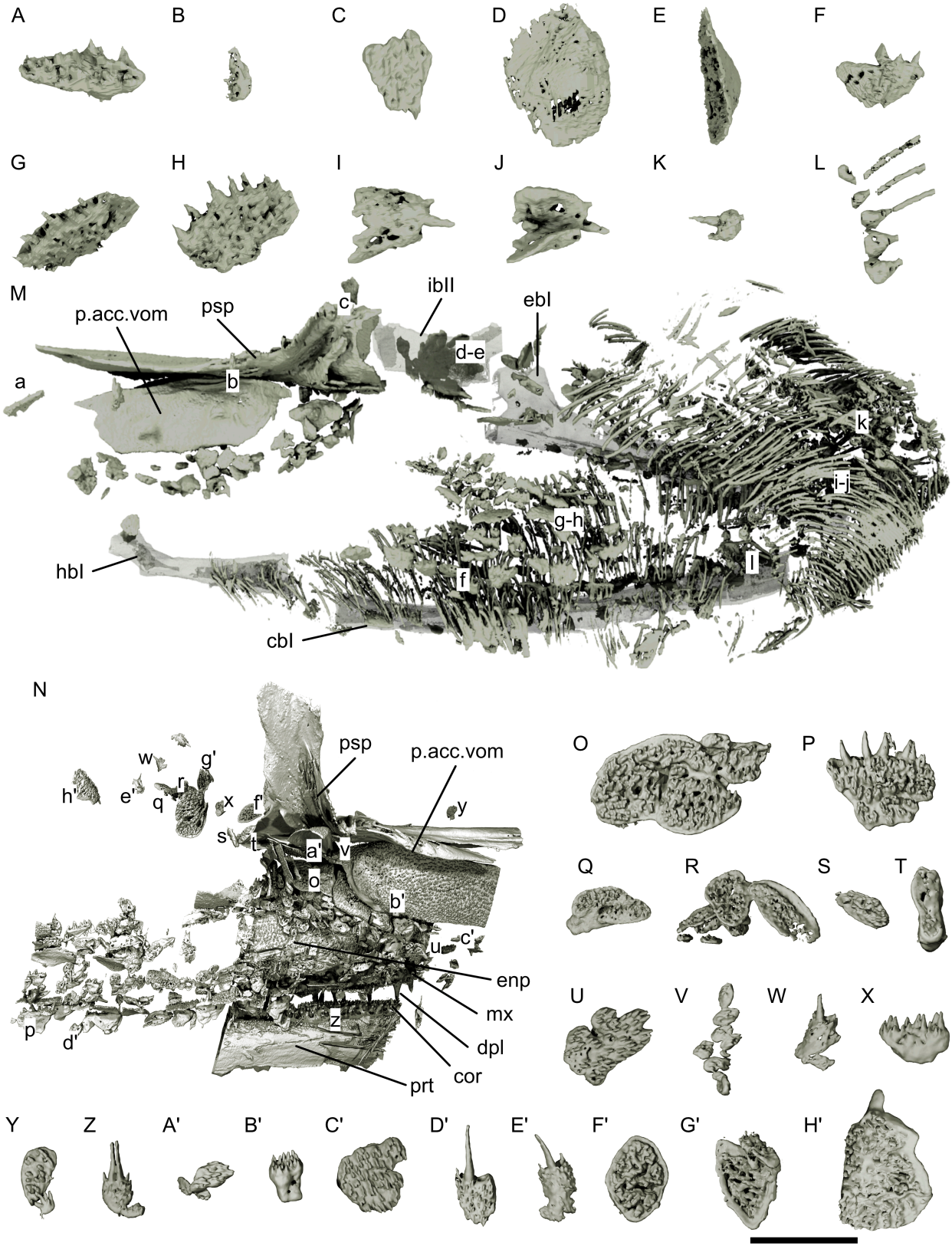
Hundreds of thin, curved, smooth gill rays are present in the specimen, in loose association with the endoskeletal gill arches but somewhat removed from life position (Fig. 2.14M). Each ray is very long and needle-like, with a tapered distal extremity and expanded proximal extremity. They are distributed in the areas around the ceratobranchials and the epibranchials, and in clusters medial to the opercula; the length, curvature and number of the rays all increase from the anterior portion of the ceratobranchials towards the epibranchials. Thickness, on the other hand, is maximum around the posterior half of the ceratobranchials. Where they are closer to life position, they are aligned perpendicular to the long axis of the gill ossifications, with the expanded head oriented close to the longitudinal groove of the host ceratobranchials or epibranchials. Small openings

arranged longitudinal rows either side of the epibranchial/ceratobranchial groove may represent attachment sites for the gill rays. Medial to each operculum, three to five gill rays are preserved a short line, with greatly expanded bulbous heads (Fig. 2.14L).

Toothplates and gill rakers. Hundreds of small toothplates are concentrated around the branchial skeleton, between the jaws and below the braincase and parasphenoid (Fig. 2.14M-N). The teeth range in size from barely visible at the XCT scan resolution, to a maximum length of about half a millimetre, which is comparable with the smaller teeth on the jaws. The morphological diversity is wide, but they can be divided into 6 main morphotypes:

1) three to four toothplates with similar morphologies are found in the snout area, close to the premaxillae (Fig. 2.14A). Thin and relatively long (about 2 mm), they bear many small teeth of different sizes and with no particular arrangement;

Figure 2.14: Distribution of toothplates and gill rays in *Pteronisculus gunnari* NHMD-73588. Morphotype 1 toothplate in ventral view (A). Morphotype 2 toothplate in lateral view (B). Morphotype 3 toothplate in ventral view (C). Morphotype 3 toothplate in dorsal (D) and lateral view (E). Morphotype 4 toothplate in lateral view (F). Morphotype 4 toothplate in dorsolateral (G) and lateral view (H). Morphotype 5 toothplate in lateral (I) and medial view (J). Morphotype 6 toothplate in lateral view (K). Gill rays with bulbous heads in lateral view (L). Toothplates and gill rays in life position in left lateral view, with branchial arch rendered partially transparent; position of individual toothplates (A-L) indicated by corresponding lower case letters in left lateral view (M). Toothplates in life position in right medial view (N); position of individual toothplates (O-H') indicated by corresponding lower case letters. A-M rendered from microCT data; N-H' rendered from synchrotron data.. Scale bar: 2 mm for A-L, O-H'; 5 mm for M-N. Abbreviations: cbI, ceratobranchial I; cor, coronoid; dpl, dermopalatine; ebI, epibranchial I; enp, entopterygoid; hbI, hypobranchial I; ibII, infrapharyngobranchial II; mx, maxilla; p.acc.vom, posterior accessory vomer; prt, prearticular; psp, parasphenoid.


A
B
C
D
E
F
G
H
I
J
K
L
M
p.acc.vom
psp
c
ibII
ebl
d-e
a
b
k
i-j
g-h
hbl
f
l
cbl
N
psp
p.acc.vom
w
g'
h'
e'
q
r
x
f'
y
s
t
a'
v
o
b'
c'
u
enp
mx
dpl
cor
prt
z
p
d'
O
P
Q
R
S
T
U
V
W
X
Y
Z
A'
B'
C'
D'
E'
F'
G'
H'

2) a couple of very small (1 mm in length) toothplates are closely associated with the ethmoids (Fig. 2.14B, Y). They have a straight toothed margin with tiny, disorganised teeth, while the opposite margin is deeper on one side and tapers down on the other;

3) flattened plates, either very thin and polygonal (Fig. 2.14C, Q, AH) or with a flat side covered in minuscule teeth and a slightly convex opposite side (Fig. 2.14D-E, U, AF-AG). These are found more commonly in the area below the parasphenoid and the braincase, reaching lengths of up to 2-3 mm;

4) plates with a polygonal, flattened base plate and between one and 10-11 conical teeth on the medial margin of the plate (Fig. 2.14F-H, P, X). These plates sometimes have one or more missing teeth—presumably lost during replacement—as shown in Figure 14G. They are concentrated between the lower jaws and can be found aligned on the lateral surfaces of the ceratobranchials, forming a "wall" between the coronoids and the gill basket. Some of them, positioned anterior to the gill bars, may represent gill rakers. They bear the biggest teeth of all toothplates and are normally 1-2 mm long;

5) plates with a concave-convex base plate, rather than flat (Fig. 2.14I-J, W). These can bear 1-3 teeth of different sizes and are mostly found posteriorly to the ceratobranchials and around the epibranchials, and thus also likely represent gill rakers. The bigger ones can be about 1 mm wide and 1.5 mm long;

6) plates with a rounded bulb-like root from which 1-4 teeth can sprout are found in the same areas of morphotype 5, about 1-2 mm long including the teeth (Fig. 2.14K, Z, AD-AE). When multiple teeth are present, one or two are considerably bigger and can have an acrodin cap. These plates appear to represent a third gill raker morphotype.

Pectoral girdle and fin. The bones of the dermal pectoral girdle comprise the extrascapulars, presupracleithrum, supracleithrum, cleithrum, postcleithrum and clavicle; the endoskeletal girdle is formed from the scapulocoracoid; the pectoral fin endoskeleton comprises proximal and distal radials, lepidotrichia and fringing fulcra. Most of the bones of both pectoral girdles are preserved in the specimen, although the scapulocoracoid shows signs of incomplete ossification and many radials are partially engulfed by pyrite, especially in the right pectoral fin.

A single pair of lateral extrascapulars are preserved in the specimen (Fig. 2.2A,C; 15A-B exsc). They are laminar, with a convex external side and a concave medial side, roughly triangular in dorsal view. The right extrascapular is partially embedded in pyrite, while the left is more complete and preserves the three-way junction of the supratemporal commissure medially, cephalic lateral line posteriorly, and supraorbital canal anteriorly. Small fragments situated close to one of the lateral extrascapulars likely represent median extrascapular elements or additional ossifications anterior the extrascapulars as described by Nielsen (1942: fig. 26c; p.116).

Both left and right presupracleithra are preserved, loosely associated with the supracleithra although somewhat displaced (Fig. 2.2A, C; 15A-B, psclth). Each presupracleithrum is roughly triangular and laminar, with a convex lateral side and concave medial side. The external surface is unornamented, except for a small area near the posteroventral edge of the bone which bears some tubercules, and sensory canals are absent.

The supracleithrum is large, thin, and roughly rectangular (Fig. 2.1B, D; Fig. 2.2A-C; Fig. 2.15A-B, sclth). It is convex, but has a distinct concavity on the anterodorsal portion of the lateral surface. The entire lateral surface is ornamented with ridges. Two canals enter the anterodorsal margin of the supracleithrum. The more dorsal, for the lateral line, is sinusoidal with a slight dorsoventral bend and exits the bone from its medial surface, roughly halfway along the posterodorsal margin (Fig. 2.15B, llc). A more ventral cavity, comprising two parallel channels, roughly follows the anteroventral margin, before exiting along a narrow ridge on the medial surface (Fig. 2.15B, cv). A narrow ridge, roughly centred on the medial surface of the bone, parallel to the long margins, may have abutted the dorsal margin of the cleithrum.

The cleithrum has a tall, pointed dorsal arm with a slightly recurved medial margin, as well as curved mediolateral, anterior and lateral faces that create a continuous surface (Fig. 2.1B; Fig. 2.2A-D; Fig. 2.15A-B, clth). The posterior and posteroventral margins, particularly around the pectoral notch, are poorly preserved; the right is exposed on the surface and the left is obscured by pyrite. The dorsal arm passes into an elongate, thin

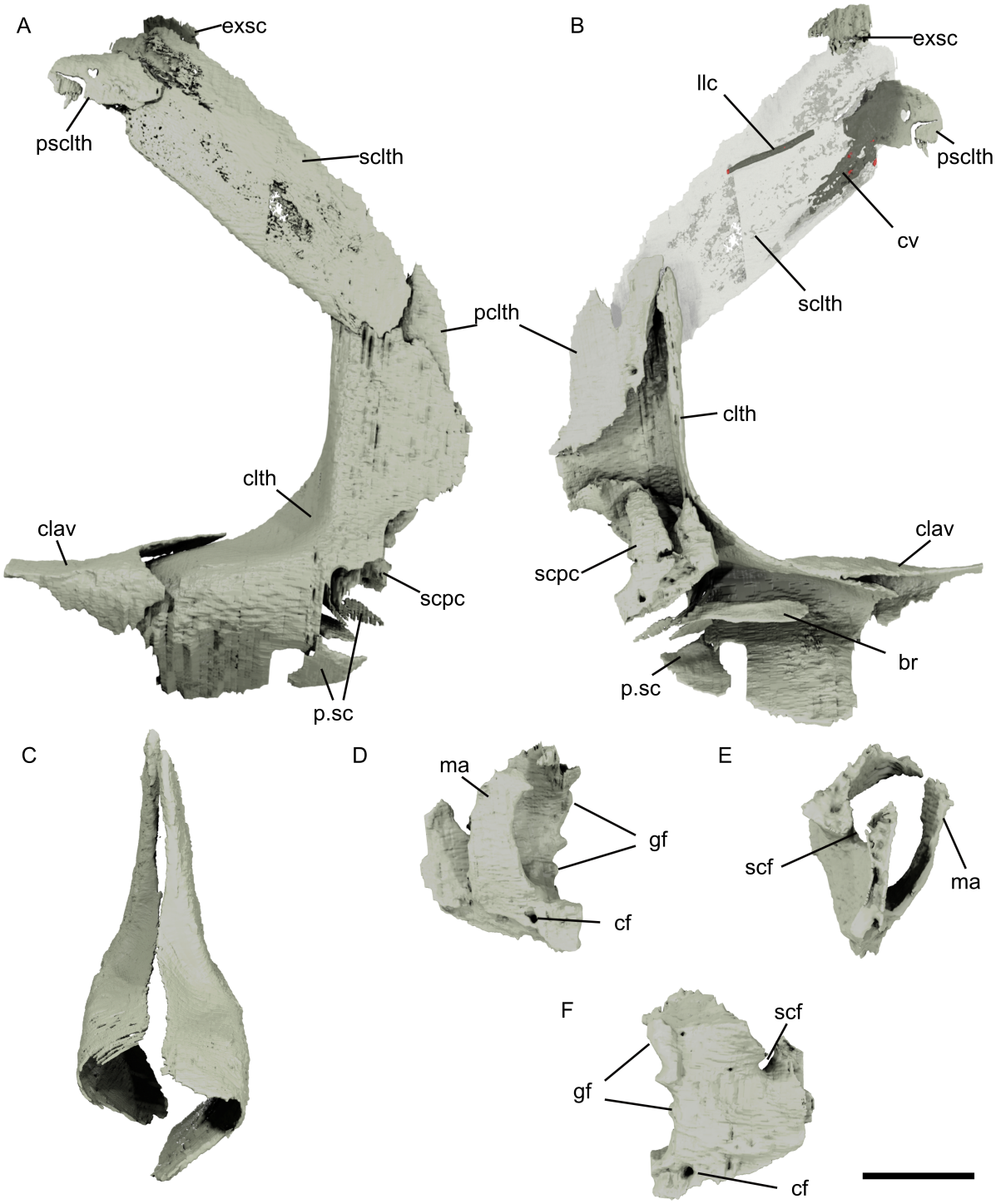


Figure 2.15: Renders of the shoulder girdle and pectoral fin endoskeleton of *Pteronisculus gunnari* NHMD–75388. Left shoulder girdle and scapulocoracoid in lateral view (A) and medial view, with supracleithrum rendered partially transparent (B). Cleithra in anterior view (C). Right scapulocoracoid in medial view (D), anterior view (E) and lateral view (F). Scale bar: 7 mm for A-C; 5 mm for D-F. Abbreviations: br, branchiostegal ray; cf, coracoid foramen; clth, cleithrum; cv, cavity; clav, clavicle; exsc, extrascapular; gf, glenoid fossa; llc, lateral line canal; ma, mesocoracoid arch; p.sc, pectoral fin scales; pclth, postcleithrum; psclth, presupracleithrum; scf, supracoracoid foramen; sclth, supracleithrum; scpc, scapulocoracoid.

triangular postbranchial lamina, which is widest at the base of the dorsal arm, close to the pectoral notch. The postbranchial lamina forms an approximately 90° angle with the triangular, curved external lamina, and with the anterior arm through a deep, anteromedially facing concavity. An unornamented strip along the anterior margin of the cleithrum would have been overlapped by the clavicle. The lateral and dorsal surfaces are otherwise ornamented with ridges. A small, thin, tear-shaped postcleithrum sits medial to the posterodorsal margin (Fig. 2.2A-B; Fig. 2.15A-B, pclth). It is relatively long, with a bifurcated anterodorsal margin and a posteroventral margin that tapers to a point. Its external surface is ornamented in delicate tubercles. The anterior margin is thickened, with a ridge to accommodate the cleithrum. The clavicle is strongly curved and overlies part of the anterior margin of the cleithrum (Fig. 2.1A-B, D; 15A-B, clav), but it is unclear how much it overlapped the ventrolateral face. It is partially engulfed by pyrite anteriorly and ventrally, obscuring some aspects of its anatomy. Convex dorsal and ventrolateral triangular faces join at an acute angle that mimics the angle between the same faces of the cleithrum. The more complete left clavicle has a concave posterior margin on the dorsal face, and an elongate posteromedial process that extends along the horizontal face of the cleithrum.

Both scapulocoracoids are preserved in the specimen, although most of the coracoid plate, and parts of the anterior and mesocoracoid processes are incompletely mineralized (Fig. 2.2A; Fig. 2.15A-E; Fig. 2.16A-B, scpc). The unossified areas are identical in both scapulocoracoids.

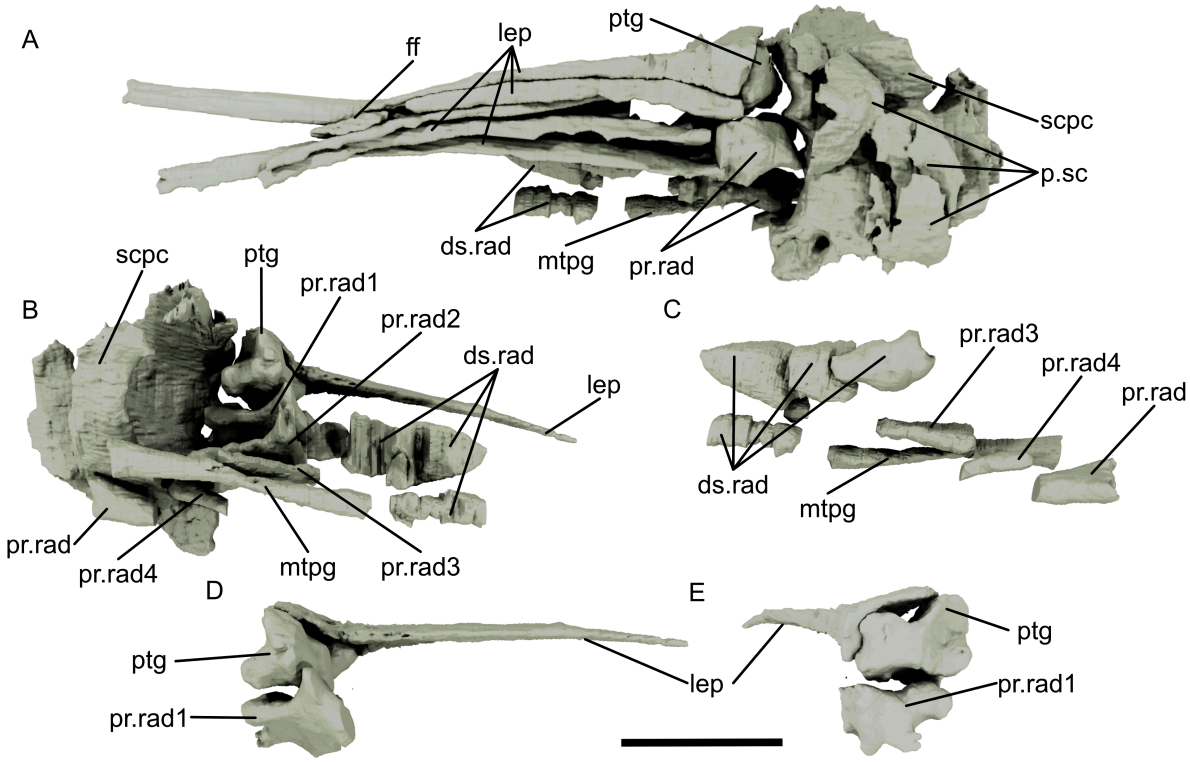


Figure 2.16: Renders of the pectoral fin of *Pteronisculus gunnari* NHMD–75388. Right pectoral fin in lateral view (A) and medial view (only first lepidotrich figured) (B). Distal radials, last three proximal radials and metapterygium in lateral view (C). Propterygium and first lepidotrich in posteromedial view (D) and anterolateral view (E). Scale bar: 5 mm. Abbreviations: ds.rad, distal radial**;** ff, fringing fulcra**;** lep, lepidotrichia; ptg, propterygium; mtpg, metapterygium; pr.rad1-4, proximal radial; p.sc, pectoral fin scale; scpc, scapulocoracoid.

As the anterior process is unmineralized, the anterior portion of the bone is present only as a small, dorsally directed stump. The supracoracoid foramen is round and opens posterodorsally, but its dorsal margin is also incompletely mineralized (Fig. 2.15C, E, scf). The mesocoracoid arch is thin and has a gentle anteroposterior curvature, more evident on the posterior margin; it is oriented such that it does not obscure the supracoracoid foramen in medial view (Fig. 2.15D-E, ma). Its lateral surface encloses the dorsal muscle canal medially, while dorsally the arch is incomplete, and as a result the canal is wide and roughly triangular in

section. The coracoid foramen lies just ventral to the posteroventral margin of the root of the mesocoracoid arch and pierces the bone in posterolateral direction (Fig. 2.15C-D, cf).

The dorsal and coracoid (ventral) portions of the bone are almost entirely unmineralized, so it is not possible to determine the shape of the ventral muscle canal or how the scapulocoracoid contacted the cleithrum. Similarly, there is no mineralized dorsal coracoid process. In contrast, the glenoid fossa is fully mineralized on the posterior margin of the bone (Fig. 2.15C-D, gf): in life position, it would have formed a roughly 30-45° angle with the vertical posterior margin of the cleithrum. Its concave margin has 3-4 protrusions for articulation with the endoskeleton radials, directed posterolaterally to ventrolaterally.

All radials appear to be preserved, but most are partially or wholly engulfed in pyrite and thus cannot be fully described. It is possible to identify the propterygium and metapterygium of the right fin, and an additional four to five proximal radials and at least three distal radials (Fig. 2.16A-E, ptg, mptg, pr.rad1-4, ds.rad). The right propterygium is well preserved and in situ, articulating with the lateral margin of the glenoid fossa (Fig. 2.16A-B, D-E, ptg). It is complex in shape, with dorsal and ventral portions almost divided in two by a deep grove on the lateral surface. The propterygium is imperforate, and this groove may have transmitted the properygial canal; alternatively, this may have passed medial to the propterygium, between it and the next radial. The propterygium is also fused to the first, fused lepidotrichia (Fig. 2.16A-B, D-

E, ptg, lep). The first radial is bulbous and blocky close to the glenoid fossa and flares out medially (Fig. 2.16A-B, D-E, pr.rad1); similarly, the second radial is smaller towards its articulation with the scapulocoracoid and flares out towards the distal radials, although is much flatter than the first radial (Fig. 2.16A-B, pr.rad2). The remaining proximal radials are rod-like with slightly flared proximal heads, but they could not be fully segmented (Fig.16A-C, pr.rad3-4). The metapterygium is roughly twice as long as the first radial and rod-like in section (Fig. 2.16A-C, mptg). Several distal radials are also present. Three have a flattened, roughly triangular or trapezoidal shape (Fig. 2.16A-C, ds.rad).

The lepidotrichia are long, slender and slightly recurved; a few representative elements were segmented and are shown in Fig. 2.1B, 2A-B and D (lep). A minimum of 30 are present for each fin. The first lepidotrichium is the shortest, formed of several conjoined lepidotrichia, and is fused to the propterygium (Fig. 2.16A-B, D-E, lep, ptg). Each lepidotrichium becomes segmented after a certain length, but the two halves do not diverge but rather remain joined together. Multiple, very thin ossifications of variable dimensions and curvature localised around both scapulocoracoids and the radials are interpreted as fin scales (Fig. 2.15A-B; Fig. 2.16A, p.sc). Fringing fulcra are also present (Fig. 2.16A, ff).

Axial skeleton. The axial skeleton comprises basidorsals, basiventrals and scales. Elements become increasingly difficult to segment more posteriorly due to artefacts from pyrite growth. At least 14-15 pairs of basidorsals are preserved, but only one complete

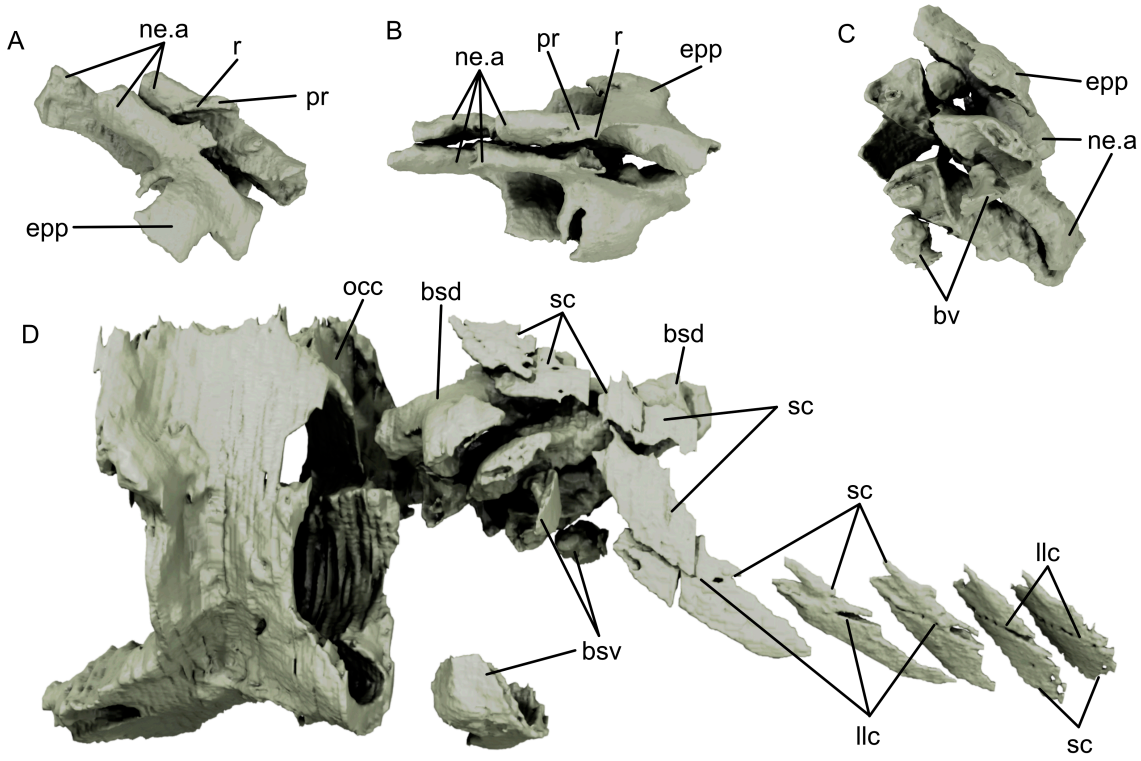


Figure 2.17: Renders of the axial skeleton of *Pteronisculus gunnari* NHMD–75388. Basidorsals in right lateral view (A), dorsal view (B) and posteroventral view (C). Occipital region of the braincase, portion of the axial skeleton and scales in left posterolateral view (D). Scale bar: 5 mm. Abbreviations: bsd, basidorsal; bsv, basiventral; epp, epineural process; int, intercalar; llc, lateral line canal; ne.a, neural arch; occ, occiput; pr, process; r, ridge; sc, scale.

basiventral, plus an incomplete basiventral associated with the second pairs of basidorsals.

The basidorsals are paired, and become more posteriorly in the vertebral column. The neural arch is oval in cross section and oriented posterodorsally (Fig. 2.17A-C, na). In smaller basidorsals, the neural arch is detached. Close to its base, a small process juts out anterodorsally (Fig. 2.17A-B, pr); the same process creates a small ridge on the medial surface of the basidorsal (Fig. 2.17A-B, r). These features become progressively smaller as the basidorsals become smaller, until they are

barely visible. The epineural process is broad and has an ovoidal cross section (Fig. 2.17A-D, ep). It is arched ventrally in the first pair of basidorsals, then becomes smaller and loses its curvature in smaller basidorsals.

Basiventrals are only associated with the first two pairs of basidorsals (Fig. 2.17C-D, bv). The only complete basiventral is "U"-shaped and has width comparable with the lower third of the notochordal canal. The anterior margin is notched. More basiventral fragments can be seen around the first two pairs of basidorsals (Fig. 2.17D, bv).

Numerous scales are preserved in the specimen, albeit disarticulated and in loose association (Fig. 2.2A-C, sc). The scale covering is essentially complete, as scales can be found all around the body. Lateral line scales show pores, corresponding to the lateral line canal. All scales are rhombic in shape and present peg-and-socket articulation on the dorsal margin (Fig. 2.17D, llc). The anterior scales are narrower and more elongated than posterior ones, while the dorsal and ventral scales are considerably smaller and with a stronger curvature.

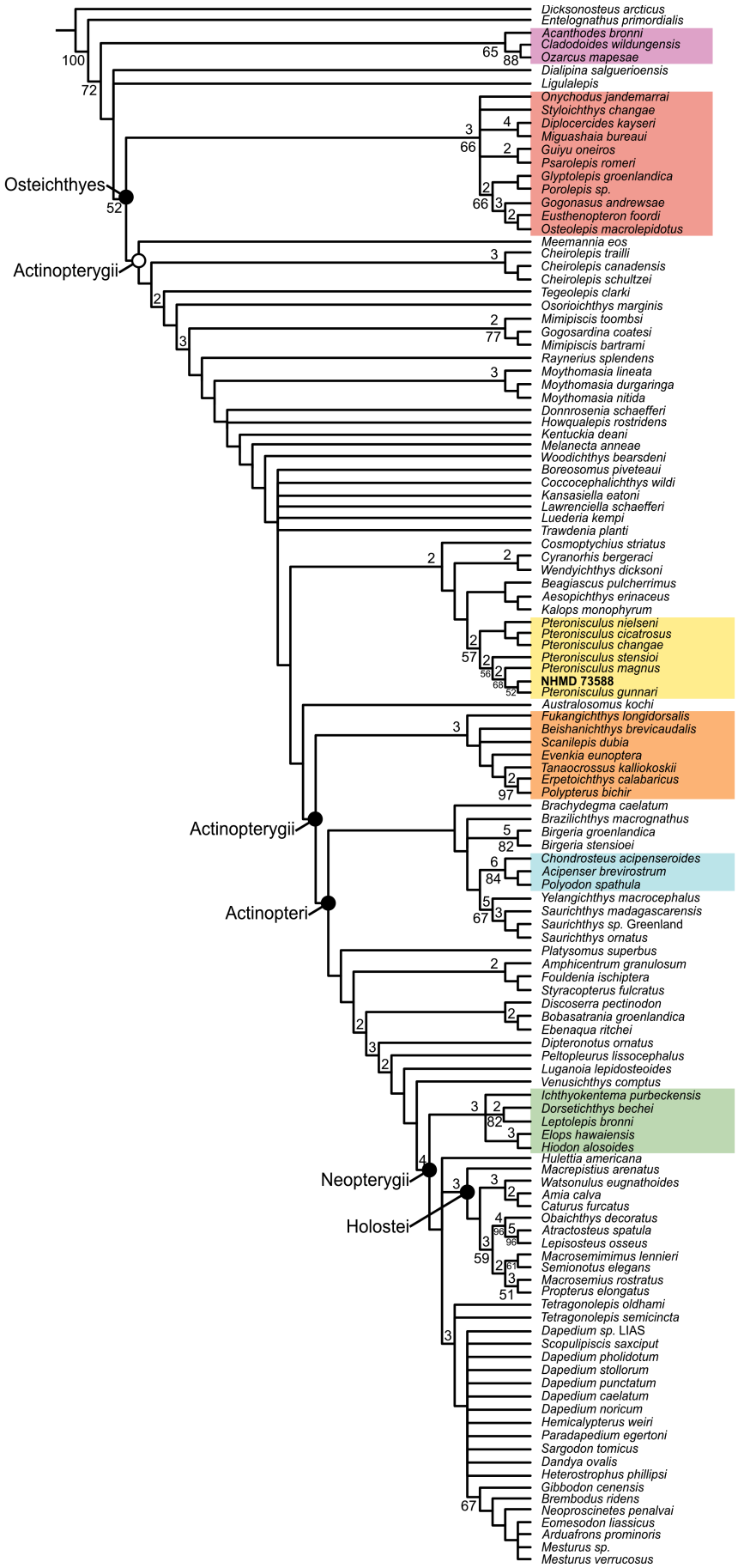
2.4.2 Phylogenetic analysis

Our equally weighted parsimony analysis retrieved 10752 most parsimonious trees of 1693 steps (Consistency Index: 0.198; Retention Index: 0.674); the strict consensus tree is shown in Figure 2.18. Sarcopterygians are recovered as monophyletic (Bremer Decay Index, BDI: 3), although most included taxa branch from a basal polytomy.

Sarcopterygians are resolved in more detail in the implied weights analysis (Appendix A, Fig. A1).

Actinopterygii is also recovered as monophyletic but receives very weak support (BDI: 1). *Meemannia* is resolved as the earliest actinopterygian, sister to a monophyletic *Cheirolepis* and all other actinopterygians. *Tegeolepis* and *Osorioichthys* fall as successive sister taxa to remaining actinopterygians (BDI: 3). Most other Palaeozoic taxa are recovered as singletons or small clades, but the topology is very weakly supported (BDI: 1-2). Several Carboniferous (*Trawdenia*, *Kansasiella*, *Coccocephalichthys*, *Lawrenciella*), Permian (*Luederia*) and Triassic (*Boreosomus*) taxa form a basal polytomy, sister to a broad clade that includes *Pteronisculus* and remaining actinopterygians. This clade, mostly made of Carboniferous taxa, is supported by an antorbital bone (ch. 50), two suborbitals (ch. 55), an operculum twice as high as the suboperculum (ch. 111) and jointed pectoral radials (ch. 247). We recover, at successive nodes: *Cosmoptychius* as the earliest-diverging member; a clade containing the rhadinichthyids *Cyranorhis* and *Wendyichthys*; and *Beagiascus* + *Aesopichthys* + *Kalops* forming the sister group to a monophyletic *Pteronisculus*. In our implied weights analysis tThe topology of the

Figure 2.18: Strict consensus tree of 10752 most parsimonious trees, equal weights analysis with outgroup topology constrained. Tree length: 1693 steps. Consistency Index: 0.198; Retention Index: 0.674. Bremer indices equal or higher than 2 are indicated above nodes. Bootstrap percentages higher than 50% are indicated below nodes. Crown group nodes (black circle) and total groups (white circle) are labelled. Shading: purple, Chondrichthyes (total group); red, Sarcopterygii (total group); yellow, *Pteronisculus*; orange, Scanilepiformes+Cladistia; light blue, Chondrostei (crown-group); green, Teleostei (total group).


Dicksonosteus arcticus
Entelognathus primordialis
Acanthodes bronni
Cladodoides wildungensis
Ozarcus mapesae
Dialipina salguerioensis
Ligulalepis
Onychodus jandemarrai
Styloichthys changae
Diplocercides kayseri
Miguashaia bureaui
Guiyu oneiros
Psarolepis romeri
Glyptolepis groenlandica
Porolepis sp.
Gogonasus andrewsae
Eusthenopteron foordi
Osteolepis macrolepidotus
Meemannia eos
Cheirolepis trailli
Cheirolepis canadensis
Cheirolepis schultzei
Tegeolepis clarki
Osorioichthys marginis
Mimipiscis toombsi
Gogosardina coatesi
Mimipiscis bartrami
Raynerius splendens
Moythomasia lineata
Moythomasia durgaringa
Moythomasia nitida
Donnrosenia schaefferi
Howqualepis rostridens
Kentuckia deani
Melanecta anneae
Woodichthys bearsdeni
Boreosomus piveteaui
Coccocephalichthys wildi
Kansasiella eatoni
Lawrenciella schaefferi
Luederia kempi
Trawdenia planti
Cosmoptychius striatus
Cyranorhis bergeraci
Wendyichthys dicksoni
Beagiascus pulcherrimus
Aesopichthys erinaceus
Kalops monophyrum
Pteronisculus nielseni
Pteronisculus cicatrosus
Pteronisculus changae
Pteronisculus stensioi
Pteronisculus magnus
NHMD 73588
Pteronisculus gunnari
Australosomus kochi
Fukangichthys longidorsalis
Beishanichthys brevicaudalis
Scanilepis dubia
Evenkia eunoptera
Tanaocrossus kalliokoskii
Erpetoichthys calabaricus
Polypterus bichir
Brachydegma caelatum
Brazilichthys macrognathus
Birgeria groenlandica
Birgeria stensioei
Chondrosteus acipenseroides
Acipenser brevirostrum
Polyodon spathula
Yelangichthys macrocephalus
Saurichthys madagascarensis
Saurichthys sp. Greenland
Saurichthys ornatus
Platysomus superbus
Amphicentrum granulosum
Fouldenia ischiptera
Styracopterus fulcratus
Discoserra pectinodon
Bobasatrania groenlandica
Ebenaqua ritchei
Dipteronotus ornatus
Peltopleurus lissocephalus
Luganoia lepidosteoides
Venusichthys comptus
Ichthyokentema purbeckensis
Dorsetichthys bechei
Leptolepis bronni
Elops hawaiensis
Hiodon alosoides
Hulettia americana
Macrepistius arenatus
Watsonulus eugnathoides
Amia calva
Caturus furcatus
Obaichthys decoratus
Atractosteus spatula
Lepisosteus osseus
Macrosemimimus lennieri
Semionotus elegans
Macrosemius rostratus
Propterus elongatus
Tetragonolepis oldhami
Tetragonolepis semicincta
Dapedium sp. LIAS
Scopulipiscis saxciput
Dapedium pholidotum
Dapedium stollorum
Dapedium punctatum
Dapedium caelatum
Dapedium noricum
Hemicalypterus weiri
Paradapedium egertoni
Sargodon tomicus
Dandya ovalis
Heterostrophus phillipsi
Gibbodon cenensis
Brembodus ridens
Neoproscinetes penalvai
Eomesodon liassicus
Arduafrons prominoris
Mesturus sp.
Mesturus verrucosus
Osteichthyes
Actinopterygii
Actinopterygii
Actinopteri
Neopterygii
Holostei

actinopterygian stem, as well as this monophyletic clade, is identical (Appendix A, Fig. A1).

The monophyly of *Pteronisculus* is supported by the presence of more than two infraorbitals (ch. 52), mandibular canal arched dorsally in the anterior half of the mandible (ch. 77), dorsalmost branchiostegal ray deeper than the adjacent one (ch. 120), lacrimal contributing to oral margin (ch. 301) and presence of teeth on the lacrimal (ch. 302) (BDI: 2). Within the genus, the Chinese and Malagasy species cluster together with weak support, united by the lack of premaxillae (ch. 2). The Greenland species are the sister group of the other species (BDI: 2), supported by the absence of contact between extrascapulae at the midline (ch. 47), presence of a sensory canal/pit line of the maxilla (ch. 71) and presence of an accessory operculum (ch. 109). *P. gunnari* and NHMD–73588 are recovered as sister taxa (Fig. 2.18).

We recover *Australosomus* as the sister taxon to crown actinopterygians. Scanilepiformes and Cladistia, are recovered as a clade (BDI: 3), which in turn is the sister group to Actinopteri (Fig. 2.18). We recover a very weakly supported stem-chondrostean assemblage comprising *Brachydegma*, the macrodont *Brazilichthys*, birgeriids (BDI: 5) and saurichthyids (BDI: 5). The Carboniferous *Platysomus* and Eurynotiformes (*Fouldenia*, *Styracopterus, Amphicentrum*), as well as other deep bodied Carboniferous, Permian and Triassic forms (*Discoserra*, *Ebenaqua*, *Bobasatrania*) are resolved as stem neopterygians, but the topology of their relationships is weakly supported (BDI: 1-2) (Fig. 2.18) and in fact the order these taxa are recovered in our

implied weights analysis is slightly different, while the relationships between Scanilepiformes, Cladistia and chondrosteans are largely confirmed (Appendix A, Fig. A1). Other relationships are largely as reported by Argyriou et al. (2022).

2.5 Discussion

2.5.1 Updates to previous descriptions

Our redescription of the holotype of *Pteronisculus gunnari* adds meaningful details to our knowledge of this species, particularly regarding aspects of internal anatomy not observed by previous authors (Nielsen 1942). The preservation is so detailed that it allowed us to reconstruct the right half of the dermal skeleton of the skull, as well as the gill skeleton and the braincase, by digitally rearticulating the bones (Fig. 2.19).

Snout. The presence of paired premaxillae is confirmed in *P. gunnari* for the first time. Premaxillae are tentatively described in *P. stensioi* and *P. magnus*, and the condition is unclear in other Greenlandic species owing to poor preservation of the snout region (Nielsen 1942); for the same reason, the condition is reported as unknown by White (1933) for *P. cicatrosus.* Premaxillae are hypothetically reconstructed in the remaining Malagasy species, although not explicitly described by Lehman (1952). Although the premaxillae of *P. gunnari* host a cavity through the length of the bone (Fig. 2.3), these do not align with the antorbital infraorbital canal and are thus unlikely to have carried the ethmoidal commissure. The nature of the cavity is uncertain: since it only opens onto

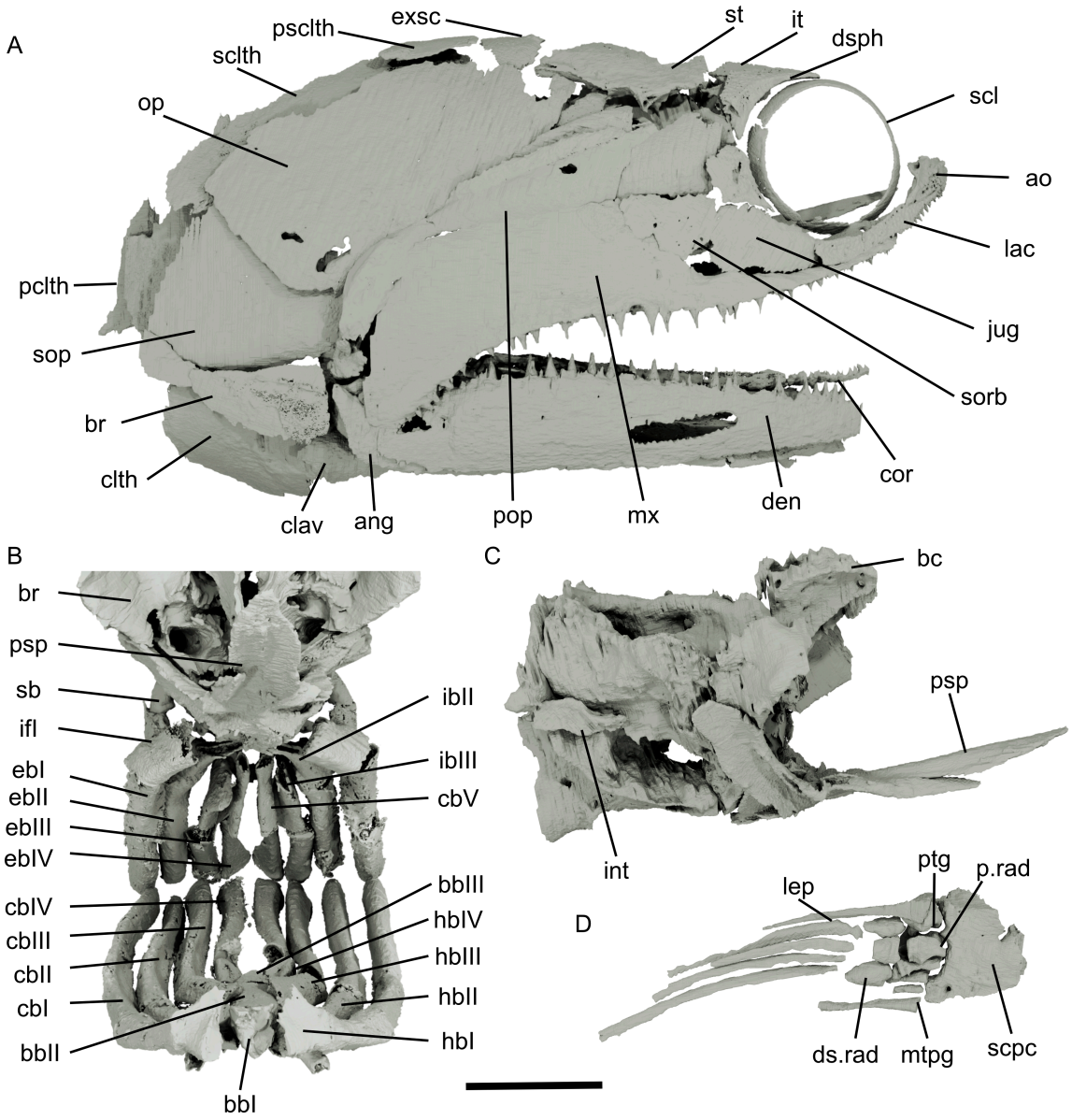


Figure 2.19: Composite reconstructions of the skeleton of *Pteronisculus gunnari* NHMD–73588. Skull and dermal pectoral girdle in right lateral view (A). Gill skeleton, parasphenoid and braincase in anterior view (B). Braincase, parasphenoid and intercalar in right lateral view (C). Right pectoral fin endoskeleton and selected lepidotrichia in ventrolateral view (D). Scale bar: 10 mm for A, D; 6 mm for B-C. Abbreviations: ang, angular; ao, antorbital; bbI-III, basibranchials; bc, braincase; br, branchiostegal ray; cbI-V, ceratobranchials; clth, cleithrum; clav, clavicle; cor, coronoid; ds.rad, distal radial; dsph, dermosphenotic; den, dentary; ebI-IV, epibranchials; exsc, extrascapular; hbI-IV, hypobranchials; ibI-III, infrapharyngobranchials; int, intercalar; it, intertemporal; jug, jugal; lac, lacrimal; lep, lepidotrichia; mtpg, metapterygium; mx, maxilla; op, operculum; p.rad, proximal radial; pclth, postcleithrum; pop, preoperculum; psclth, presupracleithrum; psp, parasphenoid; ptg, propterygium; sb, suprapharyngobranchials; scl, sclerotic ring; sclth, supracleithrum; scpc, scapulocoracoid; sorb, suborbital; sop, suboperculum; st, supratemporal.

the medial surface of the bone, it is hard to associate it with sensory organs like electroreceptors (King et al. 2018).

Parasphenoid. Previous accounts of the parasphenoid of *P. gunnari* are short (Nielsen 1942). We provide a detailed account, recognising intrageneric diversity in *Pteronisculus*: reduced tooth covering of the anterior corpus, the presence of a dorsal bony pedicel for the buccohypophyseal canal and a ventral buccohypophyseal opening, foramina for the internal carotids, the presence of an enclosed median parabasal canal, and the absence of any kind of dermal basipterygoid processes distinguish *P. gunnari* from other species. In *P. magna* and *P. stensioi*, the dermal basipterygoid process is restricted to a sheath of dermal bone underlying the corresponding endoskeletal process (Nielsen 1942; Lehman 1952). In other palaeopterygians, such as the Carboniferous *Kentuckia* (Rayner 1952), the process is entirely endoskeletal, and it is also absent in chondrosteans, amiids, Recent teleosts, and some neopterygian clades, where it may have been secondarily lost (Patterson 1975; Gardiner 1984). The lack of an endoskeletal basipterygoid process in this specimen of *P. gunnari* may be related to the submature condition of the specimen, rather than a true absence. Foramina for the internal carotids piercing the parasphenoid are a feature more commonly associated with neopterygians or teleosts (Patterson 1975; Gardiner 1984). The foramina are aligned with the posterior grooves on the lateral surface of the basisphenoid, confirming that the circulation partially passed through the median parabasal canal of

the parasphenoid (Fig. 2.10, icg), like in e.g., *Saurichthys* (Argyriou, et al. 2018), rather than in grooves on the dorsal surface of the anterior corpus, as was previously described for *P. magnus* (Nielsen 1942). In other respects, the parasphenoid resembles that of generalised post-Devonian actinopterygians, as it does not extend past the ventral otic fissure (Patterson 1975; Gardiner 1984). The number of parotic toothplates associated with the parasphenoid is higher than previously reported for *P. gunnari*, with at least three pairs rather than one (Nielsen 1942), although the peculiar morphologies are difficult to rearrange in life positions (Fig. 2.11).

Braincase. Although the braincase is only partially ossified in NHMD–73588, we are able to largely confirm previous descriptions and provide new anatomical information, including of the ethmoids. Absence of a foramen on the floor of the posterior myodome, presence of an intercalar bone, and the presence of small canals between the anterior and horizontal ampullae, jugular canal and fossa bridgei, and various nerves are the most evident differences from previous reports (Nielsen 1942). The craniospinal process of palaeopterygians was considered homologous to the intercalar of neopterygians, but lacking any dermal outgrowths (Patterson 1975). An independent, membranous intercalar with an endochondral core was historically considered a neopterygian character, while it is entirely membranous in *Amia* and extant teleosts (Schaeffer 1971; Patterson 1975; Pradel et al. 2016). The discovery of an intercalar in the stem actinopterygians *Lawrenciella*, where it appears to be dermal

(Pradel, et al. 2016), possibly in *Palaeoneiros* (Giles et al. 2023) and now in *Pteronisculus* with a dermal component, suggests that this ossification had a deeper origin, but may have been overlooked in previous descriptions of palaeopterygian braincases due to its small size or difficulties in preparation. The tomograms also show small canals connecting the trigeminal (V) and facial nerves (VII), the anterior and horizontal ampullae of the bony labyrinth, the trigeminal nerve (V) and the roof of the jugular canal, and the trigeminofacialis chamber and the floor of the fossa bridgei (Fig. 2.11). Additional microCT-based descriptions of Palaeozoic and Mesozoic actinopterygian braincases will be needed to assess whether these represent species-specific characters, variation due to incomplete ossification, or are more broadly distributed.

The unfinished nature of the endochondral ossification of the braincase allows us to infer the position of some of the primordial ossification centres, which are otherwise difficult to discern in the compact neurocrania of generalized Paleozoic–early Mesozoic actinopterygians (Nielsen 1942, 1949; Patterson 1975; but see some exceptions in Gardiner 1984; Argyriou et al. 2022). The ethmoids mineralize from independent ossification centres. The posteromedial portion of the interorbital wall is separated from the otic region by wide spaces and likely constitutes the pterosphenoid (Fig. 2.10); denser trabecular ossification around the canal for the trochlear nerve may indicate the original mineralization point. As the basisphenoid is present as a single element, and is most densely mineralized along the midline, it is most probably

unpaired. Perichondral lining of the basisphenoid is largely complete, except for two anterodorsal facets and the ventral otic fissure, indicating it may have been the first to begin ossifying (Fig. 2.10, bsp). There are no clear boundaries or ossification centres that could be associated with a prootic ossification, and the area is overall poorly ossified. The postorbital process is separated from the rest of the braincase by two almost vertical bands of reduced ossification, in the prootic area and the hyomandibular facet. The very dense endochondral ossification in the dorsolateral portion of the postorbital process could represent the ossification centre for the sphenotic. There are no meaningful variations in the density of endochondral ossification in the rest of the otic region, so discriminating potential pterotic and opisthotic ossifications is difficult. In the occipital region, a horizontal band of less dense endochondral bone, dorsal to the occipital arteries, probably divides a ventral basioccipital from the exoccipitals, although there are no clear indications of where ossification likely initiated. There are no signs of the presence of a supraoccipital ossification centre. Our inferences show good agreement with Patterson (1975), who indicated where the ossification centres may lie on a braincase of *P. magnus* described by Nielsen (1942).

Dermal cheek. Most dermal ossifications are fundamentally as described in previous accounts. However, tomograms show that several dermal bones, including the dermosphenotic (Fig. 2.4), dermohyal (Fig. 2.5) and horizontal shelf of the maxilla (Fig. 2.6), contain additional cavities that are separate from the sensory canals, and connect to the

surface of the bone via small foramina. The nature of these cavities is unclear, but they may have supplemented the primary sensory canal network: either as remnant of the “p” canal for the dermosphenotic (Northcutt 1989; Clement et al. 2018), or related to Lorenzinian ampullae, as was suggested for the Late Devonian *Howqualepis* and the stem osteichthyan ‘*Ligulalepis*’ (Long 1988; King, et al. 2018).

Palate. Previous descriptions of *Pteronisculus* only reported one vomerine ossification (‘vomer’ of Nielsen, 1942, p.138), and the upper internal tooth rows were depicted as pointing ventrally (Nielsen 1942; Lehman 1952). We document the presence of a vomer (applied to the ventral surface of the ethmoids), and anterior and posterior accessory vomers, the latter corresponding with the ‘vomer’ (sensu Nielsen) of previous accounts (Fig. 2.9, 11). The internal tooth rows borne on the ectopterygoid and dermopalatines are directed medially in NHMD–73588, and the internal and external rows are separated by an edentulous space that accommodated the dentary teeth (Fig. 2.6-2.7). This condition, along with a tooth-bearing lacrimal, are also present in a macrodont actinopterygian from the Pennsylvanian of New Mexico (Friedman et al., 2024). Discovering what this means in terms of the relationships between these two taxa will require further study.

Lower jaw. The dentary of NHMD–73588 bears a low process, lateral to the midpoint of the adductor fossa (Fig. 2.9). A line drawing of *P. magna* (Nielsen 1942, p. 166) is suggestive of a bump on the surangular, but this structure is not described in the text. A similar small process

formed by a single ossification of the lower jaw is reported in a small number of Palaeozoic taxa, including the prearticular of *Eurynotus* (Friedman et al. 2018), dentary of *Aesopichthys* (Poplin and Lund 2000), and surangular of *Coccocephalichthys* (Poplin and Véran 1996) and *Trawdenia planti* (Coates and Tietjen 2018). Although analogous in position, the shape and composition of these processes suggests they are not homologous with the coronoid process of neopterygians (e.g. Olsen 1984; Xu 2019; Argyriou, et al. 2022), which is originally formed by the dentary and surangular, with modifications in various clades of teleosts (Arratia 2015; Friedman 2015; López-Arbarello and Sferco 2018). However, it is likely that further investigation of palaeopterygians will uncover additional evidence for the widespread distribution this feature.

Operculogular series. We report the presence of a modest anterodorsal process on the suboperculum. This process is sturdy in Devonian taxa like *Mimia*, *Moythomasia* or *Donnrosenia* (Gardiner 1984; Long et al. 2008), but reduced to a weak strip in *P. gunnari*. The process is overlaid by the operculum and preoperculum, and CT-aided descriptions of additional taxa may indicate it is more widespread than previously thought.

Gill skeleton. The gill skeleton of *P. gunnari* was not previously described, only equated to the description of *P. stensioi*, and the morphology of the basibranchial series for all species within the genus was largely unknown (Nielsen 1942, p. 195). We describe the gill skeleton in its entirety, including the unfinished basibranchial series, and clarify the

presence of uncinate processes on epibranchials II and III (contra Nielsen 1942), the hook-like articulation of hypobranchial III with the basibranchial series, the simple polyhedral shape of hypobranchial IV and the long, bent shape of suprapharyngibranchial II (Fig. 2.13). The gill skeleton can be a useful diagnostic tool in extant fish, but its usefulness is limited in fossils due to a lack of detailed descriptions (Beckett et al. 2018). The development of a more extension comparative dataset may uncover new anatomical features of use in resolving relationships between early actinopterygians.

Shoulder girdle and pectoral fin. We report a different course for the lateral line canal in the supracleithrum and provide the first description of the pectoral fin of *P. gunnari*, which was previously noted as identical to that of *P. magnus* (Nielsen 1942). The preserved path of the lateral line canal through the supracleithrum of *P. gunnari* is more anterior than in other species, but the anterior portion of the bones has been replaced by pyrite and the complete course of the canal is not visible in the tomograms (Fig. 2.15). An additional cavity, separate from the sensory canal, as described in other dermal bones, is also present. We also clarified the shape of the propterygium and the first three proximal radials, and showed that the first lepidotrichium is fused to an unperforated propterygium, rather than articulated with it as previously described. In addition, we do not find that the fifth and sixth proximal radials are fused, as it was reported for a specimen of *P. gunnari* (Nielsen 1942). Our updated description shows that the propterygium is imperforate (contra Jessen

1972), a condition which is known, among palaeopterygians, only in *Cheirolepis* (Giles et al. 2015) and *Trawdenia*. In *Trawdenia*, the propterygial canal is suggested to have passed medial to the lateralmost propterygium, between it and the fused second radial (interpreted as a second propterygium by Coates & Tietjen, 2018). In addition, the first three radials of *P. gunnari* have an irregular morphology, reminiscent of Palaeozoic taxa like *Trawdenia*—except for the peculiar propterygial conformation (Coates and Tietjen 2018)—or *Mimia* and *Moythomasia* (Gardiner 1984).

Axial skeleton. We confirm most details of the previous description, but clarify the size and shape of the epineural processes on the vertebrae (Fig. 2.17; “proximal plates” of Nielsen, 1942).

2.5.2 Phylogenetic affinity of *Pteronisculus*

Pteronisculus and its taxonomic placement. Both our phylogenetic analyses recover a monophyletic *Pteronisculus*, albeit poorly supported, with NHMD–73588 forming the sister terminal to *P. gunnari*, supporting the specific attribution of Nielsen (1942). Two unambiguous synapomorphies support the monophyly of the genus: a toothed lacrimal, although we note that this has recently been reported in a Carboniferous macrodont (Friedman et al., 2024); and a lacrimal contributing to the oral margin, which was reported in the original description of *Cyranorhis* by Lund and Poplin (1997) but considered absent in a later reassessment by Mickle (2015). This latter character is also purportedly present in the Late Triassic *Turseodus*, although this taxon is not included in our data matrix

(Schaeffer 1952; Lund and Poplin 1997). Other characters supporting the monophyly of *Pteronisculus* in our phylogenetic analysis show variable degrees of homoplasy: the presence of more than two infraorbitals and the dorsalmost branchiostegal ray being deeper than the adjacent ray are common conditions in late Palaeozoic and early Mesozoic actinopterygians; and an anteriorly arched mandibular canal is present in *Australosomus*, some dapediids and Devonian forms like *Cheirolepis* and *Moythomasi*a. Within the genus *Pteronisculus*, the Greenlandic species form a clade, sister to the Malagasy and Chinese species. While Early Triassic palaeogeography lends support to this (Scotese and Schettino 2017), the latter clade is united only by the lack of premaxillae, which is fairly homoplastic among actinopterygians, (Poplin and Lund 1997) and may have been misidentified in some *Pteronisculus* species as in *P. gunnari*. In addition, both clades have older species in terminal positions (*P. gunnari* and *P. cicatrosus*)~~;~~ (Nielsen 1942; Lehman 1952). New data in the future will hopefully clarify the relationships among *Pteronisculus* species.

We recover *Pteronisculus* in a broader clade that includes taxa from the Carboniferous of the United Kingdom and the United States. However, the clade is not supported by any unambiguous synapomorphies. The number of suborbitals and the relative dimensions of the operculum and suboperculum are highly variable across actinopterygians. Similarly, an independent antorbital (housing the infraorbital-ethmoidal commissure-supraorbital commissure) is common to

many Carboniferous actinopterygians, as well as neopterygians (Gardiner 1963; Poplin and Lund 1995, 1997), and is optimized as evolving multiple times. In addition, this character unites many Palaeozoic taxa (including the majority of the *Pteronisculus* clade) for which the variability in the shape and relative positions of dermal snout bones is not fully captured in our analysis (e.g., vertical antorbital and tooth-bearing premaxilla in *Aesopichthys*, tooth-bearing antorbital and premaxilla in *Cosmoptychius* and *Watsonichthys*, absence of premaxilla and notched antorbital in *Cyranorhis* and *Wendichthys*, edentulous antorbital contributing to the oral margin and dentigerous premaxilla in *Kalops,* etc) (Gardiner 1963; Lund and Poplin 1997; Poplin and Lund 2000; Poplin and Lund 2002). Potential phylogenetic signals are obscured by the common poor preservation of the snout area in fossils and multiple, often conflicting bone naming conventions that make comparisons difficult (Poplin and Lund 1995, 1997; Mickle 2015). We suggest that future phylogenetic analyses should incorporate characters that describe the features and arrangement of dermal bones of the snout in relation to morphological elements that are univocally identifiable (e.g., number of anamestic/canal bearing bones, contribution to oral/orbit margins, number of toothed ossifications, position relative to the nares, number of paired/unpaired ossifications, etc.).

The final character uniting this clade, the presence of jointed radials, is present (among actinopterygians) only in *Pteronisculus*, *Cheirolepis canadensis* and *Cosmoptychius* (Gardiner 1963; Arratia and Cloutier 1996), but the state is unknown in more than half of the taxa in

our matrix, including most members of the *Pteronisculus* clade. While this may represent a robust synapomorphy, more data on the three-dimensional anatomy of palaeopterygian pectoral fins is needed to evaluate this.

The Palaeozoic affinities of *Pteronisculus* (e.g., rhadinichthyids, cosmoptychiids, macrodonts) are evident from our analysis, with the taxon recovered deep within a long-lived Carboniferous radiation which terminated in the Middle Triassic (Fig. 2.18). Unfortunately, broader problems with early actinopterygian evolution persist, with most branches weakly supported and largely unresolved. On a small scale, this obscures relationships among different families, and on a larger scale, obscures evolutionary trends during the Palaeozoic-Mesozoic transition (Sallan 2014; López-Arbarello and Sferco 2018). A combination of descriptions of new taxa, updates to previous descriptions and improved phylogenetic matrices are needed to discern the relationships among Devonian and Carboniferous palaeopterygians, and palaeopterygians and neopterygians.

Differences from previous analyses. Most phylogenetic analyses do not include multiple species of *Pteronisculus*, and the genus is commonly used in isolation to represent a generalized non-neopterygian taxon (e.g. Olsen 1984; López-Arbarello and Sferco 2018; Xu 2021). Where *Pteronisculus* has been included among a broader sample of palaeopterygians, its position has been variable: associated with Palaeozoic taxa in a similar way to this study (Lund et al. 1995; Cloutier

and Arratia 2004; Mickle 2012); in a position close to the neopterygian stem (Gardiner, et al. 2005; Wen et al. 2012); or in a broad polytomy (Hurley, et al. 2007). The analyses that have employed iterations of the matrix used here, have recovered *Pteronisculus* either in an extensive polytomy containing Carboniferous-Permian taxa and the actinopterygian crown (Latimer and Giles 2018); or associated with Carboniferous actinopterygians, either as sister taxon to multiple taxa (Argyriou, et al. 2018; Ren and Xu 2021) or as an early-diverging member of the radiation (Argyriou, et al. 2022; Giles, et al. 2023). The link between *Pteronisculus* and taxa from the Palaeozoic, in particular from the Carboniferous Bear Gulch fauna, is confirmed in our analysis. However, we recover *Pteronisculus* deeply nested within the Carboniferous radiation, rather than as an early diverging member.

Only Ren & Xu (2021) have previously included more than two species of *Pteronisculus* in a phylogenetic analysis (*P. stensioi*, *P. nielseni*, *P. changae*, *P. cicatrosus* and *P. magnus*). Their relationships and placement of *Pteronisculus* are broadly similar to our results, but the topology of the genus and the characters supporting it differ from our analysis. They recover the genus as closely related to *Cyranorhis* and in a clade comprising *Boreosomus*, *Trawdenia* (=*Mesopoma*; Coates & Tietjen, 2019), *Cosmoptychius*, *Beagiscus*, *Kalops* and *Aesopichthys*. Within the genus, *P. nielseni* is recovered as the earliest diverging, implying an eastern Tethys origin for *Pteronisculus*. In addition, (Ren and Xu 2021) only report three characters supporting monophyly: a toothed lacrimal,

presence of more than two infraorbitals and the supratemporal ending at the level of the posterior margin of the parietal. While Caron et al. (2023) include two species in their analysis (*P. stensioi* and *P. magnus*) they focus only on the neurocranium, and the notable differences between the braincase of the two species result in a paraphyletic *Pteronisculus*.

2.5.3 Juvenile features and comparative anatomy

Several endoskeletal features of NHMD–73588 indicate it was a juvenile or immature specimen. Although complete growth series are known for some Palaeozoic and early Mesozoic fishes (e.g. Cloutier 2010; Maxwell et al. 2018), juvenile actinopterygians are comparatively rare. Growth series of styracopterid actinopterygians from the Mississippian of Scotland reveals allometric growth of the fins and demonstrates an increase in the number of scales through ontogeny (Sallan and Coates 2013). Similarly, juvenile actinopterygians from Bear Gulch (Namurian) and Mazon Creek (Pennsylvanian) show scale covering spreading from the lateral line and the tail, and progressive ossification of the skull and pectoral girdle (Lowney 1980a; Schultze and Bardack 1987). Isolated juvenile palaeopterygian specimens are relatively more common, and have been recognized by the reduced scale covering and/or skull dermal plate development (Hutchinson 1973; Lowney 1980b; Coates 1993), the degree of sensory canal enclosure (Maxwell, et al. 2018) or limited endochondral ossification of the skull and pectoral girdle (Nielsen 1942, 1949).

Here we summarise the key features of NHMD–73588 compared to fully mature individuals, along with implications for ontogenetic ossification patterns in Palaeozoic–early Mesozoic actinopterygians.

Endoskeleton: palate. In most palaeopterygians, the palatoquadrate ossified as a single element in the adult (Gardiner 1984; Arratia and Schultze 1991 and references therein), while in other coeval taxa (e.g., *Saurichthys*) the palatoquadrate ossifies as multiple elements (Argyriou, et al. 2018). Some limited ontogenetic data with a bearing on early ossification patterns is known from Palaeozoic–early Mesozoic taxa, e.g. the Devonian *Mimia* (Gardiner 1984), *Pteronisculus* and *Boreosomus* (Nielsen 1942), and *Australosomus* (Nielsen 1949), although a complete growth series is lacking. The condition in NHMD–73588, where the quadrate, metapterygoid and autopalatine are independently ossified, corroborates Nielsen's report for some specimens of *Pteronisculus* (1942, p.143) and the previously mentioned ontogenetic data: ossification of the palatoquadrate began early in ontogeny with separate metapterygoid, quadrate and autopalatine ossification centres, which later fuse into a single element in the adult.

The palatoquadrate ossification patterns seen in extant non-teleost actinopterygians can be considered modifications of the palaeopterygian pattern. This is particularly evident in polypterids: the palatoquadrate of the Middle Triassic stem polypterid *Fukangichthys* is ossified as a single unit (Giles, et al. 2017), while in *Polypterus*, the endoskeletal palate is originally a single cartilage, but it ossifies into separate autopalatine,

metapterygoid and quadrate elements (Jollie 1984b; Arratia and Schultze 1991; Wacker et al. 2001). The condition in *Amia* is very similar, except that in the adult part of the cartilage persists between the three ossifications and the autopalatine ossifies late in ontogeny (Arratia and Schultze 1991; Grande and Bemis 1998). In *Lepisosteus*, the autopalatine is absent (Jollie 1984a; Arratia and Schultze 1991). In extant chondrosteans, the palatoquadrate is highly specialized, comprising the autopalatine plate, palatoquadrate bridge and quadrate flange, and remains cartilaginous through life (Warth et al. 2017; Tsessarsky 2023).

A palatoquadrate ossified as a single unit in the adult, formed from three ossification centres during ontogeny, appears to be the plesiomorphic state in actinopterygians and probably for Osteichthyes (Gardiner 1984). In all extant lineages (excluding chondrosteans), there is a similar trend of fragmentation of the palatoquadrate into three bones (Arratia and Schultze 1991). NHMD–73588 confirms that *Pteronisculus* retains the plesiomorphic single palatoquadrate ossification, and also that the pattern of ossification involved three initial centres that are homologous to the bones in the palatoquadrate of more recent actinopterygians.

Endoskeleton: braincase. The braincase of early actinopterygians is well ossified in most mature specimens, with poorer endochondral and perichondral development in juvenile or immature specimens. Available data from fossil taxa suggests that the braincase is preformed in cartilage and ossification commences from multiple centres, proceeding towards the ethmoidal region during ontogeny; once maturity was reached, the

braincase was normally composed of two ossifications separated by the oticoccipital fissure and ventral otic fissure (Nielsen 1942; Gardiner 1984; Pradel, et al. 2016; Caron, et al. 2023; Giles, et al. 2023). The ethmoidal region could, in some instances, ossify quite late, or not at all (Patterson 1975; Gardiner 1984; Coates 1998; Hamel and Poplin 2008). This pattern is not the only one known in early actinopterygians: macrodont taxa show limited or no ossification of the braincase, with independent ossifications separated by large gaps filled by cartilage in life (Figueroa, et al. 2019; Argyriou, et al. 2022, Friedman et al. 2024), and other taxa appear to show little or no endochondral ossification into adulthood (Pearson and Westoll 1979; Giles, et al. 2015; Giles, et al. 2023).

NHMD–73588 has a completely ossified occiput, some unfinished areas in the otic region, minimal ossification in the sphenoid region, a basisphenoid and a small ethmoid (Fig. 2.9; Fig. 2.11). This is in agreement with the ossification pattern seen in most early actinopterygians, but not entirely with past descriptions of the genus, in which the ethmoidal region is normally described as poorly ossified, or with ossification starting from the dorsal areas (Nielsen 1942; pp. 16-18, 58, 91-92, 97). The opening between the cerebral cavity, the anterior portion of the lateral cranial canal and the fossa bridgei (Fig. 2.9, lcc) is particularly noteworthy, as it indicates that in the pterotic and possibly the opisthotic and semicircular canals ossified before the endocranial walls and roof. This ephemeral connection also highlights the potential inaccuracies that can arise from incorrect interpretation of juvenile features (as discussed in Sallan and

Coates 2013): in this case, an anterior connection of the lateral cranial canal and the cranial cavity is typically optimized as a character of neopterygians (Patterson 1975; Giles et al. 2018), while in adult specimens of *Pteronisculus* and other palaeopterygians there is only a posterior connection through the loop of the posterior semicircular canal (Nielsen 1942; Gardiner 1984).

Braincase ossification in extant non-teleosts is markedly different from palaeopterygians: in *Acipenser* the braincase is largely cartilaginous, except in the largest individuals (Hilton et al. 2011; Hilton et al. 2022), while in *Polypterus,* amiids and gars the adult braincase is composed of discrete ossifications linked by greater or lesser expanses of cartilage (Gardiner 1984; Bjerring 1991; Grande and Bemis 1998). The condition we see in NHMD–73588 confirms that the palaeopterygian braincase contained ossification centres homologous to those of later actinopterygians; the difference with more recent forms lies in the ossification process, which in palaeopterygians progressed to the point of complete fusion between all ossifications, save for the cranial fissures (Patterson 1975). These considerations largely confirm previous hypotheses on the acquisition of the patterns seen in extant lineages (Patterson 1975; Gardiner 1984; Arratia 2015; López-Arbarello and Sferco 2018), with the addition that an independent intercalar has its roots outside of Neopterygii.

Endoskeleton: gill arches. As with other endoskeletal elements, ontogenetic growth of the basibranchial series begins with development of

a perichondral rind and continues with endochondral ossification, although articular areas remain unfinished throughout life. Nielsen (1942) describes *Pteronisculus* specimens in which the basibranchial series is poorly mineralized. A similar situation is reported for specimens of *Mimia* and *Moythomasia*, in which the basibranchial forms a single ossification in adults, but probably fused from three centres during ontogeny (Gardiner 1984). In NHMD–73588, basibranchial I probably represents the area between the articular surfaces for hypobranchials I and II, while basibranchial II is ossified between the articulation of hypobranchials II and III. The relationship between hypobranchials IV and basibranchial III is more difficult to assess given the small dimensions of the latter (Fig. 2.13). The incomplete ossification of the basibranchials is thus confirmed to be a good indicator of non-adult palaeopterygian specimens.

There is great variability in the development of the basibranchial series in extant non-teleosts. *Polypterus* has a single basibranchial cartilage, which ossifies as a single unit during ontogeny (Gardiner 1984; Jollie 1984b). Acipenseriformes have up to 5 cartilaginous basibranchials early in ontogeny: in time, three ossifications (copulae) coalesce, with the largest, most anterior one containing up to the first three cartilaginous elements (Warth, et al. 2017). *Polyodon* and *Amia* have three cartilaginous basibranchials early in ontogeny, but while they remain cartilaginous in the former taxon, a portion of the first basibranchial ossifies between the articulations of the second and third gill arches in the latter (Grande and Bemis 1991, 1998). Gars have two cartilaginous elements and only a

portion of the second, bigger element ossifies during ontogeny (Jollie 1984a; Grande 2010).

The condition in NHMD–73588 appears to confirm a plesiomorphic actinopterygian condition comprising three cartilaginous elements with three initial ossification centres in the basibranchial series, which fuse into a single mineralized element in the earliest palaeopterygians (e.g. *Mimipiscis*, *Raynerius*) but remain as three separate ossified elements in more derived taxa, including *Pteronisculus*.

Endoskeleton: shoulder girdle. Detailed accounts of the endoskeletal components of palaeopterygian pectoral fins are rare (Giles, et al. 2015; Giles, et al. 2023; Coates and Tietjen 2018). The cleithrum also appears to develop very early in the ontogeny of palaeopterygians, further complicating the observation of the endoskeletal shoulder girdle in juvenile specimens (Lowney 1980b; Coates 1993; Sallan and Coates 2013). Reports of incompletely ossified or unossified scapulocoracoids can be found in Nielsen (1942; 1949) for specimens of Pteronisculus, Boreosomus and Australosomus, but without any indication of the pattern of ossification. The condition in NHMD–73588 implies that the scapulocoracoid started to ossify around the dorsal muscle canal (Fig. 2.14C-E), but it remains unclear whether the ossification proceeded from one or multiple centres. Multiple scapulocoracoid plates associated with a larger ossification are also present in the small-bodied Famennian *Palaeoneiros*, which is interpreted as an adult or near-adult (Giles, et al.

2023), supporting the hypothesis that the scapulocoracoid formed from multiple ossification centres.

In extant non-teleosts, the scapulocoracoid of *Amia* persists as a single, cartilaginous element in all but the largest specimens, where small ossification centres may appear (Grande and Bemis 1998); in Acipenseriformes, the single scapulocoracoid cartilage can ossify in adult specimens (Jollie 1980; Hilton and Bemis 1999). In *Lepisosteus*, the endochondral pectoral girdle is made of an ossified scapula and a cartilaginous mesocoracoid element (Jollie 1984a). *Polypterus* has an endochondral pectoral girdle unique among actinopterygians, made of independent rod-like scapula and coracoid ossifications (Jollie 1984b). Further information is needed on the endoskeletal girdles of palaeopterygians in order for this data to be interpreted in a wider context. However, despite the impossibility to confirm the presence of multiple ossification centres, the condition in the juvenile NHMD–73588 indicates that a fusion of possibly different centres would have happened early in ontogeny for palaeopterygians.

Dermal skeleton: squamation. Incomplete scale covering is a well-documented sign of young age for ray-finned fishes. In some cases, larval-stage specimens completely lack scales, and scale covering proceeds from the lobe of the caudal fin towards the head, or from around the cleithrum towards the tail; in either case, lateral line scales tend to form before other flank scales (Lowney 1980a; Schultze and Bardack 1987; Cloutier 2010; Sallan and Coates 2013). NHMD–73588 has an essentially

complete scale covering and all dermal bones of the skull and pectoral girdle are present (Fig. 2.3G-H), indicating this specimen was probably closer to a sub-adult at the time of death. This is in line with the known growth series of palaeopterygians (Lowney 1980a; Schultze and Bardack 1987), while also showing that, in the ontogeny of *Pteronisculus*, scale covering was completed before endochondral ossification.

In *Polypterus* and *Amia*, squamation development closely resembles that of palaeopterygians, with scales appearing first on the lateral line, then extending down to the tail and across the flanks (Bartsch et al. 1997; Grande and Bemis 1998). A similar pattern is seen in *Lepisosteus*, with the first scales covering the lateral line in the posterior region of the body (Jollie 1984a). *Acipenser* differs in having longitudinally-arranged plates (or scutes) rather than scales; the first row appears on the dorsal margin of the body, while on the flanks the plates start appearing anteriorly, and the rows develop towards the tail (Jollie 1980). Apart from very specialized cases, squamation patterns seem very conservative among ray-finned fish, and more useful in identifying ontogenetic stages than taxonomic affinities.

NHMD–73588 adds a useful snapshot to our knowledge of ontogenetic changes in palaeopterygians, with implications for development in fossil and extant actinopterygians. In order to expand these considerations and map how ontogenetic development changes across clades, further descriptions of juveniles at a range of different ontogenetic stages, encompassing both dermal and endoskeletal development, are needed.

2.6 Conclusion

Our redescription of *Pteronisculus gunnari* represents the first XCT-based reinvestigation of a member of the Triassic Early Fish Fauna. We reveal new anatomical details of the braincase, parasphenoid, palatoquadrate, gill skeleton and pectoral fin endoskeleton, improving our knowledge of *P. gunnari* and of the intrageneric diversity of *Pteronisculus*, while revealing many features reminiscent of Palaeozoic forms. The juvenile or sub-adult state of NHMD–73588 allowed us to draw useful comparisons on the endoskeletal development of palaeopterygians and extant non-teleosts. A revised phylogenetic analysis confirms the Palaeozoic affinities of *Pteronisculus*, implying a ghost lineage through the Permian and suggesting it is a poor candidate for generalized "non-neopterygian" anatomies. However, broader interrelationships of palaeopterygians remain unclear, as does the topology of neopterygian evolution. Future work should continue to focus on detailed redescriptions of Palaeozoic and early Mesozoic actinopterygians in tandem with revised and expanded phylogenetic analyses.

3 | Investigating the impact of X-rays on decay: X-ray computed tomography as a non-invasive visualisation technique for sediment-based decay experiments

Iacopo Cavicchini[1], Paul F. Wilson[2], Sam Giles[1], Jake Atterby[1], Andy S. Jones[1], Mark A. Williams[2], and Thomas Clements[1,3]

1: School of Geography, Earth and Environmental Sciences, University of Birmingham, UK.
2: Centre for Imaging, Metrology and Additive Technologies (CiMAT), Warwick Manufacturing Group (WMG), University of Warwick, UK.
3: GeoZentrum Nordbayern, Friedrich-Alexander Universität Erlangen-Nürnberg, Erlangen, Germany

My contribution to this chapter involved most of the data collection, specimen preparation, data analysis, interpretation of results and production of the manuscript, including the figures and tables. The experimental designs (including XCT scanning) were produced by me and coauthors Paul Wilson and Thomas Clements. The coauthors Jake Atterby and Andrew Jones contributed to the experimental data collection. All coauthors gave feedback the drafts of the manuscript.

This chapter was submitted and is currently under review in Palaeontology. A preprint was also submitted to the repository Biorxiv and is available at: https://doi.org/10.1101/2024.05.13.593831.

3.1 Introduction

Decay experiments are a vital tool for understanding taphonomic processes that organisms undergo *postmortem* (Sansom 2014; Briggs and McMahon 2016; Purnell, et al. 2018). Experimental designs have become increasingly innovative, investigating the decay of key organismal groups, as well as how decay rates are impacted by specific environmental variables, such as pH, salinity, pressure, and the presence of different sediment types (e.g. Martin et al. 2004; Sansom 2014; Wilson and Butterfield 2014; Gäb et al. 2020; Forel et al. 2021; Clements, et al. 2022). Understanding the role of the last of these variables, sediment, is vital for understanding fossilisation, especially of soft tissues. The burial of organisms is a fundamental yet extremely complex aspect of soft tissue preservation, and encompasses many variables that influence decay, including burial speed, burial depth, and mineral availability (e.g. Brett and Baird 1986; Martin, et al. 2004; Olszewski 2004; Wilson and Butterfield 2014; McCoy, et al. 2015b; Naimark, et al. 2018a). Experimental work has shown that the mineralogy of the burying substrate influences decay and the physical stabilisation of the carcass, as well as playing a vital role in the preservational processes (e.g. mineralisation and maturation) which allow the geological stabilisation of non-biomineralized soft tissues (Butterfield 1990; Wilson and Butterfield 2014; McMahon et al. 2016).

However, the addition of substrate to a decay experiment means that the carcass is not visible, and the exhumation and/or extraction of carcasses from substrate can introduce bias by damaging the decaying

soft tissues. This results in loss of morphological data, especially if the substrate was acting to provide structural integrity to the carcass, and it can potentially skew our ability to accurately record morphological character presence/absence data in decay experiments that model burial – a possibility discussed in the literature (Wilson and Butterfield 2014; Naimark, et al. 2018b). Moreover, this bias can be compounded as a decay experiment continues – specimens that are in advanced states of decay, especially when the integrity of the carcass is compromised, are more prone to disarticulation during extraction, decreasing the accuracy of morphological character identification. Previous experiments have employed mechanical solutions to minimise data loss, such as plastic meshes that underlie the carcass to facilitate extraction, or gentle water streams to remove substrate that adhered to decaying carcasses during extraction (Allison 1988; Sansom, et al. 2010; Naimark, et al. 2018b). Additionally, the requirement for destructive sampling at each sampling point means it is often necessary to decay multiple individual carcasses simultaneously to fulfil sampling requirements for one experiment. This can increase the financial cost, setup time, and physical resources required for representative sampling. Moreover, as the number of carcasses increases, minute biological variation in individuals may introduce minor biases during long experimental runs, leading to sampling point anomalies. It is, therefore, an important pursuit to investigate new methods that could alleviate these experimental issues, and non-destructive imaging techniques like X-ray computed tomography (XCT

scanning) have been suggested to replace traditional exhumation and dissection.

Selly and Schiffbauer (2021) were the first to utilise XCT to image a decaying arthropod carcass suspended in plastic beads, demonstrating that high resolution external images can be collected *in situ* in a taphonomic experiment. While this study yielded positive imaging results of the carcass, it highlighted two gaps in our current knowledge. Firstly, it is very difficult to image internal soft tissue structures via XCT scanning without use of a staining agent (Metscher 2009a). Secondly, it is unclear what effects X-rays have on both the rate of decay and sequence of morphological character loss (as per Sansom, et al. 2010). One of the primary drivers of decay is bacterial metabolism (see Benbow et al. 2019), and the potential impact of exposure to X-rays on the necrobiome of a carcass is unconstrained. As noted by Selly and Schiffbauer (2021), studies investigating the impact of X-rays on bacteria and microbial communities have conflicting findings. High levels of X-ray exposure (much higher than utilised in XCT scanning) are reported as an effective antimicrobial sterilising technique for food items (Mahmoud 2012; Mahmoud et al. 2015), and exposing soil samples to X-rays kills selected bacterial groups (Fischer et al. 2013). Contrary to these findings, other investigations report that X-ray exposure has limited to no impact on soil bacterial communities (Zappala et al. 2013; Schmidt et al. 2015). Should X-rays impact the sequence of decay, then this would render XCT as a non-viable technique for decay experiments. As a counter to the potentially

detrimental impact of X-ray exposure on decay-related bacterial communities, Selly and Schiffbauer (2021) suggested that inoculum could be added after each imaging session, however, this could introduce a non-repeatable, confounding variable (Clements et al., in review).

Here, we report a detailed investigation into the use of XCT scanning as a potential method to non-invasively image a decaying carcass *in situ* within sediment. We undertook a series of decay experiments utilising zebrafish (*Danio rerio*) as our model organism, collecting high-resolution anatomical character presence absence data throughout decay. This study is the first, to our knowledge, to constrain the sequence of anatomical character loss in a vertebrate. Our key finding shows that X-rays have an impact on decay rates but, importantly, do not impact the sequence of character loss, and is a viable technique for decay experiments. Along with these results, our experiment reinforces some limitations of XCT imaging, predominantly the difficulty in resolving the internal anatomy due to lack of contrast between soft tissues. However, this work acts as an important proof of concept, and we outline our ongoing studies focused on designing new methods to overcome these limitations.

3.2 Materials and methods

Zebrafish (*Danio rerio*) are common model organisms in biological studies and detailed anatomical data is available (Menke et al. 2011). Mixed sex, wild-type, AB strain, adult zebrafish (Harper and Lawrence

2016) that had reached the end of their reproductive life were sourced from the husbandry unit at the University of Birmingham. The fish were euthanised using MS222, as per the University of Birmingham's policy on the use of animals in research, in compliance with the UK Government Guidance on the Operation of Animals (Scientific Procedures) Act, 1986 (Home Office 2014). All fish were used immediately after euthanising, on day 0 of the experiments outlined below.

3.2.1 Control (CTRL) and sediment matrix (SNDCTRL) experiments

Individual *D. rerio* (*n* = 96) were placed in 200 mL plastic containers filled with 100 mL of deionised water. For ease of extraction, the carcasses were placed on top of a circular piece of plastic mesh, following Sansom *et al*. (2010). All jars were kept at a constant temperature of 25°C using an IPS260 Memmert maturation chamber for the duration of the experiment. For the control experiment (CTRL), *D. rerio* carcasses (*n* = 48) and the plastic mesh were placed in deionised water and then sealed for the duration of decay. For the second experiment (SNDCTRL), *D. rerio* carcasses (*n* = 48) and the plastic mesh were buried in approximately 100 grams of 0.1 - 0.5 mm quartz sand (VWR International) and then sealed.

A sampling strategy was designed to identify the sequence of morphological character loss, with a more intensive sampling frequency at the initiation of the experiment. Capturing the early phases of decay at high resolution was necessary, as previous experiments have shown that decay of internal organs is rapid (e.g. Sansom, et al. 2010; Clements, et

al. 2022). The sampling points were as follows: 1 fish on day 0; 4 fish on days 1-4; 2 fish on days 5-7; and 1 fish on days 8-14, 16, 18, 20, 22, 24, 26, 28, 30, 33, 36, 39, 42, 45, 50, 55, 60, 65, 71, 78, 85, 92, and 120. Each carcass was carefully extracted and dissected under an optical microscope.

40 morphological characters were assessed in each carcass (see Appendix S1), recording if they were in life position, and assigning one of four decay states: pristine (visually same condition as immediately *postmortem*), decaying (morphology altered but identifiable), onset of loss (morphology altered and difficult to identify), complete loss (no longer observable or recognisable) as per the terminology designed by Sansom *et al*. (2010), with one additional character state (onset of loss) to increase the resolution of our dataset. We used 1.5 IQR tests to check for outliers in the datasets of both experiments.

In order to quantify the differences between the sequence of anatomical character loss of the CTRL and SNDCTRL experiment we assigned a numerical score to the codings of each experiment following the revised methodology of Sansom *et al.* (2010): “pristine” codings received a score of 0, “decaying” and “onset of loss” were scored as 0.5 and “complete loss” was scored as 1. The total score was calculated for each specimen, allowing a decay-through-time analysis, and Spearman's rank correlation coefficient was used to investigate variations in the sequence of anatomical character loss between specimens.

3.2.2 Computed tomography experiment

To test the impact of X-rays on decaying carcasses, we utilised an experimental protocol similar to the previously described SNDCTRL experiment: *D. rerio* carcasses were individually placed in separate 200 mL plastic containers, filled with 100 mL of deionised water and then buried in approximately 100 grams of medium to fine quartz sand. One of the requirements of XCT scanning is that X-rays must penetrate the entire sample from multiple directions, requiring that either the sample or the X-ray source and detector rotate during imaging. This study utilises the former method, and this presents an issue when designing decay experiments, as sample movement can cause carcass agitation, known to cause disarticulation of the organism (Briggs and Kear 1993b), as well as preventing accurate images to be obtained. In the past, this issue was countered by utilising plastic beads to stabilise a shrimp carcass during XCT scanning (Selly and Schiffbauer 2021). We use a quartz sand medium to stabilise the zebrafish carcasses allowing them to be imaged in situ, however, this meant that it was then necessary to test the impact of sediment on the sequence and rate of decay.

The X-ray samples were split into two batches: one batch was scanned at the start (day 0) and end (day 50) of the experiment (n = 4, hereafter referred to as samples A, B, C, D), while the second batch was only scanned at the end of the experiment (day 50; n = 4, hereafter coded E, F, G, H). At the termination of both experiments, the fish carcasses were extracted from the sediment and dissected. Between scans, the jars were kept in a water bath in a temperature controlled environment (18-22°C) in

proximity to the XCT machine. Although this setting was not ideal, as temperature was not as regulated as in the control experiment, it was necessary in order to keep the carcasses as close to the XCT machine as possible to reduce agitation between and during the scanning sessions.

XCT scanning was carried out using a Tescan Unitom XL at the National X-Ray Computed Tomography (NXCT) facility at the Centre for Imaging, Metrology and Additive Technologies (CiMAT) at the University of Warwick. All scans used the following settings: 140 kV energy, 45 W current, 1 mm tin (Sn) filter, two frames per projection, exposure time 370ms, effective voxel size of 45µm. The acquired image stacks were prepared into tomographic datasets using ImageJ software (v. 1.53t), manually cropping empty space around the fish carcasses. Segmentation of the 12 3D models was undertaken using Mimics Materialise software (v. 20 and 22; http://biomedical.materialise.com/mimics; Materialise, Leuven, Belgium), relying mostly on density threshold tools and automated algorithms, limiting the amount of hand-drawn segmentation to a minimum. This method prevents potential human bias that can be introduced during segmentation, at the cost of a grainy surface texture.

To quantify the differences between SNDCTRL and the specimens that were scanned using XCT (samples A-H), we used binary coding (presence/absence) for all specimens involved and omitted the “gonads” character, as this can be hard to observe in male zebrafish. To compare the decay rates, we calculated the percentage of absent characters for A-H and for specimen # 39 from SNDCTRL (this specimen is the

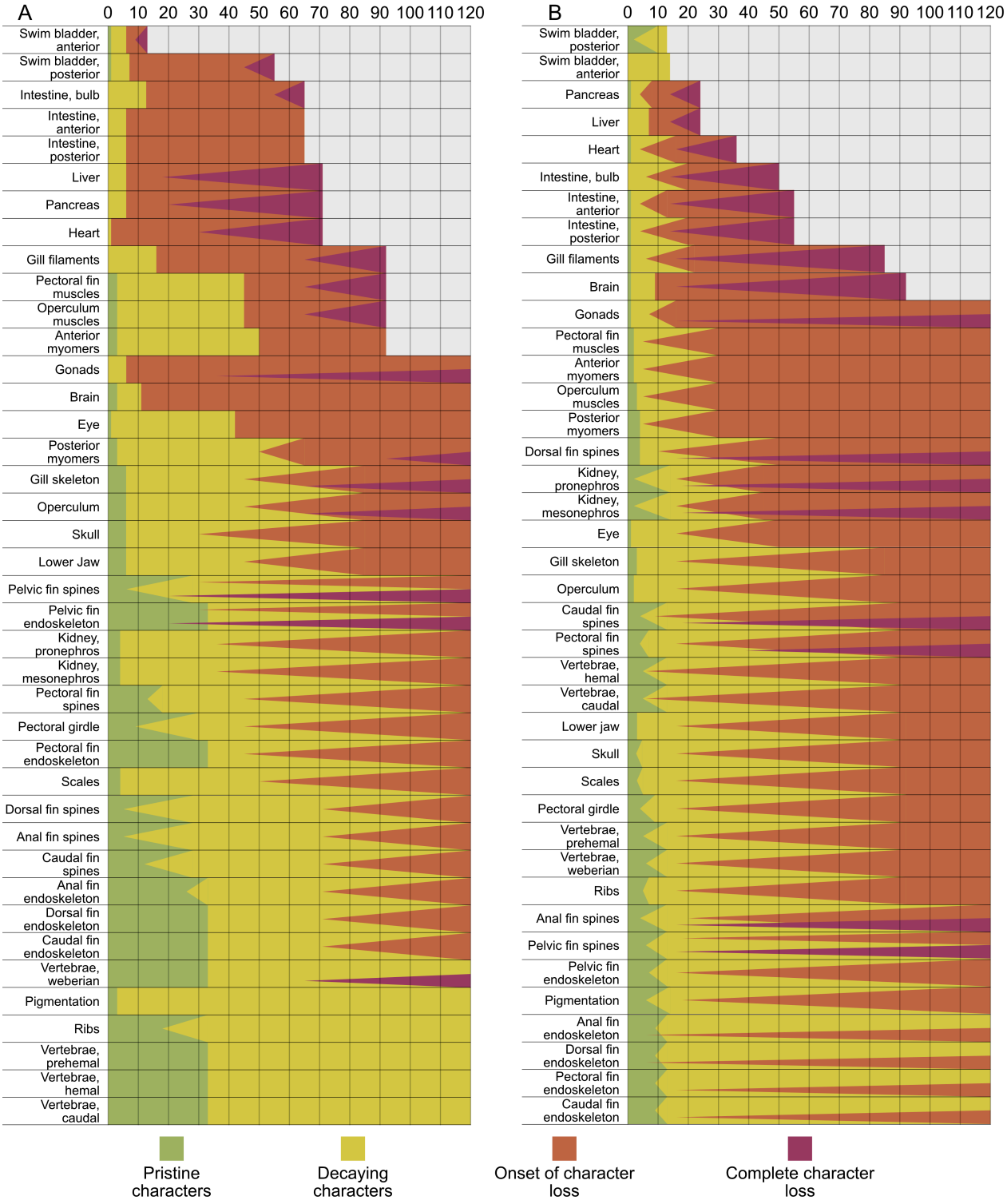
corresponding carcass that was extracted at day 50). To test whether our ability to accurately code characters in a decaying carcass is impacted by the method of data collection, we compared the percentages of presence/absence from two sources: (1) character presence/absence solely from the dissections performed after XCT scanning and (2) character presence/absence from the dissections and incorporating the characters observed via tomograms.

Finally, to test whether the sequence of anatomical character loss is impacted by XCT scanning, we ranked the characters of A-H and specimen # 39 from SNDCTRL using the revised methodology from Sansom *et al.* (2010, see previous paragraph) to perform Spearman's rank correlation coefficient: firstly, scoring the characters of A-H only from dissections, then only from XCT images, and finally coding characters that were recognisable with either method.

3.2.3 3D model mesh comparison

Specimens A, B, C and D were XCT scanned twice (on day 0 and day 50), allowing 3D volumetric mesh models for each specimen at the start and end of the experiment to be created. We imported the mesh pairs

Figure 3.1: Sequence of anatomical character loss in zebrafish decaying in water (CTRL; A) and quartz sand substrate (SNDCTRL; B). Experiment days indicated at top and key of character states at bottom. Characters are ordered based on the last occurrence during the experiment (most decay resistance at bottom). Character score ties were broken based on (in order of priority): transition to onset of loss; first occurrence of complete loss; first occurrence of onset of loss; transition to decaying, first occurrence of decaying. Triangles indicate transition periods between character states. Character state definitions: pristine (same condition as at *postmortem*), decaying (morphology altered but easily identifiable), onset of loss (morphology altered and difficult to identify), complete loss (no longer observable or recognisable).


A
0 10 20 30 40 50 60 70 80 90 100 110 120
Swim bladder, anterior
Swim bladder, posterior
Intestine, bulb
Intestine, anterior
Intestine, posterior
Liver
Pancreas
Heart
Gill filaments
Pectoral fin muscles
Operculum muscles
Anterior myomers
Gonads
Brain
Eye
Posterior myomers
Gill skeleton
Operculum
Skull
Lower Jaw
Pelvic fin spines
Pelvic fin endoskeleton
Kidney, pronephros
Kidney, mesonephros
Pectoral fin spines
Pectoral girdle
Pectoral fin endoskeleton
Scales
Dorsal fin spines
Anal fin spines
Caudal fin spines
Anal fin endoskeleton
Dorsal fin endoskeleton
Caudal fin endoskeleton
Vertebrae, weberian
Pigmentation
Ribs
Vertebrae, prehemal
Vertebrae, hemal
Vertebrae, caudal
B
0 10 20 30 40 50 60 70 80 90 100 110 120
Swim bladder, posterior
Swim bladder, anterior
Pancreas
Liver
Heart
Intestine, bulb
Intestine, anterior
Intestine, posterior
Gill filaments
Brain
Gonads
Pectoral fin muscles
Anterior myomers
Operculum muscles
Posterior myomers
Dorsal fin spines
Kidney, pronephros
Kidney, mesonephros
Eye
Gill skeleton
Operculum
Caudal fin spines
Pectoral fin spines
Vertebrae, hemal
Vertebrae, caudal
Lower jaw
Skull
Scales
Pectoral girdle
Vertebrae, prehemal
Vertebrae, weberian
Ribs
Anal fin spines
Pelvic fin spines
Pelvic fin endoskeleton
Pigmentation
Anal fin endoskeleton
Dorsal fin endoskeleton
Pectoral fin endoskeleton
Caudal fin endoskeleton
Pristine characters
Decaying characters
Onset of character loss
Complete character loss

into CloudCompare (Ver. 2.13, 2023), then aligned them using the CloudCompare Fine Registration (ICP) algorithm allowing the geometry (and thus volume) of the two meshes to be compared. We used the Cloud to Mesh distance algorithm to compute the distance in millimetres between each point on the surface of the day 50 mesh and the closest point on the surface of the day 0 mesh; the difference was output as a heat map plotted onto the day 0 meshes.

3.3 Results

3.3.1 A chronological report of the control experiment: *D. rerio* carcasses decaying in water (CTRL)

The first visible signs of decay observed in the zebrafish carcasses occur on day 1 (Fig. 3.1; Appendix B2, Fig. B1-B2). The eye becomes clouded, darker, and often a small air bubble forms below the lens, while the heart becomes smaller and loses its normal red coloration, becoming pink. On day 2 the female gonads begin to lose structural integrity – this paired organ contains hundreds of oocytes and upon rupture, the oocytes can fill the body cavity; if this occurs, they remain observable for the duration of the experiment. Between day 2 and 6, the internal organs start to show signs of decay: the liver and pancreas, normally visible around the intestinal bulb as areas of (respectively) dark red-brown and yellow-green coloration, become harder to identify and start to lose structural integrity (day 2); the three parts of the intestine (anterior, bulb, and posterior) lose

their original tube-like shape and appear flattened (day 2); the gills start losing colour, transitioning from red to pink (day 3); and both swim bladders rupture (day 3-4). The zebrafish kidney is detectable as a filamentous structure attached to the roof of the coelom, extending from the back of the skull almost to the end of the body cavity. It remains visually identifiable throughout the whole experiment, but parts of it disarticulate and detach from the coelom roof from day 4. The external pigmented stripes on the skin and fins begin to fade from day 4 as well, although they are never entirely lost. The skin becomes flaccid and more difficult to pierce between day 4 and 5, but rarely splits or ruptures. From day 8, the zebrafish bones, typically starting with the skull and pectoral girdle, become translucent and disarticulate readily during dissections. The heart, liver, and pancreas are often completely absent by day 11. On day 11, the brain “liquifies”, completely losing its structural integrity, with the ‘liquid’ remaining confined within the braincase. From day 13, the fin rays lose their normal rigidity and articulation, and the membranes no longer sustain the structure: as a result, the fins are found compressed and bent. The anterior swim bladder is undetectable after day 13, except on a few occasions where the deflated membrane persists. On day 16, the gill filaments start to lose ultrastructure, becoming gelatinous.

By day 30, the intestine loses structural integrity and can rupture. On day 36, the male gonads decay and are no longer identifiable. At this time, the vertebral column and ribs become translucent and prone to disarticulation. Around day 40, the skull, pectoral girdle, and scales

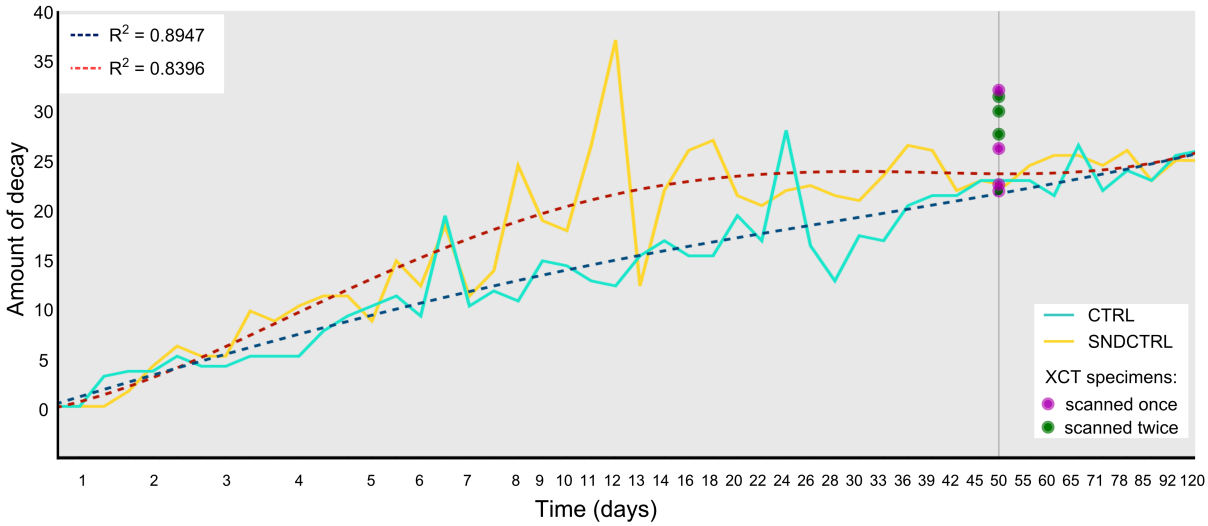


Figure 3.2: Decay rates of zebrafish in water (CTRL) and in a quartz sand substrate (SNDCTRL). Cyan line: zebrafish in water (CTRL experiment); blue dotted line: line of best fit for CTRL. Yellow line: zebrafish in quartz sand and water (SNDCTRL experiment); red dotted line: line of best fit for SNDCTRL. Vertical axis: amount of decay is an accumulative character state score for each character: pristine, 0; decaying, onset of loss: 0.5; complete loss, 1. Minimum: 0 (pristine fish); maximum: 40 (complete loss of the whole carcass). Scores of the XCT scanned fish are reported at day 50.

become semi-transparent and disarticulate more readily during dissections. Fin rays are often found with the tips missing and lose all remaining rigidity. The fin membranes lose rigidity as well and become saggy, but usually remain articulated. The eyes are typically opaque and, if the cornea loses structural integrity and collapses, the eye looks completely black. At this time, the muscle tissues lose their structure and become gelatinous. On day 45, the posterior swim bladder decays and is not detectable anymore, followed on day 65 by all the parts of the intestine. The heart, liver, and pancreas decay by day 71 and muscle tissues and gill filaments become unidentifiable on day 92.

The water in the plastic jars becomes progressively murkier between days 2 and 10, with an increasing amount of floating residue.

Between day 13 and day 45, a film of dark hydrolysed fats (adipocere) often forms on the water surface. By day 30, any suspended residue falls from suspension, settling on the jar floor, and the water becomes clear again. An exception to this occurs if portions of the carcass become disarticulated, causing the water to remain murky and filled with suspended residue. The residue was not identified during this investigation.

During the control experiment, most fish carcasses conformed to the 'normal' sequence of anatomical character loss described above, but some carcasses deviated from it. In the second carcass sampled on day 6, elements of the head and the pectoral girdle were disarticulated from the rest of the body and unidentifiable, which caused early loss of the heart and gill filaments (Fig. 3.2; Appendix B2, Fig. B1-B2). The carcass sampled on day 24 was in an advanced decay state compared to the other individuals sampled at this time point, with complete loss of the head, pelvic fins, and all internal organs (except for the kidney).

3.3.2 A chronological report of carcasses decaying within a sand matrix (SNDCTRL)

The first visible signs of decay occurred on day 2 (Fig. 3.1; Appendix B2, Fig. B1-B2). The eye appears glassy, opaque and develops a small air bubble below the lens, the anterior swim bladder and female gonads rupture, the gill filaments and the brain begin to lose integrity, the heart appears smaller and darker, the liver and pancreas start to lose their overall structure but remain detectable as does the the intestinal bulb, and each part of the intestine appears darker and reduced in volume. The

posterior swim bladder persists longer than the anterior one, retaining its structure and the gas inside it as late as day 10. Between days 3 and 4, the skull and pectoral girdle bones become translucent and less resistant to disarticulation during dissections. Between days 4 and 5, the fin rays lose rigidity, and the fins can be found bent in unnatural positions. In the following days, the loss of volume of the heart continues (day 4-10), the liver and pancreas lose their overall structure (day 7-10), and the three parts of the intestine (anterior, bulb and posterior) appear flattened (day 4-7). From day 9, the vertebral column becomes less resistant to disarticulation during dissection, and individual vertebrae become translucent. The brain finally loses any detectable structure on day 9, although the liquified remains normally persist, trapped inside the braincase. On day 14, both swim bladders become undetectable and the muscles become gelatinous. From day 16, portions of the filamentous structure of the kidney can detach from the roof of the coelom. From day 20, the fin rays often lose their distalmost portions and the scales become translucent and hard to detect. The liver and pancreas become unidentifiable on day 24, while the intestine remains detectable albeit flattened, discoloured, and often with its parts disconnected from each other. On day 33 the skull, pectoral girdle, and axial skeleton become transparent and have almost no resistance to disarticulation during dissections. On day 36, the heart becomes unidentifiable. The same happens to the gill filaments on day 50, while the entire intestine and the brain become unidentifiable on day 55.

The water in the jars becomes murky from day 2, and the suspended organic residue persists until day 20, when it settles on the surface of the sand. From day 7, an adipocere layer develops on the water surface: it can vary in colour from grey to black and persists for the whole experiment.

A number of carcasses deviated from the typical sequence of anatomical character loss (Fig. 3.2; Appendix B2, Fig. B1-B2) during the experiment. In the specimen sampled on day 8 the gill filaments, heart, liver, pancreas, swim bladders and kidney were already unidentifiable, its skeleton was translucent with little resistance to disarticulation and the fin ray tips were partially missing. Another carcass sampled on day 11 had the body cavity filled with unrecognisable remains of the internal organs and the ovaries, its fin rays had the tips missing, the anal fin was not recovered, and its axial muscles already had a gelatinous texture. The carcass sampled on day 12 was substantially decomposed and disarticulated – the entire body was almost completely lost, save for a few scales, the posterior-most portion of the trunk with associated vertebrae and musculature, and fragments of the jaw.

In contrast to specimens that decayed quicker than expected, the day 13 specimen deviated from the expected sequence of anatomical character loss by decaying more slowly. The fin rays showed only minor signs of decay, the vertebral column was in pristine condition and all the internal organs were still recognisable, although the brain had lost its structural integrity.

The carcasses sampled on days 16 and 18 showed decay that deviated from the norm, with notable differences in the skeletal elements. In both fish, the fins were either unidentifiable or in advanced decay states, with no rigidity and the tips of the fin rays missing. Furthermore, in both specimens, the vertebrae, ribs and skull were transparent and opposed no resistance to disarticulation during dissection. In addition, in the day 16 specimen the posterior portion of the vertebral column and the caudal fin were disarticulated from the rest of the carcass, while in the day 18 specimen the head was disarticulated from the rest of the body. Finally, the fish sampled on day 85 represents another occurrence of slower decay rate. The skeleton was almost intact, retaining some resistance to disarticulation, and some delicate internal organs persisted – the heart, gill filaments and brain were greatly reduced in volume and had lost most of their structural integrity, but were detectable. The fin rays lost their rigidity but the overall structure was intact.

3.3.3 Comparison between the control experiment (CTRL) and carcasses decaying in sediment (SNDCTRL)

We compared the numerical scores of the carcasses in the CTRL and SNDCTRL experiments, obtained following the revised methodology of Sansom *et al.* (2010) (see Methods section). The scores of carcasses in the SNDCTRL are typically higher than those of the CTRL between day 2 and day 85, indicating a higher amount of decay, and also have a larger range than the CTRL (Fig. 3.2). The maximum difference is reached between day 8 and day 18, and subsequently the two experiments converge to similar amounts of decay for the last 3 sampling points (days

85-120). The rate of decay for the CTRL is constant throughout the experiment (Fig. 3.2). In contrast, the initial rate of decay for the SNDCTRL is faster than the CTRL until day 12, when the rate begins to slow, and then subsequently plateaus around day 16 - 20. Eventually, around day 85 the rates of decay of the CTRL and SNDCTRL intersect. Detailed investigation of the timing of anatomical character loss using the four state character coding (pristine, decaying, onset of loss, and complete loss) demonstrates that burial within a substrate impacts, not only the rate, but also the onset of decay.

Anatomical characters typically lose their 'pristine' coding faster in the SNDCTRL than in the CTRL samples (Fig. 3.1; Appendix B2, Fig. B1-B2). We see a similar trend in that the percentage of anatomical characters coded as 'onset of loss' also increases faster in the SNDCTRL specimens than those in the CTRL (Appendix B2, Fig. B2). There are two obvious spikes in the proportion of lost characters: one on day 24 for the CTRL and one on day 12 for the SNDCTRL (Fig. 3.2; Appendix B2, Fig. B2). A 1.5 IQR test reports that both specimens are anomalous and are statistically outliers in their respective datasets. When the numerical scores are used to assign a rank to each character (thus quantifying the sequence of character loss), the Spearman's rank correlation coefficient and the associated *p* value indicate that there is no significant difference between the sequence of anatomical character loss between the fish decayed in the CTRL and in the SNDCTRL (R_S coefficient = 0.87, $P < 0.0001$; Table S1). In both experiments the swim bladders are the first to

be lost, followed by the rest of the organs in the body cavity (liver, pancreas, heart, intestine) and the gill filaments. Kidney, brain, gonads and musculature can be lost or persist for the duration of the experiment, while the skeleton is always persistent at the timescale of our investigation (Fig. 3.1).

3.3.4 Cataloguing the morphological decay of carcasses using XCT scanning

XCT imaging allowed us to obtain 12 renderings of zebrafish carcasses *in situ* (Fig. 3.3). The resulting 3D models have a rough surface texture due to sand grains adhering to the external surface of the carcasses, which segmentation algorithms fail to separate from the carcass. This problem was mitigated as much as possible with the available automated algorithms, because they were found to be more precise and consistent than manual segmentation. Despite this, the resolution of the scans is high enough that details of external features such as the eye, mouth, operculum, and fins can be identified from the 3D models (Fig. 3.3A1-H). All of the carcasses remained intact for the duration of the experiment, with limited visible disarticulation. At the initiation of the experiment, the carcasses have gas trapped in the body, either within the still intact swim bladders or as isolated bubbles within the intestinal tract or the mouth. As the carcasses decay the swim bladders rupture, and the gas they contain is released into the coelom. Bubbles of gas are still visible in all of the day 50 XCT images, and the gases escaped the body and the sediment cover during extraction. There were two exceptions to this trend: specimen G, XCT scanned on day 50 only, was devoid of gas;

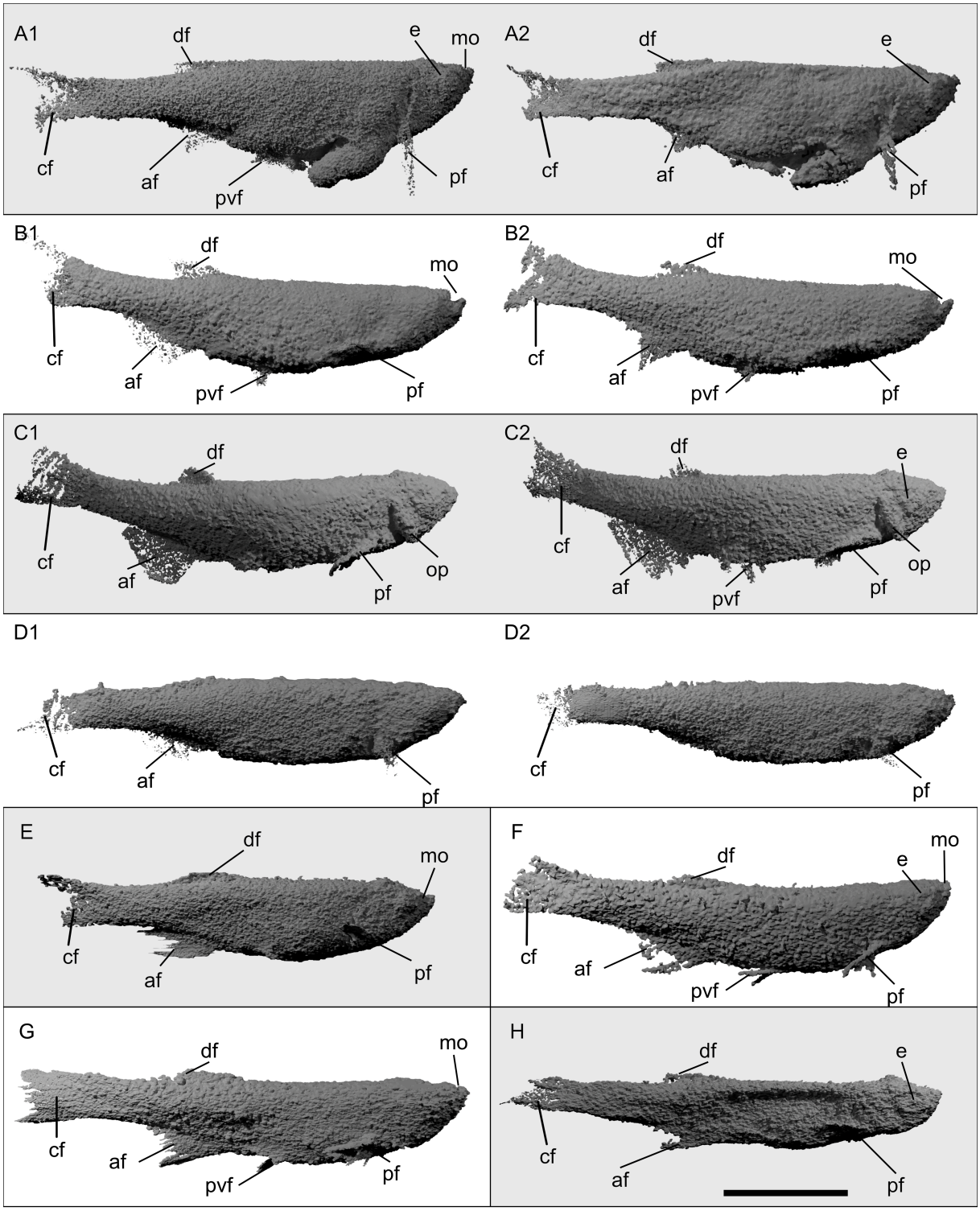


Figure 3.3: 3D XCT models of zebrafish in various stages of decay in right-lateral view. A1-A2, specimen A on day 0 and on day 50; B1-B2, specimen B on day 0 and day 50; C1-C2, specimen C on day 0 and day 50; D1-D2, specimen D on day 0 and day 50; E, specimen E on day 50; F, specimen F on day 50; G, specimen G on day 50; H, specimen H on day 50. Scale bar: 1 cm. Abbreviations: af, anal fin; cf, caudal fin; df, dorsal fin; e, eye; mo, mouth; op, operculum; pf, pectoral fin; pvf, pelvic fin.

and specimen C, which may have suffered accidental damage to the swim bladders during experimental set-up, and has a minimal volume of gas visible in the day 0 XCT scan (Supp. Mat.). The day 50 scan of specimen C, however, shows more and larger gas bubbles than the day 0 scan, probably as a result of gas build up during decay.

The scans also allow us to observe the orientation and shape of the carcasses. Most specimens were oriented laterally (*n* = 4), or dorsolaterally (*n* = 3), while only one specimen was oriented dorsoventrally. Specimen H was laterally flattened – more so than the other specimens (Fig. 3.3H). This suggests collapse of the coelom and loss of the internal organs, which was confirmed by dissecting the carcass (see below). Specimen A had a rupture along the ventral side, probably developed during burial, with a portion of the intestine extruding outside of the body cavity and detectable in the XCT images on day 0 and day 50 (Fig. 3.3A1-A2).

All carcasses in the XCT experiment were dissected immediately after they were scanned on day 50 in order to allow data on the state of morphological decay to be collected and compared with data from the SNDCTRL (*n* = 8). Here, we report the state of morphological decay of the scanned carcasses at day 50.

Specimen A: the body had disarticulated into several unidentifiable fragments and some distinct sections of articulated spine and associated axial musculature. The head had disarticulated from the rest of the body and the eyes were darkened, with both lenses unidentifiable. Some larger

fragments of the body retained the pigmented stripes on the skin. No fins were recovered. No internal organs were identifiable. The skull and the discernible portions of the vertebral column were semi-transparent and disarticulated readily when examined during the dissection.

Specimen B: the body had disarticulated into several pieces, the larger of which retained associated skeletal elements and musculature. The head was separated from the body. The eyes were black, but the lens was still intact and identifiable. Only portions of the pelvic and pectoral fins were able to be identified. The brain and the internal organs were not identifiable. All parts of the skull and the identifiable portions of the axial skeleton were semi-transparent.

Specimen C: the body remained intact. The eyes were dark but the lens was visible and in life position. Most of the musculature was gelatinous but still identifiable. Pigmentation on the body was fading but still visible. The pelvic fins were not recovered, but all others were present. The anal and caudal fins were particularly intact, although the overall structure was starting to lose robustness. The internal organs and the brain were no longer observable. The skull and pectoral girdle were semi-transparent and disarticulated readily during the dissection, while the vertebral column showed a higher resistance to disarticulation during dissection.

Specimen D: the body remained intact. The eyes were dark but with the lens intact and in life position. All the musculature was gelatinous but still detectable. Pigmented stripes on the body were faint but visible. All

the fins were present, although their robustness was lost. The brain had no structural integrity, however, the liquified remains were still within the braincase. The heart, liver, pancreas, and anterior swim bladder were not identifiable, although the deflated posterior swim bladder was detected. Likewise, the three major sections of the intestine were identifiable, albeit flattened and discoloured. Elements of the kidney were also identifiable on the roof of the coelom. All the skeleton was translucent, but retained articulation, resisting disarticulation during dissection.

Specimen E: the body remained intact. The eyes were black but structurally intact, with the lens still in life position. All the muscles were gelatinous but identifiable. Colouration on the body was faded but still visible. The fins were identifiable but had lost their structural robustness. As with the previous specimen, the brain had liquified, but only part of it was still visible in the braincase. The heart, liver, pancreas, and anterior swim bladder were not identifiable. The posterior swim bladder was still present but deflated. The intestine was identifiable but discoloured and flattened. The kidney had disarticulated but fragments were identifiable. The entire skeleton was translucent and retained some resistance to disarticulation during dissections, except for the bones around the skull roof. These bones were transparent and less resistant to disarticulation during dissection.

Specimen F: the specimen had disarticulated. Most of the head, pectoral girdle and anterior musculature were not recovered. The eyes were black and the lenses had disarticulated. The posterior portion of the

body had disarticulated and most of the associated axial musculature was unidentifiable. Some of the pigmented stripes were visible on the fins and where the dermis persisted. The pectoral and anal fin were not found, and other fins had lost some rays. The fin membranes had lost their robustness. The brain and the internal organs were not recovered. The portions of the skeleton that were identifiable were semi-transparent and disarticulated readily when dissected.

Specimen G: the body remained intact. The eyes were black and the lens was still identifiable and in life position. The musculature was gelatinous. The pigmented stripes on the body were faint but visible. All the fins were found albeit without any remaining structural robustness. As with previous specimens, the brain had liquified and a pale matter in suspension (with a similar consistency to milk) was still partially visible in the braincase. The heart, liver, pancreas, anterior swim bladder, and posterior portion of the intestine were not identifiable. The posterior swim bladder was identifiable but deflated. The remaining two parts of the intestine were pale and flattened. Elements of the kidney were still visible. All the skeleton was translucent and retained some resistance to disarticulation during dissection.

Specimen H: the specimen was disarticulated. The head and the pectoral girdle were detached from the rest of the body and the body cavity was ruptured ventrally. The eyes were still visible but entirely black and the lenses could not be identified. The muscles were gelatinous but detectable, including the pectoral muscles. The dark stripes were still

visible in the areas covered by dermis. The dorsal and anal fin were not found, while the pectoral, pelvic and caudal fins were visible but, as in all the previous specimens, their structural robustness was lost. No internal organs were identifiable, save for the intestine bulb, which was flat and pale in colour.

3.3.5 Comparison between the carcasses decaying in sediment (SNDCTRL) and the XCT scanned carcasses

Our experiment investigating the impact of XCT scanning on decay resulted in two datasets for each carcass: one with decay states recorded from the dissections (described in the previous paragraph), and one with decay states recorded from the tomograms. This allowed us to compare the resulting percentages of lost morphological characters and to utilise Spearman's rank correlation coefficient to test whether XCT scanning impacts the sequence of anatomical character loss of a decaying carcass. Specimen # 39 from the SNDCTRL experiment was used as the comparator.

We first performed the comparison and the analysis using the datasets resulting from dissections. We record advanced decay states for most of the XCT scanned carcasses during dissections (n = 5), with extensive disarticulation of the skeleton and most of the internal organs lost. The remaining carcasses (n = 3) lost some internal organs (e.g. swim bladders, liver, pancreas) and were largely articulated. As a result, more than half of the carcasses (n = 5) have a percentage of lost characters 2-3 times higher than the control, most of them (n = 3) are among the carcasses XCT scanned twice during the experiment (Table 3.1). This

		Batch 1				Batch 2			
Specimens	**# 39**	**A**	**B**	**C**	**D**	**E**	**F**	**G**	**H**
Present	32	16	20	25	35	35	15	34	25
Absent	7	23	19	14	4	4	24	5	14
Percentage of absence	17.95	58.97	48.72	35.90	10.26	10.26	61.54	12.82	35.90
Spearman coefficient		0.254	0.346	0.346	0.723	0.723	0.232	0.620	0.346
p value		0.059	0.015	0.015	0.000	0.000	0.077	0.000	0.015

Table 3.1: Summary of comparisons and Spearman's rank analysis using presence/absence data from dissection. Specimens A-D are in batch 1 (XCT scanned at the initiation of the experiment and at its termination on day 50); specimens E-H are in batch 2 (XCT scanned at the termination of the experiment on day 50). Specimen # 39 from our sediment-based control experiment (SNDCTRL) is the reference for both analyses. P-value significance level: 0.05.

indicates that XCT at the start of the experiment may cause an elevated rate of decay when compared to carcasses buried in quartz sand. The Spearman's rank shows that the majority of carcasses are statistically similar to the control in terms of sequence of anatomical character loss (n = 6) (Table 3.1). The carcasses that deviate from this trend are also the ones with the highest percentages of lost characters (samples A, F) (Table 3.1; Appendix B2, Fig. B1-B2).

The datasets resulting from the tomograms are largely limited to the mineralised tissues (Appendix B1). It is known that XCT scanning does not allow to image soft tissues without staining agents, in fact the non-mineralised morphology of the carcasses appears featureless and grey in our tomograms. Nonetheless, we were able to confirm the presence and full articulation of the skeleton of all the samples (Fig. 3.3). We combined the dissection and tomographic data for each carcass, reporting any

		Batch 1				Batch 2			
Specimens	**# 39**	**A**	**B**	**C**	**D**	**E**	**F**	**G**	**H**
Present	32	28	28	28	35	35	27	34	29
Absent	7	10	11	11	4	4	12	5	10
Percentage of absence	17.95	25.64	28.21	28.21	10.26	10.26	30.77	12.82	25.64
Spearman coefficient		0.337	0.449	0.449	0.723	0.723	0.557	0.620	0.490
p value		0.018	0.002	0.002	0.000	0.000	0.000	0.000	0.001

Table 3.2: Summary of comparisons and Spearman's rank analysis using combined presence/absence data from dissections and tomograms. Specimens A-D are in batch 1 (XCT scanned at the initiation of the experiment and at its termination on day 50); specimens E-H are in batch 2 (XCT scanned at the termination of the experiment on day 50). Specimen # 39 from our sediment-based control experiment (SNDCTRL) is the reference for both analyses. P-value significance level: 0.05.

character visible in either method as present. We find that this combined dataset has generally lower percentages of absent characters when compared to the dissection dataset alone, although most carcasses (*n* = 5) still have higher percentages of loss than the control (Table 3.2). In addition, the Spearman's rank correlation coefficient show that all carcasses have a constant sequence of anatomical character loss (Table 3.2; Appendix B2, Table B1).

3.3.6 Carcass orientation within substrate and 3D model mesh comparison

Here we report the results of the mesh comparison conducted on specimens A-D, which were XCT scanned on both day 0 and day 50 (Fig. 3.4).

Specimens A and B were oriented on their lateral side at the initiation of the experiment (left lateral for A, right lateral for B). Both carcasses show

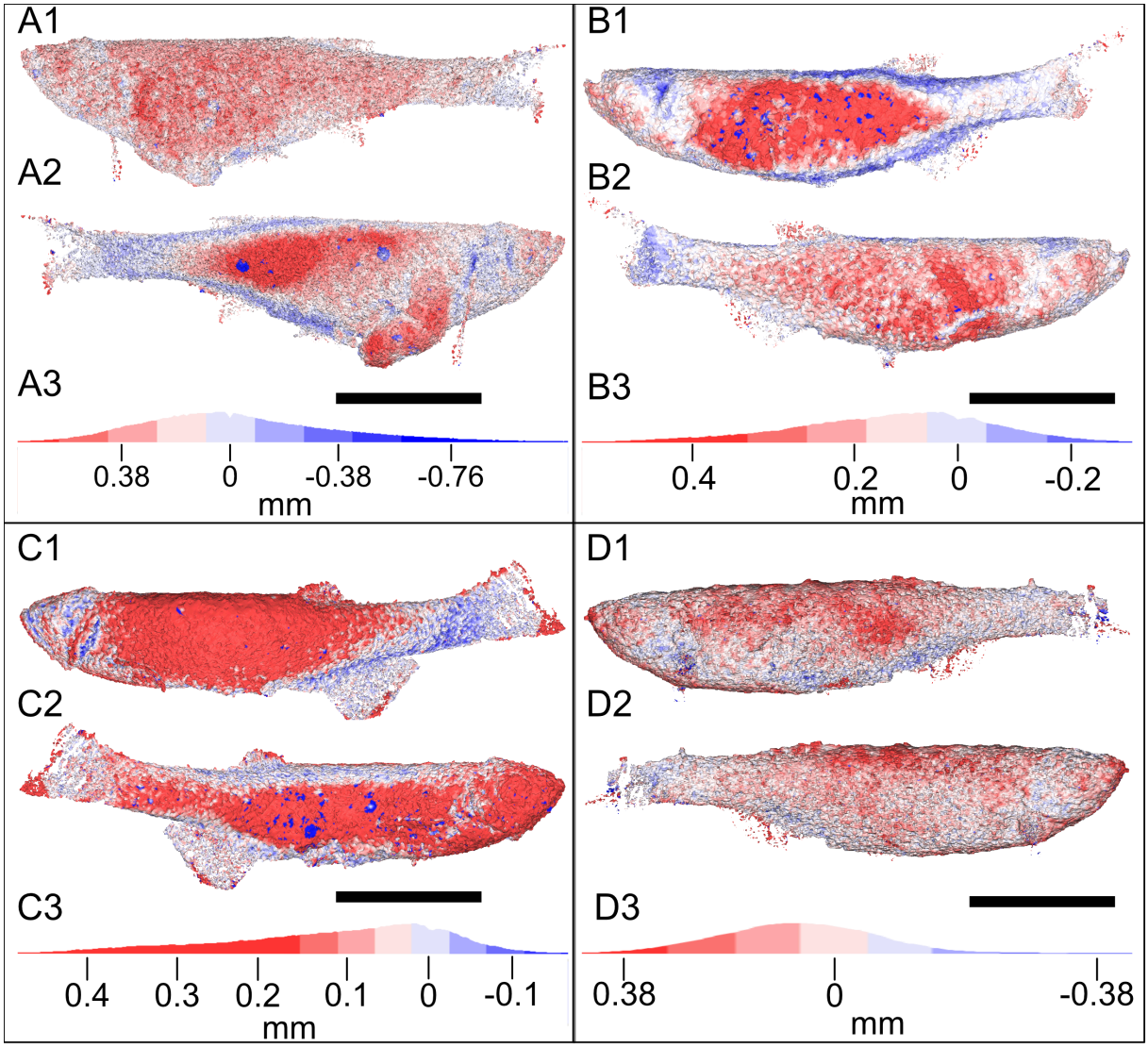


Figure 3.4: Comparison of carcass volume change during decay. CT renderings of specimens (A-D) at day 0. A1-A2, specimen A. B1-B2, specimen B. C1-C2, specimen C. D1-D2, specimen D. Volume changes of the carcass at day 50 are plotted on the renderings as a heatmap representing distance between nearest points on the day 0 and day 50 meshes. Red hues indicate areas of volume decrease over time (i.e. day 0 models are larger than day 50 models); blue hues indicate areas of volume increase over time (i.e. day 0 models are smaller than day 50 models). A3, B3, C3, D3: keys showing distortion values in mm and corresponding colour hues. Specimens A - C decayed laterally (A2, B1, and C2 are upward). Specimen D decayed with dorsal edge upward. Scale bar: 1 cm. Mean distance (mm): -0.06063 (specimen A); 0.1066 (specimen B); 0.1204 (specimen C); 0.1393 (specimen D). Standard deviation: 0.3933 (specimen A); 0.1798 (specimen B); 0.1654 (specimen C); 0.1995 (specimen D).

volume reduction over time on both lateral surfaces. Post-decay, the upward facing side of each fish displays an ovoid area of volume reduction

from behind the skull to the caudal peduncle (0.1–0.5 mm) and, in specimen A, an area of volume reduction is also observed in the extruded intestine (Fig. 3.4A1). Narrow areas along the dorsal and ventral margins of the body, as well as the posterior margin of the skull and operculogular series, show a volume expansion instead (0.2–0.5 mm) (Fig. 3.4A1, B1). The volume reduction on the downward facing side of the fish is less pronounced but more widespread across the entire lateral surface of the body (Fig. 3.4A1, B1). A modest volume expansion is seen along the dorsal margin of the specimen and the caudal fin.

Specimen C decayed lying on its left lateral side, as with specimen A, but curved into a wide "U" shape such that the head and caudal fin extended higher up in the sediment than the rest of the body. Areas of equally pronounced volume reduction (> 0.2 mm) are seen on both sides of the body (Fig. 3.4C1). On the downwards facing side, the reduction in volume is concentrated between the back of the skull and the anal fin, and particularly pronounced on the portion of the body that was the lowest in the sediment. Small areas of expansion are seen along the ventral margin of the body in proximity to the anal fin, the caudal peduncle, and around the skull and operculum. The upwards facing surface of the specimen displays a wide area of volume reduction running the length of the body, from the head to the tail. Very minor expansion is visible along the dorsal margin of the body, as well as in a narrow area near the anal fin (Fig. 3.4C1).

Specimen D decayed in the sediment with its dorsal margin facing upwards. This orientation caused volume reduction to be concentrated in the dorsal and dorsolateral areas of the body (0.1-0.3 mm), with some minor reductions in the ventral region and around the mouth (Fig. 3.4D1). Expansion with time is minor (typically < 0.2 mm), and localised in the ventrolateral regions of the body, around the caudal fin, and in correspondence of the operculum (Fig. 3.4D1).

Our data suggest that the orientation of the carcass has an impact on the amount of decay. When comparing the amount of decay on day 50, carcasses that were buried laterally have higher percentages of character loss (specimens A, B, C; 58.9-35.9%) than the one buried dorsally (specimen D; 10.2%) (Table 3.1).

3.4 Discussion

Our control experiment confirms that the loss of anatomical characters during decay in zebrafish is not random. To our knowledge, this is the first time this has been demonstrated in a non-cyclostome vertebrate (Sansom, et al. 2010; Sansom et al. 2013; Murdock et al. 2014; Sansom 2014). This is a taphonomically important finding, as it expands the groups of organisms that have consistent, repeatable, and therefore modellable, decay sequences. This lends further evidence that decay sequences of extant organisms can be used to interpret the fossil remains of related ancient organisms. Furthermore, our secondary experiment shows that burial in a quartz sand substrate does not alter the sequence of

anatomical character loss in zebrafish carcasses (Fig. 3.1; Appendix B2, Table B1). This is unsurprising, as previous decay experiments that utilise sediments have not generated results where the carcasses deviate from 'expected' decay sequences of anatomical character loss (e.g. Wilson and Butterfield 2014).

In fact, one of the key findings of Wilson and Butterfield (2014) is that the incorporation of sediment impacted the rate of decay; they investigated the impact of sediment type on decay by burying polychaete and shrimp carcasses in kaolinite, calcite, quartz, and Ca-montmorillonite sediments. Their results demonstrate that some mineralogies 'enhance' decay, while others can retard it, and that the effects are taxon-specific. They noted that *Nereis* buried in quartz sand appeared to have 'accelerated' decay, and our data confirm a similar effect in zebrafish (Fig. 3.2). Unfortunately, Wilson and Butterfield (2014) only examined the carcasses at the termination of a 4 month experiment in a qualitative study making it difficult to draw direct comparisons with. Our high-resolution temporal data allows a more detailed investigation of the timing of anatomical character loss in carcasses buried in sediment. One interesting result is that in the first 16 - 18 days of zebrafish carcass decay, we observe a faster onset of loss in the specimens buried in quartz sand (SNDCTRL) than in the control (CTRL) and a faster decay rate (Fig. 3.1; Appendix B2, Fig. B1-B2).

What causes quartz to hasten the onset of decay and increase the rate? We can exclude the effects of any enhanced chemical interactions

between the quartz and the carcasses: quartz sand is inert, and we found no evidence of early or enhanced decay of the external surfaces, such as the scales or dermis, in any of the carcasses. In fact, our data show that soft tissue decay proceeds from the internal tissues outwards, with organs lost first, then musculature, and finally (beyond the timescale of our investigation) dermis. It has been shown experimentally that decay by-products and fluids in the proximity of a decaying carcass create a localised geochemical environment that can influence decay rates and soft tissue preservation potential (e.g. Sagemann et al. 1999; Clements et al. 2017; Clements, et al. 2022). Quartz sand has relatively high permeability, thus we would expect this localised decay environment to diffuse away from the carcass; given the lack of any kind of pore water flow in our experiment, it is possible that the sand grains prevent or at least slow the diffusion of fluids away from the proximity of the carcasses, resulting in a closed microenvironment that enhances decay (as per McCoy, et al. 2015b). Our data supports the hypothesis that the formation of localised geochemical environments around a carcass in quartz sediment must occur rapidly, more so than in water alone, and this may explain why onset of decay occurs sooner. Wilson and Butterfield (2014) noted that some clays, such as kaolinite, appeared to retard decay, and while they too would act to trap decay fluids, clays have been experimentally shown to inhibit bacteria (McMahon, et al. 2016). Eventually the pronounced rate of decay in quartz sand slows to be more similar to the control; presumably, as decay proceeds, the exhaustion of metabolites within the carcass slows

bacterial respiration, causing the intensity of geochemical gradients around the carcass to diminish, slowing the rate of decay which will eventually normalise with the sediment-free control.

3.4.1 The impact of XCT scanning on carcasses in decay experiments

Conceptually, techniques such as XCT scanning can negate the need for exhumation during decay experiments by non-destructively imaging carcasses *in situ*. However, until now, it was not clear if subjecting a carcass to X-rays can have an adverse effect on decay, potentially invalidating the use of XCT scanning in decay experiments.

Our data suggest that exposure to X-rays from XCT imaging at the initiation of a decay experiment may have an impact on the rate of decay, as the carcasses XCT scanned on day 0 show generally higher amounts of decay at the termination of the experiment, compared to the carcasses XCT scanned only at the termination of the experiment (Table 3.1). As noted previously, rate of decay can be influenced by environmental variables, especially temperature (Briggs and Kear 1993b; Briggs and Kear 1994). Within our experiment, it is difficult to determine whether the increased decay rate was caused directly by the XCT scanning or by temperature variations in the environment that the samples were stored in during the analysis (see Methods section). Furthermore, sample agitation could be a factor, although careful handling and burial in quartz sediment attempted to minimise this as much as was practicable. Further investigation is required to fully resolve this, although we note that an elevated rate of decay does not render XCT as a non-practical tool for

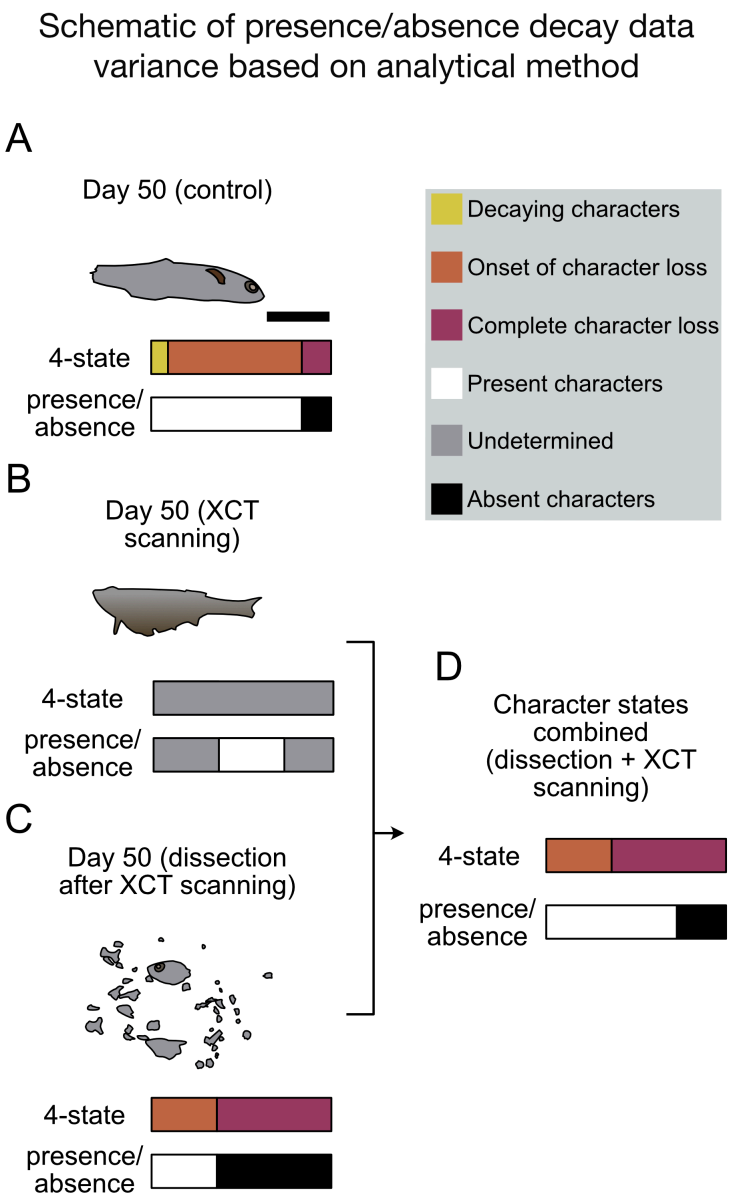


Figure 3.5: A comparative schematic showing variance in appearance and anatomical character coding of a decaying zebrafish in quartz sand substrate on day 50. A, characters and line drawing of specimen # 39 from the SNDCTRL experiment after extraction. B, characters and body outline of the 3D model of specimen A from the XCT experiment still *in situ* within quartz substrate. C, characters and line drawing of specimen A after extraction from substrate. D, characters of specimen A after combining data from tomogram and dissection. The combined data has better accuracy than any of the components. Specimens have two datasets: (1) '4-state' refers to the percentage of each character coding: pristine (same condition as death), decaying (morphology altered but easily identifiable), onset of loss (morphology altered and difficult to identify), complete loss (no longer observable or recognisable), (2) P/A is a simplified percentage of present versus absent characters. Scale bar: 1 cm.

decay experiments. Importantly for decay experiments, our results indicate

that the sequence of anatomical character loss is not impacted by exposure to XCT scanning, when compared to the control (Table 3.1-3.2). As it is believed that the sequence of anatomical character loss is governed primarily by the interaction between bacteria and the intrinsic structural properties of biological tissues within a carcass (as per Briggs 2003; Hilal et al. 2021), we hypothesise that the internal microbial communities do not appear to be affected by exposure to X-rays at the commencement of the experiment. Therefore, our results suggest that XCT scanning is a valid technique for use in decay experiments at any point during an experiment, and it is theoretically possible to XCT scan a carcass multiple times.

There are some shortcomings of the application of XCT in decay experiments. The barriers to imaging internal anatomy or the endoskeleton are a consequence of the scarce radiodensity of soft tissues, which causes them to be transparent to X-rays (Metscher 2009a, b; Mizutani and Suzuki 2012; Gignac et al. 2016). Therefore, the impossibility for unaided XCT scanning to image soft tissues means that dissections remain necessary and the advantages of imaging *in situ* cannot be fully explored. In our experimental design, this is exacerbated by the sand and water surrounding the fish carcasses: both media are relatively dense, and water also typically overlaps in density with organic tissues when XCT scanned, limiting the available scan settings (Pauwels et al. 2013). A high beam energy (kV) is required to ensure sufficient penetration of the sediment but decreases the contrast in the resulting images. Sufficient filtration (in the

form of thin sheets of metal applied between the source of the X-rays and the specimen) can provide increased contrast by selectively absorbing lower energy X-rays, but increases noise in the resulting images. Thus, the interrelation of a higher kV and the need for filtration in response directly reduces image contrast and image quality in our experiment (per Zwanenburg et al. 2022). We are currently exploring ways to mitigate this by the use of contrast agents, such as Lugol's iodine, phosphotungstic acid (PTA) or other media (Rawson et al. 2020). Typically, immersion of soft-tissue samples in a staining medium results in passive absorption in relative amounts, based upon the tissue types within the sample (Metscher 2009a). This process creates artificial density differentiation between tissue types, resulting in greater contrast between them during XCT scanning. This ongoing research will define a viable protocol for the use of contrast agents within taphonomic experiments using sediment.

Despite this shortcoming, the ability to non-destructively image a carcass *in situ* has important implications for the accuracy of decay experiments. Tomograms show that carcasses remained articulated within the sediment before extraction (Fig. 3.3). This is significant, as five out of eight specimens partially or almost completely disarticulated during exhumation (e.g., specimen A, which from the beginning of the experiment had its body cavity ruptured, with partial extrusion of the intestine: Fig. 3.3A1-A2 and Fig. 3.4A1-A2). The remaining three carcasses had a similar appearance. This confirms that the exhumation process can be a source of potential bias, especially to carcasses that are in advanced decay

states. Our data show that combining the anatomical data collected from the tomograms with the data collected from exhumation and dissection meant samples were typically more similar to the control experiment in terms of anatomical completeness and amount of decay (Fig. 3.5; Table 3.2). Therefore, we argue that a combined approach of XCT scanning and traditional exhumation and dissection techniques would constitute best practice, yielding increasingly accurate anatomical presence/absence data in decay experiments that utilise sediment.

3.4.2 Burial orientation and stabilisation: the role of sediment visualised by XCT

While the primary purpose of this experiment was to investigate the use of XCT in taphonomic investigations, our experiments yield interesting results pertaining to the role of sediment in carcass stabilisation. It is well established that sediment influences carcass articulation during decay: burial prevents transport/agitation by currents, which is a source of disarticulation especially in carcasses that are in advanced states of decay (Duncan et al. 2003; Bath Enright et al. 2017; Bath Enright et al. 2021). Sediment also acts as a substrate that microbial mats can grow onto, thus indirectly enhancing preservation by adhesion to the substrate (the “stick ‘n peel” effect, see Orr, et al. 2016) or engulfment of carcasses by the mats themselves, preventing disarticulation (Darroch et al. 2012; Iniesto, et al. 2013; Iniesto et al. 2015). In addition, anoxic conditions within the sediment can prevent scavenging organisms from disturbing carcasses, thus promoting the preservation of soft tissues (Allison 1988; Briggs 2003; Clements and Gabbott 2021). Our tomograms show that all the carcasses

XCT scanned at the termination of our experiment were fully articulated *in situ* (Fig. 3.3), but then most of them disarticulated when extracted from the sediment. This confirms that quartz sand had a stabilising effect, maintaining the structural integrity of the carcass for longer periods of time and preventing soft tissue disarticulation, despite the advanced state of decay.

Our experiment also highlights an additional aspect of burial during decay, which as far as we know is unexplored in the literature: the orientation of the carcasses in sediment can influence decay. During the burial phase of our XCT scanning experiment setup we ensured that carcasses were fully buried in sediment, but we did not control their orientation. As a result, orientation varied among the carcasses, and the 3D mesh comparison highlighted a relationship between orientation, patterns of volume variation and, interestingly, amount of decay. Our data show that zebrafish carcasses buried laterally in quartz sand have a distinctive pattern of volume reduction along both flanks, more pronounced on the uppermost flank, and moderate volume increase along the dorsal and ventral margins of the body (Fig. 3.4A1-C3); this is paired with a higher percentage of lost characters when compared to different orientations (A, B, C from batch 1; F from batch 2; Table 3.1-3.2); three of these specimens disarticulated during extraction (A, B, F) demonstrating that the substrate was maintaining carcass integrity. If the carcasses are buried with their dorsal margin uppermost in the sediment, volume reduction is localised mostly dorsally and dorsolaterally, while there is a

modest volume increase ventrolaterally (Fig. 3.4D1-D3). This is accompanied by a lower percentage of lost characters when compared to laterally buried carcasses (D from batch 1; Table 3.1-3.2). Specimens E, G, and H were slightly tilted, with one of the dorsolateral margins uppermost in the sediment, and the resulting amount of decay varies (Table 3.1-3.2). To our knowledge, this is the first time that the effects of carcass orientation on decay have been observed and recorded in a decay experiment. Our data suggest that carcass orientation could be a currently unknown variable that impacts decay rates, and the entombing sediment may play a role. We hypothesise that the differences in volume variations during decay (Fig. 3.4) are caused by variations in the orientation of the carcass relative to the application of sediment overburden. If the fish carcass is buried dorso-ventrally, the vertebral column is capable of resisting overburden compression during the early phases of the decay process, causing small volume variations and a diminished amount of decay (Fig. 3.4D1-D3). Conversely, when overburden loading is lateral (i.e. the carcass is buried on its side), the ribs are not able to resist compaction, so overburden causes larger deformations and higher amounts of soft tissue decay in the same amount of time (Fig. 3.4A1-C3). In all the specimens but one (specimen G), gas is visible in the tomograms, trapped inside the body, therefore, suggesting that burial orientation does not seem to promote the escape of decay related gases from the carcass.

The effect of burial orientation on carcass geometry when overburdened would probably compound over time and be exacerbated by increasing overburden, compaction, and diagenetic processes. Further investigation is needed.

3.5 Conclusion

As decay experiments increase in complexity, many studies are utilising sediment in their experimental design. However, observation of the carcass is not possible in many 'natural' sediments (such as sand, clays, etc.) and so exhumation and extraction are required to collect character loss data, but these processes may cause carcass disarticulation and potential data loss. In order to mitigate these issues, XCT has been a proposed method to visualise decaying carcasses, however, the impact of exposing a decaying carcass to X-rays is currently unknown. Our data show that while XCT scanning may increase the rate of decay, it does not impact the sequence of anatomical character loss in zebrafish during decay and is therefore a viable technique for non-destructive observation in decay experiments. XCT data confirm that a substrate acts to physically stabilise a decaying carcass, preventing disarticulation over the timescale of our experiment. Interestingly, our data show a new potential variable that affects rate of decay – the post burial orientation of the carcass influences volume change via overburden, and importantly also influences the rate of decay: a carcass lying laterally in

sediment decays more than a carcass buried in a dorsal-ventral burial position.

Our control experiments show that burial of zebrafish carcasses in quartz sediment hastens the onset of character loss and increases the rate of decay when compared to carcasses decayed in water alone. Further work is needed to investigate the role of sediment types on this phenomenon.

The use of XCT in decay experiments is limited by difficulty in imaging the internal anatomy of carcasses. However, our data show that XCT scanning during decay experiments allows a more thorough and accurate investigation of a carcass when compared to dissection alone. Furthermore, XCT has other experimental design benefits such as requiring fewer individual carcasses. The work presented here provides a basis for our future investigations seeking to increase the accuracy of XCT scanning in decay experiments (e.g. the implementation of staining protocols).

4 | Dicing with decay: diceCT scanning as a visualisation tool to aid decay experiments

Iacopo Cavicchini[1], Paul F. Wilson[2], Sam Giles[1], Mark A. Williams[2], and Thomas Clements[1,3]

1: School of Geography, Earth and Environmental Sciences, University of Birmingham, UK.
2: Centre for Imaging, Metrology and Additive Technologies (CiMAT), Warwick Manufacturing Group (WMG), University of Warwick, UK.
3: GeoZentrum Nordbayern, Friedrich-Alexander Universität Erlangen-Nürnberg, Erlangen, Germany

My contribution to this chapter involved most of the data collection, specimen preparation and transport, data analysis, interpretation of results and production of the manuscript, including the figures and tables. The experimental designs (including the staining protocols and XCT scanning) were produced by me and coauthors Paul Wilson and Thomas Clements. All coauthors gave feedback the drafts of the manuscript.

4.1 Introduction

Decay experiments are a vital tool for understanding the processes that result in exceptionally preserved fossils (e.g. Sansom 2014; Briggs and McMahon 2016; Purnell, et al. 2018). In particular, decay data informs us about the decomposition of the biological substrates that preservational processes must act upon govern to allow preservation of soft tissues in the fossil record (e.g. Briggs and Kear 1993b; Briggs and Kear 1994; Briggs and McMahon 2016; Purnell, et al. 2018; Gabbott, et al. 2021). Traditionally, decay experiments are carried out by dissecting carcasses to visually assess the state of morphological characters at varying stages of their decay through time (Sansom, et al. 2011, 2013; Murdock, et al. 2014; Cavicchini et al., 2024; see Chapter 3). Sediment can be incorporated in the experimental design to investigate the impact of burial and/or sediment composition on decay (Briggs and Kear 1994; Martin, et al. 2004; Wilson and Butterfield 2014; Naimark, et al. 2018b), but this introduces complications: the exhumation of carcasses from sediment disturbs the carcasses and can introduce biases to anatomical presence/absence character decay data (Cavicchini et al., 2024; see Chapter 3). To mitigate this, new decay experiment methodologies must be developed: Micro computed tomography (XCT scanning) can mitigate the bias introduced by exhumations and dissections by imaging carcasses *in situ* without the need to disturb the carcass (e.g. Selly and Schiffbauer 2021; Waskom, et al. 2023; Cavicchini et al., 2024; see Chapter 3). Recently, Cavicchini et al. (2024; see Chapter 3) identified that exposure to X-rays did not

significantly impact decay, allowing higher resolution decay data to be collected by employing XCT in conjunction with dissections. However, Cavicchini et al. (2024; see Chapter 3) did find shortfalls with this method: the low electron density of internal biological, non-mineralised tissues makes them difficult to visualise, either *in situ* or after exhumation (Metscher 2009a, b; Mizutani and Suzuki 2012; Gignac, et al. 2016), hindering a wider usage of XCT in decay experiments.

To successfully image biological tissues, a methodology called diffusible contrast-enhanced computed tomography (diceCT scanning) is often used in descriptive biology. Organic samples are immersed in a solution containing heavy metal elements (staining agent) that preferentially bind to different molecules to increase their radiodensity (staining process) prior to XCT scanning (Pauwels, et al. 2013; Descamps et al. 2014). This process increases the X-ray attenuation of soft tissues enough to make them observable using regular X-ray based imaging techniques, such as XCT scanning (Metscher 2009b; Descamps, et al. 2014; Rawson, et al. 2020). One commonly used staining agent is Lugol's solution (I_2KI, iodine potassium iodide), which binds iodine to organic molecules (Metscher 2009a; Mizutani and Suzuki 2012; Gignac, et al. 2016), but other staining agents can be used for different results, depending on the binding molecules and the staining process (Johnson et al. 2006; Metscher 2009a; Vickerton et al. 2013; Gignac, et al. 2016).

In the field of taphonomic decay experiments, so far only Selly and Schiffbauer (2021) have employed diceCT scanning, using Lugol’s

solution to stain decaying shrimp carcasses. This allowed the internal anatomy of the carcasses to be imaged by XCT scanning, thus demonstrating that this methodology has a promising application to decay experiments. However, while Selly and Schiffbauer (2021) was an excellent proof of concept that showed that this technique could be employed experimentally, more work is required to critically assess the impact of diceCT scanning on decay, and therefore the viability of use of the technique in decay experiments. Here, we present a thorough proof of concept study of the feasibility of diceCT scanning in decay experiments, using Lugol's solution as the staining agent and vertebrates (zebrafish) as the model organism, first in water and then *in situ* under quartz sand.

Due to the nature of the chemicals involved, implementing diceCT protocols with Lugol's solution in a decay experiment requires modifications to the normal experimental designs. Firstly, Lugol's staining agent contains iodine, which has well known antiseptic and bactericide properties (Klebanoff 1967; Larson 1988; Yasuda et al. 1997; Wagner et al. 2008; Bigliardi et al. 2017; Grønseth et al. 2017; Grønseth et al. 2023), which causes problems for decay experiments; bacteria can induce and drive the decay process in a carcass (Sagemann, et al. 1999; Briggs 2003; Briggs and McMahon 2016; Butler, et al. 2015; Benbow, et al. 2019), so it is reasonable to expect that the introduction of an iodine-based staining agent in the vessels of a decay experiment should have an impact on decay, potentially slowing or halting it during staining time. However, the potential effect of iodine on the decay process of a carcass has never

been confirmed nor quantified. Secondly, an excessive quantity of staining agent (overstaining) can cause shrinkage in soft tissues, skewing anatomical observations by modifying the appearance of organs, musculature, etc (Callahan et al. 2021; Dawood et al. 2021). Therefore, to record the decay state of anatomical characters accurately, it is paramount to conduct a calibration phase to identify the optimal amount of staining agent prior to the main experiment(s). Lastly, designing a diceCT protocol for a carcass *in situ*, while reducing disturbance as much as possible, presents difficulties because of the multiple operations required to execute a diceCT protocol (e.g. addition of staining solution, removal of all liquid prior to XCT scanning, dehydration, washing up with ethanol, etc.) that can cause disturbances (Metscher 2009a). Selly and Schiffbauer (2021) partially circumvented the issue by having plastic beads as a high-porosity, low X-ray attenuating “sediment”, and employing a syringe to remove the incubation water from the vessels, add the staining solution, and substitute it with water prior to XCT scanning. Their positive results, despite the caveats previously discussed, prove that finding a diceCT protocol that can visualise a decaying carcass within sediment without requiring exhumation is highly desirable, in order to transition from destructive, bias-inducing assessing to non-destructive observations of the morphological decay of soft tissues *in situ*.

Herein, we devise and implement a diceCT protocol for decay experiments utilising sediment, testing its accuracy and reliability. We chose Lugol’s solution as the staining agent, since it is compatible with an

aqueous medium (Metscher 2009b), and vertebrate carcasses (zebrafish) as the specimens to stain (Menke, et al. 2011). The diceCT protocol successfully enhanced the density contrast between soft tissues, allowing decay assessment through diceCT imaging even in decayed specimens. Our statistical comparisons corroborate the effectiveness of this methodology. Finally, we highlight shortcomings with the technique (such as assessment of skeletal decay) and report good practices while conducting diceCT decay experiments.

4.2 Materials and methods

4.2.1 Specimens and decay assessment

Zebrafish (*Danio rerio*) was chosen as the study organism as it is commonly used as a model animal in both biological studies (Menke, et al. 2011) as well as decay experiments (Cavicchini, et al., 2024; see Chapter 3). The fish were wild type AB strain (Harper and Lawrence 2016) that were culled by the animal husbandry unit at the University of Birmingham at the end of their reproductive life cycle.

Fish were euthanised on day 0 of each experiment using MS222 anaesthetic, in compliance with the current UK Government Guidance on the Operation of Animals (Home Office 2014). All the specimens were then prepared in individual vessels and transported to where staining protocols and XCT scanning would be carried out (outlined below). XCT scanning was undertaken at the Tescan Unitom XL at the National X-Ray Computed Tomography (NXCT) facility at the Centre for Imaging, Metrology, and Additive Technologies (CiMAT), Warwick Manufacturing Group (WMG),

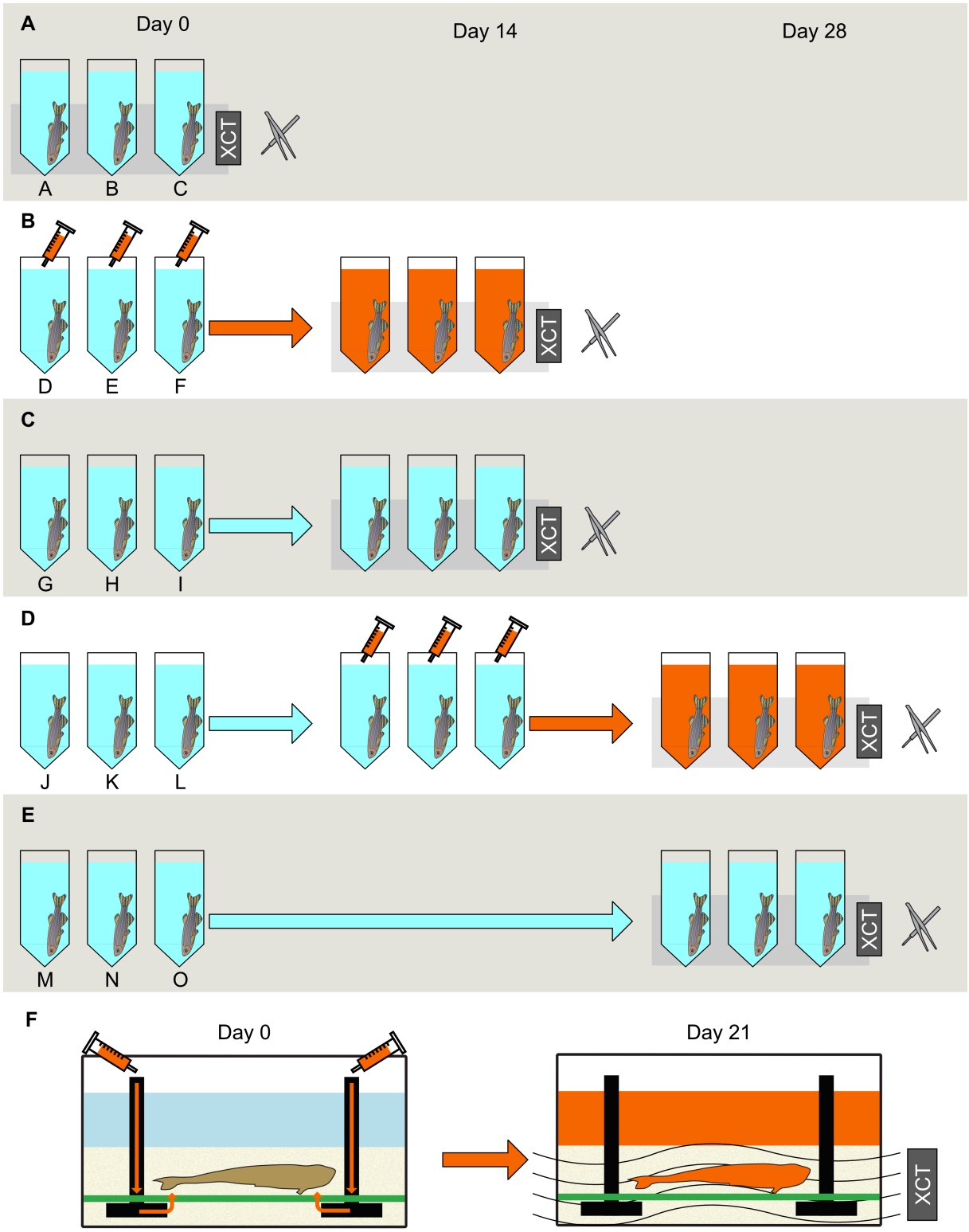


Fig. 4.1: Graphical representation of the protocol of the W-diceCT experiment (A-E) and the S-diceCT experiment for specimen C (F). A, unstained day 0 specimens (A-C). B, stained day 0 specimens (D-F). C, unstained day 14 specimens (G-I). D, stained day 14 specimens (J-L). E, unstained day 28 specimens (M-O). F, day 0 stained specimen (C) of the S-diceCT experiment illustrating the *in situ* staining protocol employed.

University of Warwick, UK. We chose to employ Lugol's solution as a staining agent (Pro-Lab Diagnostics™ Lugol's Iodine Stain; Ethanol 2.5 - <5%, Potassium Iodide 1 - <2.5%, Iodine 0.5 - <1%, Methanol 0.25 - <0.5%) in an aqueous medium (deionised water) for all the staining protocols. During maturation and staining time, the specimens were kept in the temperature-controlled environment (18-22°C) as physically close to the XCT machine as possible to avoid carcass agitation.

The methodology of Cavicchini *et al* (in review; see Chapter 3) was used to assess the decay of the morphological characters.

4.2.2 Experimental protocols

Preliminary experimental trial: diceCT for decayed specimens in deionised water. Once we identified a suitable staining protocol for fresh specimens, the preliminary experiment (from now on referred to as W-diceCT, with W for "water") was designed to test the feasibility of staining decayed carcasses. On day 0, 15 zebrafish specimens were prepared in polypropylene, screw-top 50 mL falcon tubes with 40 mL of deionised water. The experiment was conducted as follows (Fig. 4.1A):

- *n* = 3 (specimens A, B, C) were XCT scanned on day 0. These specimens will be referred to as 'day 0 unstained'.
- *n* = 3 (D, E, F) were stained on day 0 by adding 10 mL of Lugol's solution directly into the falcon tubes, and XCT scanned on day 14 after 2 weeks of staining time. These specimens will be referred to as 'day 0 stained'.

- *n* = 3 (G, H, I) decayed for 2 weeks and then were XCT scanned. These specimens will be referred to as ‘day 14 unstained’.
- *n* = 3 (J, K, L) decayed for 2 weeks, were stained on day 14 by adding 10 mL of Lugol's solution directly into the falcon tubes, and were XCT scanned on day 28 after 2 weeks of staining time. These specimens will be referred to as ‘day 14 stained’.
- *n* = 3 (M, N, O) decayed for 4 weeks and were XCT scanned on day 28. These specimens will be referred to as ‘day 28 unstained’.

For all the specimens, maturation water and staining agent were syringed out of the falcon tubes prior to XCT scanning to prevent the specimens from moving during the procedure, and the tubes with the specimens were mounted vertically to keep an aspect ratio of the specimens as uniform as possible during the scans.

The unstained specimens (A, B, C, G, H, I, M, N, O) were scanned at 40 kV energy, 20 W current and using no filtration. Two frames per projection were acquired, with exposure time of 95 ms and effective voxel size of 45 µm.

The stained specimens (D, E, F, J, K, L) were scanned at 50 kV energy, 20 W current and using a 0.5 mm aluminium (Al) filter. Two frames per projection were acquired, with exposure time of 120 ms and effective voxel size of 45 µm.

All specimens were dissected after XCT scanning to assess the decay state. In order to keep the time between scanning and dissection to a

minimum, there was no de-staining phase prior to dissection for the stained carcasses.

Statistical comparisons. Despite the low number of specimens used in this investigation, it was possible to conduct statistical comparisons between day 14 stained specimens (J, K, L) and the controls. To do that, the character assessment was modified following a methodology used by Sansom *et al.* (2010): “pristine” states received a score of 0, “decaying” and “onset of loss” were scored as 0.5 and “complete loss” was scored as 1. This way, by tallying the totals for each fish, completely pristine would receive a score of 0, while completely destroyed would receive a score of 40. The scores for each fish were compared and used to build a decay through time reference at the timescale of the investigation.

In a separate analysis, the previously outlined numerical scores (0 for pristine, 0.5 for decaying and onset of loss, 1 for complete loss) were tallied for each singular character (rather than for each fish), considering the codings in each group of 3 specimens that shared the same experimental conditions (A, B, C; D, E, F; G, H, I, etc.). This way, the minimum possible score for a character (0) would mean that the character was always pristine in the group of specimens, and the maximum score (3) would indicate that all the specimens in the group had lost the character. The character-specific totals were then used to test for variations in the sequence of anatomical character loss. The sequence of character loss has been used to highlight biases in the fossil record of early vertebrates

and it was proven to be species-specific and independent from environmental variables such as sediment composition (Sansom et al., 2010; 2013; Cavicchini et al., 2024; see Chapter 3). The character-specific calculation was performed three times for each group of specimens, each time changing the assessment method the scores were derived from (dissection, XCT tomograms, diceCT tomograms) thus allowing to perform multiple comparisons: (1) Dissections of day 14 stained specimens versus dissections of day 14 unstained specimens, in order to test if and in what measure iodine can impact a decay assessment from a dissection without a de-staining phase. (2) Tomograms of day 14 stained specimens versus dissections of day 14 unstained specimens, to test if subjecting carcasses to diceCT protocols can impact the decay process. (3) Tomograms of day 14 stained specimens versus dissections of the same specimens, to test for differences in the appearance of a specimen with different methods of collecting decay data.

Main experiment - diceCT in situ for carcasses buried in sediment. Following the test of a viable protocol for staining and XCT scanning decayed carcasses in water, the viability of a similar protocol for *in situ* staining and XCT scanning of carcasses in sediment was tested. On day 0 of our second experiment (termed S-diceCT, S for "sediment"), 5 specimens (A, B, C, D, E) were placed in plastic jars with 200 mL of deionised water. The carcasses were placed on top of plastic mesh to facilitate extraction and staining. Specimens A, B, C, E were buried in sediment (0.1-0.5 mm quartz sand, VWR International). For specimens A-

C, the staining agent was delivered to the carcasses *in situ*, using PVC irrigation tubes and connectors as per Fig. 4.1B. This way, the staining agent could be syringed into the tubes and diffuse directly in the sediment around the buried carcass; the surface of the connectors was punctured to help the diffusion of the staining agent. The final preparation for each specimen reflected the necessity to test various staining agent concentrations, to account for the presence of sediment and the in situ staining, and was as follows: (1) Specimen A was prepared with 3 tubes and 5.26 mL of Lugol's, for a final concentration of 5%. (2) Specimen B was prepared with 4 tubes and 11.1 mL of Lugol's, for a final concentration of 10%. (3) Specimen C was prepared with 6 tubes and 25 mL of Lugol's, for a final concentration of 20%. (4) Specimens D and E are the control: they were stained with 25 mL of Lugol's each, but were kept in deionised water (D) and buried in sediment, but the staining agent was not delivered *in situ,* rather just added to the water, to act as a control of the staining agent delivery method (E). Staining was unsuccessful for specimens A and B, for insufficient concentration of staining agent, and for specimen E because the staining agent remained suspended above the sediment. Specimens C and D, for which the staining was successful, were XCT scanned after 21 days of staining time. Specimen D was scanned after removal of the water, to avoid movement during the scan, at 80 kV energy, 45 W current and using a 0.25 mm copper (Cu) filter. Two frames per projection were acquired, with exposure time of 120 ms and effective voxel size of 45 µm. Specimen C was initially scanned *in situ*, at 180 kV energy,

45 W current and using a 1.5 mm tin (Sn) filter. Two frames per projection were acquired, with exposure time of 350 ms and effective voxel size of 45 µm. The carcass was visible in the resulting tomograms but the level of detail was not satisfactory. Therefore, a second, longer scan was attempted at 150 kV energy, 35 W current, 1 mm tin (Sn) plus 2.5 mm copper (Cu) filters, two frames per projection, exposure time 1500 ms and voxel size 35 µm. After this second attempt, it became clear that it was impossible to improve the level of detail of the tomograms, while keeping the carcass *in situ*. However, there were areas of the carcass with barely visible staining, so after exhumation and gentle rinsing off of the sand from the carcass, a third scan was done, with the same parameters as specimen D.

Segmentation. The acquired image stacks for all the XCT scanned specimens were prepared into tomographic datasets using the ImageJ software (v. 1.53t), manually cropping empty space around the fish carcasses. Segmentation was undertaken for specimens A-O (W-diceCT) and C-D (S-diceCT) using the Mimics software (v. 22-25; http://biomedical.materialise.com/mimics; Materialise, Leuven, Belgium). Specimens A, B, C, G, H, I, M, N, O (W-diceCT) were segmented mostly using density threshold tools to prevent operator bias and keep the resulting 3D models consistent. Specimens D, E, F, J, K, L (W-diceCT) and C-D (S-diceCT) were impossible to segment relying solely on algorithms so most of the segmentation of the soft tissues was done by hand. It is worth noting that the resolution of the tomograms was high enough to

show diminutive anatomical structures that are impossible to assess with the unaided eye during dissection.

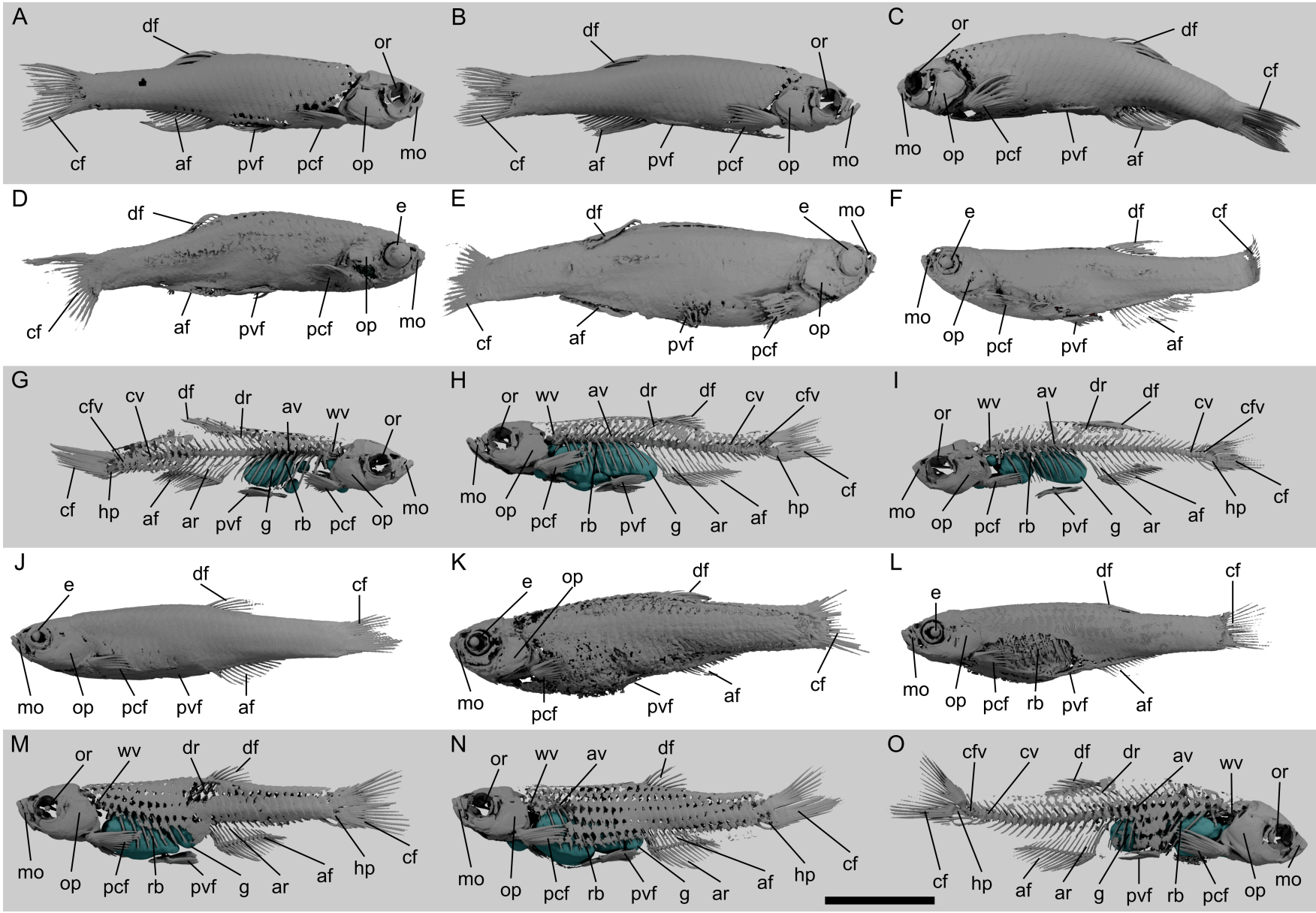
4.3 Results

4.3.1 Preliminary experimental trial (W-diceCT experiment).

Day 0 (no staining): specimens A, B, C were XCT scanned on day 0, then dissected. A density threshold algorithm is able to detect most of the scales and the entire skeleton, including the fin rays, without needing any additional operations (Fig. 4.2A-C, pcf, pvf, df, af, cf). The swim bladders are detectable because of the gas trapped inside them and are the only non-skeletal structure visible inside of the body, albeit indirectly (Fig. 4.2A-C). The dissections performed on the specimens confirm the pristine state of their internal anatomy.

Day 0 staining: specimens D, E, F were XCT scanned on day 14 after 2 weeks of staining time, then dissected. Staining was successful and allowed the observation of the internal anatomy via tomograms, without any notable shrinkage of the tissues (Fig. 4.3A1-C2). Density contrast between soft tissues is not enough to completely segment each morphological character of interest relying only on automated algorithms

Fig. 4.2: 3D models of the external morphology of specimens from the W-diceCT experiment. A-C, unstained day 0 specimens (A-C). D-F, stained day 0 specimens (D-F). G-I, unstained day 14 specimens (G-I). J-L, stained day 14 specimens (J-L). M-O, unstained day 28 specimens (M-O). Scale bar is 1 cm. Abbreviations: af, anal fin; ar, anal fin radials; av, anterior vertebrae; cf, caudal fin; cfv, caudal fin vertebrae; cv, caudal vertebrae; df, dorsal fin; dr, dorsal fin radials; e, eye; g, gas bubble; hp, hypurals; mo, mouth; op, operculum; or, orbit; pcf, pectoral fin; pvf, pelvic fin; rb, rib; wv, weberian vertebrae.


A
df
or
cf
af
pvf
pcf
op
mo
B
df
or
cf
af
pvf
pcf
op
mo
C
or
df
cf
mo
op
pcf
pvf
af
D
df
e
cf
af
pvf
pcf
op
mo
E
df
e
mo
cf
af
pvf
pcf
op
F
e
df
cf
mo
op
pcf
pvf
af
G
cfv
cv
df
dr
av
wv
or
cf
hp
af
ar
pvf
g
rb
pcf
op
mo
H
or
wv
av
dr
df
cv
cfv
mo
op
pcf
rb
pvf
g
ar
af
hp
cf
I
or
wv
av
dr
df
cv
cfv
mo
op
pcf
rb
pvf
g
ar
af
hp
cf
J
e
df
cf
mo
op
pcf
pvf
af
K
e
op
df
mo
pcf
pvf
af
cf
L
df
cf
e
mo
op
pcf
rb
pvf
af
M
or
wv
dr
df
mo
op
pcf
rb
pvf
g
ar
af
hp
cf
N
or
wv
av
df
mo
op
pcf
rb
pvf
g
ar
af
hp
cf
O
cfv
cv
df
dr
av
wv
or
cf
hp
af
ar
g
pvf
rb
pcf
op
mo

and density threshold tools, so segmentation was refined manually. As iodine binds differentially to different soft tissues, density values vary within the same carcass: we record the highest in the eyes, around the braincase and the jaws, the proximal portion of the pectoral fin rays, the dorsal and ventral margins of the body, small clusters of spherules in the body cavity (not associated with any organ), around the anus, around the hypurals, and caudal fin vertebrae. The trunk muscles have variable density, highest posteriorly, in streaks running along the flanks, and around the horizontal myoseptum. Most of the internal organs, the skeleton, and the pectoral fin muscles have medium density values. We record the lowest values (which are still higher than the surrounding air and the remains of the staining solution) in the gill filaments, fin rays, and spinal cord. Specimens E and F also contain clusters of relatively high-density material in their intestine (most probably partially digested food).

Soft tissues: The eye is visible as a halo of medium-high density around a disk of higher density, which is the lens (Fig. 4.3, e). The brain completely fills the braincase, with minor density variations; the telencephalon and the optic tectum are detectable but the density contrast worsens anteriorly, so the olfactory bulbs are not always visible. Individual gill filaments are visible at medium-low density owing to the empty space surrounding them. The heart is nested between and ventrally to the gills; the staining agent is probably differentially absorbed, with the ventricle being the main detectable structure and the atrium and bulbus arteriosus being barely visible. Liver and pancreas are low density volumes that wrap

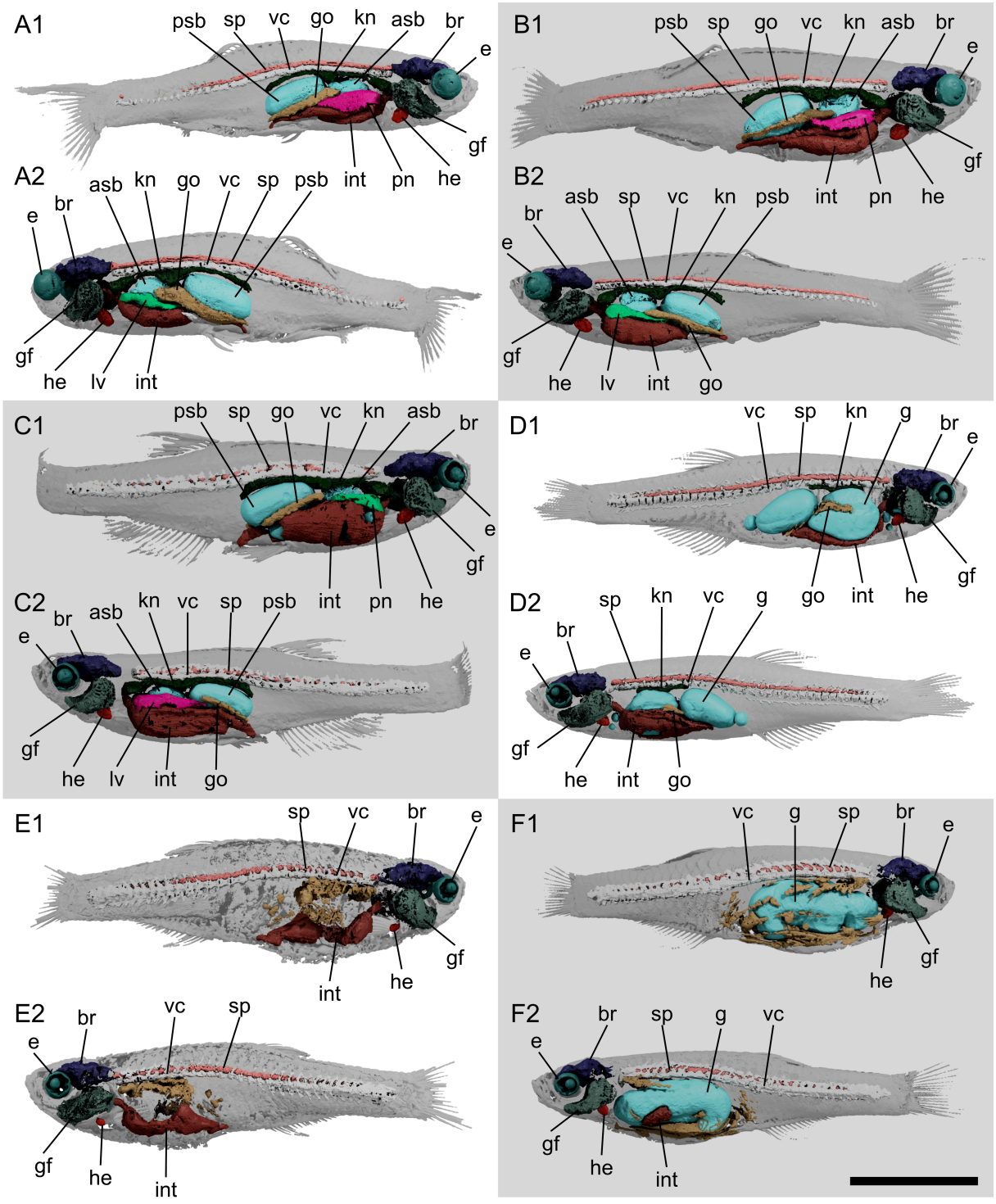


Fig. 4.3: 3D models of the internal anatomy of diceCT scanned specimens from the W-diceCT experiment. Internal morphology is opaque, external morphology is rendered in partial transparency for all the specimens. A-C, day 0 stained specimens (D-F) in right and left lateral view. D-F, day 14 stained specimens (J-L) in right and left lateral view. Scale bar is 1 cm. Abbreviations: asb, anterior swim bladder; br, brain; e, eye; g, gas bubble; gf, gill filaments; go, gonad; he, heart; int, intestine; kn, kidney; lv, liver; pn, pancreas; psb, posterior swim bladder; sp, spinal cord; vc, vertebral column.

around the anterodorsal portion of the intestine and the lower half of the anterior swim bladder. Smaller structures in the area, like the gallbladder and the spleen, are not detectable at the resolution of this investigation. The intact swim bladders are readily apparent as low density gas bubbles. The posterior portion of the pneumatic duct (connecting the swim bladder to the oesophagus) is sometimes visible, as well as the ductus communicans between the anterior and posterior bladders. The contrast of the intestines varies between individuals and also between different portions within an individual. The internal volume of the intestine bulb is sometimes the densest portion of the organ, possibly because of partially digested food. The posterior most tract of the intestine is usually harder to detect, because of the high density area around the anus. The male gonads are low density strips with no discernible internal structures that surround the posterior swim bladder on either side, with an expanded anterior portion and tapering out towards the anus. The bilobed anterior portion (head) is the largest part of the kidney and despite the medium to low density, is normally visible in the tomograms dorsally and anteriorly to the anterior swim bladder; the rest of the kidney extends dorsal to and between the swim bladders, but it can be harder to detect for its density, very close to that of the overlying vertebral centra and trunk muscles. Axial and pectoral muscles are visible and are normally at medium density. While the pectoral muscles appear as a uniform volume, the dorsal and anal fin muscles, as well as the different myomeres of the axial musculature, are discernible. Bands of higher density can be seen along

both flanks of the carcasses, in correspondence of the horizontal myoseptum, and more apparent posteriorly.

Mineralised tissues: The entire skeleton is articulated. The density of the skeleton is variable, and the ease of identification of the bones depends on the surrounding tissues. Fin rays and scales are not entirely surrounded by soft tissues, so they are easiest to identify. For the pectoral fin rays, density can be higher proximally and decrease distally. In the caudal fin, an area of very high density normally engulfs the hypurals, the caudal fin vertebrae and can extend to part of the rays. Streaks of very high density mask portions of the scales from detection along the dorsal and ventral margins of the body, except where the attachment of the unpaired fins are positioned, and along the horizontal myoseptum. Among the bones of the skull and pectoral girdle, the easiest to identify are those of the upper jaw, the operculum, the gill arches, and the skull roof. The vertebral centra, ribs, and radials of the unpaired fins have a density that is normally similar or lower than the surrounding muscles, potentially because of incomplete saturation by the staining agent, so they can be harder to detect.

Dissection: The staining agent causes the carcasses to become stiff, making the dissection process more difficult than normal. The iodine in the tissues also changes their colour to a bright orange, hindering the visual assessment of some morphological structures (e.g., brain, heart, liver, pancreas, kidney, gonads). The dissection, except for the changes

induced by the iodine, confirm the pristine state of the internal anatomy of the carcasses.

Day 14 (no staining): specimens G, H, I were XCT scanned on day 14 with no prior staining, then dissected. Density threshold algorithms have difficulties in including the entire scale covering without manual operations, while all parts of the skeleton are easily segmented automatically (Fig. 4.2G-I). Both the scale cover and the skeleton appear complete and articulated; in addition, size and shape of the body are not significantly different from any of the pristine carcasses. Gas is present inside the body cavity of each carcass, but the size, shape and number of the bubbles suggest that the swim bladders have ruptured (Fig. 4.2G-I; 3X). As expected, no additional details about the state of the internal anatomy are discernible through the tomograms.

Dissection: The eye is clouded and opaque, with gas forming under the lens. All the musculature is gelatinous; the scales appear translucent, and the external pigmentation begins to fade. Heart, liver, gonads and pancreas are unidentifiable, both swim bladders have ruptured and are not detectable (save for the posterior bladder in specimen I). Brain and gill filaments are losing their structural integrity but are still detectable. The intestine is flattened and discoloured. Some filaments of the kidney have partially detached from the coelom roof. All the bones of the carcass are pale and are less resistant to disarticulation. All the fins have lost elasticity.

Day 14 staining: specimens J, K, L were XCT scanned on day 28, after 14 days of decay and 14 days of staining time, then dissected. Staining was once again successful, without any visible shrinkage, and it was possible to observe the decayed internal anatomy via XCT (Fig. 4.3). The resulting density contrast is not enough to separate the tissues using only automated tools during segmentation, and density tools fail to determine the whole integument, despite the absence of ruptures (Fig. 4.2X). However the additional manual segmentation required is low, because of the high amount of decay obliterating portions of the internal anatomy (see below). The absorption of iodine from the tissues looks generally lower than in the pristine carcasses, but the highest density areas remain similar: the eyes, around the braincase and the jaws, and in small spherical clusters in the body cavity (not associated with any organ). Other high-density areas of the day 0 carcasses show reduced density in specimens J-L: around the anus, the hypurals, and on the dorsal and ventral margins of the body. The streaks of high density along the flanks of the body are absent in all specimens. Trunk muscles retain a variable, but generally medium-low density and the pectoral fin muscles have exceptionally low density. Intestine, gill filaments and the brain are less dense than the day 0 specimens–density also decreases posteriorly for the brain. Similar to the day 0 specimens, the visible portion of the heart retains a medium density. The skeleton has a higher density than in the day 0 specimens: in particular, ribs and vertebral centra are more clearly

visible in the tomograms and have very high density in specimens J and L. High density material, potentially remnants of the epithelium, is visible in the intestine of specimens J and K.

Soft tissue: The eye is still clearly detectable and retains the high-density lens and the halo around it, but the disk of the lens appears smaller and can be slightly displaced from the middle of the eye (Fig. 4.3D1-F2). The anterior portion of the brain, starting from the optic tectum, is markedly denser than the posterior portion, which can be hard to visualise. Gill filaments are still identifiable albeit at very low density. The ventricle of the heart is detectable, with density similar to the day 0 specimens. The liver and pancreas are no longer identifiable. Gas bubbles are present in specimens J and L, suggesting rupture of the swim bladders and an additional build-up of gaseous by-products of decay; in the latter specimen, the gas has invaded most of the body cavity (Fig. 4.3F1-F2). Small, irregular, high density volumes are scattered in the body cavity of specimens K and L (Fig. 4.3E1-F2). The intestine is often partially filled by gas and high density epithelium remnants. The gas build up can cause deformations to the organ (specimen L). In two of the three specimens the kidney is not detectable, while in specimen J a small tract of the tail is visible and the head is probably masked by some high density ellipsoidal volumes (Fig. 4.3D1-F2). The gonads are partially visible in specimen J and lost in the remaining two. Axial and pectoral muscles are still visible at a lower density, the latter having the lowest density and no internal structures discernible. The myomeres, dorsal and anal fin muscles are still

identifiable. Bands of higher density along the flanks of the carcasses are no longer visible, but the overall density still increases posteriorly towards the caudal fin. The ventral margin of the body, between the pectoral and pelvic fins, is slightly deformed in specimen L (Fig. 4.3F1-F2).

Mineralised tissues: The skeleton is articulated. The bones appear denser and are more easily identifiable than in the day 0 specimens, because of reduced density values for the surrounding tissues. Fin rays have low density, similar to the day 0 specimens; scales, on the other hand, can be identified easily as all the posterior margins point slightly away from the body. The area of high density around the caudal fin vertebrae is reduced in size, but still present.

Dissection: All the carcasses are stiffer than day 14 unstained carcasses because of the staining agent, and the colouration is altered both externally and within the body cavity. A visual assessment is generally impractical due to the presence of the iodine, e.g. the musculature, which is visible but impossible to assess further, because of the artificial stiffness of the tissue.

The eye is pale and partially collapsed on itself. Individual scales appear translucent, and the body pigmentation is visibly partially faded despite the iodine. Inside the head, the structural integrity of the brain and the gill filaments is lost and only gelatinous remnants are visible. Heart, liver, gonads, pancreas and anterior swim bladder are unidentifiable. Remnants of the flattened and ruptured posterior swim bladder are only detectable in specimen J. The intestine is generally flattened and

discoloured, while in specimens J and L has also partially lost integrity. In all specimens, the kidney is identifiable, suffering only minor detachments of fibres. The skeleton appears translucent and the presence of the staining agent may artificially increase the resistance to disarticulation. The fin membranes have lost elasticity.

Day 28 (no staining): specimens M, N, O were XCT scanned on day 28 with no prior staining, then dissected. The skeleton is easily segmented using density threshold tools, while the scale covering is only partially picked up without manual inputs (Fig. 4.2M-O). All three specimens are comparable to the rest in size and shape, and the skeleton is complete and articulated. Gaseous by-products of decay and the gas from the ruptured swim bladders are still trapped inside the body cavity (Fig. 4.2G-I). The internal anatomy is not discernible through the tomograms.

Dissection: The eye has collapsed on itself and is opaque. All muscles are gelatinous and lost their structure. Scales are almost transparent and the external striped pigmentation has faded considerably. The brain is “liquified” but still trapped in the braincase. Gill filaments, liver, gonads, pancreas and swim bladders are no longer detectable. A small remnant of the heart is identifiable only in specimen M. The intestine structural integrity is lost and can be discontinuous or ruptured. Filaments of the head and tail of the kidney can detach. All the bones are translucent

and have lost almost all resistance to disarticulation. The fin membranes no longer sustain the overall structure and the fins are bent and collapsed.

Comparison with previous investigations on the decay of zebrafish. A previous investigation has constrained the rate of decay and sequence of anatomical character loss in zebrafish decaying in deionised water (Cavicchini, et al., in review; see Chapter 3). Model organism, timescale and conditions of that investigation are similar to the present study, allowing for a meaningful comparison of the assessment of the amount of decay at day 14. In fact, all the day 14 specimens (G-L) of the W-diceCT experiment have amounts of decay that vary depending on the assessment method, while the 14 days-old specimen from Cavicchini *et al.* (specimen 26) was just dissected (Fig. 4.4).

Firstly, dissections of day 14 specimens (G-L) yield total amounts of decay higher than specimen 26 (Fig. 4.4). The main difference lies in the mineralised characters: in all the W-diceCT specimens the entire skeleton is translucent and has diminished resistance to disarticulation, while only parts of it (fin spines, skull, pectoral girdle) are in a similar state in specimen 26 (Cavicchini, et al., in review; see Chapter 3). When assessed through diceCT tomograms, day 14 unstained specimens have low amounts of decay (Fig. 4.4), however, the datum is not significant since it is entirely due to the impossibility of imaging soft tissue with unaided tomography. Finally, the day 14 stained specimens (J-L) when assessed through diceCT tomograms, have amounts of decay that vary

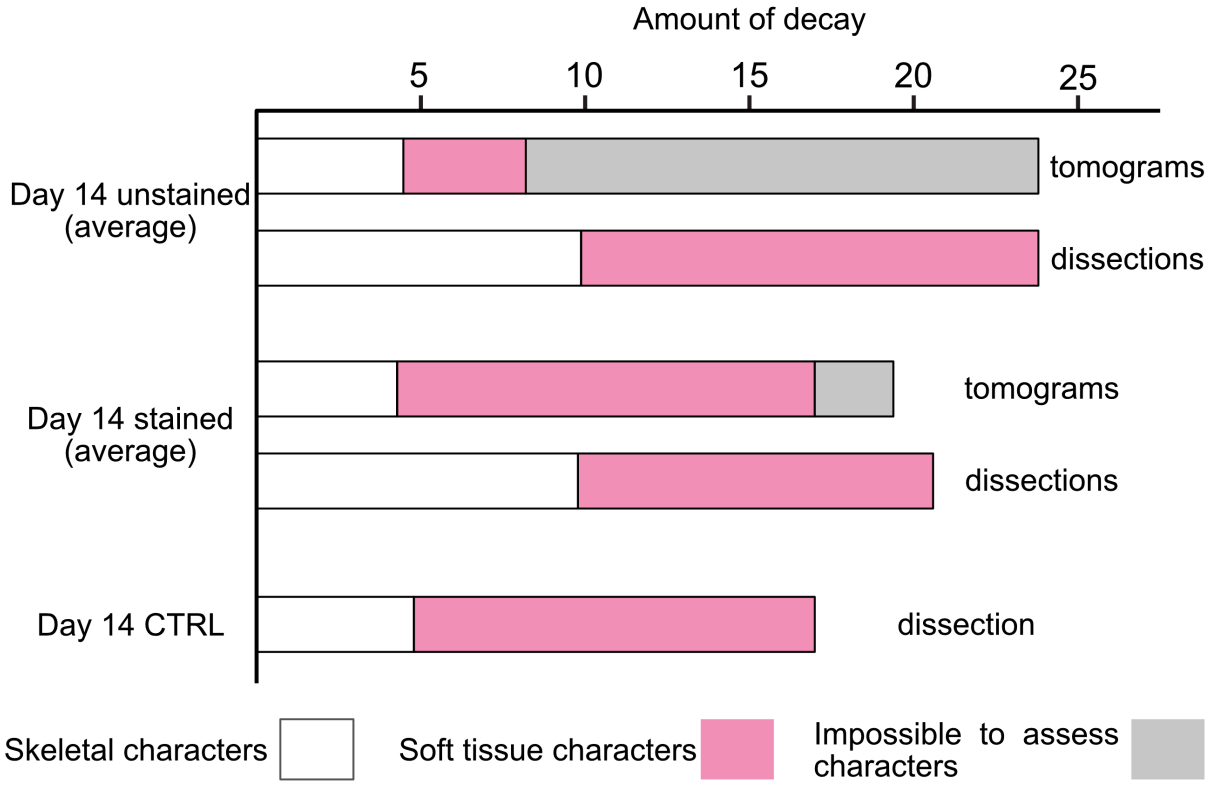


Fig. 4.4: Comparison of the amount of decay between selected specimens across different assessment methods. Comparison includes all day 14 specimens from the W-diceCT experiment (unstained G, H, I; stained J, K, L) and the day 14 specimen from the CTRL experiment of Cavicchini *et al*. (in review, see Chapter 3). The amount of decay is averaged for each group of 3 specimens with equal experimental pathways. The total amount of decay is obtained as the sum of the amount of decay for skeletal characters (white) and soft tissue characters (pink). The impossible to assess characters (grey), where present, are indicated to show the level of uncertainty of the assessment method.

among the individuals but are comparable to or lower than specimen 26 (Fig. 4.4).

4.3.2 Main experiment (S-diceCT experiment)

Specimen C was stained *in situ* while buried in quartz sand and XCT scanned after 14 days of staining time. For the first tomography of specimen C, undertaken with the carcass *in situ* under sediment, the X-ray attenuation of the quartz sand is too high to reveal any meaningful details beyond the general shape of the carcass (Supp. Mat.). The lenses and

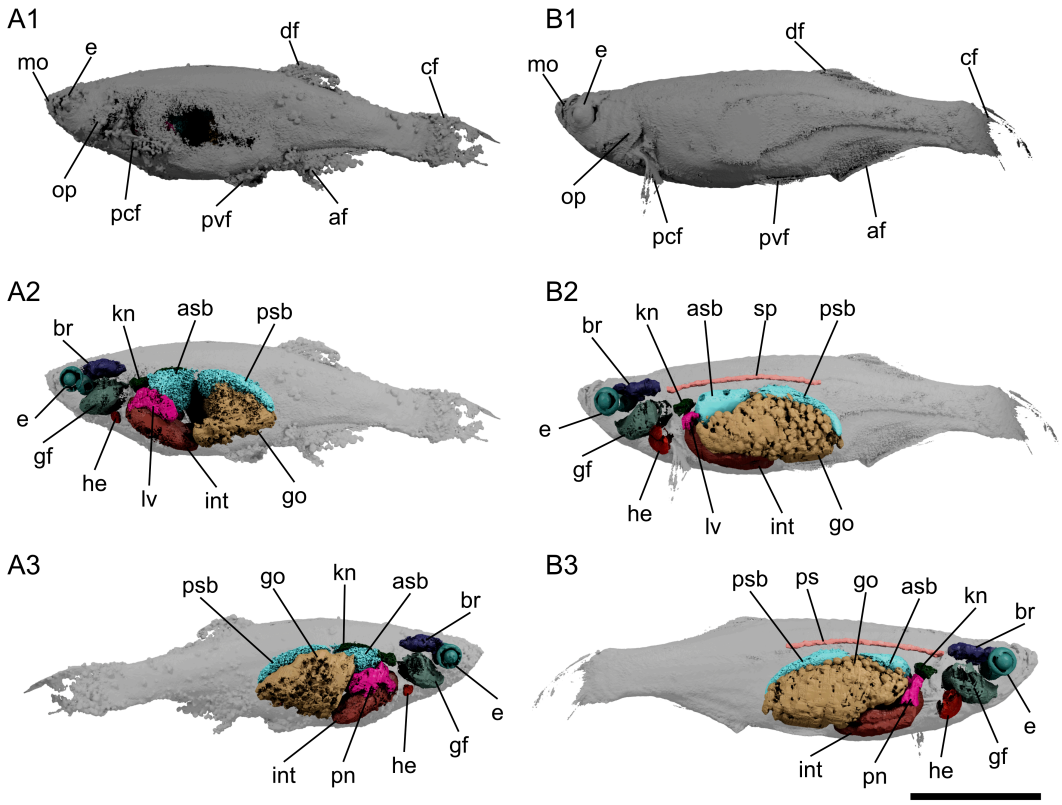


Fig. 4.5: 3D models of diceCT scanned specimens from the S-diceCT experiment. Internal morphology is opaque, external morphology is rendered in partial transparency for A2-A3 and B2-B3. A1, external morphology of specimen C in left lateral view. A2, internal anatomy of specimen C in left lateral view. A3, internal anatomy of specimen C in right lateral view. B1, external morphology of specimen D in left lateral view. B2, internal anatomy of specimen D in left lateral view. B3, internal anatomy of specimen D in right lateral view. The hole in the specimen in panel A1 is an artefact of the segmentation process. Scale bar is 1 cm. Abbreviations: af, anal fin; asb, anterior swim bladder; br, brain; cf, caudal fin; df, dorsal fin; e, eye; gf, gill filaments; go, gonad; he, heart; int, intestine; kn, kidney; lv, liver; mo, mouth; op, operculum; pcf, pectoral fin; pn, pancreas; psb, posterior swim bladder; pvf, pelvic fin; sp, spinal cord.

haloes of the eyes are visible, as well as the otoliths. The axial musculature, the hypurals, and the ventral portion of the ovaries appear slightly brighter than the rest of the carcass, but it is impossible to discern any other details.

The second tomography of specimen C, with the carcass exhumed and gently washed to remove as much sand as possible (the granules visible

around the body in the 3D model are sand grains that were not removed by the water stream) proves that the *in situ* staining protocol was successful (Fig. 5.4B). Segmentation is refined by hand for all the internal structures of the carcass, due to insufficient density contrast between the different soft tissues, but not for the skin and scales. The posterior third of the body has no detectable shrinkage, despite absorbing a higher quantity of iodine than the anterior portion. Staining quality is orientation-dependent for some tissues (axial musculature, scales and ovaries), in fact the downward-facing side of the carcass is darker and less defined, to the point that the integument is intact, but there is a hole in one of the flanks of the 3D model (Fig. 5.4B). In addition, the quality of staining in the body cavity worsens slightly towards the centre of the coelom, making the contrast between the swim bladders, liver, pancreas and the rest of the cavity unclear in places.

The highest resulting density values can be seen in the lens of the eye, some areas of the skull (skull roof, along both jaws and around the eye), along the dorsal and ventral margins of the body and around the hypurals of the caudal fin, to the point that the latter are not discernible. Muscles and the oocytes in the ovaries have orientation-dependant medium to high density. The internal organs have generally low density, except for an irregularly distributed volume within the intestine bulb. The vertebral centra and spinal cord have irregular density, often very similar to that of the surrounding muscles, so they are not segmented out. Ribs have the lowest density of all the bones.

Soft tissues. The lens and the high-density halo around the eye are clearly visible. Staining for the brain and the gills is comparable to other specimens of our previous experiments, but the morphology of both structures is less clearly defined in the tomograms. Only a ventricle of the heart is visible. The liver and pancreas are poorly defined but visible, especially in their anterior most portion. Both swim bladders are intact, but not as clearly visible as expected, due to a diminished density contrast with the centre of the coelom. All parts of the intestine are visible including the thin posterior portion between the ovaries. The intestine bulb is partially occupied by gas and partially by highly dense material (possibly undigested food). The head and part of the tail are visible for the kidney, while the density contrast is not enough to single out the posterior portion, dorsal to the posterior swim bladder. Visualisation and staining quality decrease medially for the female gonads, which are by far the largest organ in the body while intact. Tthe oocytes close to the ventral and right lateral margins of the body are individually visible, while in other areas the gonads are less definite. All the muscles have an unusually high resulting density, but the internal fibres and the myomeres are clearly visible, particularly for the axial muscles and the ventral cephalic muscles.

Mineralised tissues. The skeleton is visible but is generally hard to identify single bones due to the very high-density areas in the skull and the varying density contrast along the vertebral column. The fin rays are visible, although many sand grains are stuck to the membranes. The radials of the unpaired fins and the hypurals are impossible to assess

because of the high density of the surrounding tissues. The ribs are visible as thin strips of very low density.

Control specimen. Specimen D was stained and XCT scanned after 14 days. The staining protocol was very effective, without any overstaining. The amount of detail visible in the tomograms is superior to that of all previous specimens of this investigation (Fig. 4.5B1-B3). Still, segmentation is refined by hand due to insufficient density contrast in some areas of the body cavity and along the vertebral column. The highest density areas are generally in agreement with the other specimens but are generally less dense, and the high-density strip on the flanks is only visible on the posterior half of the upwards facing side.

Soft tissues. The eye appears similar to all other stained specimens, with a high-density halo at the base and the lens in the middle. In the brain, the optic tectum and the cerebellum are visible, while the telencephalon is not as nitid. Gill filaments are very nitid and both the soft and mineralised structures are visible, sometimes allowing visualisation of individual filaments. This is also the only specimen in which the ventricle and atrium of the heart are both visible. Liver and pancreas are visible but appear smaller than in previous specimens. Fluid appears to have invaded the swim bladders, with only a small gas bubble remaining, but without causing damage to the membrane of the bladders. The intestine is visible in its entirety with such detail that the structure of the intestinal epithelium is partially visible within the intestine bulb. The ovaries are visible in full,

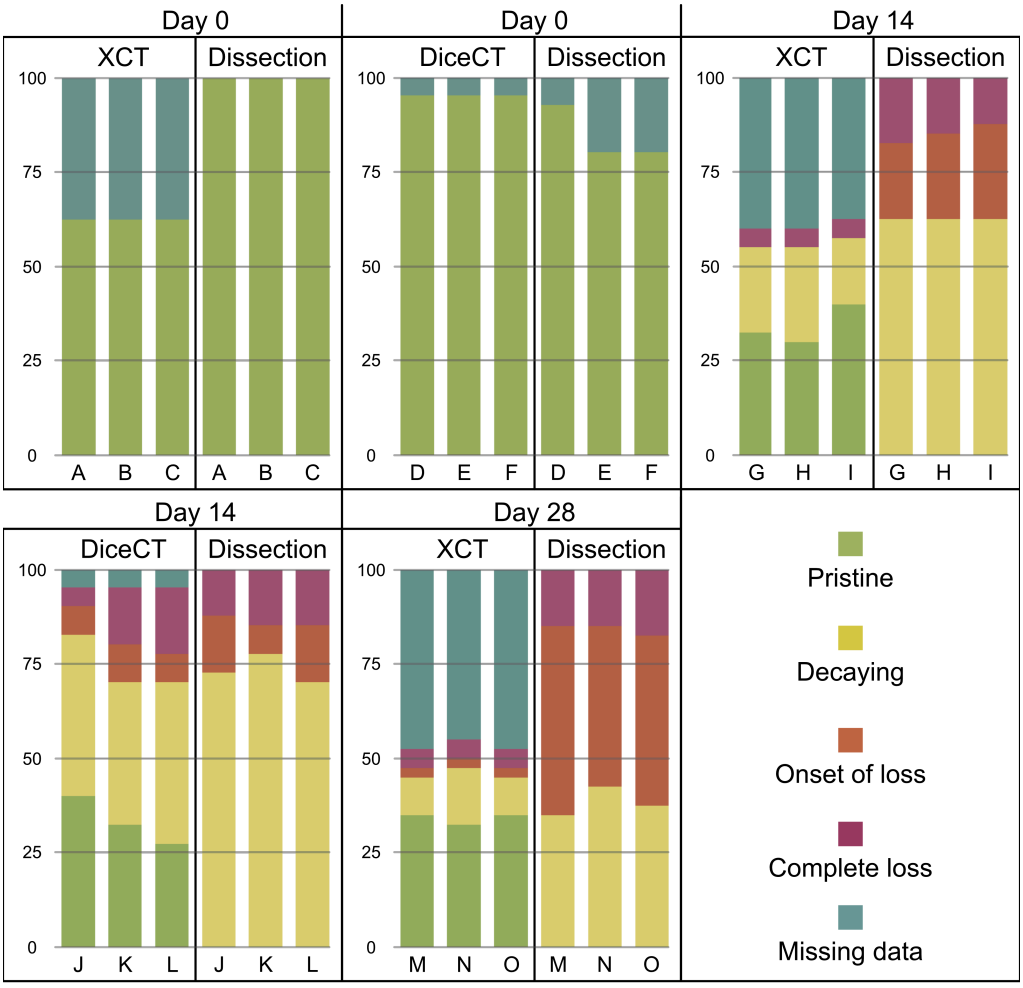


Fig. 4.6: Bar graphs comparing the 4-states character coding for the specimens in the W-diceCT experiment through different assessment methods.

extending from the anterior margin of the anterior swim bladder to the posterior margin of the coelom, and the oocytes are individually visible throughout. Only the bilobed head of the kidney is visible, for lack of density contrast in the tail portion. The structure of cephalic and pectoral fin muscles are visible with high fidelity - including bands of muscular fibres, as well as the myomeres of the axial musculature.

Mineralised tissues. Good density contrast makes most bones identifiable, including the skull, the radials of the unpaired fins and the

hypurals of the caudal fin. The ribs have very low density, while the density contrast of vertebral centra improves in the posterior half of the body.

4.3.3 Accuracy of diceCT in decay experiments

Completeness of decay assessment. For specimens that were XCT scanned without staining, then dissected (A, B, C, G, H, I, M, N, O), dissections were the most complete assessment method, with 100% of the characters identifiable (Fig. 4.5). Through tomograms the skeleton is visible in its entirety, but 37-47% of morphological characters (internal organs, musculature) are impossible to assess. As noted by Cavicchini et al (in review; see Chapter 3), a combined approach yields the highest number of morphological characters.

In contrast, for specimens that were stained, XCT scanned and then dissected (D, E, F, J, K, L), the tomograms were the most complete assessment method, with just 2.5-5% of morphological characters impossible to assess (pigmentation, caudal fin endoskeleton). During dissections, the identification of some characters was hindered by the presence of iodine, with 8-17% unidentifiable characters for specimens D, E, F, and 10% for J, K, and L (Fig. 4.5).

Amount of decay. The total scores were calculated twice for each specimen: once considering the scores from tomograms, once considering the scores from dissections (Appendix C1).

Day 0 unstained specimens (A-C) have a score of 0 through the tomograms and through dissections, but in the first case a significant amount of soft tissue characters (15 out of 40) are missing from the totals.

Day 0 stained specimens (D-F) have a score of 0 as well, but only one character (pigmentation) is missing from the tomograms, and a modest number (3-8) are missing from the dissections, due to the presence of iodine.

Day 14 unstained specimens (G-I) have scores of 5.5-7 through the tomograms, with 15-16 characters missing. For the dissections, the scores are 22.5-23.5 with no missing characters.

Day 14 stained specimens (J-L) have scores of 14-18 (1-2 missing characters) from the tomograms and scores of 20.5-21 (4 missing characters) through dissections. The missing characters in the latter case are those regarding the musculature and were made impossible to assess because of the iodine artificially increasing the stiffness of the tissue.

Day 28 unstained specimens (M-O) have scores of 4.5-5.5 through the tomograms, with 18-19 missing characters. Through dissections the scores are between 23 and 23.5, with no missing data.

Sequence of anatomical character loss. The sequence resulting from the dissection of day 14 stained specimens (J-L) was compared to the dissections of day 14 unstained specimens (G-I), to test for potential differences induced by the presence of iodine (Appendix C1). For this comparison we excluded 4 characters that were impossible to assess in stained specimens (cephalic muscles, pectoral fin muscles, anterior

myomeres, posterior myomeres). The two sequences compared in this way are not statistically different ($p < 0.000001$).

We then considered the sequence derived from tomograms of day 14 stained specimens (J-L), and compared it to the sequences resulting from the dissections of the same specimens and of day 14 unstained specimens (G-I), to test the reliability of decay assessment through diceCT imaging: the sequences are not statistically different ($p = 0.002$ and $p = 0.0002$, respectively). However, caution is needed when interpreting these results due the small sample size.

4.4 Discussion

4.4.1. Assessment of using diceCT in decay experiments.

4.4.1.1 Our data show that using iodine-based staining agents halts decay

To use staining techniques with precision in a decay experiment, care must be taken when considering the temporal implication of sampling. Decay is a continuum, and typically decay experiments record the amount of decay at specific time intervals allowing temporal patterns of decay to be discerned (e.g. Briggs and Kear, 1993; Clements et al., 2022). However, it was previously unclear if the time between the addition of the staining solution and the data collection (through XCT scanning or other methods) was additional decay time, or if the staining solution halts decay at the start of the staining time. Our data shows that, at the resolution of our tomograms, there is no notable difference between the internal morphology of a pristine control zebrafish and our day 0 specimens

(Menke et al., 2011; Cavicchini et al., *in review*; see Chapter 3). This includes organs like the swim bladders, which typically show signs of decay rapidly – as early as one day after death (Cavicchini et al., *in review*; see Chapter 3). This is also true of the day 14 stained and unstained specimens: they do not differ significantly in amount of decay for soft tissues (Fig. 4.4), nor in sequence of anatomical character loss, as confirmed by Spearman's Rank analyses (Appendix C1).

This data indicates that the introduction of iodine into the vessels with the specimens likely halts the decay process. Therefore, any specimen stained with Lugol's solution in an aqueous medium should be considered only as a temporal sampling point from the start of the staining process. This is not surprising, given the known antibacterial and antiseptic properties of iodine (Selvaggi et al. 2003; Vasudevan and Tandon 2010), which can kill bacterial cells in in as little as 20-30 seconds (Yasuda, et al. 1997; Bigliardi, et al. 2017). However, the disruption caused to the decay process by the introduction of iodine means that it is not possible to examine the same specimen twice, barring any longitudinal studies of decay and potentially introducing point errors (e.g. Cavicchini et al., *in review*, see Chapter 3). In addition, our experiment only utilised iodine and it should be noted that not all staining agents may have the same effect on decay. The usage of a different chemical in a decay experiment would require careful calibration.

4.4.1.2 DiceCT can be used to visually assess the decay state of zebrafish anatomical characters

The use of diceCT in decay experiments is in its infancy, and our investigation is the first time (to our knowledge) that diceCT has been used to image the internal anatomy of a decaying vertebrate carcass. Furthermore, this investigation represents the first test of the accuracy and reliability of diceCT during a decay experiment, to establish a foundation for future experimentation.

Our data show that, when using the same anatomical character list as a traditional dissection experiment to assess the amount of decay, diceCT tomograms are comparable in terms of precision and completeness (Fig. 4.4, 4.6), although there is a caveat: some characters are impossible to see through XCT scanning due to the nature of the technology involved (e.g., pigmentation). DiceCT tomograms allow a complete decay assessment for both day 0 and day 14 stained specimens (Appendix C1), so that pristine and decayed specimens can be easily compared, both visually and in terms of amount of decay (Fig. 4.2; Appendix C1). Organs lost in the day 14 specimens correlate with the control experiments of previous decay investigations using zebrafish (Cavicchini et al., *in review*; see Chapter 3). The accuracy of data obtained through diceCT scanning is further corroborated by the results of the Spearman's Rank (Appendix C1). The lack of significant differences in the sequence of anatomical character loss between specimens of the same age indicates that subjecting specimens to diceCT protocols does not impact the decay process, when compared to a stain- and CT scan-free

control. DiceCT tomograms are therefore a viable method to collect anatomical decay data.

4.4.1.3 DiceCT can assess decay at higher resolution than dissections

DiceCT scanning unlocks a completely new way to conduct decay experiments by collecting high resolution decay data in 3D without disturbing the carcasses. Our data show that it is possible for anatomical structures to be detected and analysed by looking at the diceCT tomograms; this technique does not disturb the carcass, and therefore is less likely to induce disarticulation or damage to the carcass, which can occur during dissections. For example, the heart and gill filaments of day 14 stained specimens (J-L), which were assessed as only partially decayed or even pristine from the tomograms (Fig. 4.3), while the dissections assessed these organs as unidentifiable (heart) or visibly decayed and gelatinous (gill filaments). This difference demonstrates that dissection can disturb and potentially damage delicate structures such as the heart and gill filaments, artificially increasing their decay state. In addition, diceCT scanning at high resolution can allow the visualisation of minute morphological structures impossible to observe through dissections (e.g., visualisation of the nervous system or the brain in non-decayed biological samples; Gignac et al., 2018; Camilieri-Asch et al., 2020). Even with a limitation on the maximum resolution of the XCT images imposed by our decision to image the entire carcass, the diceCT tomograms allowed the 3D visualisation of delicate structures that are not normally seen in

traditional dissections, such as the different areas of the zebrafish brain (e.g. optic tectum, telencephalon, cerebellum), the spinal cord, or each individual gill filament. This allows higher resolution mapping of the decay of anatomical characters and is a strong benefit of the use of diceCT in decay experiments.

Finally, numerous high-density, diminutive and irregular disarticulated organic fragments were observed in the body cavity of day 14 stained specimens (J-L) (Fig. 4.3D1-F2). These fragments are not ascribable to any particular internal organ, and they probably represent remnants of the organs that are no longer identifiable (e.g. swim bladders, gonads, liver). Identification of these fragments could be resolved by diceCT scanning at high temporal resolution. This is a good example of how decay data collection could be revolutionised by diceCT scanning, rather than recording presence/absence data by dissection.

4.4.1.4 Assessing the shortcomings of diceCT visualisation in decay experiments

Despite its promise, we identified shortcomings using diceCT scanning for decay experiments, which can cause inaccuracies in the decay assessment of carcasses. For example, occasionally structures that are entirely embedded in a separate tissue can be impossible to visualise in tomograms, making the decay assessment of these characters unreliable, especially if the surrounding tissues are relatively dense from excessive iodine intake. In our experiments, this happened occasionally to the hypurals and the radials of the unpaired fins (specimens K and L from

the W-diceCT experiment; specimen C from the S-diceCT experiment), while the intermuscular bones, typical of Teleostei such as the zebrafish, were not detected at all (Fiedler et al. 2019). Further methodological investigation is required to determine the optimal amount of staining agent and the length of the staining time required to fully visualise the anatomy of the chosen taxon.

More generalised problems encountered when using diceCT are (1) discrepancies in the perceived amount of decay of the skeleton, (2) the build-up of gaseous products of decomposition, and (3) the presence of high density adipose deposits.

(1) It is known from a previous investigation on the decay of zebrafish that, in the first phases of decay, the skeleton can appear translucent, with diminished resistance to disarticulation (Cavicchini et al., *in review*; see Chapter 3). Dissections of all day 14 specimens in this investigation also showed this trait. However, the decay of the skeleton could not be visualised in the diceCT tomograms. DiceCT decay assessment cannot visualise the loss of robustness via the variation in density of mineralised tissues, if it is not accompanied by distinct morphological change or disarticulation.

(2) The buildup of decomposition gases may hinder penetration of staining agents. In specimens K and L, the intestine and kidney were not recognisable in the diceCT tomograms. This was surprising, as dissections of these specimens revealed that both the kidney and the intestine were in fact present, albeit the latter was flattened and partially ruptured. We

cannot fully ascertain while these organs were not visible, but we hypothesise that the build-up of decomposition gases in the body cavity, which was particularly evident in specimens K and L (Fig. 4.3E1-F2), could have hindered the penetration of the staining agent.

(3) The highest density areas of the carcasses are not associated with any organs. These areas closely correspond to lipid deposits are located in zebrafish ((Minchin and Rawls 2017). Iodine seems to preferentially bind to lipids, and this can cause issues when interpreting the tomograms, especially because lipids seem to persist during decay; adipose deposits generally persist for over 14 days in zebrafish. This is unsurprising, the hydrolysis of lipids can last for a long time during decay (Dyer and Fraser 1959; Janssen et al. 2022).

We would note that these caveats do not invalidate the use of diceCT in decay experiments, but rather underline that the technique requires further refinement, and highlights that robust control experimentation is required to be able to identify potential methodological issues. We suggest that future work should increase the number of replicates and/or the number of specimens per replicate, in order to improve our understanding of variance in decay rates and limitations of diceCT.

4.4.1.5 DiceCT visualisation of internal anatomy of stained carcasses in situ under sediment is currently not possible.

In the sediment-based diceCT experiment (S-diceCT), the system of irrigation tubes was successful in staining a carcass *in situ* (Fig. 4.5). However, the decay assessment of specimen C is the least complete of all

the specimens in this investigation. The deviation is caused by an excessive iodine intake, localised mostly in the musculature, masking the endoskeleton of the unpaired fins. The issue is probably caused by the surrounding sediment, acting to trap the staining agent around the carcass and creating a microenvironment super-saturated in iodine. Future investigations seeking to stain carcasses *in situ* under sediment should account for this effect, by using lower concentrations of staining agents and/or shorter staining times.

Overstaining is not the only obstacle to diceCT scanning *in situ*: in fact, despite the successful staining procedure, due to the high radiodensity of quartz sand it was not possible to obtain tomograms of the internal anatomy of specimen C from the S-diceCT without exhuming the carcass (Supp. Mat. maybe). It is known that, in presence of a dense medium, higher energy (kV) and a higher degree of filtration are needed to ensure X-ray penetration during XCT scanning, at the cost of reducing the image quality (Zwanenburg, et al. 2022). We, therefore, believe that, at present, tomography setups available for commercial use seem incapable of imaging the internal anatomy of a carcass *in situ* when buried in dense sediment (e.g. quartz sand), even when the density of soft tissues is increased by a staining agent. We cannot, however, rule out the possibility of conducting a diceCT decay experiment entirely *in situ* in different conditions. We suggest that future work could try to improve the resolution of *in situ* scans by using more powerful machines (e.g., synchrotrons), and by focussing on different experimental setups (e.g. less dense sediment,

smaller vessels for specimens) that were not included in this investigation for time and budget related constrains.

_

4.4.2. The logistical cost of diceCT in decay experiments.

While the use of DiceCT in decay experiments is in its infancy, this paper demonstrates that the internal anatomy of carcasses can be imaged during decay – opening exciting new possibilities for decay experiments. However, there are serious logistical and financial aspects of diceCT decay experiments that should be considered before implementation. Robust hyposthesis-driven decay experiments are already expensive, but can be conducted with consumables and equipment (e.g. microscopes, maturation chambers, pH meters) that are readily found in taphonomy laboratories. With the introduction of diceCT, XCT scanning inevitably becomes a major, and often prohibitive, cost for a decay experiment. The expenses are exacerbated by the need for specialist training, facilities, and additional consumables (e.g. staining agent, PPE) required for handling the toxic staining agents. It is also worth noting that conducting experiments this way is more time-consuming, because of the time required to complete the CT scanning and all the data processing (e.g. reconstruction of the volume in 3D, segmentation of the various anatomical structures, creation of 3D models). In addition, all the post-processing requires computational power, access to softwares that can perform the required operations (valid open-access options exist, but any

licensed option would increase the costs) and enough data storage to keep the files, which can reach up to 100 GB per scan or more. When considering the benefits of diceCT scanning for future decay experiments, we believe that the higher costs can be justified in certain scenarios, e.g. in samples that cannot be dissected, to visualize the internal anatomy without the need for dissection, or where precise anatomical data collection is paramount.

4.4.3. Experiments demonstrate that decay in a restricted space is a proxy for sediment

Cavicchini *et al.* (*in review*; see Chapter 3) undertook high resolution decay experiments of zebrafish that are directly comparable with the present study, allowing for comparative investigations, not only of the decaying anatomy, but also the of the impact of the 'decay environment'.

When compared to a specimen that has decayed for 14 days from Cavicchini *et al*. (*in review*; see Chapter 3), day 14 stained specimens (J-L) of the W-diceCT experiment have similar amounts of anatomical character loss, while day 14 unstained specimens (G-I) have a higher amount of anatomical character loss (Fig. 4.6). If we interrogate the data and look at the difference between mineralised and soft tissue characters, the skeleton of specimens G-I has an abnormally high amount of decay, while the amount for soft tissues is comparable across all specimens and investigations (Fig. 4.6). An explanation for this discrepancy may lie in the differences between the experimental setup of this investigation and that

of Cavicchini *et al.* (*in review*; see Chapter 3). The volume of the maturation vessels was the major difference in experimental design: 50 mL screw-top falcon tubes in this study versus the 200 mL plastic jars used in Cavicchini *et al.* (*in review*; see Chapter 3). It is known that restricted circulation can trap the byproducts of decay around a carcass, allowing steep geochemical gradients to form, and creating a 'microenvironment' that accelerates the onset of decay and is hypothesised to trigger mineralisation in amenable environmental conditions (e.g. Sagemann et al., 1999; Clements et al. 2017; 2022; Cavicchini et al., *in review*; see Chapter 3). Our data confirm that decomposition of a carcass in a restricted space, even without sediment, does directly impact decay: (1) decay onsets more rapidly, and (2) while soft tissues decay at a constant rate regardless of surrounding environment, biomineralised tissues appear to decay at an accelerated rate. Although further testing is required, this could explain why, unless stabilised by diagenetic processes, biomineralised remains (e.g. skeletons) are not always present in strata. As our data indicate that zebrafish decayed in restricted vials show more similar levels of anatomical character loss to zebrafish decayed in sediment that to zebrafish decayed in water alone. This suggests that restricting the space around carcasses could act as a physical (but not geochemical) proxy for sediment in decay experiments.

4.5 Conclusion

Our data represents the first time the decaying internal anatomy of a vertebrate is imaged through diceCT scanning, obtaining a high fidelity “photograph” of the internal anatomy of a decaying zebrafish. This technique unlocks new types of experimental investigation because diceCT allows the decay-related internal morphological changes to be visualized without the need for bias inducing dissection. DiceCT holds the potential to revolutionize decay experiments: the scans of the decaying carcasses are fully 3D, allowing an unprecedented level of detail and accuracy of the morphological changes of individual organs and tissues while *in situ.* Therefore, diceCT allows the direct observation of particular decaying tissues through time without compromising the carcass. As stated here, however, diceCT is an expensive and labour-intensive technique, that requires staining of the carcass which is methodologically difficult (especially if sediment is involved)., however, we believe that these limitations can be overcome with further investigation.

5 | Summary and future directions

5.1 Summary

In this thesis I present various examples of how the novel application of techniques can generate data or open the way to entirely new methodologies, in the hope that the gaps in our knowledge can be filled. In this perspective, the main technique I present is micro computed tomography (XCT scanning), both in descriptive palaeontology and in taphonomic decay experiments, the latter being a field that is just starting to adopt XCT scanning.

In chapter 2 I corroborate how collection specimens, despite being well-known, at times for more than 50 years, can provide new data if re-examined through a different lens (e.g. Sallan and Coates 2013; Coates and Tietjen 2018; Giles, et al. 2023). It is the case for the holotype of *Pteronisculus gunnari*, from the Early Triassic of Greenland, which was discovered and described in the 1940's (Nielsen 1942). Its exquisite 3D preservation allows me to redescribe it using computed tomography, adding a wealth of detail about the endochondral ossification (e.g. braincase, gill arches, pectoral girdle) to the species diagnosis. In addition, the specimen is a juvenile and the ossification patterns confirm a Palaeozoic affinity for the taxon.

I am able to confirm that most species of *Pteronisculus* are indeed part of the same genus, although the intrageneric diversity is higher than previously thought. The new data included in a phylogenetic analysis resolves *Pteronisculus* nested within a Carboniferous radiation of actinopterygians, rather than as a generalised stem actinopterygian (e.g. Xu and Gao 2011; López-Arbarello and Sferco 2018; Ren and Xu 2021), although the resulting tree still has widespread instability.

My results thus add to the picture of the Early Triassic Fish Fauna, composed by a mosaic of 'palaeopterygians' of Carboniferous descent, but with unresolved ghost lineages (e.g. *Pteronisculus*), taxa that belong to long-lived lineages (e.g. *Saurichthys*, *Bobasatrania*), and some of the first stem neopterygians (e.g. *Watsonulus*) (Brinkmann, et al. 2010; Tintori, et al. 2014a; Romano 2021).

Chapters 3 and 4 represent a suite of experiments designed to test the feasibility of X-ray based imaging techniques in the data collection phase of decay experiments. In chapter 3 I constrain for the first time the decay sequence in zebrafish, and test the effect of X-ray exposure on the decay process of zebrafish carcasses, something that was never done before despite tomography having been employed in decay experiments (Selly and Schiffbauer 2021; Waskom, et al. 2023). The sequence of anatomical character loss, a key species-specific parameter (e.g. Sansom, et al. 2010), is unaffected by exposure to X-rays, making tomography a viable and reliable imaging technique in decay experiments. I illustrate how a non-invasive imaging technique has multiple advantages over

dissections, such as collecting data *in situ*, thus avoiding the biases induced by exhuming and dissecting a carcass, while being able to visualise useful parameters like carcass position and volume change over time.

In addition, through the results of my control experiments, I constrain the decay sequence in zebrafish, something that was never done before. Tomography, however, cannot resolve the internal anatomy of a carcass because soft tissues normally lack enough radiodensity (Metscher 2009a). To try to circumvent this limitation, in chapter 4 I test the use of staining protocols and tomography (diceCT scanning) in the context of a decay experiment. The use of iodine (Lugol's solution) does enhance the radiodensity of soft tissues enough for them to be visualised in tomograms (Metscher 2009a; Pauwels, et al. 2013; Gignac, et al. 2016), and my results show that this is applicable to fresh and decayed tissues. The results of a decay assessment through diceCT tomograms are comparable to those obtained with the traditional dissection method in control specimens, proving that diceCT scanning is viable for an entire decay experiment. Non-destructive imaging exceeds the resolution of a traditional dissection, and has the added advantage of obtaining images and 3D models of the decaying anatomy as it appears *in situ*, rather than assessing the state of a carcass after exhumation and dissection. However, the costs of a diceCT decay experiment are higher than a regular decay experiment and at present, with commercially available

tomography setups, it is possible to stain a carcass under sediment, but it is not possible to image said carcass *in situ*.

To summarise, the work and the findings I present in this thesis are a contribution to solve the many, still unresolved issues about the impact of the PTME on actinopterygians. The details I describe about the anatomy, ontogeny and phylogenetic position of *Pteronisculus* shed more light on one, interesting aspect of the Early Triassic Fish Fauna, showing that more taxa than previously thought come from quite long lineages. In addition, the exquisite preservation of the fossil led to a very detailed description that will hopefully serve as a comparison for future investigations on non-neopterygians.

The results of my experiments with decay and tomography represent the intention to find a precise and reliable way to conduct decay experiment with sediment that does not rely on exhumation, a necessity in order to discover more about preservation trends and biases in the fossil record. The non-invasiveness and increased precision of tomography, especially when paired with staining protocols, make it a useful visualisation aid to decay experiments, yielding interesting information previously not available to taphonomists.

5.2 Future directions

The results of this thesis represent demonstrations of methodologies as stepping stones for future investigations. Chapter 2 provides useful information on 'palaeopterygian' anatomy and ontogeny,

as well as a very detailed description of one taxon that was severely under-described, due to a lack of appropriate descriptive techniques at the time of its discovery. However, Nielsen (1942) perhaps foresaw the potential of the fossil NHMD–73588 in declaring it the holotype of the species, and the application of XCT scanning to the fossil, more than 60 years later, proved him right. This concept can be extended to hundreds, if not thousands of specimens that sit in collections worldwide, acknowledged but not described formally, or described only partially. A more systematic application of modern analytic techniques, such as XCT scanning, will yield more and more data.

Focusing on actinopterygians and the PTME, hopefully additional taxa in the future will receive a treatment similar to what is done with *Pteronisculus* in this work, in order to clarify their anatomy and phylogenetic relationships. Some already have, like *Saurichthys* (Argyriou, et al. 2018; Maxwell, et al. 2018), while a number of recent investigations have also deepened our knowledge of Late Permian and Early Triassic fish by describing new taxa, or previously unknown fossiliferous locations (e.g. Wang, et al. 2007; Hampe, et al. 2013; Romano, et al. 2016c; Romano, et al. 2017; Romano, et al. 2019; Ren and Xu 2021). Only by having a broader and more precise picture of actinopterygian faunas on either side of the PTME, will the effects of the extinction on the clade be clarified.

Concerning phylogenetic relationships, the results obtained are weakly supported and thus leave some open questions that tie into the

bigger picture of Palaeozoic and early Mesozoic actinopterygians. Answering these questions will require a massive increase in the number of known taxa, in the amount of detail known for each taxon, and in the quality of sampling of the fossil record (Friedman and Sallan 2012; Sallan 2014; Henderson, et al. 2022; Henderson, et al. 2023). Focussing on *Pteronisculus*, in the future additional data will be needed to confirm the exact nature of its ancestors (potentially Carboniferous and Permian, if the results of this work will be confirmed).

On the taphonomy side, chapters 3 and 4 ground-truth the use of tomography in sediment-based decay experiments, showing what kind of data can be obtained, advantages and disadvantages of the technique. The value of moving away from practices that induce bias in the data collected, like exhumation of carcasses from the sediment and dissections, cannot be overstated. In the future, efforts should be directed at the correction of problems that arose from unforeseen circumstances, like the build-up of gases inside the carcasses decreasing the accuracy of staining, and towards the creation of setups that allow to conduct experiments with carcasses entirely *in situ*. In addition, this work has put the foundations for the creation of decay atlases, in which the decay process is described by a continuum of images, respecting its nature as an active phenomenon.

Bibliography

ALDINGER, H. 1937. Permische ganoidfische aus Ostgrönland. Reitzels Forlag.

ALFARO, M. E., FAIRCLOTH, B. C., HARRINGTON, R. C., SORENSON, L., FRIEDMAN, M., THACKER, C. E., OLIVEROS, C. H., ČERNÝ, D. and NEAR, T. J. 2018. Explosive diversification of marine fishes at the Cretaceous–Palaeogene boundary. *Nature Ecology and Evolution*, **2**, 688-696.

ALGEO, T. J., KUWAHARA, K., SANO, H., BATES, S., LYONS, T., ELSWICK, E., HINNOV, L., ELLWOOD, B., MOSER, J. and MAYNARD, J. B. 2011. Spatial variation in sediment fluxes, redox conditions, and productivity in the Permian–Triassic Panthalassic Ocean. *Palaeogeography, Palaeoclimatology, Palaeoecology*, **308**, 65-83.

ALLEN, B. J., WIGNALL, P. B., HILL, D. J., SAUPE, E. E. and DUNHILL, A. M. 2020. The latitudinal diversity gradient of tetrapods across the Permo-Triassic mass extinction and recovery interval. *Proceedings of the Royal Society B*, **287**, 20201125.

ALLISON, P. A. 1988. The role of anoxia in the decay and mineralization of proteinaceous macro-fossils. *Paleobiology*, **14**, 139-154.

ANDERSON, K., WOODS, A. D., MIN, L. and YUAN, W. 2013. Taphonomy of Early Triassic fish fossils of the Vega-Phroso Siltstone Member of the

Sulphur Mountain Formation near Wapiti Lake, British Columbia, Canada. *Journal of Palaeogeography*, **2**, 321-343.

ARGYRIOU, T., GILES, S. and FRIEDMAN, M. 2022. A Permian fish reveals widespread distribution of neopterygian-like jaw suspension. *Elife*, **11**.

ARGYRIOU, T., GILES, S., FRIEDMAN, M., ROMANO, C., KOGAN, I. and SANCHEZ-VILLAGRA, M. R. 2018. Internal cranial anatomy of Early Triassic species of *Saurichthys* (Actinopterygii: Saurichthyiformes): implications for the phylogenetic placement of saurichthyiforms. *BMC Evolutionary Biology*, **18**, 161.

ARRATIA, G. 2013. Morphology, taxonomy, and phylogeny of Triassic pholidophorid fishes (Actinopterygii, Teleostei). *Journal of Vertebrate Paleontology*, **33**, 1-138.

ARRATIA, G. 2015. Complexities of early Teleostei and the evolution of particular morphological structures through time. *Copeia*, **103**, 999-1025.

ARRATIA, G. and CLOUTIER, R. 1996. Reassessment of the morphology of *Cheirolepis canadensis* (Actinopterygii). In Schultze, H.P. & Cloutier, R. (eds.) *Devonian fishes and plants of Miguasha, Quebec, Canada*, 165-197.

ARRATIA, G. and SCHULTZE, H. P. 1991. Palatoquadrate and its ossifications: development and homology within osteichthyans. *Journal of Morphology*, **208**, 1-81.

BARTSCH, P., GEMBALLA, S. and PIOTROWSKI, T. 1997. The embryonic and larval development of *Polypterus senegalus* Cuvier, 1829:

its staging with reference to external and skeletal features, behaviour and locomotory habits. *Acta Zoologica*, **78**, 309-328.

BATH ENRIGHT, O. G., MINTER, N. J. and SUMNER, E. J. 2017. Palaeoecological implications of the preservation potential of soft-bodied organisms in sediment-density flows: testing turbulent waters. *Royal Society Open Science*, **4**, 170212.

BATH ENRIGHT, O. G., MINTER, N. J., SUMNER, E. J., MÁNGANO, M. G. and BUATOIS, L. A. 2021. Flume experiments reveal flows in the Burgess Shale can sample and transport organisms across substantial distances. *Communications Earth & Environment*, **2**, 104.

BAUD, A., RICHOZ, S. and PRUSS, S. 2007. The Lower Triassic anachronistic carbonate facies in space and time. *Global and Planetary Change*, **55**, 81-89.

BEAUCHAMP, B. and BAUD, A. 2002. Growth and demise of Permian biogenic chert along northwest Pangaea: evidence for end-Permian collapse of thermohaline circulation. *Palaeogeography, Palaeoclimatology, Palaeoecology*, **184**, 37-63.

BECKER, L., POREDA, R., BASU, A., POPE, K., HARRISON, T., NICHOLSON, C. and IASKY, R. 2004. Bedout: a possible end-Permian impact crater offshore of northwestern Australia. *Science*, **304**, 1469-1476.

BECKER, L., POREDA, R. J., HUNT, A. G., BUNCH, T. E. and RAMPINO, M. 2001. Impact event at the Permian-Triassic boundary: Evidence from extraterrestrial noble gases in fullerenes. *Science*, **291**, 1530-1533.

BECKETT, H., GILES, S. and FRIEDMAN, M. 2018. Comparative anatomy of the gill skeleton of fossil Aulopiformes (Teleostei: Eurypterygii). *Journal of Systematic Palaeontology*, **16**, 1221-1245.

BEHRENSMEYER, A. K., KIDWELL, S. M. and GASTALDO, R. A. 2000. Taphonomy and paleobiology. *Paleobiology*, **26**, 103-147.

BELTAN, L. 1996. Overview of systematics, paleobiology, and paleoecology of Triassic fishes of northwestern Madagascar. In G. Arratia & G. Viohl (eds.) *Mesozoic Fishes− Systematics and Paleoecology*, Verlag Dr. Friedrich Pfeil, München, Germany 479-500.

BELTAN, L. and JANVIER, P. 1978. Un nouveau Saurichthyidae (Pisces, Actinopterygii), *Saurichthys nepalensis* n. sp., du Trias inférieur des Annapurnas (Thakkhola, Nepal) et sa signification Paléobiogéograhique. *Cybium*, **3**, 17-24.

BENBOW, M. E., BARTON, P. S., ULYSHEN, M. D., BEASLEY, J. C., DEVAULT, T. L., STRICKLAND, M. S., TOMBERLIN, J. K., JORDAN, H. R. and PECHAL, J. L. 2019. Necrobiome framework for bridging decomposition ecology of autotrophically and heterotrophically derived organic matter. *Ecological Monographs*, **89**, e01331.

BENDER, P. 2008. A review of the Early Triassic fish remains from Tasmania. *Kanunnah*, **3**, 27-40.

BENDER, P. A. and HANCOX, P. J. 2004. Newly discovered fish faunas from the Early Triassic, Karoo Basin, South Africa, and their correlative implications. *Gondwana Research*, **7**, 185-192.

BENSON, R. B. and BUTLER, R. J. 2011. Uncovering the diversification history of marine tetrapods: ecology influences the effect of geological sampling biases. *Geological Society, London, Special Publications*, **358**, 191-208.

BENTON, M. J., DONOGHUE, P. C., ASHER, R. J., FRIEDMAN, M., NEAR, T. J. and VINTHER, J. 2015. Constraints on the timescale of animal evolutionary history. *Palaeontologia Electronica,* **18**, 1-106

BENTON, M. J., TVERDOKHLEBOV, V. P. and SURKOV, M. 2004. Ecosystem remodelling among vertebrates at the Permian–Triassic boundary in Russia. *Nature*, **432**, 97-100.

BENTON, M. J., ZHANG, Q., HU, S., CHEN, Z.-Q., WEN, W., LIU, J., HUANG, J., ZHOU, C., XIE, T., TONG, J. and CHOO, B. 2013. Exceptional vertebrate biotas from the Triassic of China, and the expansion of marine ecosystems after the Permo-Triassic mass extinction. *Earth-Science Reviews*, **125**, 199-243.

BERRELL, R. W., BOISVERT, C., TRINAJSTIC, K., SIVERSSON, M., ALVARADO-ORTEGA, J., CAVIN, L., SALISBURY, S. W. and KEMP, A. 2020. A review of Australia's Mesozoic fishes. *Alcheringa: An Australasian Journal of Palaeontology*, **44**, 286-311.

BETANCUR-R, R., ORTÍ, G. and PYRON, R. A. 2015. Fossil-based comparative analyses reveal ancient marine ancestry erased by extinction in ray-finned fishes. *Ecology Letters*, **18**, 441-450.

BIGLIARDI, P. L., ALSAGOFF, S. A. L., EL-KAFRAWI, H. Y., PYON, J.-K., WA, C. T. C. and VILLA, M. A. 2017. Povidone iodine in wound healing: A

review of current concepts and practices. *International Journal of Surgery*, **44**, 260-268.

BJERAGER, M., SEIDLER, L., STEMMERIK, L. and SURLYK, F. 2006. Ammonoid stratigraphy and sedimentary evolution across the Permian–Triassic boundary in East Greenland. *Geological Magazine*, **143**, 635-656.

BJERRING, H. C. 1991. Two intracranial ligaments supporting the brain of the brachiopterygian fish *Polypterus senegalus*. *Acta Zoologica*, **72**, 41-47.

BLIECK, A. 2011. The André Dumont medallist lecture: From adaptive radiations to biotic crises in Palaeozoic vertebrates: a geobiological approach. *Geologica Belgica,* **14**, 203-227.

BOAST, J. and NAIRN, A. 1982. An outline of the geology of Madagascar. In *The ocean basins and margins: the Indian Ocean* (pp. 649-696). Boston, MA: Springer US.

BOND, D. P. and WIGNALL, P. B. 2010. Pyrite framboid study of marine Permian–Triassic boundary sections: a complex anoxic event and its relationship to contemporaneous mass extinction. *GSA Bulletin*, **122**, 1265-1279.

BRAND, U., POSENATO, R., CAME, R., AFFEK, H., ANGIOLINI, L., AZMY, K. and FARABEGOLI, E. 2012. The end-Permian mass extinction: A rapid volcanic CO^2 and CH^4-climatic catastrophe. *Chemical Geology*, **322**, 121-144.

BRAYARD, A., KRUMENACKER, L. J., BOTTING, J. P., JENKS, J. F., BYLUND, K. G., FARA, E., VENNIN, E., OLIVIER, N., GOUDEMAND, N., SAUCEDE, T., CHARBONNIER, S., ROMANO, C., DOGUZHAEVA, L.,

THUY, B., HAUTMANN, M., STEPHEN, D. A., THOMAZO, C. and ESCARGUEL, G. 2017. Unexpected Early Triassic marine ecosystem and the rise of the Modern evolutionary fauna. *Science Advances*, **3**, 1-11.

BRAYARD, A., VENNIN, E., OLIVIER, N., BYLUND, K. G., JENKS, J., STEPHEN, D. A., BUCHER, H., HOFMANN, R., GOUDEMAND, N. and ESCARGUEL, G. 2011. Transient metazoan reefs in the aftermath of the end-Permian mass extinction. *Nature Geoscience*, **4**, 693-697.

BRETT, C. E. and BAIRD, G. C. 1986. Comparative taphonomy: a key to paleoenvironmental interpretation based on fossil preservation. *Palaios*, 207-227.

BRIGGS, D. E. 1995. Experimental taphonomy. *Palaios*, 539-550.

BRIGGS, D. E. 2003. The role of decay and mineralization in the preservation of soft-bodied fossils. *Annual review of earth and planetary sciences*, **31**, 275-301.

BRIGGS, D. E. and KEAR, A. J. 1993a. Decay of *Branchiostoma*: implications for soft-tissue preservation in conodonts and other primitive chordates. *Lethaia*, **26**, 275-287.

BRIGGS, D. E. G. and KEAR, A. J. 1993b. Decay and preservation of polychaetes: taphonomic thresholds in soft-bodied organisms. *Paleobiology*, **19**, 107-135.

BRIGGS, D. E. and KEAR, A. J. 1994. Decay and mineralization of shrimps. *Palaios*, 431-456.

BRIGGS, D. E. and MCMAHON, S. 2016. The role of experiments in investigating the taphonomy of exceptional preservation. *Palaeontology*, **59**, 1-11.

BRINKMANN, W., ROMANO, C., BUCHER, D. and WARE, D. 2010. Palaeogeography and stratigraphy of advanced gnathostomian fishes (Chondrichthyes and Osteichthyes) in the Early Triassic and from selected Anisian localities (Report 1863 - 2009). *Zentralblatt für Geologie und Paläontologie II*, **2009**, 765-812.

BURGESS, S. D., BOWRING, S. and SHEN, S.-Z. 2014. High-precision timeline for Earth's most severe extinction. *Proceedings of the National Academy of Sciences*, **111**, 3316-3321.

BURROW, C. J., TURNER, S., NOWLAN, G. S. and DENISON, R. H. 2013. Vertebrate microremains from the Late Silurian of Arisaig, Nova Scotia, Canada. *Journal of Paleontology*, **87**, 1041-1059.

BUTLER, A. D., CUNNINGHAM, J. A., BUDD, G. E. and DONOGHUE, P. C. 2015. Experimental taphonomy of *Artemia* reveals the role of endogenous microbes in mediating decay and fossilization. *Proceedings of the Royal Society B: Biological Sciences*, **282**, 20150476.

BUTTERFIELD, N. J. 1990. Organic preservation of non-mineralizing organisms and the taphonomy of the Burgess Shale. *Paleobiology*, **16**, 272-286.

CALLAHAN, S., CROWE-RIDDELL, J. M., NAGESAN, R. S., GRAY, J. A. and DAVIS RABOSKY, A. R. 2021. A guide for optimal iodine staining and

high-throughput diceCT scanning in snakes. *Ecology and evolution*, **11**, 11587-11603.

CAMILIERI-ASCH, V., SHAW, J. A., MEHNERT, A., YOPAK, K. E., PARTRIDGE, J. C. and COLLIN, S. P. 2020. diceCT: A valuable technique to study the nervous system of fish. *eneuro*, **7**.

CAMPBELL, K. and PHUOC, L. D. 1983. A Late Permian actinopterygian fish from Australia. *Palaeontology*, **26**, 33-70.

CAO, C., LOVE, G. D., HAYS, L. E., WANG, W., SHEN, S. and SUMMONS, R. E. 2009. Biogeochemical evidence for euxinic oceans and ecological disturbance presaging the end-Permian mass extinction event. *Earth and Planetary Science Letters*, **281**, 188-201.

CARON, A., VENKATARAMAN, V., TIETJEN, K. and COATES, M. 2023. A fish for Phoebe: a new actinopterygian from the Upper Carboniferous Coal Measures of Saddleworth, Greater Manchester, UK, and a revision of *Kansasiella eatoni*. *Zoological Journal of the Linnean Society*, **198 (4)**, 957-981.

CAU, A., BEYRAND, V., VOETEN, D. F., FERNANDEZ, V., TAFFOREAU, P., STEIN, K., BARSBOLD, R., TSOGTBAATAR, K., CURRIE, P. J. and GODEFROIT, P. 2017. Synchrotron scanning reveals amphibious ecomorphology in a new clade of bird-like dinosaurs. *Nature*, **552**, 395-399.

CAVICCHINI, I., HEYWORTH, H. C., DUFFIN, C. J., HILDEBRANDT, C. and BENTON, M. J. 2018. A Rhaetian microvertebrate fauna from Stowey

Quarry, Somerset, UK. *Proceedings of the Geologists' Association*, **129**, 144-158.

CAVICCHINI, I., WILSON, P., GILES, S., ATTERBY, J., JONES, A., WILLIAMS, M. A. and CLEMENTS, T. 2024. Investigating the impact of X-rays on decay: X-ray computed tomography as a non-invasive visualisation technique for sediment-based decay experiments. *bioRxiv*, 2024.05. 13.593831.

CHELLOUCHE, P., FÜRSICH, F. T. and MÄUSER, M. 2012. Taphonomy of neopterygian fishes from the Upper Kimmeridgian Wattendorf Plattenkalk of Southern Germany. *Palaeobiodiversity and Palaeoenvironments*, **92**, 99-117.

CHEN, J., BEATTY, T. W., HENDERSON, C. M. and ROWE, H. 2009. Conodont biostratigraphy across the Permian–Triassic boundary at the Dawen section, Great Bank of Guizhou, Guizhou Province, South China: implications for the Late Permian extinction and correlation with Meishan. *Journal of Asian Earth Sciences*, **36**, 442-458.

CHEN, Z.-Q. and BENTON, M. J. 2012. The timing and pattern of biotic recovery following the end-Permian mass extinction. *Nature Geoscience*, **5**, 375-383.

CHEN, Z.-Q., YANG, H., LUO, M., BENTON, M. J., KAIHO, K., ZHAO, L., HUANG, Y., ZHANG, K., FANG, Y. and JIANG, H. 2015. Complete biotic and sedimentary records of the Permian–Triassic transition from Meishan section, South China: ecologically assessing mass extinction and its aftermath. *Earth-Science Reviews*, **149**, 67-107.

CLAPHAM, M. E., SHEN, S. and BOTTJER, D. J. 2009. The double mass extinction revisited: reassessing the severity, selectivity, and causes of the end-Guadalupian biotic crisis (Late Permian). *Paleobiology*, **35**, 32-50.

CLARKSON, M. O., WOOD, R. A., POULTON, S. W., RICHOZ, S., NEWTON, R. J., KASEMANN, S. A., BOWYER, F. and KRYSTYN, L. 2016. Dynamic anoxic ferruginous conditions during the end-Permian mass extinction and recovery. *Nature Communications*, **7**, 12236.

CLEMENT, A. M., KING, B., GILES, S., CHOO, B., AHLBERG, P. E., YOUNG, G. C. and LONG, J. A. 2018. Neurocranial anatomy of an enigmatic Early Devonian fish sheds light on early osteichthyan evolution. *Elife*, **7**, e34349.

CLEMENTS, T., COLLEARY, C., DE BAETS, K. and VINTHER, J. 2017. Buoyancy mechanisms limit preservation of coleoid cephalopod soft tissues in Mesozoic Lagerstätten. *Palaeontology*, **60**, 1-14.

CLEMENTS, T. and GABBOTT, S. 2021. Exceptional preservation of fossil soft tissues. *eLS*, **2**, 1-10.

CLEMENTS, T., GOODALL, R., GABBOTT, S., MURDOCK, D., CLOKIE, M., MILLARD, A., TURKINGTON, C., BATH-ENRIGHT, O. and PURNELL, M. A. 2024. The relationship between microbial community succession, decay, and anatomical character loss in non-biomineralised animals. *bioRxiv*, 2024.07. 01.601543.

CLEMENTS, T., PURNELL, M. and GABBOTT, S. 2019. The Mazon Creek Lagerstätte: a diverse late Paleozoic ecosystem entombed within siderite concretions. *Journal of the Geological Society*, **176**, 1-11.

CLEMENTS, T., PURNELL, M. A. and GABBOTT, S. 2022. Experimental analysis of organ decay and pH gradients within a carcass and the implications for phosphatization of soft tissues. *Palaeontology*, **65**, e12617.

CLOSE, R., BENSON, R. B., SAUPE, E., CLAPHAM, M. and BUTLER, R. 2020. The spatial structure of Phanerozoic marine animal diversity. *Science*, **368**, 420-424.

CLOUTIER, R. 2010. The fossil record of fish ontogenies: Insights into developmental patterns and processes. *Seminars in Cell Developmental Biology*. Elsevier, 400-413.

CLOUTIER, R. and ARRATIA, G. 2004. Early diversification of actinopterygians. *Recent advances in the origin and early radiation of vertebrates*, 217-270.

COATES, M. 1993. Actinopterygian and acanthodian fishes from the Viséan of East Kirkton, West Lothian, Scotland. *Earth and Environmental Science Transactions of the Royal Society of Edinburgh*, **84**, 317-327.

COATES, M. 1998. Actinopterygians from the Namurian of Bearsden, Scotland, with comments on early actinopterygian neurocrania. *Zoological Journal of the Linnean Society*, **122**, 27-59.

COATES, M. I. and TIETJEN, K. 2018. 'This strange little palaeoniscid': a new early actinopterygian genus, and commentary on pectoral fin conditions and function. *Earth and Environmental Science Transactions of the Royal Society of Edinburgh*, **109**, 15-31.

COX, C. B. and SMITH, D. G. 1973. A review of the Triassic vertebrate faunas of Svalbard. *Geological Magazine*, **110**, 405-418.

DAI, X., DAVIES, J. H., YUAN, Z., BRAYARD, A., OVTCHAROVA, M., XU, G., LIU, X., SMITH, C. P., SCHWEITZER, C. E. and LI, M. 2023. A Mesozoic fossil lagerstätte from 250.8 million years ago shows a modern-type marine ecosystem. *Science*, **379**, 567-572.

DARROCH, S. A. F., LAFLAMME, M., SCHIFFBAUER, J. D. and BRIGGS, D. E. G. 2012. Experimental formation of a microbial death mask. *Palaios*, **27**, 293-303.

DAWOOD, Y., HAGOORT, J., SIADARI, B. A., RUIJTER, J. M., GUNST, Q. D., LOBE, N. H. J., STRIJKERS, G. J., DE BAKKER, B. S. and VAN DEN HOFF, M. J. B. 2021. Reducing soft-tissue shrinkage artefacts caused by staining with Lugol's solution. *Scientific Reports*, **11**, 19781.

DESCAMPS, E., SOCHACKA, A., DE KEGEL, B., VAN LOO, D., VAN HOOREBEKE, L. and ADRIAENS, D. 2014. Soft tissue discrimination with contrast agents using micro-CT scanning. *Belgian Journal of Zoology*, **144**, 20-40.

DICKINS, J. M. and MCTAVISH, R. A. 1963. Lower Triassic marine fossils from the Beagle Ridge (BMR 10) Bore, Perth Basin, Western Australia. *Journal of the Geological Society of Australia*, **10**, 123-140.

DIEDRICH, C. G. 2009. A coelacanthid-rich site at Hasbergen (NW Germany): taphonomy and palaeoenvironment of a first systematic excavation in the Kupferschiefer (Upper Permian, Lopingian). *Palaeobiodiversity and Palaeoenvironments*, **89**, 67-94.

DINEEN, A. A., ROOPNARINE, P. D. and FRAISER, M. L. 2019. Ecological continuity and transformation after the Permo-Triassic mass extinction in northeastern Panthalassa. *Biology Letters*, **15**, 20180902.

DUNCAN, I. J., TITCHENER, F. and BRIGGS, D. E. 2003. Decay and disarticulation of the cockroach: implications for preservation of the blattoids of Writhlington (Upper Carboniferous), UK. *Palaios*, **18**, 256-265.

DYER, W. and FRASER, D. I. 1959. Proteins in fish muscle. 13. Lipid hydrolysis. *Journal of the Fisheries Board of Canada*, **16**, 43-52.

DZIEWA, T. J. 1980. Early Triassic osteichthyans from the Knocklofty Formation of Tasmania. *Papers and Proceedings of the Royal Society of Tasmania*, **114**, 145-160.

ELDER, R. L. and SMITH, G. R. 1988. Fish taphonomy and environmental inference in paleolimnology. *Palaeogeography, Palaeoclimatology, Palaeoecology*, **62**, 577-592.

ERWIN, D. H. 2003. Impact at the Permo-Triassic boundary: a critical evaluation. *Astrobiology*, **3**, 67-74.

ERWIN, D. H., BOWRING, S. A. and YUGAN, J. 2002. End-Permian mass extinctions: a review. *Special Papers-Geological Society of America*, 363-384.

EZCURRA, M. D. and BUTLER, R. J. 2018. The rise of the ruling reptiles and ecosystem recovery from the Permo-Triassic mass extinction. *Proceedings of the Royal Society B: Biological Sciences*, **285**.

FAIRCLOTH, B. C., SORENSON, L., SANTINI, F. and ALFARO, M. E. 2013. A Phylogenomic perspective on the radiation of ray-finned fishes

based upon targeted sequencing of ultraconserved elements (UCEs). *PLoS ONE*, **8**.

FAUX, C. M. and PADIAN, K. 2007. The opisthotonic posture of vertebrate skeletons: postmortem contraction or death throes? *Paleobiology*, **33**, 201-226.

FENG, Q. and ALGEO, T. J. 2014. Evolution of oceanic redox conditions during the Permo-Triassic transition: Evidence from deepwater radiolarian facies. *Earth-Science Reviews*, **137**, 34-51.

FERNÁNDEZ, F. J., MONTALVO, C. I., FERNÁNDEZ-JALVO, Y., ANDREWS, P. and LÓPEZ, J. M. 2017. A re-evaluation of the taphonomic methodology for the study of small mammal fossil assemblages of South America. *Quaternary Science Reviews*, **155**, 37-49.

FERNÁNDEZ-JALVO, Y., SCOTT, L. and ANDREWS, P. 2011. Taphonomy in palaeoecological interpretations. *Quaternary Science Reviews*, **30**, 1296-1302.

FIEDLER, I., ZEVELEVA, S., DUARTE, A., ZHAO, X., DEPALLE, B., CARDOSO, L., JIN, S. and BERTEAU, J. 2019. Microstructure, mineral and mechanical properties of teleost intermuscular bones. *Journal of biomechanics*, **94**, 59-66.

FIGUEROA, R. T., FRIEDMAN, M. and GALLO, V. 2019. Cranial anatomy of the predatory actinopterygian *Brazilichthys macrognathus* from the Permian (Cisuralian) Pedra de Fogo Formation, Parnaíba Basin, Brazil. *Journal of Vertebrate Paleontology*, **39**, e1639722.

FIGUEROA, R. T., GOODVIN, D., KOLMANN, M. A., COATES, M. I., CARON, A. M., FRIEDMAN, M. and GILES, S. 2023. Exceptional fossil preservation and evolution of the ray-finned fish brain. *Nature*, **614**, 486-491.

FISCHER, D., PAGENKEMPER, S., NELLESEN, J., PETH, S., HORN, R. and SCHLOTER, M. 2013. Influence of non-invasive X-ray computed tomography (XRCT) on the microbial community structure and function in soil. *Journal of Microbiological Methods*, **93**, 121-123.

FLANNERY SUTHERLAND, J. T., MOON, B. C., STUBBS, T. L. and BENTON, M. J. 2019. Does exceptional preservation distort our view of disparity in the fossil record? *Proceedings of the Royal Society B*, **286**, 20190091.

FOREL, M.-B., POULET-CROVISIER, N. and KORAT, L. 2021. Ostracods like ghosts in their shells: input of X-ray computed tomography for taxonomy and taphonomy of Early Triassic *Hollinella*. *Revue de Micropaléontologie*, **72**, 100528.

FRAISER, M. L. and BOTTJER, D. J. 2005. Restructuring in benthic level-bottom shallow marine communities due to prolonged environmental stress following the end-Permian mass extinction. *Comptes Rendus Palevol*, **4**, 583-591.

FRAISER, M. L., CLAPHAM, M. E. and BOTTJER, D. J. (2011). Mass Extinctions and Changing Taphonomic Processes. In: ALLISON, P.A. and BOTTJER, D.J. Allison, (eds) *Taphonomy. Aims & Scope Topics in Geobiology Book Series, vol 32*. Springer, Dordrecht.

FRAISER, M. L., TWITCHETT, R. J. and BOTTJER, D. J. 2005. Unique microgastropod biofacies in the Early Triassic: indicator of long-term biotic stress and the pattern of biotic recovery after the end-Permian mass extinction. *Comptes Rendus Palevol*, **4**, 543-552.

FRIEDMAN, M. 2015. The early evolution of ray-finned fishes. *Palaeontology*, **58**, 213-228.

FRIEDMAN, M. 2022. The macroevolutionary history of bony fishes: a paleontological view. *Annual Review of Ecology, Evolution, and Systematics*, **53**, 353-377.

FRIEDMAN, M., FIGUEROA, R.T., HODNETT, J.P.M., LUCAS, S.G., HIGGINS, R., PIERCE, S. and GILES, S., 2024. A new genus and species of large macrodont actinopterygian from the Pennsylvanian (Kasimovian/ Missourian) Atrasado Formation of New Mexico. *Contributions from the Museum of Palaeontology, University of Michigan,* **36**, 8-42.

FRIEDMAN, M. and GILES, S. 2016. Actinopterygians: the ray-finned fishes—an explosion of diversity. 17-49. *In* CLACK, J. A., FAY, R. R. and POPPER, A. N. (eds). *Evolution of the Vertebrate Ear : Evidence from the Fossil Record*. Springer International Publishing, Cham, pp. Custom 7.

FRIEDMAN, M., PIERCE, S. E., COATES, M. and GILES, S. 2018. Feeding structures in the ray-finned fish *Eurynotus crenatus* (Actinopterygii: Eurynotiformes): implications for trophic diversification among Carboniferous actinopterygians. *Earth and Environmental Science Transactions of the Royal Society of Edinburgh*, **109**, 33-47.

FRIEDMAN, M. and SALLAN, L. C. 2012. Five hundred million years of extinction and recovery: A Phanerozoic survey of large-scale diversity patterns in fishes. *Palaeontology*, **55**, 707-742.

GÄB, F., BALLHAUS, C., STINNESBECK, E., KRAL, A. G., JANSSEN, K. and BIERBAUM, G. 2020. Experimental taphonomy of fish - role of elevated pressure, salinity and pH. *Scientific Reports*, **10**, 1-10.

GABBOTT, S. E., SANSOM, R. S. and PURNELL, M. A. 2021. Systematic analysis of exceptionally preserved fossils: correlated patterns of decay and preservation. *Palaeontology*, **64**, 789-803.

GARDINER, B. G. 1963. Certain palaeoniscoid fishes and the evolution of the snout in actinopterygians. *Bulletin of the British Museum (Natural History), Geology Series*, **8**, 2 pls.

GARDINER, B. G. 1984. The relationships of the palaeoniscid fishes, a review based on new specimens of *Mimia* and *Moythomasia* from the Upper Devonian of Western Australia. *Bulletin of the British Museum (Natural History), Geology Series*, **37**, 173-428.

GARDINER, B. G. and JUBB, R. A. 1975. A new palaeoniscid from the Lower Beaufort Series of South Africa. Annals of the South African Museum, **67**, 441-445.

GARDINER, B. G. and SCHAEFFER, B. 1989. Interrelationships of lower actinopterygian fishes. *Zoological Journal of the Linnean Society*, **97**, 135-187.

GARDINER, B. G., SCHAEFFER, B. and MASSERIE, J. A. 2005. A review of the lower actinopterygian phylogeny. *Zoological Journal of the Linnean Society*, **144**, 511-525.

GIGNAC, P. M. and KLEY, N. J. 2018. The utility of diceCT imaging for high-throughput comparative neuroanatomical studies. *Brain Behavior and Evolution*, **91**, 180-190.

GIGNAC, P. M., KLEY, N. J., CLARKE, J. A., COLBERT, M. W., MORHARDT, A. C., CERIO, D., COST, I. N., COX, P. G., DAZA, J. D. and EARLY, C. M. 2016. Diffusible iodine-based contrast-enhanced computed tomography (diceCT): an emerging tool for rapid, high-resolution, 3-D imaging of metazoan soft tissues. *Journal of Anatomy*, **228**, 889-909.

GILES, S., COATES, M. I., GARWOOD, R. J., BRAZEAU, M. D., ATWOOD, R., JOHANSON, Z. and FRIEDMAN, M. 2015. Endoskeletal structure in *Cheirolepis* (Osteichthyes, Actinopterygii), An early ray-finned fish. *Palaeontology*, **58**, 849-870.

GILES, S., FEILICH, K., WARNOCK, R. C., PIERCE, S. E. and FRIEDMAN, M. 2023. A Late Devonian actinopterygian suggests high lineage survivorship across the end-Devonian mass extinction. *Nature Ecology & Evolution*, **7**, 10-19.

GILES, S., ROGERS, M. and FRIEDMAN, M. 2018. Bony labyrinth morphology in early neopterygian fishes (Actinopterygii: Neopterygii). *Journal of Morphology*, **279**, 426-440.

GILES, S., XU, G.-H., NEAR, T. J. and FRIEDMAN, M. 2017. Early members of ‘living fossil ’lineage imply later origin of modern ray-finned fishes. *Nature*, **549**, 265-268.

GOLOBOFF, P. A., FARRIS, J. S. and NIXON, K. C. 2008. TNT, a free program for phylogenetic analysis. *Cladistics*, **24**, 774-786.

GOLOBOFF, P. A. and MORALES, M. E. 2023. TNT version 1.6, with a graphical interface for MacOS and Linux, including new routines in parallel. *Cladistics*, **39**, 144-153.

GOLOBOFF, P. A., TORRES, A. and ARIAS, J. S. 2018. Weighted parsimony outperforms other methods of phylogenetic inference under models appropriate for morphology. *Cladistics*, **34**, 407-437.

GOUDEMAND, N., ROMANO, C., LEU, M., BUCHER, H., TROTTER, J. A. and WILLIAMS, I. S. 2019. Dynamic interplay between climate and marine biodiversity upheavals during the early Triassic Smithian-Spathian biotic crisis. *Earth-Science Reviews*, **195**, 169-178.

GRANDE, L. 2010. An empirical synthetic pattern study of gars (Lepisosteiformes) and closely related species, based mostly on skeletal anatomy. The resurrection of Holostei. *Ichthyology & Herpetology*, **10**, 1-871.

GRANDE, L. and BEMIS, W. E. 1991. Osteology and phylogenetic relationships of fossil and recent paddlefishes (Polyodontidae) with comments on the interrelationships of Acipenseriformes. *Journal of Vertebrate Paleontology*, **11**, 1-121.

GRANDE, L. and BEMIS, W. E. 1998. A comprehensive phylogenetic study of amiid fishes (Amiidae) based on comparative skeletal anatomy. An empirical search for interconnected patterns of natural history. *Journal of Vertebrate Paleontology*, **18**, 1-696.

GREENWOOD, D. R. and DONOVAN, S. 1991. The taphonomy of plant macrofossils. In DONOVAN, S.K. (ed) *The processes of Fossilization*, Columbia University Press, New York, 141-169.

GRØNSETH, T., OVCHINNIKOV, K. V., CARLSEN, H., BENTH, J. Š., DIEP, D. B., VON UNGE, M. and SILVOLA, J. T. 2023. Lugol's solution and Gentian violet eradicate methicillin-resistant *Staphylococcus aureus* biofilm in skin wound infections. *International Wound Journal*, **20**, 120-130.

GRØNSETH, T., VESTBY, L. K., NESSE, L. L., THOEN, E., HABIMANA, O., VON UNGE, M. and SILVOLA, J. T. 2017. Lugol's solution eradicates Staphylococcus aureus biofilm in vitro. *International Journal of Pediatric Otorhinolaryngology*, **103**, 58-64.

GROVES, J. R., ALTINER, D. and RETTORI, R. 2005. Extinction, survival, and recovery of lagenide foraminifers in the Permian–Triassic boundary interval, central Taurides, Turkey. *Journal of Paleontology*, **79**, 1-38.

GUPTA, A. 2009. Ichthyofauna of the Lower Triassic Panchet Formation, Damodar Valley basin, West Bengal, and its implications. *Indian Minerals*, **63**, 275-286.

HAIG, D. W., MARTIN, S. K., MORY, A. J., MCLOUGHLIN, S., BACKHOUSE, J., BERRELL, R. W., KEAR, B. P., HALL, R., FOSTER, C. B., SHI, G. R. and BEVAN, J. C. 2015. Early Triassic (early Olenekian) life

in the interior of East Gondwana: Mixed marine-terrestrial biota from the Kockatea Shale, Western Australia. *Palaeogeography, Palaeoclimatology, Palaeoecology*, **417**, 511-533.

HAMEL, M.-H. and POPLIN, C. 2008. The braincase anatomy of *Lawrenciella schaefferi*, actinopterygian from the Upper Carboniferous of Kansas (USA). *Journal of Vertebrate Paleontology*, **28**, 989-1006.

HAMPE, O., HAIRAPETIAN, V., DORKA, M., WITZMANN, F., AKBARI, A. M. and KORN, D. 2013. A first late Permian fish fauna from Baghuk Mountain (Neo-Tethyan shelf, central Iran). *Bulletin of Geosciences*, **88**, 1-20.

HARPER, C. and LAWRENCE, C. 2016. *The laboratory zebrafish*. Crc Press, Boca Raton.

HENDERSON, C. M. 1997. Uppermost Permian conodonts and the Permian-Triassic boundary in the western Canada sedimentary basin. *Bulletin of Canadian Petroleum Geology*, **45**, 693-707.

HENDERSON, S., DUNNE, E. M., FASEY, S. A. and GILES, S. 2023. The early diversification of ray-finned fishes (Actinopterygii): hypotheses, challenges and future prospects. *Biological Reviews*, **98**, 284-315.

HENDERSON, S., DUNNE, E. M. and GILES, S. 2022. Sampling biases obscure the early diversification of the largest living vertebrate group. *Proceedings of the Royal Society B*, **289**, 20220916.

HERAK, M., SCAVNICAR, B., SUSNJARA, A., DURDANIVIC, Z., KRYSTYN, L. and GRUBER, B. 1983. The Lower Triassic of Muc. Proposal for a standard section of the European upper Scythian. *Neue*

Beiträge zur Biostratigraphie der Tethys-Trias: Schriftenreihe Erdwissenschaftlichen Kommissionen, Osterreichische Akademie Wissenschaften, **5**, 93-106.

HILAL, M. G., YU, Q., ZHOU, R., WANG, Y., FENG, T., LI, X. and LI, H. 2021. Exploring microbial communities, assessment methodologies and applications of animal's carcass decomposition: a review. *FEMS Microbiology Ecology*, **97**, fiab098.

HILTON, E. J. and BEMIS, W. E. 1999. Skeletal variation in shortnose sturgeon (*Acipenser brevirostrum*) from the Connecticut River: implications for comparative osteological studies of fossil and living fishes. In Arratia G. & Schultze H.P. (eds.) *Mesozoic Fishes 2*, Verlag Dr. Friedrich Pfeil, München, Germany, 69-94.

HILTON, E. J., DILLMAN, C. B., PARASCHIV, M. and SUCIU, R. 2022. Cranial morphology of the Stellate Sturgeon, *Acipenser stellatus* Pallas 1771 (Acipenseriformes, Acipenseridae), with notes on the skulls of other sturgeons. *Acta Zoologica*, **103**, 57-77.

HILTON, E. J., GRANDE, L. and BEMIS, W. E. 2011. Skeletal anatomy of the shortnose sturgeon, *Acipenser brevirostrum* Lesueur, 1818, and the systematics of sturgeons (Acipenseriformes, Acipenseridae). *Fieldiana Life and Earth Sciences*, **2011**, 1-168.

HOCHULI, P. A., VIGRAN, J. O., HERMANN, E. and BUCHER, H. 2010. Multiple climatic changes around the Permian-Triassic boundary event revealed by an expanded palynological record from mid-Norway. *Bulletin*, **122**, 884-896.

HOME OFFICE, 2014. Guidance on the operation of the Animals (Scientific Procedures) Act 1986.

HOFMANN, R. 2016. The end-Permian mass extinction. The Trace-Fossil Record of Major Evolutionary Events: Volume 1: Precambrian and Paleozoic, **1**, 325-349.

HORACEK, M., POVODEN, E., RICHOZ, S. and BRANDNER, R. 2010. High-resolution carbon isotope changes, litho-and magnetostratigraphy across Permian-Triassic Boundary sections in the Dolomites, N-Italy. New constraints for global correlation. *Palaeogeography, Palaeoclimatology, Palaeoecology*, **290**, 58-64.

HUANG, C., TONG, J., HINNOV, L. and CHEN, Z. Q. 2011. Did the great dying of life take 700 ky? Evidence from global astronomical correlation of the Permian-Triassic boundary interval. *Geology*, **39**, 779-782.

HURLEY, I. A., MUELLER, R. L., DUNN, K. A., SCHMIDT, E. J., FRIEDMAN, M., HO, R. K., PRINCE, V. E., YANG, Z., THOMAS, M. G. and COATES, M. I. 2007. A new time-scale for ray-finned fish evolution. *Proceedings of the Royal Society B: Biological Sciences*, **274**, 489-498.

HUTCHINSON, P. 1973. A revision of the redfieldiiform and perleidiform fishes from the Triassic of Bekker's Kraal (South Africa) and Brookvale (New South Wales). *Bulletin of the British Museum (Natural History) Geology,* **22**, 233-254.

INIESTO, M., LAGUNA, C., FLORIN, M., GUERRERO, M. C., CHICOTE, A., BUSCALIONI, A. D. and LOPEZ-ARCHILLA, A. I. 2015. The impact of

microbial mats and their microenvironmental conditions in early decay of fish. *Palaios*, **30**, 792-801.

INIESTO, M., LOPEZ-ARCHILLA, A. I., FREGENAL-MARTÍNEZ, M., BUSCALIONI, A. D. and GUERRERO, M. C. 2013. Involvement of microbial mats in delayed decay: an experimental essay on fish preservation. *Palaios*, **28**, 56-66.

INIESTO, M., THOMAZO, C. and FARA, E. 2019. Deciphering the exceptional preservation of the Early Triassic Paris Biota (Bear Lake County, Idaho, USA). *Geobios*, **54**, 81-93.

IRMIS, R. B. and WHITESIDE, J. H. 2012. Delayed recovery of non-marine tetrapods after the end-Permian mass extinction tracks global carbon cycle. *Proceedings of the Royal Society B: Biological Sciences*, **279**, 1310-1318.

ISOZAKI, Y. 1997. Permo-Triassic boundary superanoxia and stratified superocean: records from lost deep sea. *Science*, **276**, 235-238.

ISOZAKI, Y. 2009. Integrated “plume winter” scenario for the double-phased extinction during the Paleozoic–Mesozoic transition: the G-LB and P-TB events from a Panthalassan perspective. *Journal of Asian Earth Sciences*, **36**, 459-480.

ISOZAKI, Y., SHIMIZU, N., YAO, J., JI, Z. and MATSUDA, T. 2007. End-Permian extinction and volcanism-induced environmental stress: the Permian–Triassic boundary interval of lower-slope facies at Chaotian, South China. *Palaeogeography, Palaeoclimatology, Palaeoecology*, **252**, 218-238.

IVANOV, A. and KLETS, T. 2007. Triassic marine fishes from Siberia, Russia. *The Global Triassic (Lucas, SG, Spielmann, JA, eds.) NMMNH Sci Bull*, **41**, 108-109.

JABLONSKI, D., ROY, K. and VALENTINE, J. W. 2006. Out of the tropics: evolutionary dynamics of the latitudinal diversity gradient. *Science*, **314**, 102-106.

JANSSEN, K., MÄHLER, B., RUST, J., BIERBAUM, G. and MCCOY, V. E. 2022. The complex role of microbial metabolic activity in fossilization. *Biological Reviews*, **97**, 449-465.

JESSEN, H. L. 1972. Schultergürtel und Pectoralflosse bei Actinopterygiern. *Schultergürtel und Pectoralflosse bei Actinopterygiern*, **1**, 1-101.

JIN, F. 2006. An overview of Triassic fishes from China. *Vertebrata PalAsiatica,* **44**, 28-42.

JIN, Y., WANG, Y., WANG, W., SHANG, Q., CAO, C. and ERWIN, D. H. 2000. Pattern of marine mass extinction near the Permian-Triassic boundary in South China. *Science*, **289**, 432-436.

JOHNSON, J. T., HANSEN, M. S., WU, I., HEALY, L. J., JOHNSON, C. R., JONES, G. M., CAPECCHI, M. R. and KELLER, C. 2006. Virtual histology of transgenic mouse embryos for high-throughput phenotyping. *PLoS Genetics*, **2**, e61.

JOHNSTON, R. M. and MORTON, A. 1889. Notes on the discovery of a ganoid fish in the Knocklofty Sandstones, Hobart. *Papers Proceedings of the Royal Society of Tasmania,* **1889**, 102-104.

JOHNSTON, R. M. and MORTON, A. 1890. Description of a second ganoid fish from the lower Mesozoic sandstones near Tinder-box Bay. *Papers and Proceedings of the Royal Society of Tasmania,* **1890**, 152-154.

JOLLIE, M. 1980. Development of head and pectoral girdle skeleton and scales in *Acipenser*. *Copeia*, **1980**, 226-249.

JOLLIE, M. 1984a. Development of cranial and pectoral girdle bones of *Lepisosteus* with a note on scales. *Copeia*, **1984**, 476-502.

JOLLIE, M. 1984b. Development of the head and pectoral skeleton of *Polypterus* with a note on scales (Pisces: Actinopterygii). *Journal of Zoology*, **204**, 469-507.

KAIHO, K., KAJIWARA, Y., NAKANO, T., MIURA, Y., KAWAHATA, H., TAZAKI, K., UESHIMA, M., CHEN, Z. and SHI, G. R. 2001. End-Permian catastrophe by a bolide impact: evidence of a gigantic release of sulfur from the mantle. *Geology*, **29**, 815-818.

KAIHO, K., OBA, M., FUKUDA, Y., ITO, K., ARIYOSHI, S., GORJAN, P., RIU, Y., TAKAHASHI, S., CHEN, Z.-Q., TONG, J. and YAMAKITA, S. 2012. Changes in depth-transect redox conditions spanning the end-Permian mass extinction and their impact on the marine extinction: Evidence from biomarkers and sulfur isotopes. *Global and Planetary Change*, **94-95**, 20-32.

KAKUWA, Y. 1996. Permian-Triassic mass extinction event recorded in bedded chert sequence in southwest Japan. *Palaeogeography, Palaeoclimatology, Palaeoecology*, **121**, 35-51.

KAUFFMAN, E. G. and HARRIES, P. J. 1996. The importance of crisis progenitors in recovery from mass extinction. *Geological Society, London, Special Publications*, **102**, 15-39.

KIDDER, D. L. and WORSLEY, T. R. 2004. Causes and consequences of extreme Permo-Triassic warming to globally equable climate and relation to the Permo-Triassic extinction and recovery. *Palaeogeography, Palaeoclimatology, Palaeoecology*, **203**, 207-237.

KING, B., HU, Y. and LONG, J. A. 2018. Electroreception in early vertebrates: survey, evidence and new information. *Palaeontology*, **61**, 325-358.

KING, W. 1850. A monograph of the Permian fossils of England. *Palaeontographical Society*, London.

KLEBANOFF, S. J. 1967. Iodination of bacteria: a bactericidal mechanism. *The Journal of Experimental Medicine*, **126**, 1063-1078.

KNOLL, A. H., BAMBACH, R. K., PAYNE, J. L., PRUSS, S. and FISCHER, W. W. 2007. Paleophysiology and end-Permian mass extinction. *Earth and Planetary Science Letters*, **256**, 295-313.

KOEBERL, C., FARLEY, K. A., PEUCKER-EHRENBRINK, B. and SEPHTON, M. A. 2004. Geochemistry of the end-Permian extinction event in Austria and Italy: no evidence for an extraterrestrial component. *Geology*, **32**, 1053-1056.

KOGAN, I. and ROMANO, C. 2016a. A new postcranium of Saurichthys from the Early Triassic of Spitsbergen. Freiberger Forschungshefte. Reihe C: Geowissenschaften, Palaeontologie, 205-222.

KOGAN, I. and ROMANO, C. 2016b. Redescription of *Saurichthys madagascariensis* Piveteau, 1945 (Actinopterygii, Early Triassic), with implications for the early saurichthyid morphotype. *Journal of Vertebrate Paleontology*, **36**.

KONSTANTINOV, K. M., BAZHENOV, M. L., FETISOVA, A. M. and KHUTORSKOY, M. D. 2014. Paleomagnetism of trap intrusions, East Siberia: Implications to flood basalt emplacement and the Permo–Triassic crisis of biosphere. *Earth and Planetary Science Letters*, **394**, 242-253.

KORTE, C., PANDE, P., KALIA, P., KOZUR, H. W., JOACHIMSKI, M. M. and OBERHÄNSLI, H. 2010. Massive volcanism at the Permian–Triassic boundary and its impact on the isotopic composition of the ocean and atmosphere. *Journal of Asian Earth Sciences*, **37**, 293-311.

KRULL, E. S. and RETALLACK, G. J. 2000. δ13C depth profiles from paleosols across the Permian-Triassic boundary: Evidence for methane release. *Geological Society of America Bulletin*, **112**, 1459-1472.

KRYSTYN, L., RICHOZ, S., BAUD, A. and TWITCHETT, R. J. 2003. A unique Permian–Triassic boundary section from the neotethyan Hawasina basin, Central Oman Mountains. *Palaeogeography, Palaeoclimatology, Palaeoecology*, **191**, 329-344.

LAMBE, L. M. 1914. Description of a new species of Platysomus from the neighbourhood of Banff, Alberta. Summary Report of the Geological Survey Department of Mines for the Calendar Year 1912, **1305**, 397-403.

LAMBE, L. M. 1916. Ganoid fishes from near Banff, Alberta. *Transactions of Royal Society of Canada, ser. 3, sect. 4*, **10**, 35-44.

LARSON, E. 1988. Guideline for use of topical antimicrobial agents. *American Journal of Infection Control*, **16**, 253-266.

LATIMER, A. E. and GILES, S. 2018. A giant dapediid from the Late Triassic of Switzerland and insights into neopterygian phylogeny. *Royal Society Open Science*, **5**, 180497.

LEHMAN, J.-P. 1952. Etude complémentaire des poissons de l'Eotrias de Madagascar. *Kungliga Svenska Vetenskaps-akademiens Hangdlingar*, **2**, 1-201.

LEHRMANN, D. J., RAMEZANI, J., BOWRING, S. A., MARTIN, M. W., MONTGOMERY, P., ENOS, P., PAYNE, J. L., ORCHARD, M. J., HONGMEI, W. and JIAYONG, W. 2006. Timing of recovery from the end-Permian extinction: Geochronologic and biostratigraphic constraints from south China. *Geology*, **34**, 1053-1056.

LI, M., SONG, H., WIGNALL, P. B., SHE, Z., DAI, X., SONG, H. and XIAO, Q. 2019. Early Triassic oceanic red beds coupled with deep sea oxidation in South Tethys. *Sedimentary Geology*, **391**, 105519.

LI, Q. 2009. A new parasemionotid-like fish from the Lower Triassic of Jurong, Jiangsu province, South China. *Palaeontology*, **52**, 369-384.

LIU, X. and WEI, F. 1988. A new saurichthyid from the Upper Permian of Zhejiang, China. *Vertebrata PalAsiatica*, **26**, 77-89.

LLOYD, G. T. and FRIEDMAN, M. 2013. A survey of palaeontological sampling biases in fishes based on the Phanerozoic record of Great Britain. *Palaeogeography, Palaeoclimatology, Palaeoecology*, **372**, 5-17.

LO, C.-H., CHUNG, S.-L., LEE, T.-Y. and WU, G. 2002. Age of the Emeishan flood magmatism and relations to Permian–Triassic boundary events. *Earth and Planetary Science Letters*, **198**, 449-458.

LONG, J. 1988. New palaeoniscoid fishes from the Late Devonian and Early Carboniferous of Victoria. *Memoirs of the Association of Australasian Palaeontology,* **7**, 1-64

LONG, J. A., CHOO, B. and YOUNG, G. C. 2008. A new basal actinopterygian fish from the Middle Devonian Aztec Siltstone of Antarctica. *Antarctic Science*, **20**, 393-412.

LOOY, C. V., TWITCHETT, R. J., DILCHER, D. L., VAN KONIJNENBURG-VAN CITTERT, J. H. and VISSCHER, H. 2001. Life in the end-Permian dead zone. *Proceedings of the National Academy of Sciences*, **98**, 7879-7883.

LÓPEZ-ARBARELLO, A. 2004. The record of Mesozoic fishes from Gondwana (excluding India and Madagascar). In Arratia G. & Schultze H.P. (eds.) *Mesozoic Fishes 3*, Verlag Dr. Friedrich Pfeil, München, Germany, 597-624.

LÓPEZ-ARBARELLO, A. and SFERCO, E. 2018. Neopterygian phylogeny: the merger assay. *Royal Society Open Science*, **5**, 172337.

LOWNEY, K. A. 1980a. Certain Bear Gulch (Namurian A, Montana) Actinopterygii (Osteichthyes) and a reevaluation of the evolution of the Paleozoic actinopterygians. Ph.D. dissertation, New York University.

LOWNEY, K. A. 1980b. A revision of the family Haplolepidae (Actinopterygii, Paleonisciformes) from Linton, Ohio (Westphalian D, Pennsylvanian). *Journal of Paleontology*, 942-953.

LUND, R. and POPLIN, C. 1997. The rhadinichthyids (paleoniscoid actinopterygians) from the Bear Gulch Limestone of Montana (USA, Lower Carboniferous). *Journal of Vertebrate Paleontology*, **17**, 466-486.

LUND, R., POPLIN, C. and MCCARTHY, K. 1995. Preliminary analysis of the interrelationships of some Paleozoic Actinopterygii. *Geobios*, **28**, 215-220.

LUPPO, T., DE LUCHI, M. G. L., RAPALINI, A. E., DOPICO, C. I. M. and FANNING, C. M. 2018. Geochronologic evidence of a large magmatic province in northern Patagonia encompassing the Permian-Triassic boundary. *Journal of South American Earth Sciences*, **82**, 346-355.

LYCKEGAARD, A., JOHNSON, G. and TAFFOREAU, P. 2011. Correction of ring artifacts in X-ray tomographic images. *International Journal of Tomography and Statistics*, **18**, 1-9.

MAHMOUD, B. S. 2012. Control of *Listeria* monocytogenes and spoilage bacteria on smoked salmon during storage at 5 C after X-ray irradiation. *Food Microbiology*, **32**, 317-320.

MAHMOUD, B. S., CHANG, S., WU, Y., NANNAPANENI, R., SHARMA, C. S. and COKER, R. 2015. Effect of X-ray treatments on *Salmonella enterica* and spoilage bacteria on skin-on chicken breast fillets and shell eggs. *Food Control*, **57**, 110-114.

MALENDA, H. F., SIMPSON, E. L., SZAJNA, M. J., FILLMORE, D. L., HARTLINE, B. W., HENESS, E. A., KRAAL, E. R. and WILK, J. L. 2012. Taphonomy of lacustrine shoreline fish-part conglomerates in the Late Triassic age Lockatong Formation (Collegeville, Pennsylvania, USA): Toward the recognition of catastrophic fish kills in the rock record. *Palaeogeography, Palaeoclimatology, Palaeoecology*, **313**, 234-245.

MANCUSO, A. C. 2003. Continental fish taphonomy: A case study in the Triassic of Argentina. *Journal of South American Earth Sciences*, **16**, 275-286.

MARTIN, D., BRIGGS, D. E. and PARKES, R. J. 2004. Experimental attachment of sediment particles to invertebrate eggs and the preservation of soft-bodied fossils. *Journal of the Geological Society*, **161**, 735-738.

MAXWELL, E. E., ARGYRIOU, T., STOCKAR, R. and FURRER, H. 2018. Re-evaluation of the ontogeny and reproductive biology of the Triassic fish *Saurichthys* (Actinopterygii, Saurichthyidae). *Palaeontology*, **61**, 559-574.

MCCOY, V. E. 2014. Concretions as agents of soft-tissue preservation: A review. *The Paleontological Society Papers*, **20**, 147-162.

MCCOY, V. E., YOUNG, R. T. and BRIGGS, D. E. 2015a. Factors controlling exceptional preservation in concretions. *Palaios*, **30**, 272-280.

MCCOY, V. E., YOUNG, R. T. and BRIGGS, D. E. 2015b. Sediment permeability and the preservation of soft-tissues in concretions: an experimental study. *Palaios*, **30**, 608-612.

MCGOWAN, A. J. and SMITH, A. B. 2008. Are global Phanerozoic marine diversity curves truly global? A study of the relationship between regional

rock records and global Phanerozoic marine diversity. *Paleobiology*, **34**, 80-103.

MCMAHON, S., ANDERSON, R. P., SAUPE, E. E. and BRIGGS, D. E. G. 2016. Experimental evidence that clay inhibits bacterial decomposers: Implications for preservation of organic fossils. *Geology*, **44**, 867-870.

MENKE, A. L., SPITSBERGEN, J. M., WOLTERBEEK, A. P. and WOUTERSEN, R. A. 2011. Normal anatomy and histology of the adult zebrafish. *Toxicologic Pathology*, **39**, 759-775.

METCALFE, I. and ISOZAKI, Y. 2009. Current perspectives on the Permian–Triassic boundary and end-Permian mass extinction: Preface. *Journal of Asian Earth Sciences*, **36**, 407-412.

METSCHER, B. D. 2009a. MicroCT for comparative morphology: simple staining methods allow high-contrast 3D imaging of diverse non-mineralized animal tissues. *BMC physiology*, **9**, 1-14.

METSCHER, B. D. 2009b. MicroCT for developmental biology: A versatile tool for high-contrast 3D imaging at histological resolutions. *Developmental Dynamics: an Official Publication of the American Association of Anatomists*, **238**, 632-640.

MICKLE, K. E. 2012. Unraveling the Systematics of Palaeoniscoid Fishes--Lower Actinopterygians in Need of a Complete Phylogenetic Revision. Ph.D. dissertation, University of Kansas.

MICKLE, K. E. 2015. Identification of the bones of the snout in fossil lower actinopterygians—a new nomenclature scheme based on characters. *Copeia*, **103**, 838-857.

MINCHIN, J. E. and RAWLS, J. F. 2017. A classification system for zebrafish adipose tissues. *Disease Models & Mechanisms*, **10**, 797-809.

MINIKH, M. G. and MINIKH, A. V. 1997. Ichthyofaunal correlation of the Triassic deposits from the northern Cis-Caspian and southern Cis-Urals regions. *Geodiversitas*, **19**, 279-292.

MIRONE, A., BRUN, E., GOUILLART, E., TAFFOREAU, P. and KIEFFER, J. 2014. The PyHST2 hybrid distributed code for high speed tomographic reconstruction with iterative reconstruction and a priori knowledge capabilities. *Nuclear Instruments and Methods in Physics Research Section B: Beam Interactions with Materials and Atoms*, **324**, 41-48.

MISHRA, V. P., MEHROTRA, D. K., PANDER, A. C. and ALI, M. D. A. 1990. A teleostean fish from the Lower Triassic of Chamba, Himachal Pradesh. *Journal of the Palaeontological Society of India,* **35**, 73-76.

MITTELBACH, G. G., SCHEMSKE, D. W., CORNELL, H. V., ALLEN, A. P., BROWN, J. M., BUSH, M. B., HARRISON, S. P., HURLBERT, A. H., KNOWLTON, N. and LESSIOS, H. A. 2007. Evolution and the latitudinal diversity gradient: speciation, extinction and biogeography. *Ecology Letters*, **10**, 315-331.

MIZUTANI, R. and SUZUKI, Y. 2012. X-ray microtomography in biology. *Micron*, **43**, 104-115.

MONTENEGRO, A., SPENCE, P., MEISSNER, K., EBY, M., MELCHIN, M. and JOHNSTON, S. 2011. Climate simulations of the Permian-Triassic boundary: Ocean acidification and the extinction event. *Paleoceanography*, **26**.

MØRK, A., ELVEBAKK, G., FORSBERG, A. W., HOUNSLOW, M. W., NAKREM, H. A., VIGRAN, J. O. and WEITSCHAT, W. 1999. The type section of the Vikinghogda formation: A new lower triassic unit in central and eastern Svalbard. *Polar Research*, **18**, 51-82.

MURDOCK, D. J., GABBOTT, S. E., MAYER, G. and PURNELL, M. A. 2014. Decay of velvet worms (Onychophora), and bias in the fossil record of lobopodians. *BMC evolutionary biology*, **14**, 1-10.

MURRAY, A. M. 2000. The Palaeozoic, Mesozoic and Early Cenozoic fishes of Africa. *Fish and Fisheries*, **1**, 111-145.

MUTO, S., TAKAHASHI, S., YAMAKITA, S. and ONOUE, T. 2020. Scarcity of chert in upper Lower Triassic Panthalassic deep-sea successions of Japan records elevated clastic inputs rather than depressed biogenic silica burial flux following the end-Permian extinction. *Global and Planetary Change*, **195**, 103330.

MUTTER, R. J., CARTANYÀ, J. and BASARABA, S. A. U. 2008. New evidence of *Saurichthys* from the Lower Triassic with an evaluation of early saurichthyid diversity. In Arratia G., Schultze H.P. & Wilson M.V.H. (eds.) *Mesozoic Fishes 4*, Verlag Dr. Friedrich Pfeil, München, Germany, 103-127.

NAIMARK, E., KALININA, M. and BOEVA, N. 2018a. Persistence of external anatomy of small crustaceans in a long term taphonomic experiment. *Palaios*, **33**, 154-163.

NAIMARK, E., KALININA, M., SHOKUROV, A., BOEVA, N., MARKOV, A. and ZAYTSEVA, L. 2016. Decaying in different clays: implications for soft-tissue preservation. *Palaeontology*, **59**, 583-595.

NAIMARK, E., KALININA, M., SHOKUROV, A., MARKOV, A., ZAYTSEVA, L. and BOEVA, N. 2018b. Mineral composition of host sediments influences the fossilization of soft tissues. *Canadian Journal of Earth Sciences*, **55**, 1271-1283.

NELSON, J. S., GRANDE, T. C. and WILSON, M. V. 2016. *Fishes of the World*. John Wiley Sons, Hoboken.

NEUMAN, A. G. 2015. Fishes from the Lower Triassic portion of the Sulphur Mountain Formation in Alberta, Canada: geological context and taxonomic composition. *Canadian Journal of Earth Sciences*, **52**, 557-568.

NEUMAN, A. G. and MUTTER, R. J. 2005. *Helmolepis cyphognathus*, sp. nov., a new platysiagid actinopterygian from the Lower Triassic Sulphur Mountain Formation (British Columbia, Canada). *Canadian Journal of Earth Sciences*, **42**, 25-36.

NEWELL, A. J., SENNIKOV, A. G., BENTON, M. J., MOLOSTOVSKAYA, I. I., GOLUBEV, V. K., MINIKH, A. V. and MINIKH, M. G. 2010. Disruption of playa–lacustrine depositional systems at the Permo-Triassic boundary: evidence from Vyazniki and Gorokhovets on the Russian Platform. *Journal of the Geological Society*, **167**, 695-716.

NEWMAN, S., KLEPAC-CERAJ, V., MARIOTTI, G., PRUSS, S., WATSON, N. and BOSAK, T. 2017. Experimental fossilization of mat-forming

cyanobacteria in coarse-grained siliciclastic sediments. *Geobiology*, **15**, 484-498.

NIELSEN, E. 1932. Permo-Carboniferous fishes from East Greenland. Reitzel, København.

NIELSEN, E. 1935. The Permian and Eotriassic Vertebrate-bearing Beds at Godthaab Gulf (East Greenland): Treaarsexpeditionen Til Christian Den X's Land 1931-34 Under Ledelse Af Lauge Koch. Reitzel, København.

NIELSEN, E. 1936. Some Few Preliminary Remarks on Triassic Fishes from East Greenland: Treaarsexpeditionen Til Christian Den X's Land 1931-34 Under Ledelse Af Lauge Koch. Reitzel, København.

NIELSEN, E. 1942. Studies on Triassic Fishes from East Greenland 1. Glaucolepis and Boreosomus. Reitzel, København.

NIELSEN, E. 1949. Studies on Triassic Fishes from East Greenland: Australosomus and Birgeria. Reitzel, København.

NORTHCUTT, R. G. 1989. The phylogenetic distribution and innervation of craniate mechanoreceptive lateral lines. 17-78. *In* COOMBS, S., GÖRNER, P. and MÜNZ, H. (eds). *The Mechanosensory Lateral Line*. Springer New York, New York, NY.

NORTHWOOD, C. 1999. Actinopterygians from the Early Triassic Arcadia Formation, Queensland, Australia. *Memoirs-Queensland Museum*, **43**, 787-796.

OLSEN, P. E. 1984. The skull and pectoral girdle of the parasemionotid fish *Watsonulus eugnathoides* from the Early Triassic Sakamena Group of

Madagascar, with comments on the relationships of the holostean fishes. *Journal of Vertebrate Paleontology*, **4**, 481-499.

OLSZEWSKI, T. D. 2004. Modeling the influence of taphonomic destruction, reworking, and burial on time-averaging in fossil accumulations. *Palaios*, **19**, 39-50.

ORR, P. J., ADLER, L. B., BEARDMORE, S. R., FURRER, H., MCNAMARA, M. E., PEÑALVER-MOLLÁ, E. and REDELSTORFF, R. 2016. “Stick ‘n’ peel”: Explaining unusual patterns of disarticulation and loss of completeness in fossil vertebrates. *Palaeogeography, Palaeoclimatology, Palaeoecology*, **457**, 380-388.

PAGANIN, D., MAYO, S. C., GUREYEV, T. E., MILLER, P. R. and WILKINS, S. W. 2002. Simultaneous phase and amplitude extraction from a single defocused image of a homogeneous object. *Journal of Microscopy*, **206**, 33-40.

PAN, Y., FÜRSICH, F. T., CHELLOUCHE, P. and HU, L. 2019. Taphonomy of fish concentrations from the Upper Jurassic Solnhofen Plattenkalk of Southern Germany. *Neues Jahrbuch für Geologie und Paläontologie-Abhandlungen*, **292**, 73-92.

PAN, Y., FÜRSICH, F. T., ZHANG, J., WANG, Y. and ZHENG, X. 2015. Biostratinomic analysis of *Lycoptera* beds from the Early Eretaceous Yixian Formation, Western Liaoning, China. *Palaeontology*, **58**, 537-561.

PARRISH, J. T. 1993. Climate of the supercontinent Pangaea. *The Journal of Geology*, **101**, 215-233.

PATTERSON, C. 1975. The braincase of pholidophorid and leptolepid fishes, with a review of the actinopterygian braincase. *Philosophical Transactions of the Royal Society of London. B, Biological Sciences*, **269**, 275-579.

PAUWELS, E., VAN LOO, D., CORNILLIE, P., BRABANT, L. and VAN HOOREBEKE, L. 2013. An exploratory study of contrast agents for soft tissue visualization by means of high resolution X-ray computed tomography imaging. *Journal of Microscopy*, **250**, 21-31.

PAYNE, J. L. and CLAPHAM, M. E. 2012. End-Permian mass extinction in the oceans: An ancient analog for the twenty-first century? *Annual Review of Earth and Planetary Sciences*, **40**, 89-111.

PAYNE, J. L., LEHRMANN, D. J., WEI, J., ORCHARD, M. J., SCHRAG, D. P. and KNOLL, A. H. 2004. Large perturbations of the carbon cycle during recovery from the end-Permian extinction. *Science*, **305**, 506-509.

PEARSON, D. M. and WESTOLL, T. S. 1979. The Devonian actinopterygian Cheirolepis Agassiz. Earth and Environmental Science Transactions of the Royal Society of Edinburgh, **70**, 337-399.

PHUOC, L. D. 1980. Late Permian actinopterygian fishes from Blackwater, Queensland. M.Sc. Thesis. Australian National University, Canberra.

PICKERING, A. D. 1981. *Stress and fish*. Academic Press, New York/ London.

PIETSCH, C., RITTERBUSH, K. A., THOMPSON, J. R., PETSIOS, E. and BOTTJER, D. J. 2019. Evolutionary models in the Early Triassic marine realm. *Palaeogeography, Palaeoclimatology, Palaeoecology*, **513**, 65-85.

PIVETEAU, J. 1929. Sur un type de Poisson fossile provenant du Nord de Madagascar. *Camptes-Rendus Hebdomadaires des Séances de l'Académie des Sciences, Paris*, **189**, 1017-1019.

PIVETEAU, J. 1935. Les Poissons du trias inferieur: Contribution a l'etude des Actinopterygiens. Annales de Paleontologie**, 23**, 81-183.

POPLIN, C. and LUND, R. 1995. Fates of the rostral; postrostral and premaxillary in the early history of actinopterygians. *Geobios*, **28**, 225-230.

POPLIN, C. and LUND, R. 1997. Evolution of the premaxillary in the primitive fossil actinopterygians. *Geodiversitas*, **19**, 557-565.

POPLIN, C. and LUND, R. 2000. Two new deep-bodied palaeoniscoid actinopterygians from Bear Gulch (Montana, USA, Lower Carboniferous). *Journal of Vertebrate Paleontology*, **20**, 428-449.

POPLIN, C. M. and LUND, R. 2002. Two Carboniferous fine-eyed palaeoniscoids (Pisces, Actinopterygii) from Bear Gulch (USA). *Journal of Paleontology*, **76**, 1014-1028.

POPLIN, M. and VÉRAN, M. 1996. A revision of the actinopterygian fish *Coccocephalus wildi* from the Upper Carboniferous of Lancashire. *Special Papers in Palaeontology*, **52**, 7-30.

PRADEL, A., MAISEY, J. G., MAPES, R. H. and KRUTA, I. 2016. First evidence of an intercalar bone in the braincase of “palaeonisciform” actinopterygians, with a virtual reconstruction of a new braincase of *Lawrenciella* Poplin, 1984 from the Carboniferous of Oklahoma. *Geodiversitas*, **38**, 489-504.

PRETO, N., KUSTATSCHER, E. and WIGNALL, P. B. 2010. Triassic climates—state of the art and perspectives. *Palaeogeography, Palaeoclimatology, Palaeoecology*, **290**, 1-10.

PRIEM, F. 1924. Paléontologie de Madagascar: XII-Les poissons fossiles. *Annales de Paleontologie*, **13**, 105-132.

PRINOTH, H. and POSENATO, R. 2007. Late Permian nautiloids from the Bellerophon Formation of the Dolomites (Italy). *Palaeontographica abteilung a paläozoologie, stratigraphie,* **282**, 135-165.

PRUSS, S. B. and BOTTJER, D. J. 2004. Early Triassic trace fossils of the Western United States and their implications for prolonged environmental stress from the End-Permian mass extinction. *Palaios*, **19**, 551-564.

PRUSS, S. B. and BOTTJER, D. J. 2005. The reorganization of reef communities following the end-Permian mass extinction. *Comptes Rendus Palevol*, **4**, 553-568.

PURNELL, M. A., DONOGHUE, P. J., GABBOTT, S. E., MCNAMARA, M. E., MURDOCK, D. J. and SANSOM, R. S. 2018. Experimental analysis of soft-tissue fossilization: opening the black box. *Palaeontology*, **61**, 317-323.

PUTTICK, M. N., KRIWET, J., WEN, W., HU, S., THOMAS, G. H. and BENTON, M. J. 2017. Body length of bony fishes was not a selective factor during the biggest mass extinction of all time. *Palaeontology*, **60**, 727-741.

QIU, X., XU, Y., CHEN, Z. Q., BENTON, M. J., WEN, W., HUANG, Y. and WU, S. 2019. The Early Triassic Jurong fish fauna, South China: Age,

anatomy, taphonomy, and global correlation. *Global and Planetary Change*, **180**, 33-50.

RACKI, G. and WIGNALL, P. B. 2005. Late Permian double-phased mass extinction and volcanism: an oceanographic perspective. *Developments in Palaeontology and Stratigraphy*. Elsevier, **20**, 263-297.

RAISWELL, R. 1976. The microbiological formation of carbonate concretions in the Upper Lias of NE England. *Chemical Geology*, **18**, 227-244.

RAUP, D. M. 1976. Species diversity in the Phanerozoic: an interpretation. *Paleobiology*, **2**, 289-297.

RAWSON, S. D., MAKSIMCUKA, J., WITHERS, P. J. and CARTMELL, S. H. 2020. X-ray computed tomography in life sciences. *BMC Biology*, **18**, 21.

RAYNER, D. H. 1952. III.—On the Cranial Structure of an Early Palæoniscid, Kentuckia, gen. nov. *Earth and Environmental Science Transactions of The Royal Society of Edinburgh*, **62**, 53-83.

REDMOND, A. K., CASEY, D., GUNDAPPA, M. K., MACQUEEN, D. J. and MCLYSAGHT, A. 2023. Independent rediploidization masks shared whole genome duplication in the sturgeon-paddlefish ancestor. *Nature Communications*, **14**, 2879.

REN, Y. and XU, G. 2021. A new species of *Pteronisculus* from the Middle Triassic (Anisian) of Luoping, Yunnan, China, and phylogenetic relationships of early actinopterygian fishes. *Vertebrata PalAsiatica*, **59**, 169-199.

RETALLACK, G. J. 1999. Postapocalyptic greenhouse paleoclimate revealed by earliest Triassic paleosols in the Sydney Basin, Australia. *Geological Society of America Bulletin*, **111**, 52-70.

RETALLACK, G. J., SHELDON, N. D., CARR, P. F., FANNING, M., THOMPSON, C. A., WILLIAMS, M. L., JONES, B. G. and HUTTON, A. 2011. Multiple Early Triassic greenhouse crises impeded recovery from Late Permian mass extinction. *Palaeogeography, Palaeoclimatology, Palaeoecology*, **308**, 233-251.

RETALLACK, G. J., SMITH, R. M. and WARD, P. D. 2003. Vertebrate extinction across Permian–Triassic boundary in Karoo Basin, South Africa. *GSA Bulletin*, **115**, 1133-1152.

RETALLACK, G. J., VEEVERS, J. J. and MORANTE, R. 1996. Global coal gap between Permian–Triassic extinction and Middle Triassic recovery of peat-forming plants. *Geological Society of America Bulletin*, **108**, 195-207.

ROMANO, C. 2021. A Hiatus Obscures the Early Evolution of Modern Lineages of Bony Fishes. *Frontiers in Earth Science*, **8**, 618853.

ROMANO, C., GOUDEMAND, N., VENNEMANN, T. W., WARE, D., SCHNEEBELI-HERMANN, E., HOCHULI, P. A., BRÜHWILER, T., BRINKMANN, W. and BUCHER, H. 2013. Climatic and biotic upheavals following the end-Permian mass extinction. *Nature Geoscience*, **6**, 57-60.

ROMANO, C., JENKS, J. F., JATTIOT, R., SCHEYER, T. M., BYLUND, K. G. and BUCHER, H. 2017. Marine Early Triassic Actinopterygii from Elko County (Nevada, USA): Implications for the Smithian equatorial vertebrate eclipse. *Journal of Paleontology*, **91**, 1025-1046.

ROMANO, C., KOGAN, I., JENKS, J., JERJEN, I. and BRINKMANN, W. 2012. *Saurichthys* and other fossil fishes from the late Smithian (Early Triassic) of Bear Lake County (Idaho, USA), with a discussion of saurichthyid palaeogeography and evolution. *Bulletin of Geosciences*, **87**, 543-570.

ROMANO, C., KOOT, M. B., KOGAN, I., BRAYARD, A., MINIKH, A. V., BRINKMANN, W., BUCHER, H. and KRIWET, J. 2016. Permian-Triassic Osteichthyes (bony fishes): Diversity dynamics and body size evolution. *Biological Reviews*, **91**, 106-147.

ROMANO, C., LÓPEZ-ARBARELLO, A., WARE, D., JENKS, J. F. and BRINKMANN, W. 2019. Marine Early Triassic Actinopterygii from the Candelaria Hills (Esmeralda County, Nevada, USA). *Journal of Paleontology*, **93**, 971-1000.

ROMANO, C., WARE, D., BRÜHWILER, T., BUCHER, H. and BRINKMANN, W. 2016c. Marine Early Triassic Osteichthyes from Spiti, Indian Himalayas. *Swiss Journal of Palaeontology*, **135**, 275-294.

ROMANO, M., BERNARDI, M., PETTI, F. M., RUBIDGE, B., HANCOX, J. and BENTON, M. J. 2020. Early Triassic terrestrial tetrapod fauna: a review. *Earth-Science Reviews*, **210**, 1-35.

SAGEMANN, J., BALE, S. J., BRIGGS, D. E. and PARKES, R. J. 1999. Controls on the formation of authigenic minerals in association with decaying organic matter: an experimental approach. *Geochimica et Cosmochimica Acta*, **63**, 1083-1095.

SALLAN, L. C. 2014. Major issues in the origins of ray-finned fish (Actinopterygii) biodiversity. *Biological Reviews*, **89**, 950-971.

SALLAN, L. C. and COATES, M. I. 2013. Styracopterid (Actinopterygii) ontogeny and the multiple origins of post-Hangenberg deep-bodied fishes. *Zoological Journal of the Linnean Society*, **169**, 156-199.

SANSOM, R. S. 2014. Experimental decay of soft tissues. *The Paleontological Society Papers*, **20**, 259-274.

SANSOM, R. S., GABBOTT, S. E. and PURNELL, M. A. 2010. Non-random decay of chordate characters causes bias in fossil interpretation. *Nature*, **463**, 797-800.

SANSOM, R. S., GABBOTT, S. E. and PURNELL, M. A. 2011. Decay of vertebrate characters in hagfish and lamprey (Cyclostomata) and the implications for the vertebrate fossil record. *Proceedings of the Royal Society B: Biological Sciences*, **278**, 1150-1157.

SANSOM, R. S., GABBOTT, S. E. and PURNELL, M. A. 2013. Atlas of vertebrate decay: a visual and taphonomic guide to fossil interpretation. *Palaeontology*, **56**, 457-474.

SAUNDERS, A. and REICHOW, M. 2009. The Siberian Traps and the End-Permian mass extinction: A critical review. *Chinese Science Bulletin*, **54**, 20-37.

SCHAEFFER, B. 1952. The palaeoniscoid fish *Turseodus* from the Upper Triassic Newark group. *American Museum novitates*, **1581**, 1-24.

SCHAEFFER, B. 1971. The braincase of the holostean fish *Macrepistius*, with comments on neurocranial ossification in the Actinopterygii. *American Museum novitates*, **2459**, 1-34.

SCHAEFFER, B. and MANGUS, M. 1976. An Early Triassic fish assemblage from British Columbia. *Bulletin of the American Museum of Natural History*, **156**, 519-563.

SCHAUMBERG, G. 1989. *Muensterichthys buergeri* ngn sp., ein neuer Palaeoniscoide (Actinopterygii, Pisces) aus dem permischen Kupferschiefer von Richelsdorf (Hessen, West-Deutschland). *Paläontologische Zeitschrift*, **63**, 119-131.

SCHEYER, T. M., ROMANO, C., JENKS, J. and BUCHER, H. 2014. Early Triassic marine biotic recovery: The predators' perspective. *PLoS ONE*, **9**.

SCHMIDT, H., VETTERLEIN, D., KÖHNE, J. M. and EICKHORST, T. 2015. Negligible effect of X-ray µ-CT scanning on archaea and bacteria in an agricultural soil. *Soil Biology and Biochemistry*, **84**, 21-27.

SCHULTZE, H.-P. and BARDACK, D. 1987. Diversity and size changes in palaeonisciform fishes (Actinopterygii, Pisces) from the Pennsylvanian Mazon Creek Fauna, Illinois, USA. *Journal of Vertebrate Paleontology*, **7**, 1-23.

SCOTESE, C. and SCHETTINO, A. 2017. Late Permian-Early Jurassic paleogeography of western Tethys and the world. *Permo-Triassic salt provinces of Europe, North Africa and the Atlantic margins*. Elsevier, 57-95.

SEILACHER, A., REIF, W.-E. and WESTPHAL, F. 1985. Sedimentological, ecological and temporal patterns of fossil Lagerstätten. *Philosophical Transactions of the Royal Society of London. B, Biological Sciences*, **311**, 5-24.

SELLY, T. and SCHIFFBAUER, J. D. 2021. X-ray tomographic microscopy as a means to systematically track experimental decay and fossilization. *Palaios*, **36**, 216-224.

SELVAGGI, G., MONSTREY, S., LANDUYT, K. V., HAMDI, M. and BLONDEEL, P. 2003. The role of iodine in antisepsis and wound management: a reappraisal. *Acta Chirurgica Belgica*, **103**, 241-247.

SENNIKOV, A. and GOLUBEV, V. 2005. Unique Vyazniki biotic complex of the terminal Permian from the Central Russia and the global ecological crisis at the Permo-Triassic boundary. *The non-marine Permian, New Mexico Museum Natural History Science Bulletin*, **30**, 302-304.

SENNIKOV, A. and GOLUBEV, V. 2006. Vyazniki biotic assemblage of the terminal Permian. *Paleontological Journal*, **40**, S475-S481.

SENNIKOV, A. and GOLUBEV, V. 2012. On the faunal verification of the Permo-Triassic boundary in continental deposits of eastern Europe: 1. Gorokhovets-Zhukov ravine. *Paleontological Journal*, **46**, 313-323.

SENNIKOV, A., GOLUBEV, V., BULANOV, V., IVAKHNENKO, M. and KURKIN, A. 2003. A new oryctocenosis of the aquatic vertebrate community from the Late Permian of central Russia. *Paleontological Journal*, **37**, 417–424.

SHEN, J., CHEN, J., ALGEO, T. J., YUAN, S., FENG, Q., YU, J., ZHOU, L., O'CONNELL, B. and PLANAVSKY, N. J. 2019. Evidence for a prolonged Permian–Triassic extinction interval from global marine mercury records. *Nature Communications*, **10**, 1-9.

SHEN, J., SCHOEPFER, S. D., FENG, Q., ZHOU, L., YU, J., SONG, H., WEI, H. and ALGEO, T. J. 2015. Marine productivity changes during the end-Permian crisis and Early Triassic recovery. *Earth-Science Reviews*, **149**, 136-162.

SHEN, S.-Z., CROWLEY, J. L., WANG, Y., BOWRING, S. A., ERWIN, D. H., SADLER, P. M., CAO, C.-Q., ROTHMAN, D. H., HENDERSON, C. M. and RAMEZANI, J. 2011a. Calibrating the end-Permian mass extinction. *Science*, **334**, 1367-1372.

SHEN, Y., FARQUHAR, J., ZHANG, H., MASTERSON, A., ZHANG, T. and WING, B. A. 2011b. Multiple S-isotopic evidence for episodic shoaling of anoxic water during Late Permian mass extinction. *Nature Communications*, **2**, 1-5.

SHISHKIN, M. and NOVIKOV, I. 2017. Early stages of recovery of the East European tetrapod fauna after the end-Permian crisis. *Paleontological Journal*, **51**, 612-622.

SIDOR, C. A., VILHENA, D. A., ANGIELCZYK, K. D., HUTTENLOCKER, A. K., NESBITT, S. J., PEECOOK, B. R., STEYER, J. S., SMITH, R. M. and TSUJI, L. A. 2013. Provincialization of terrestrial faunas following the end-Permian mass extinction. *Proceedings of the National Academy of Sciences*, **110**, 8129-8133.

SMITH, A. B. 2001. Large–scale heterogeneity of the fossil record: implications for Phanerozoic biodiversity studies. *Philosophical Transactions of the Royal Society of London. Series B: Biological Sciences*, **356**, 351-367.

SMITH, A. B. and MCGOWAN, A. J. 2011. The ties linking rock and fossil records and why they are important for palaeobiodiversity studies. *Geological Society, London, Special Publications*, **358**, 1-7.

SMITH, G. R., STEARLEY, R. F. and BADGLEY, C. E. 1988. Taphonomic bias in fish diversity from Cenozoic floodplain environments. *Palaeogeography, Palaeoclimatology, Palaeoecology*, **63**, 263-273.

SMITHWICK, F. M. and STUBBS, T. L. 2018. Phanerozoic survivors: Actinopterygian evolution through the Permo-Triassic and Triassic-Jurassic mass extinction events. *Evolution*, **72**, 348-362.

SONG, H., HUANG, S., JIA, E., DAI, X., WIGNALL, P. B. and DUNHILL, A. M. 2020. Flat latitudinal diversity gradient caused by the Permian–Triassic mass extinction. *Proceedings of the National Academy of Sciences*, **117**, 17578-17583.

SONG, H., WIGNALL, P. B., CHEN, Z.-Q., TONG, J., BOND, D. P., LAI, X., ZHAO, X., JIANG, H., YAN, C. and NIU, Z. 2011. Recovery tempo and pattern of marine ecosystems after the end-Permian mass extinction. *Geology*, **39**, 739-742.

SONG, H., WIGNALL, P. B. and DUNHILL, A. M. 2018. Decoupled taxonomic and ecological recoveries from the Permo-Triassic extinction. *Science Advances*, **4**, eaat5091.

SONG, H., WIGNALL, P. B., TONG, J., BOND, D. P., SONG, H., LAI, X., ZHANG, K., WANG, H. and CHEN, Y. 2012. Geochemical evidence from bio-apatite for multiple oceanic anoxic events during Permian–Triassic transition and the link with end-Permian extinction and recovery. *Earth and Planetary Science Letters*, **353**, 12-21.

SONG, H., WIGNALL, P. B., TONG, J. and YIN, H. 2013. Two pulses of extinction during the Permian–Triassic crisis. *Nature Geoscience*, **6**, 52-56.

SPERLING, E. A. and INGLE JR, J. C. 2006. A Permian–Triassic boundary section at Quinn River Crossing, northwestern Nevada, and implications for the cause of the Early Triassic chert gap on the western Pangaean margin. *Geological Society of America Bulletin*, **118**, 733-746.

STANLEY, S. M. 2009. Evidence from ammonoids and conodonts for multiple Early Triassic mass extinctions. *Proceedings of the National Academy of Sciences*, **106**, 15264-15267.

STEMMERIK, L., BENDIX-ALMGREEN, S. E. and PIASECKI, S. 2001. The Permian–Triassic boundary in central East Greenland: past and present views. *Bulletin of the Geological Society of Denmark*, **48**, 159-167.

STENSIÖ, E. A. 1925a. Triassic fishes from Spitzbergen. *Journal of Geology*, **33**, 753-753.

STENSIÖ, E. A. 1925b. Triassic fishes from Spitzbergen-Part II. *Journal of Geology*, **33**, 753-753.

STENSIÖ, E. A. 1921a. Triassic fishes from Spitzbergen. A. Holzhausen.

STENSIÖ, E. A. 1921b. Triassic fishes from Spitzbergen-Part I. A. Holzhausen.

STENSIÖ, E. A. 1932. Triassic Fishes from East Greenland: Collected by the Danish Expeditions in 1929-31:[de Østgrønlandske Expeditioner Til Kong Christian Den X's Land Udført i Aarene 1926-27 Od 1929-30 Under Ledelse Af Lauge Koch]. Reitzel.

SUN, Y., JOACHIMSKI, M. M., WIGNALL, P. B., YAN, C., CHEN, Y., JIANG, H., WANG, L. and LAI, X. 2012. Lethally hot temperatures during the Early Triassic greenhouse. *Science*, **338**, 366-370.

SUN, Z., TINTORI, A., JIANG, D. and MOTANI, R. 2013. A new perleidid from the Spathian (Olenekian, Early Triassic) of Chaohu, Anhui Province, China. *Rivista Italiana di Paleontologia e Stratigrafia*, **119**, 275-285.

SURLYK, F., BJERAGER, M., PIASECKI, S. and STEMMERIK, L. 2017. Stratigraphy of the marine Lower Triassic succession at Kap Stosch, Hold with Hope, North-East Greenland. *Bulletin of the Geological Society of Denmark*, **65**, 87-123.

SZABÓ, M., BOTFALVAI, G. and ŐSI, A. 2019. Taxonomical and palaeoecological investigations of the chondrichthyan and osteichthyan fish remains from the Middle-Late Triassic deposits of the Villány Hills (Southern Hungary). *Geobios*, **57**, 111-126.

SZURLIES, M., BACHMANN, G. H., MENNING, M., NOWACZYK, N. R. and KÄDING, K.-C. 2003. Magnetostratigraphy and high-resolution lithostratigraphy of the Permian–Triassic boundary interval in Central Germany. *Earth and Planetary Science Letters*, **212**, 263-278.

TINTORI, A. 1992. Fish taphonomy and Triassic anoxic basins from the Alps: a case history. *Rivista Italiana di Paleontologia e Stratigrafia*, **97**.

TINTORI, A., HITIJ, T., JIANG, D., LOMBARDO, C. and SUN, Z. 2014a. Triassic actinopterygian fishes: The recovery after the end-Permian crisis. *Integrative Zoology*, **9**, 394-411.

TINTORI, A., HUANG, J. D., JIANG, D. A. Y., SUN, Z. Y. U., MOTANI, R. and CHEN, G. 2014b. A new *Saurichthys* (Actinopterygii) from the Spathian (Early Triassic) of Chaohu (Anhui Province, China). *Rivista Italiana di Paleontologia e Stratigrafia*, **120**, 157-164.

TONG, J., ZHOU, X., ERWIN, D. H., ZUO, J. and ZHAO, L. 2006. Fossil fishes from the Lower Triassic of Majiashan, Chaohu, Anhui Province, China. *Journal of Paleontology*, **80**, 146-161.

TSESSARSKY, A. 2023. What is missing from the sturgeon jaw: Developmental morphology of the upper jaw in *Acipenser*. *Journal of Anatomy,* **244**, 42-62.

VASUDEVAN, P. and TANDON, M. 2010. Antimicrobial properties of iodine based products. *Journal of Scientific and Industrial Research,* **69**, 376-383.

VÁZQUEZ, P. and CLAPHAM, M. E. 2017. Extinction selectivity among marine fishes during multistressor global change in the end-Permian and end-Triassic crises. *Geology*, **45**, 395-398.

VICKERTON, P., JARVIS, J. and JEFFERY, N. 2013. Concentration-dependent specimen shrinkage in iodine-enhanced micro CT. *Journal of Anatomy*, **223**, 185-193.

VIGLIETTI, P. 2020. Biostratigraphy of the *Daptocephalus* Assemblage Zone (Beaufort Group, Karoo Supergroup), South Africa. *South African Journal of Geology*, **123**, 191-206.

VILHENA, D. A. and SMITH, A. B. 2013. Spatial bias in the marine fossil record. *PLoS One*, **8**, e74470.

VISSCHER, H., BRINKHUIS, H., DILCHER, D. L., ELSIK, W. C., ESHET, Y., LOOY, C. V., RAMPINO, M. R. and TRAVERSE, A. 1996. The terminal Paleozoic fungal event: evidence of terrestrial ecosystem destabilization and collapse. *Proceedings of the National Academy of Sciences*, **93**, 2155-2158.

WACKER, K., BARTSCH, P. and CLEMEN, G. 2001. The development of the tooth pattern and dentigerous bones in *Polypterus senegalus* (Cladistia, Actinopterygii). *Annals of Anatomy-Anatomischer Anzeiger*, **183**, 37-52.

WAGNER, E. J., ARNDT, R. E., BILLMAN, E. J., FOREST, A. and CAVENDER, W. 2008. Comparison of the efficacy of iodine, formalin, salt, and hydrogen peroxide for control of external bacteria on rainbow trout eggs. *North American Journal of Aquaculture*, **70**, 118-127.

WALKER, F. M., DUNHILL, A. M. and BENTON, M. J. 2020. Variable preservation potential and richness in the fossil record of vertebrates. *Palaeontology*, **63**, 313-329.

WANG, N., JIN, F., WANG, W. and ZHU, X. 2007. Actinopterygian fishes from the Permian–Triassic Boundary beds in Zhejiang and Jiangxi

provinces, South China and fish mass extinction, recovery and radiation. *Vertebrate PalAsiatica*, **45**, 307-329.

WANG, Y., SADLER, P. M., SHEN, S.-Z., ERWIN, D. H., ZHANG, Y.-C., WANG, X.-D., WANG, W., CROWLEY, J. L. and HENDERSON, C. M. 2014. Quantifying the process and abruptness of the end-Permian mass extinction. *Paleobiology*, **40**, 113-129.

WARD, P. D., BOTHA, J., BUICK, R., DE KOCK, M. O., ERWIN, D. H., GARRISON, G. H., KIRSCHVINK, J. L. and SMITH, R. 2005. Abrupt and gradual extinction among Late Permian land vertebrates in the Karoo Basin, South Africa. *Science*, **307**, 709-714.

WARREN, P. S. 1936. Two new fossil fish from the Canadian Rockies. *Transactions of the Royal Society of Canada, Section IV, 3rd series*, **30**, 55-58.

WARTH, P., HILTON, E. J., NAUMANN, B., OLSSON, L. and KONSTANTINIDIS, P. 2017. Development of the skull and pectoral girdle in Siberian sturgeon, *Acipenser baerii*, and Russian sturgeon, *Acipenser gueldenstaedtii* (Acipenseriformes: Acipenseridae). *Journal of Morphology*, **278**, 418-442.

WASKOM, M., LOSSO, S. and ORTEGA-HERNÁNDEZ, J. 2023. Stuck in the mud: experimental taphonomy and computed tomography demonstrate the critical role of sediment in three-dimensional carcass stabilization during early fossil diagenesis. PREPRINT (Version 1) available at Research Square [https://doi.org/10.21203/rs.3.rs-3192621/v1]

WEN, W., ZHANG, Q.-Y., HU, S.-X., ZHOU, C.-Y., XIE, T., HUANG, J.-Y., CHEN, Z. Q. and BENTON, M. J. 2012. A new basal actinopterygian fish from the Anisian (Middle Triassic) of Luoping, Yunnan Province, southwest China. *Acta Palaeontologica Polonica*, **57**, 149-160.

WESTOLL, T. S. 1941. The Permian fishes Dorypterus and Lekanichthys. Proceedings of the Zoological Society of London, **B111**, 39-58.

WHITE, E. I. 1932. V.—On a new Triassic fish from North-East Madagascar. *Journal of Natural History*, **10**, 80-83.

WHITE, E. I. and MOY-THOMAS, J. A. 1940. VII.—Notes on the nomenclature of fossil fishes.—Part II. Homonyms D-L. *Annals and Magazine of Natural History*, **6**, 98-103.

WIGNALL, P. B. 2008. The end-Permian crisis, aftermath and subsequent recovery. 43-48. Origin and Evolution of Natural Diversity: Proceedings of the International Symposium, The Origin and Evolution of Natural Diversity, held from 1-5 October 2007 in Sapporo, Japan. 21st Century COE for Neo-Science of Natural History, Hokkaido University,

WIGNALL, P. B. and NEWTON, R. 2003. Contrasting deep-water records from the Upper Permian and Lower Triassic of South Tibet and British Columbia: evidence for a diachronous mass extinction. *Palaios*, **18**, 153-167.

WIGNALL, P. B. and TWITCHETT, R. J. 2002. Extent, duration, and nature of the Permian-Triassic superanoxic event. *Special Papers-Geological Society of America*, **356**, 395-414.

WILSON, C. D., MANSKY, C. F. and ANDERSON, J. S. 2021. A platysomid occurrence from the Tournaisian of Nova Scotia. *Scientific Reports*, **11**, 8375.

WILSON, L. A. and BUTTERFIELD, N. J. 2014. Sediment effects on the preservation of Burgess Shale–type compression fossils. *Palaios*, **29**, 145-154.

WILSON, M. V. and BARTON, D. G. 1996. Seven centuries of taphonomic variation in Eocene freshwater fishes preserved in varves: paleoenvironments and temporal averaging. *Paleobiology*, **22**, 535-542.

WOODS, A. D. 2005. Paleoceanographic and paleoclimatic context of Early Triassic time. *Comptes Rendus Palevol*, **4**, 463-472.

XU, G.-H. 2019. Osteology and phylogeny of *Robustichthys luopingensis*, the largest holostean fish in the Middle Triassic. *PeerJ*, **7**, e7184.

XU, G.-H. 2021. A new stem-neopterygian fish from the Middle Triassic (Anisian) of Yunnan, China, with a reassessment of the relationships of early neopterygian clades. *Zoological Journal of the Linnean Society*, **191**, 375-394.

XU, G.-H., GAO, K.-Q. and FINARELLI, J. A. 2014a. A revision of the Middle Triassic scanilepiform fish *Fukangichthys longidorsalis* from Xinjiang, China, with comments on the phylogeny of the Actinopteri. *Journal of Vertebrate Paleontology*, **34**, 747-759.

XU, G.-H., SHEN, C.-C. and ZHAO, L.-J. 2014b. *Pteronisculus nielseni* sp. nov., a new stem-actinopteran fish from the Middle Triassic of Luoping, Yunnan Province, China. Vertebrata PalAsiatica, **52**, 364-380.

XU, G. H. and GAO, K. Q. 2011. A new scanilepiform from the Lower Triassic of northern Gansu Province, China, and phylogenetic relationships of non-teleostean Actinopterygii. *Zoological Journal of the Linnean Society*, **161**, 595-612.

XU, G. H., GAO, K. Q. and COATES, M. I. 2015. Taxonomic revision of *Plesiofuro mingshuica* from the Lower Triassic of northern Gansu, China, and the relationships of early neopterygian clades. *Journal of Vertebrate Paleontology*, **35**.

YASUDA, T., YOSHIMURA, Y., TAKADA, H., KAWAGUCHI, S., ITO, M., YAMAZAKI, F., IRIYAMA, J., ISHIGO, S. and ASANO, Y. 1997. Comparison of bactericidal effects of commonly used antiseptics against pathogens causing nosocomial infections. *Dermatology*, **195**, 19-28.

YOSHIDA, H., YAMAMOTO, K., MINAMI, M., KATSUTA, N., SIN-ICHI, S. and METCALFE, R. 2018. Generalized conditions of spherical carbonate concretion formation around decaying organic matter in early diagenesis. *Scientific Reports*, **8**, 6308.

ZAPPALA, S., HELLIWELL, J. R., TRACY, S. R., MAIRHOFER, S., STURROCK, C. J., PRIDMORE, T., BENNETT, M. and MOONEY, S. J. 2013. Effects of X-ray dose on rhizosphere studies using X-ray computed tomography. *PloS One*, **8**, e67250.

ZATOŃ, M., NIEDŹWIEDZKI, G., RAKOCIŃSKI, M., BLOM, H. and KEAR, B. P. 2018. Earliest Triassic metazoan bioconstructions from East Greenland reveal a pioneering benthic community in the immediate

aftermath of the end-Permian mass extinction. *Global and Planetary Change*, **167**, 87-98.

ZHANG, G., ZHANG, X., LI, D., FARQUHAR, J., SHEN, S., CHEN, X. and SHEN, Y. 2015. Widespread shoaling of sulfidic waters linked to the end-Guadalupian (Permian) mass extinction. *Geology*, **43**, 1091-1094.

ZHARKOV, M. and CHUMAKOV, N. 2001. Paleogeography and sedimentation settings during Permian–Triassic reorganizations in biosphere. *Stratigraphy and Geological Correlation*, **9**, 340-363.

ZHOU, M.-F., MALPAS, J., SONG, X.-Y., ROBINSON, P. T., SUN, M., KENNEDY, A. K., LESHER, C. M. and KEAYS, R. R. 2002. A temporal link between the Emeishan large igneous province (SW China) and the end-Guadalupian mass extinction. *Earth and Planetary Science Letters*, **196**, 113-122.

ZIDEK, J. 1992. Late Pennsylvanian Chondrichthyes, Acanthodii, and deep-bodied Actinopterygii from the Kinney Quarry, Manzanita Mountains, New Mexico. *New Mexico Bureau of Mines and Mineral Resources Bulletin*, **138**, 145-182.

ZIEGLER, A., ESHEL, G., REES, P. M., ROTHFUS, T., ROWLEY, D. and SUNDERLIN, D. 2003. Tracing the tropics across land and sea: Permian to present. *Lethaia*, **36**, 227-254.

ZIEGLER, A., SCOTESE, C. and BARRETT, S. F. 1982. Mesozoic and Cenozoic paleogeographic maps. *Tidal friction and the Earth's rotation II*. Springer, pp. 242-250.

ZUCHUAT, V., SLEVELAND, A., TWITCHETT, R., SVENSEN, H., TURNER, H., AUGLAND, L. E., JONES, M. T., HAMMER, Ø., HAUKSSON, B. and HAFLIDASON, H. 2020. A new high-resolution stratigraphic and palaeoenvironmental record spanning the End-Permian Mass Extinction and its aftermath in central Spitsbergen, Svalbard. *Palaeogeography, Palaeoclimatology, Palaeoecology*, **554**, 109732.

ZWANENBURG, E. A., WILLIAMS, M. A. and WARNETT, J. M. 2022. Review of high-speed imaging with lab-based x-ray computed tomography. *Measurement Science and Technology*, **33**, 012003.

Appendices

A | A Portrait of a Young Fish: Redescription of *Pteronisculus gunnari* (Nielsen, 1942) from a juvenile specimen from the Early Triassic of East Greenland, with implications for ontogenetic development in early actinopterygians

A.1 Phylogenetic matrix and analysis

Phylogenetic matrix and script for the analyses of this chapter can be found and downloaded at: https://doi.org/10.25500/edata.bham.00001171.

A.2 Additional characters and taxa of the phylogenetic analysis

General notes. This matrix is based on that of Argyriou et al. (2022), with 3 additional characters and 6 additional taxa. These taxa were added to the analysis in order to understand the relationships within the *Pteronisculus* genus. These comprise NHMD–73588, *Pteronisculus gunnari, Pteronisculus magnus* (Nielsen, 1942), *Pteronisculus changae* (Ren & Xu, 2021), *Pteronisculus nielseni* (Xu et al., 2014) and *Pteronisculus cicatrosus* (Lehman, 1952). The characters added (see below) were sourced from the character matrix of Ren & Xu (2021). The present matrix comprises 303 characters and 123 taxa. The following characters are ordered: 89, 91, 152, 173, 248, 258.

Character codes updates (annotated)~~d~~ from Argyriou et al. (2022).

Pteronisculus stensioi:

char. 37: 1 to 0; incorrectly coded in Argyriou et al. (2022). *P. stensioi* has intertemporal and supratemporal bones rather than a single dermopterotic (Nielsen, 1942).

char. 38: - to 0; incorrectly coded in Argyriou et al. (2022). Changed to reflect the presence of intertemporal and supratemporal bones (Nielsen, 1942).

char. 39: 0 to 1; incorrectly coded in Argyriou et al. (2022). Changed to reflect the presence of intertemporal and supratemporal bones (Nielsen, 1942).

char. 40: 1 to 0; incorrectly coded in Argyriou et al. (2022). Changed to reflect the presence of intertemporal and supratemporal bones (Nielsen, 1942).

char. 41: 0 to 1; incorrectly coded in Argyriou et al. (2022). Changed to reflect the presence of intertemporal and supratemporal bones (Nielsen, 1942).

char. 66: 0 to 1; incorrectly coded in Argyriou et al. (2022). Dermohyal not fused to the hyomandibula (Nielsen, 1942).

char. 68: 0 to 1; incorrectly coded in Argyriou et al. (2022). Maxilla present (Nielsen, 1942).

char. 111: 1 to 0; incorrectly coded in Argyriou et al. (2022). Operculum significantly higher than subopercular (Nielsen, 1942).

char. 127: 1 to 0; incorrectly coded in Argyriou et al. (2022). Internasal cavity absent (Nielsen, 1942).

char. 166: 0 to ?; coding changed to reflect the discovery of an intercalar bone in *P. gunnari* (the bone may have not been detected in other species of *Pteronisculus*, rather than being absent)

char. 224: ? to 0; incorrectly coded in Argyriou et al. (2022). Symplectic shape known and splint-like (Nielsen, 1942).

char. 225: ? to 1; incorrectly coded in Argyriou et al. (2022). Symplectic position known (medial to posterior margin of quadrate) (Nielsen, 1942).

char. 231: 0 to 1; incorrectly coded in Argyriou et al. (2022). Uncinate processes on epibranchials present (Nielsen, 1942).

char. 249: 0 to 1; incorrectly coded in Argyriou et al. (2022). Pectoral fin rays present terminal segmentation (Nielsen, 1942).

char. 281: 1 to 0. incorrectly coded in Argyriou et al. (2022). Parasphenoid does not wing around the basiocciput (Nielsen, 1942).

New characters

301: Lacrimal contributing to oral margin: 0, absent; 1, present.

302 Teeth on lacrimal: 0, absent; 1, present.

303 Dermosphenotic position: 0, extending well below dermopterotic; 1, located at same horizontal level than dermopterotic.

A.3 Characters list

1. Large dermal plates (Forey, 1980; Gardiner, 1984; Zhu & Schultze, 2001; Zhu et al., 2001; Zhu & Yu, 2002; Zhu et al., 2006; Friedman, 2007; Brazeau, 2009; Zhu et al., 2009; Friedman & Brazeau; 2010; Davis et al., 2012; Zhu et al., 2013; Brazeau & Friedman, 2014; Giles et al., 2015b,c; Giles et al., 2017.)

0 absent

1 present

2. Sensory lines (Brazeau, 2009; Zhu et al., 2013; Giles et al., 2015b; Giles et al., 2017.)

0 preserved as open grooves

1 pass through canals

Dermal skull

3. Premaxilla as distinct ossification (Hurley et al. 2007; Xu et al. 2014; Giles et al., 2017. Typically, the premaxilla is a short, paired or median bone that contributes to the orbital margin anterior to the maxilla. However, considerable variation is present, and we have attempted to consistently code this variation as laid out here and in the following character descriptions. A premaxilla may be completely absent (e.g. *Acipenser*, *Cyranorhis*) or dorsally expanded into a midline bone (possibly fused with the rostral; e.g. *Bobasatrania*, *Styracopterus*). These two latter states are coded as '1' here.)

0 present

1 absent

4. Premaxillae, contact at midline (Cloutier & Ahlberg, 1996; Taverne, 1997; Schultze & Cumbaa, 2001; Zhu & Schultze, 2001; Zhu & Yu, 2002; Cloutier & Arratia, 2004; Friedman & Blom, 2006; Zhu et al., 2006; Friedman, 2007; Long et al., 2008; Swartz, 2009; Choo, 2011; Giles et al., 2017. Coded as inapplicable in taxa lacking any ossification in the position typically occupied by the premaxilla (e.g. *Acipenser*, *Cyranorhis*) and where the premaxilla appears fused with the rostral (e.g. *Bobasatrania*, *Styracopterus*).

0 present

1 absent

5. Premaxilla fused at midline (Xu et al., 2011; Xu et al., 2015; Xu & Zhao, 2016; Giles et al., 2017. Coded as inapplicable in taxa lacking any ossification in the position typically occupied by the premaxilla (e.g.

Acipenser, *Cyranorhis*) and where the premaxilla appears fused with the rostral (e.g. *Bobasatrania*, *Styracopterus*) and where the premaxilla appears fused with the rostral (e.g. *Bobasatrania*, *Styracopterus*).)

0 absent

1 present

6. Premaxilla (Friedman, 2007; Giles et al., 2015b; Giles et al., 2017. Coded as inapplicable in taxa lacking any ossification in the position typically occupied by the premaxilla (e.g. *Acipenser*, *Cyranorhis*) and in taxa where the premaxillae do not contact at the midline.)

0 Reaches or extends past anterior margin of orbit

1 Confined to region anterior to orbit

7. Premaxilla contributes to orbital margin (Cloutier & Ahlberg, 1996; Schultze & Cumbaa, 2001; Zhu & Schultze, 2001; Zhu et al., 2001; Zhu & Yu, 2002; Cloutier & Arratia, 2004; Zhu et al., 2006; Friedman, 2007; Long et al., 2008; Swartz, 2009; Zhu et al., 2009; Xu & Gao, 2011; Zhu et al., 2013; Xu et al., 2014; Giles et al., 2017. Coded as inapplicable in taxa lacking any ossification in the position typically occupied by the premaxilla (e.g. *Acipenser*, *Cyranorhis*), where the premaxilla appears fused with the rostral (e.g. *Bobosatrania*, *Styracopterus*), and where the premaxilla is restricted anterior to the orbit.)

0 absent

1 present

8. Teeth on premaxillae (Cloutier & Arratia 2004, Xu et al. 2014; Giles et al., 2017. Coded as inapplicable in taxa lacking any ossification in

the position typically occupied by the premaxilla (e.g. *Acipenser*, *Cyranorhis*).)

0 present

1 absent

9. Mobile premaxilla (Arratia 1999; Cavin & Suteethorn 2006; Hurley et al. 2007; Giles et al., 2017. Coded as inapplicable in taxa lacking any ossification in the position typically occupied by the premaxilla (e.g. *Acipenser*, *Cyranorhis*) and where the premaxilla appears fused with the rostral (e.g. *Bobasatrania*, *Styracopterus*).

0 absent

1 present

10. Olfactory nerve pierces premaxilla (Grande 2010; Xu et al., 2015; Xu & Shen, 2015; Xu & Zhao, 2016; Giles et al., 2017. Coded as inapplicable in taxa lacking any ossification in the position typically occupied by the premaxilla (e.g. *Acipenser*, *Cyranorhis*) and where the premaxilla appears fused with the rostral (e.g. *Bobasatrania*, *Styracopterus*).)

0 absent

1 present

11. Nasal process of premaxilla (Gardiner & Schaeffer 1989; Olsen & McCune 1991; Gardiner et al. 1996; Gardiner et al. 2005; Cavin & Suteethorn 2006; Hurley et al. 2007; Grande 2010; López-Arbarello 2012; Xu & Wu 2012; Xu et al. 2014; Bermúdez-Rochas & Poyato-Ariza 2015; Poyato-Ariza 2015; Thies & Waschkewitz, 2015; Xu & Shen, 2015; Gibson

2016; Xu & Zhao, 2016; Giles et al., 2017; López-Arbarello & Sferco 2018. Coded as inapplicable in taxa lacking any ossification in the position typically occupied by the premaxilla (e.g. *Acipenser*, *Cyranorhis*) and where the premaxilla appears fused with the rostral (e.g. *Bobasatrania*, *Styracopterus*).)

0 absent

1 short

2 long, reaches skull roof

12. Sensory canal on premaxilla (Giles et al., 2017. Coded as inapplicable in taxa lacking any ossification in the position typically occupied by the premaxilla (e.g. *Acipenser*, *Cyranorhis*) and where the premaxilla appears fused with the rostral (e.g. *Bobasatrania*, *Styracopterus*).)

0 present

1 absent

13. Postrostrals (element[s] immediately anterior to frontals but not in contact with premaxillae) (Cloutier & Ahlberg, 1996; Taverne, 1997; Lund, 2000; Schultze & Cumbaa, 2001; Zhu & Schultze, 2001; Lund & Poplin, 2002; Cloutier & Arratia, 2004; Friedman & Blom, 2006; Long et al., 2008; Swartz, 2009; Choo, 2011; Xu et al., 2014; Giles et al., 2015b; Giles et al., 2017.)

0 present

1 absent

14. Single median dermal bone capping snout (Gardiner & Schaeffer, 1989; Taverne, 1997; Friedman & Blom, 2006; Long et al., 2008; Swartz, 2009; Choo, 2011; Giles et al., 2015b; Poyato-Ariza 2015; Giles et al., 2017.)

0 absent

1 present

15. Median rostral (Gardiner et al. 1996; Hurley et al. 2007; Giles et al., 2017.)

0 plate-like

1 tube-like

16. Pores for rostral organ (Friedman, 2007; Giles et al., 2015b; Giles et al., 2017.)

0 absent

1 present

17. Nasal bone as single consolidated ossification (i.e. bone(s) carrying supraorbital canal between premaxilla and anterior margin of frontals) (Taverne, 1997; Schultze & Cumbaa, 2001; Friedman & Blom, 2006; Long et al., 2008; Swartz, 2009; Choo, 2011; Giles et al., 2015b; Giles et al., 2017.)

0 absent

1 present

18. Contact of nasals on midline (Giles et al., 2017.)

0 separated by dermal bones

1 contacting or separated by gap unfilled by bone

19. Nasal contributes to orbital margin (Xu & Wu 2012; Xu et al. 2014; Xu & Zhao, 2016; Giles et al., 2017; López-Arbarello & Sferco 2018.)

0 absent

1 present

20. Mesial margin of (anterior) nasal (Lund et al., 1995; Ahlberg & Johanson, 1998; Ahlberg et al., 2000; Lund, 2000; Poplin & Lund, 2000; Schultze & Cumbaa, 2001; Lund & Poplin, 2002; Cloutier & Arratia, 2004; Zhu & Ahlberg, 2004; Daeschler et al., 2006; Long et al., 2006; Zhu et al., 2006; Zhu et al., 2009; Choo, 2011; Giles et al., 2015b; Giles et al., 2017; López-Arbarello & Sferco 2018.)

0 not notched

1 notched

21. Both nostrils accommodated within single dermal ossification

0 absent

1 present

22. Posterior nostril in complete communication with orbital fenestra (Friedman & Blom, 2006; Long et al., 2008; Choo, 2011; Giles et al., 2015b; Giles et al., 2017. This character refers to the opening of the posterior nostril with reference to the surrounding dermal bones.)

0 absent

1 present

23. Posterior nostril - contribution to margin by premaxillae (Friedman & Blom, 2006; Long et al., 2008; Choo, 2011; Giles et al., 2015b; Giles et al., 2017.)

0 absent

1 present

24. Tectals (sensu Cloutier & Ahlberg 1996, not counting the posterior tectal of Jarvik) (Lund et al., 1995; Cloutier & Ahlberg, 1996; Lund, 2000; Schultze & Cumbaa, 2001; Zhu & Schultze, 2001; Zhu et al., 2001; Lund & Poplin, 2002; Zhu & Yu, 2002; Cloutier & Arratia, 2004; Zhu et al., 2006; Friedman, 2007; Swartz, 2009; Zhu et al., 2009; Zhu et al., 2013; Giles et al., 2015b; Giles et al., 2017.)

0 absent

1 present

25. Dermal intracranial joint (Cloutier & Ahlberg, 1996; Ahlberg & Johanson, 1998; Zhu & Ahlberg, 2004; Zhu & Schultze, 2001; Zhu et al., 2001; Zhu & Yu, 2002; Daeschler et al., 2006; Long et al., 2006; Zhu et al., 2006; Friedman, 2007; Brazeau, 2009; Zhu et al., 2009; Choo, 2011; Davis et al., 2012; Zhu et al., 2013; Giles et al., 2015b; Giles et al., 2017.)

0 absent

1 present

26. Pineal foramen (Cloutier & Ahlberg, 1996; Taverne, 1997; Schultze & Cumbaa, 2001; Zhu & Schultze, 2001; Zhu & Yu, 2002; Friedman & Blom, 2006; Friedman, 2007; Long et al., 2008; Brazeau, 2009; Swartz, 2009; Davis et al., 2012; Zhu et al., 2013; Xu et al., 2014;

Giles et al., 2015b,c; Giles et al., 2017. A pineal foramen is variably present in *Cheirolepis canadensis* (Pearson & Westoll, 1979; Arratia & Cloutier, 1996), *C. trailli* (Pearson & Westoll, 1979), *Kentuckia deani* (Rayner, 1951) and *Meemannia* (Zhu et al., 2010), and these taxa are coded '0/1' to reflect this polymorphism.)

0 present

1 absent

27. Pineal eminence (Friedman, 2007; Zhu et al., 2009; Giles et al., 2015b; Giles et al., 2017. Can only be coded in taxa that lack a pineal foramen.)

0 absent

1 present

28. Shape of parietals (sarcopterygian postparietals) (Dietze, 2000; Schultze & Cumbaa, 2001; Cloutier & Arratia, 2004; Friedman & Blom, 2006; Long et al., 2008; Swartz, 2009; Choo, 2011; Xu et al., 2014; Giles et al., 2015b; Giles et al., 2017.)

0 rectangular, with long axis parallel to midline

1 quadrate

29. Relative lengths of frontals and parietals (sarcopterygian parietals and postparietals) (Lund et al., 1995; Taverne, 1997; Dietze, 2000; Lund, 2000; Poplin & Lund, 2000; Schultze & Cumbaa, 2001; Lund & Poplin, 2002; Cloutier & Arratia, 2004; Friedman & Blom, 2006; Zhu et al., 2006; Long et al., 2008; Swartz, 2009; Choo, 2011; López-Arbarello 2012; Xu et al., 2014; Bermúdez-Rochas & Poyato-Ariza 2015; Thies &

Waschkewitz, 2015; Gibson 2016; Giles et al., 2015b; Giles et al., 2017; López-Arbarello & Sferco 2018.)

0 frontal shorter than parietal

1 frontal approximately equal to parietal

2 frontal longer than parietal

30. Frontals broad posteriorly and tapering anteriorly (Arratia 1999; López-Arbarello 2012; Bermúdez-Rochas & Poyato-Ariza 2015; Thies & Waschkewitz, 2015; Gibson 2016; Giles et al., 2017; López-Arbarello & Sferco 2018.)

0 absent

1 present

31. Anterior pit line (Giles et al., 2015b,c; Giles et al., 2017. Although not figured, an anterior pit line is described for *Miguashaia* (Cloutier 1996).)

0 absent

1 present

32. Otic canal extends through parietals(Giles et al., 2015b,c; Giles et al., 2017.)

0 absent

1 present

33. Posterior junction between supraorbital and infraorbital canals (López-Arbarello 2012; Bermúdez-Rochas & Poyato-Ariza 2015; Poyato-Ariza 2015; Giles et al., 2017; López-Arbarello & Sferco 2018. The supraorbital canal may terminate in the frontal/parietal, or it may become

confluent with the infraorbital canal. The exact position of this junction is highly variable, and typically occurs in the region of the frontal, dermosphenotic, dermopterotic.)

0 absent

1 present

34. Anterior branch of infraorbital sensory canal (Giles et al., 2017. In some taxa (e.g. *Dapedium*), the infraorbital canal continues anteriorly above the orbit a short way.)

0 absent

1 present

35. Tabular (Lund et al., 1995; Cloutier & Ahlberg, 1996; Schultze & Cumbaa, 2001; Zhu & Schultze, 2001; Cloutier & Arratia, 2004; Long et al., 2008; Swartz, 2009; Giles et al., 2015b; Giles et al., 2017.)

0 present

1 absent

36. Tabular pit line (Giles et al., 2015b,c; Giles et al., 2017.)

0 absent

1 present

37. Number of bones carrying otic portion of lateral line canal between dermosphenotic and posterior edge of skull roof. (Gardiner & Schaeffer 1989; Cloutier & Arratia, 2004; Hurley et al. 2007; Choo, 2011; Giles et al., 2015b; Xu & Zhao, 2016; Giles et al., 2017. This character is reformulated from Choo's character 'Dermopterotic: present/absent'. Rather than designating bones as an intertemporal (or supratemporal or

dermosphenotic) a priori, we consider the number of bones carrying the otic portion of the lateral line canal between the dermosphenotic and the posterior edge of the skull roof. Where two bones are present, these are treated as the intertemporal and supratemporal; where only one is present, this is treated as the dermopterotic. Anamestic bones between the dermosphenotic and frontal are not included in this count.)

0 at least two (i.e. intertemporal and supratemporal)

1 one (i.e. dermopterotic)

38. Intertemporal - relative length (Taverne, 1997; Friedman & Blom, 2006; Choo, 2011; Giles et al., 2015b; Giles et al., 2017. Coded as inapplicable in taxa with a dermopterotic. Coded as inapplicable in taxa with a dermopterotic.)

0 shorter than supratemporal

1 of similar length to supratemporal

2 longer than supratemporal

39. Intertemporal - contact with supratemporal anterior to that between frontal and parietal (Friedman & Blom, 2006; Choo, 2011; Giles et al., 2015b; Giles et al., 2017. Coded as inapplicable in taxa with a dermopterotic.)

0 absent

1 present

40. Intertemporal contacts nasal (Xu & Gao, 2011; Xu et al., 2014; Giles et al., 2015b; Giles et al., 2017. Coded as inapplicable in taxa with a dermopterotic.)

0 absent

1 present

41. Supratemporal - narrow anterolateral flange forming ventral margin of spiracular opening (Choo, 2011; Giles et al., 2015b; Giles et al., 2017. Coded as inapplicable in taxa with a dermopterotic.)

0 absent

1 present

42. Parietal fused to dermopterotic (Xu & Gao 2011; Xu et al. 2014; Giles et al., 2017. Coded as inapplicable in taxa with a separate intertemporal and supertemporal, and in taxa lacking these bones entirely.)

0 absent

1 present

43. Bone carrying otic portion of lateral line canal extends past posterior margin of parietals (Lu et al. 2016; Giles et al., 2017.)

0 absent

1 present

44. Number of paired extrascapulars (Gardiner & Schaeffer, 1989; Lund et al., 1995; Cloutier & Ahlberg, 1996; Grande & Bemis 1998; Coates, 1998; Lund, 2000; Poplin & Lund, 2000; Schultze & Cumbaa, 2001; Zhu & Schultze, 2001; Lund & Poplin, 2002; Cloutier & Arratia, 2004; Friedman & Blom, 2006; Long et al., 2008; Swartz, 2009; Choo, 2011; López-Arbarello 2012; Zhu et al., 2013; Bermúdez-Rochas & Poyato-Ariza 2015; Poyato-Ariza 2015; Giles et al., 2015b; Thies &

Waschkewitz, 2015; Xu et al., 2015; Gibson 2016; Xu & Zhao, 2016; Giles et al., 2017; López-Arbarello & Sferco 2018.)

0 one pair

1 two pairs

2 three or more pairs

45. Extrascapular reaches lateral edge of skull roof (Giles et al., 2015b,c; Giles et al., 2017. The skull roof of *Moythomasia* as shown in Fig. 103 (Gardiner, 1984) is a restoration (see also Choo 2015: fig. 13). The only skull roof directly figured by Gardiner does not preserve the extrascapulars in situ (fig. 83). However, in specimens viewed by us, as well as in published photos of articulated material (e.g. Choo 2015: fig 8), the lateral extrascapular of *M. durgaringa* is clearly excluded from the lateral margin of the skull roof.)

0 absent

1 present

46. Single median extrascapular (Dietze, 2000; Cloutier & Arratia, 2004; Long et al., 2008; Swartz, 2009; Choo, 2011; Xu & Gao, 2011; Zhu et al., 2013; Xu et al., 2014; Giles et al., 2015b; Giles et al., 2017.)

0 present

1 absent

47. Extrascapulae contact each other at midline (Giles et al., 2015b,c; Giles et al., 2017. Inapplicable for taxa that possess a median extrascapular, as it is logically impossible for the lateral extrascapulae to meet in the midline.)

0 absent

1 present

48. Medially-directed branch of sensory canal in extrascapulae (Choo, 2011; Giles et al., 2015b; Giles et al., 2017.)

0 present

1 absent

49. Extratemporal (Cloutier & Ahlberg, 1996; Ahlberg & Johanson, 1998; Zhu & Schultze, 2001; Zhu et al., 2001; Zhu & Yu, 2002; Zhu & Ahlberg, 2004; Daeschler et al., 2006; Long et al., 2006; Zhu et al., 2006; Friedman, 2007; Zhu et al., 2009; Giles et al., 2015b; Giles et al., 2017.)

0 absent

1 present

50. Antorbital bone (Gardiner & Schaeffer 1989; Lund et al. 2000; Cloutier & Arratia, 2004; Hurley et al. 2007; Choo, 2011; Xu & Gao, 2011; Xu et al., 2014; Giles et al., 2015b; Giles et al., 2017; López- Arbarello & Sferco 2018.)

0 absent

1 present

51. Tube-like canal bearing anterior arm of antorbital (Grande 2010; Xu & Wu 2012; Xu et al. 2014; Poyato-Ariza 2015; Xu & Shen, 2015; Xu & Zhao, 2016; Giles et al., 2017; López-Arbarello & Sferco 2018.)

0 absent

1 present

52. Infraorbitals (Cloutier & Arratia, 2004; Gardiner et al., 2005; Choo, 2011; Xu & Gao, 2011; Xu et al., 2014; Giles et al., 2015b; Giles et al., 2017; López-Arbarello & Sferco 2018.)

0 one

1 two

2 more than two

53. Anterior expansion of lacrimal (Taverne, 1997; Friedman & Blom, 2006; Long et al., 2008; Swartz, 2009; Choo, 2011; Giles et al., 2015b; Giles et al., 2017.)

0 absent

1 present

54. Notch in anterior margin of jugal (Cloutier & Arratia, 2004; Friedman & Blom, 2006; Long et al., 2008; Swartz, 2009; Choo, 2011; Giles et al., 2015b; Giles et al., 2017; Xu et al., 2014.

0 absent

1 present

55. Suborbitals (non-canal bearing ossifications separating jugal and maxilla)

(Gardiner & Schaeffer 1989; Olsen & McCune 1991; Taverne, 1997; Schultze & Cumbaa, 2001; Friedman & Blom, 2006; Long et al., 2008; Choo, 2011; López-Arbarello 2012; Xu & Gao 2011; Bermúdez-Rochas & Poyato-Ariza 2015; Poyato-Ariza 2015; Giles et al., 2015b; Thies & Waschkewitz, 2015; Xu et al., 2015; Gibson 2016; Xu & Zhao, 2016; Giles et al., 2017; López-Arbarello & Sferco 2018.)

0 absent

1 one

2 two

3 three or more

56. Multiple rami of infraorbital canal in jugal (Giles et al., 2015b,c; Giles et al., 2017. Multiple branches radiate from the infraorbital canal in the jugal of many Carboniferous and younger actinopterygians.)

0 absent 1 present

57. Dermosphenotic with distinct posterior ramus (Gardiner & Schaeffer, 1989; Coates, 1998; Schultze & Cumbaa, 2001; Cloutier & Arratia, 2004; Friedman & Blom, 2006; Zhu et al., 2006; Long et al., 2008; Zhu et al., 2009; Choo, 2011; Giles et al., 2015b; Xu et al., 2015; Giles et al., 2017. The dermosphenotic of *Moythomasia* illustrated by (Gardiner 1984, fig 69) lacks a posterior limb, but this is from a small individual and most likely reflects ontogenetic variability, with a posterior limb being developed in larger individuals (B. Choo, pers. comm.; Choo 2015: fig. 8). The posterior limb of the dermosphenotic is variably developed in *Mesopoma* (Coates, 1999), so this taxon is scored '0/1' to reflect this polymorphism.)

0 absent

1 present

58. Dermosphenotic- contact with frontals blocked by intertemporal or dermopterotic (Friedman & Blom, 2006; Choo, 2011; Giles et al., 2015b; Giles et al., 2017.)

0 absent

1 present

59. Supraorbital (Gardiner & Schaeffer 1989; Grande & Bemis 1998; Hurley et al. 2007; Xu & Gao 2011; Xu et al. 2014; Poyato-Ariza 2015; Xu et al., 2015; Xu & Zhao, 2016; Giles et al., 2017; López-Arbarello & Sferco 2018.)

0 absent

1 one or two

2 three or more

60. Anterior-most infraorbital anterior to orbit (i.e. does not contribute to orbital margin) (Olsen & McCune 1991; Cavin & Suteethorn 2006; López-Arbarello 2012; Bermúdez- Rochas & Poyato-Ariza 2015; Thies & Waschkewitz, 2015; Gibson 2016; Giles et al., 2017; López-Arbarello & Sferco 2018.)

0 absent

1 present

61. Three or more lacrimals (Grande 2010; Xu & Wu 2012; Xu et al. 2014, 2015; Bermúdez-Rochas & Poyato-Ariza 2015; Poyato-Ariza 2015; Thies & Waschkewitz, 2015; Gibson 2016; Xu & Zhao, 2016; Giles et al., 2017. The first lachrymal is regarded here as the anteriormost canal-bearing bone that contributes to orbital margin.)

0 absent

1 present

62. Circumorbital ring (Wiley 1976; López-Arbarello 2012; Bermúdez-Rochas & Poyato-Ariza 2015; Poyato-Ariza 2015; Thies & Waschkewitz, 2015; Gibson 2016; Giles et al., 2017; López-Arbarello & Sferco 2018.)

0 Supraorbitals do not contact infraorbitals at the anterior rim of the orbit.

1 Supraorbitals contact infraorbitals, closing the orbit.

63. Jugal canal (Patterson, 1982; Lauder & Liem, 1983; Gardiner, 1984; Cloutier & Arratia, 2004; Brazeau, 2009; Friedman & Brazeau, 2010; Choo, 2011; Davis et al., 2012; Zhu et al., 2013; Giles et al., 2015b,c; Giles et al., 2017.)

0 absent

1 present

64. Dermohyal (Patterson, 1982; Gardiner & Schaeffer, 1989; Lund et al., 1995; Cloutier & Ahlberg, 1996; Coates, 1998; Dietze, 2000; Lund, 2000; Schultze & Cumbaa, 2001; Zhu & Schultze, 2001; Zhu et al., 2001; Lund & Poplin, 2002; Zhu & Yu, 2002; Cloutier & Arratia, 2004; Gardiner et al., 2005; Friedman & Blom, 2006; Zhu et al., 2006; Friedman, 2007; Long et al., 2008; Swartz, 2009; Zhu et al., 2009; Choo, 2011; Xu & Gao, 2011; Xu et al., 2014; 2015; Giles et al., 2015b; Xu & Zhao, 2016; Giles et al., 2017. This region of the cheek is missing in *Coccocephalichthys* (Poplin, 1974; Poplin & Véran, 1996), and was presumably removed by Watson (1925) when he first described the specimen. It is unclear from the surviving cast whether a dermohyal and/or accessory operculum were present, and as such this taxon is coded as ‘?’.)

0 absent

1 present

65. Head of dermohyal projects above dorsal margin of operculum (Giles et al., 2015b,c; Giles et al., 2017. The dermohyal is not preserved in *Melanecta* (Coates, 1998), but it is clear from the surrounding bones that it would not have projected above the dorsal surface of the operculum.)

0 absent

1 present

66. Dermohyal (Gardiner et al., 2005; Coates, 1999; Xu & Gao, 2011; Xu et al., 2014; Giles et al., 2015b; Giles et al., 2017.)

0 fused to hyomandibular

1 separate from hyomandibular

67. Complete enclosure of spiracle by bones bearing otic and infraorbital canals (Friedman, 2007; Zhu et al., 2009; Giles et al., 2015b; Giles et al., 2017.)

0 absent

1 present

Jaws and palate

68. Maxilla (Zhu & Yu, 2002; Friedman, 2007; Xu et al., 2014, 2015; Giles et al., 2015b; Xu & Zhao, 2016; Giles et al., 2017; López-Arbarello & Sferco 2018.)

0 absent

1 present

69. Expanded dorsal lamina of maxilla (Lund et al., 1995; Lund, 2000; Poplin & Lund, 2000; Schultze & Cumbaa, 2001; Zhu & Schultze, 2001; Zhu et al., 2001; Zhu & Yu, 2002; Lund & Poplin, 2002; Cloutier & Arratia, 2004; Zhu et al., 2006; Friedman, 2007; Zhu et al., 2009; Zhu et al., 2013; Giles et al., 2015b,c; Giles et al., 2017; López-Arbarello & Sferco 2018.)

0 absent

1 present

70. Contribution by maxilla to posterior margin of cheek (Friedman, 2007; Zhu et al., 2009; Zhu et al., 2013; Giles et al., 2015b,c; Giles et al., 2017; López-Arbarello & Sferco 2018.)

0 absent

1 present

71. Sensory canal/pit line associated with maxilla (Grande & Bemis 1998; Friedman, 2007; Zhu et al., 2009; Zhu et al., 2013; Giles et al., 2015b; Giles et al., 2017.)

0 absent

1 present

72. Teeth on maxilla (Poyato-Ariza & Wenz, 2002; Cloutier & Arratia, 2004; López-Arbarello 2012; Xu et al. 2014, 2015; Bermúdez-Rochas & Poyato-Ariza 2015; Poyato-Ariza 2015; Thies & Waschkewitz, 2015; Gibson 2016; Xu & Zhao, 2016; Giles et al., 2017; Cawley & Kriwet 2018; López-Arbarello & Sferco 2018.)

0 present

1 absent

73. Mobile maxilla in cheek (Patterson 1973; Gardiner & Schaeffer 1989; Olsen & McCune 1991; Gardiner et al. 1996; Gardiner et al. 2005; Coates 1999; Hurley et al. 2007; Xu & Gao 2011; Poyato-Ariza 2015; Xu et al. 2014, 2015; Xu & Zhao, 2016; Giles et al., 2017.)

0 absent

1 present

74. Peg-like anterior process of maxilla (Grande 2010; Xu & Wu 2012; Xu et al. 2014; Poyato-Ariza 2015; Giles et al., 2017.)

0 absent

1 present

75. Posterior maxillary notch (Grande & Bemis 1998; Xu & Wu 2012; Xu et al. 2014, 2015. Arratia 2013; Xu & Zhao, 2016; Giles et al., 2017; López-Arbarello & Sferco 2018.)

0 absent

1 present

76. Supramaxilla (Grande & Bemis 1998; Gardiner & Schaeffer 1989; Olsen & McCune 1991; Gardiner et al. 1996; Gardiner et al. 2005; Coates 1999; Hurley et al. 2007; Xu & Gao 2011; Xu et al. 2014, 2015; Bermúdez-Rochas & Poyato-Ariza 2015; Poyato-Ariza 2015; Xu & Shen, 2015; Thies & Waschkewitz, 2015; Gibson 2016; Xu & Zhao, 2016; Giles et al., 2017; López-Arbarello & Sferco 2018.)

0 absent

1 one

2 two

77. Course of mandibular canal (Friedman & Blom, 2006; Long et al., 2008; Swartz, 2009; Choo, 2011; Giles et al., 2015b; Giles et al., 2017.)

0 traces ventral margin of jaw along entire length

1 arches dorsally in anterior half of jaw

78. Mandibular canal reaches anterior margin of mandible (Giles et al., 2015b,c; Giles et al., 2017.)

0 present

1 absent

79. Mandibular canal (Patterson, 1982; Cloutier & Ahlberg, 1996; Coates, 1998; Schultze & Cumbaa, 2001; Zhu & Schultze, 2001; Zhu et al., 2001; Zhu & Yu, 2002; Cloutier & Arratia, 2004; Zhu et al., 2006; Friedman, 2007; Zhu et al., 2009; Choo, 2011; Zhu et al., 2013; Giles et al., 2015b; Giles et al., 2017.)

0 primarily carried by infradentaries

1 primarily carried by dentary

80. Relative length of dentary (Ahlberg & Johanson, 1998; Zhu et al., 2001; Zhu & Yu, 2002; Zhu & Ahlberg, 2004; Friedman, 2007; Zhu et al., 2009; Giles et al., 2015b; Giles et al., 2017.)

0 long (constitutes most of the length of the lower jaw)

1 short (constitutes less than half of jaw length)

81. Teeth on dentary (Cloutier & Arratia 2004, Xu et al. 2014; Giles et al., 2017; López-Arbarello & Sferco 2018.)

0 present

1 absent

82. Dentary with conspicuously reflexed distal tip (Friedman & Blom, 2006; Long et al., 2008; Swartz, 2009; Choo, 2011; Giles et al., 2015b; Giles et al., 2017.)

0 absent

1 present

83. Enlarged series of parasymphysial teeth on dentary (Friedman & Blom, 2006; Long et al., 2008; Swartz, 2009; Choo, 2011; Giles et al., 2017.)

0 absent

1 present

84. Facet for parasymphysial tooth-whorl on anterior dentary (Choo, 2011; Giles et al., 2015b; Giles et al., 2017.)

0 present

1 absent

85. Teeth of outer dental arcade (Friedman, 2007; Giles et al., 2015b; Poyato-Ariza 2015; Giles et al., 2017; López-Arbarello & Sferco 2018. Coates (1998) states that the maxilla of *Melanecta* bears large teeth interspersed with smaller teeth, but it is unclear how these teeth are arranged. As such, this taxon is coded '?'.)

0 several rows of disorganized teeth

1 two rows, with large teeth lingually and small teeth labially

2 single row of teeth

86. Jaw margins overlain by lateral lamina (Giles et al. 2017. In *Styracopterus*, *Fouldenia* and *Amphicentrum*, a lateral lamina of bone obscures the maxillary dentition (Sallan & Coates 2013).)

0 absent

1 present

87. Acrodin caps on teeth (Patterson, 1982; Gardiner, 1984; Maisey, 1986; Gardiner & Schaeffer, 1989; Cloutier & Ahlberg, 1996; Taverne, 1997; Coates, 1999; Poplin & Lund, 2000; Schultze & Cumbaa, 2001; Zhu & Schultze, 2001; Zhu et al., 2001; Zhu & Yu, 2002; Cloutier & Arratia, 2004; Gardiner et al., 2005; Friedman & Blom, 2006; Zhu et al., 2006; Friedman, 2007; Long et al., 2008; Zhu et al., 2009; Friedman & Brazeau, 2010; Choo, 2011; Xu & Gao, 2011; Zhu et al., 2013; Xu et al., 2014; Giles et al., 2015b,c; Giles et al., 2017.)

0 absent

1 present

88. Plicidentine (Zhu & Yu 2002; Friedman 2007; López-Arbarello 2012; Bermúdez-Rochas & Poyato-Ariza 2015; Poyato-Ariza 2015; Thies & Waschkewitz, 2015; Gibson 2016; Giles et al., 2017; López-Arbarello & Sferco 2018.)

0 absent

1 present

89. Ossification of mentomeckelian region: (Friedman & Blom, 2006; Long et al., 2008; Swartz, 2009; Grande 2010; Choo, 2011; Xu et al., 2014; Giles et al., 2015b; Poyato-Ariza 2015; Giles et al., 2017.)

0 present

1 absent

90. Number of infradentaries (Friedman & Blom, 2006; Friedman, 2007; Long et al., 2008; Choo, 2011; Xu & Gao, 2011; Xu et al., 2014; Giles et al., 2015b; Poyato-Ariza 2015; Giles et al., 2017; López-Arbarello & Sferco 2018.)

0 more than two

1 two (angular and surangular)

2 one (angular only)

91. Coronoids (sensu stricto, excluding parasymphysial tooth whorl or anterior coronoid) (Schultze and Cumbaa, 2001; Zhu and Schultze, 2001; Zhu et al., 2001; Zhu and Yu, 2002; Zhu et al., 2006; Friedman, 2007; Zhu et al., 2009; Giles et al., 2015b,c; Poyato-Ariza 2015; Giles et al., 2017; López-Arbarello & Sferco 2018.)

0 present

1 absent

92. Number of coronoids (Ahlberg & Clack, 1998; Daeschler et al., 2006; Long et al., 2006; Friedman, 2007; Zhu et al., 2009; Zhu et al., 2013; Giles et al., 2015b; Giles et al., 2017. A single specimen of *Pteronisculus stensioi* has at least five or six coronoids anterior to the prearticular region. However, these appear to correspond to the three

coronoids present in most specimens, so the taxon is coded here as '2'. Two coronoids are reported in *Boreosomus* (Nielsen, 1942).)

0 five

1 four or more

2 three

3 two

4 one

93. Posterior coronoid (Cloutier & Ahlberg, 1996; Ahlberg & Johanson, 1998; Zhu & Ahlberg, 2004; Daeschler et al., 2006; Long et al., 2006; Giles et al., 2015b; Giles et al., 2017.)

0 morphologically similar to anterior coronoids

1 expanded

94. Coronoid process of lower jaw (Patterson 1973; Gardiner & Schaeffer 1989; Olsen & McCune 1991; Poyato-Ariza & Wenz, 2002; Zhu & Yu, 2002; Friedman, 2007; Friedman, 2007; Xu & Gao 2011; Xu et al. 2014, 2015; Giles et al., 2015b; Poyato-Ariza 2015; Xu & Zhao, 2016; Giles et al., 2017; Cawley & Kriwet 2018; Cawley & Kriwet 2018; López-Arbarello & Sferco 2018.)

0 absent

1 present

95. Coronoid process contributed to by (Modified from Patterson 1973; Olsen & McCune 1991; Gardiner et al. 2005; Poyato-Ariza 2015; Giles et al., 2017; López-Arbarello & Sferco 2018.)

0 prearticular only

1 surangular only

2 dentary plus postdentary bones

3 angular only

96. Leptolepid notch (Arratia 2013; Giles et al., 2017; López-Arbarello & Sferco 2018. A distinct notch in the posterior margin of the dentary is seen in taxa such as *Leptolepis*.)

0 absent

1 present

97. Accessory hyoid element involvement in jaw joint (Grande & Bemis 1998; Olsen & McCune 1991; Grande 2010; Xu & Wu 2012; Xu et al. 2014, 2015; López-Arbarello 2012; Bermúdez-Rochas & Poyato-Ariza 2015; Poyato-Ariza 2015; Thies & Waschkewitz, 2015; Gibson 2016; Xu & Zhao, 2016; Giles et al., 2017; López-Arbarello & Sferco 2018.)

0 absent

1 present

98. Retroarticular process (Friedman, 2007; Giles et al., 2015b; Giles et al., 2017.)

0 present

1 absent

99. Palatal bite (Giles et al., 2017.)

0 absent

1 present

100. Palatal articulation with basipterygoid process (Revised from Friedman, 2007; Brazeau, 2009; Zhu et al., 2009; Friedman & Brazeau, 2010; Davis et al., 2012; Zhu et al., 2013; Giles et al., 2015b,c; Giles et al., 2017; López-Arbarello & Sferco 2018. This character is expanded from previous formulations, which only considered whether a basipterygoid fenestra was absent or present. Where a basipterygoid process is absent, the dorsal margin of the palate may be flat, or the metapterygoid may bear a distinct notch.)

0 articulation not obvious

1 via basipterygoid fenestra

2 via metapterygoid process/notch

101. Palatoquadrate ossifications (Giles et al., 2017.)

0 comineralized

1 separate ossification centres

102. Palatoquadrate symphysis (Giles et al., 2017. This character captures whether the palatoquadrates contact at the midline.

0 absent

1 present

103. Dorsal margin of palate (Giles et al., 2017.)

0 high posterior extension

1 flat dorsal margin

104. Metapterygoid posterior to quadrate (Giles et al., 2017.)

0 absent

1 present

105. Number of dermopalatines (Friedman, 2007; Giles et al., 2015b; Giles et al., 2017.)

0 multiple

1 single

106. Prearticular (Poyato-Ariza 2015; Giles et al., 2017; López-Arbarello & Sferco 2018.)

0 present

1 absent

107. Vomers (Patterson 1973; Olsen & McCune 1991; López-Arbarello 2012; Arratia 2013; Xu & Wu, 2012; Bermúdez-Rochas & Poyato-Ariza 2015; Poyato-Ariza 2015; Thies & Waschkewitz, 2015; Gibson 2016; Xu & Zhao, 2016; Giles et al., 2017; López-Arbarello & Sferco 2018.)

0 paired

1 single

108. Vomer sutured to parasphenoid (Patterson 1973; Olsen & McCune 1991; Hurley et al. 2007; Giles et al., 2017.)

0 absent

1 present

Operculogular system

109. Accessory operculum (Schultze & Cumbaa, 2001; Cloutier & Arratia, 2004; Friedman & Blom, 2006; Long et al., 2008; Swartz, 2009; Giles et al., 2015b; Giles et al., 2017. This region of the cheek was removed in Coccocephalichthys (Poplin, 1974; Poplin & Véran, 1996),

presumably by Watson (1925) when he first described the specimen. It is unclear from the surviving cast whether a dermohyal and/or accessory operculum were present, and as such this taxon is coded as '?'.)

0 absent

1 present

110. Operculum

0 absent

1 present

111. Operculum - relative size (Modified from Lund et al., 1995; Lund, 2000; Lund & Poplin, 2002; Cloutier & Arratia, 2004; Long et al., 2008; Swartz, 2009; Choo, 2011; López-Arbarello 2012; Bermúdez-Rochas & Poyato-Ariza 2015; Xu et al., 2015; Giles et al., 2015b; Thies & Waschkewitz, 2015; Gibson 2016; Xu & Zhao, 2016; Giles et al., 2017; López-Arbarello & Sferco 2018.)

0 at least twice as high as subopercular

1 subequal

2 smaller than subopercular

111. Subopercle (Poyato-Ariza & Wenz, 2002; Xu et al. 2014; Giles et al., 2017; Cawley & Kriwet 2018.)

0 present

1 absent

113. Anterodorsal process of subopercular (Long et al., 2008; Choo, 2011; López-Arbarello 2012; Bermúdez-Rochas & Poyato-Ariza 2015; Giles et al., 2015b; Thies & Waschkewitz, 2015; Poyato-Ariza 2015;

Gibson 2016; Giles et al., 2017; López-Arbarello & Sferco 2018. An anterodorsal process is present some non-neopterygian actinopterygians and 'semionotiforms'. Although these processes do not appear to be homologous they are coded within the character.)

0 absent

1 present

114. Anteroventral process of suboperculum (Giles et al., 2017.)

0 absent

1 present

115. Number of cheek bones bearing pre-opercular canal posterior to jugal

(Friedman, 2007; Zhu et al., 2009; Zhu et al., 2013; Giles et al., 2015b; Xu & Zhao, 2016; Giles et al., 2017.)

0 one

1 multiple

2 series of small ossicles

116. Preoperculum orientation (Modified from Patterson 1973; Olsen & McCune 1991; Grande & Bemis 1998; Gardiner et al., 2005; Swartz 2009; López-Arbarello 2012; Bermúdez-Rochas & Poyato-Ariza 2015; Thies & Waschkewitz, 2015; Poyato-Ariza 2015; Gibson 2016; Giles et al., 2017; López- Arbarello & Sferco 2018. This character is reformulated from its original (compound) formulation, which considered both maxilla and preoperculum shape. Primitively in actinopterygians the preoperculum is wholly or partially developed dorsal to the maxilla as an

anterodorsal-posteroventrally oriented bone, either with (e.g. *Mimipiscis*, *Moythomasia*) or without (e.g. *Cheirolepis*) a dorsoventrally oriented limb. The preoperculum may also be near-vertical, with no distinct anterodorsal or anteroventral extensions (e.g. *Boreosomus*, *Peltopleurus*), or developed as an anteroventral-posterodorsally-directed bone largely ventral to the maxilla (e.g. *Discoserra*, *Propterus*).)

0 prounounced dorsal limb

1 vertical

2 pronounced ventral limb

117. Junction between preopercular and more anterior cheek bones

(Modified from López-Arbarello 2012; Bermúdez-Rochas & Poyato-Ariza 2015; Poyato- Ariza 2015; Thies & Waschkewitz, 2015; Gibson 2016; Giles et al., 2017; López-Arbarello & Sferco 2018.)

0 Infraorbitals (including jugal) or suborbitals suture with or abut preopercular

1 Infraorbitals (including jugals) and suborbitals broadly overlap preopercular

118. Posterior border of preopeculum notched ventrally (López-Arbarello 2012; Bermúdez-Rochas & Poyato-Ariza 2015; Giles et al., 2017; Thies & Waschkewitz, 2015; Gibson 2016; López-Arbarello & Sferco 2018.)

0 absent

1 present

119. Interopercle (Patterson 1973; Grande & Bemis 1998; Gardiner & Schaeffer 1989; Olsen & McCune 1991; Poyato-Ariza & Wenz, 2002; Xu & Gao 2011; Xu et al. 2014, 2015. Gardiner & Schaeffer 1989; Olsen & McCune 1991; Gardiner et al. 1996; Gardiner et al. 2005; Cavin & Suteethorn 2006; Hurley et al. 2007; López-Arbarello 2012; Bermúdez-Rochas & Poyato-Ariza 2015; Poyato-Ariza 2015; Thies & Waschkewitz, 2015; Gibson 2016; Xu & Zhao, 2016; Giles et al., 2017; Cawley & Kriwet 2018; López-Arbarello & Sferco 2018.)

0 absent

1 present

120. Branchiostegal rays - dorsal-most in series (Lund et al., 1995; Cloutier & Arratia, 2004; Choo, 2011; Giles et al., 2015b; Giles et al., 2017.)

0 of similar depth to adjacent branchiostegal ray

1 deeper than adjacent branchiostegal ray

121. Lateral gulars (Olsen & McCune 1991; Xu et al., 2014; Giles et al., 2017.) 0 present

1 absent

122. Lateral gulars (Gardiner & Schaeffer, 1989; Cloutier & Ahlberg, 1996; Taverne, 1997; Lund & Poplin, 1997; Coates, 1999; Schultze & Cumbaa, 2001; Zhu & Schultze, 2001; Cloutier & Arratia, 2004; Friedman & Blom, 2006; Long et al., 2008; Swartz, 2009; Brazeau, 2009; Xu & Gao, 2011; Davis et al., 2012; Zhu et al., 2013; Xu et al., 2014; Giles et al., 2015b,c; Giles et al., 2017. The condition in *Boreosomus* (Nielsen,

1942) is unique: instead of lateral gulars flanking a median gular, there appears to be a second median gular. This may well represent a fusion of the two, longer lateral gulars, is coded as such.)

0 extending most of the length of the lower jaw

1 restricted to the anterior third of the lower jaw (no longer than the width of three

branchiostegals)

123. Median gular (Olsen & McCune 1991; Lund et al., 1995; Cloutier & Ahlberg, 1996; Coates, 1999; Lund, 2000; Schultze & Cumbaa, 2001; Zhu & Schultze, 2001; Zhu et al., 2001: Lund & Poplin, 2002; Zhu & Yu, 2002; Cloutier & Arratia, 2004; Zhu et al., 2006; Friedman, 2007; Zhu et al., 2009; Xu & Gao, 2011; López-Arbarello 2012; Zhu et al., 2013; Bermúdez-Rochas & Poyato-Ariza 2015; Poyato-Ariza 2015; Xu et al., 2014, 2015; Giles et al., 2015b,c; Thies & Waschkewitz, 2015; Xu & Zhao, 2015; Gibson 2016; Giles et al., 2017; López-Arbarello & Sferco 2018. Pearson & Westoll (1979: p. 365) state that a median gular is not known in *Cheirolepis canadensis*. Although a median gular is reconstructed by Cloutier & Arratia

(1996: fig. 7), this bone is not present in any specimen photos and is not mentioned in the text. As such, this taxon is coded as '?'.)

0 absent

1 present

124. Relative length of median gular (Giles et al., 2015b,c; Giles et al., 2017. The condition in *Boreosomus* (Nielsen, 1942) is unique: instead

of lateral gulars flanking a median gular, there appears to be a second median gular. This may well represent a fusion of the two, longer lateral gulars, and is coded as such.)

0 much shorter than jaw length

1 more than half of law length

Braincase

125. Fenestra ventrolateralis (Schultze & Cumbaa, 2001; Zhu & Schultze, 2001; Zhu et al., 2001; Zhu & Yu, 2002; Zhu et al., 2006; Friedman, 2007; Zhu et al., 2009; Zhu et al., 2013; Giles et al., 2015b; Giles et al., 2017.)

0 absent

1 present

126. Palatal opening surrounded by premaxilla, maxilla, dermopalatine and vomer (choana) (Zhu & Yu, 2002; Friedman, 2007; Giles et al., 2015b; Giles et al., 2017. Character can only be coded in taxa which possess all of these bones.)

0 absent

1 present

127. Internasal cavity (Ahlberg & Johanson, 1998; Zhu & Yu, 2002; Zhu & Ahlberg, 2004; Daeschler et al., 2006; Long et al., 2006; Friedman, 2007; Zhu et al., 2009; Zhu et al., 2013; Giles et al., 2015b,c; Giles et al., 2017.)

0 absent

1 present

128. Interorbital septum (Friedman, 2007; Zhu et al., 2009; Brazeau, 2009; Friedman & Brazeau, 2010; Davis et al., 2012; Zhu et al., 2013; Giles et al., 2015b,c; Giles et al., 2017.)

0 broad

1 narrow

129. Optic foramen (Giles et al., 2017. Primitively in actinopts, the optic nerve exits the cranial cavity into the orbit through paired foramina approximately halfway up the orbital wall. In many Carboniferous and younger taxa, much of the orbital wall is unossified (the optic fenestra). The optic nerves may exit through openings just posterior to (e.g. *Pteronisculus*) or confluent with (e.g. *Pholidophorus*) the optic fenestra. In polypterids and *Fukangichthys*, the optic nerve exits ventrally through paired foramina that abut the parasphenoid.)

0 dorsally positioned

1 ventrally positioned (i.e. abuts parasphenoid)

130. Pronounced median anterior crista on dorsal surface of braincase (Giles et al., 2015b,c; Giles et al., 2017. Carboniferous and younger actinopts such as *Lawrenciella* (Hamel & Poplin, 2008) have a median crista anterior to the anterior dorsal fontanelle upon which the skull roof sits.)

0 absent

1 present

131. Expanded anterior dorsal fontanelle (Giles et al., 2015b,c; Giles et al., 2017. The anterior dorsal fontanelle of many Carboniferous

and younger actinopts is greatly expanded, in contrast to the smaller fontanelle of Devonian taxa such as *Mimipiscis* (Gardiner, 1984).)

0 absent

1 present

132. Endoskeletal intracranial joint (Cloutier & Ahlberg, 1996; Ahlberg & Johanson, 1998; Zhu & Ahlberg, 2004; Zhu et al., 2001; Zhu & Yu, 2002; Daeschler et al., 2006; Long et al., 2006; Friedman, 2007; Brazeau, 2009; Zhu et al., 2009; Friedman & Brazeau, 2010; Davis et al., 2013; Zhu et al., 2013; Giles et al., 2015b,c; Giles et al., 2017.)

0 absent

1 present

133. Eye stalk or unfinished area for similar structure (Zhu & Schultze, 2001; Zhu et al., 2001; Zhu & Yu, 2002; Zhu et al., 2006; Friedman, 2007; Zhu et al., 2009; Zhu et al., 2013; Giles et al., 2015b,c; Giles et al., 2017. This character is coded as absent for taxa that possess a large interorbital fenestra (e.g. *Pteronisculus*, *Coccocephalichthys*, *Kentuckia deani*), as, if present, the eyestalk area would be visible posterior to the opening for the optic nerve.)

0 absent

1 present

134. Roof of posterior myodome perforated by palatine branch of facial nerve (VII) (Coates, 1999; Giles et al., 2015b; Giles et al., 2017.)

0 absent

1 present

135. Foramen for abducens nerve (VI) dorsally positioned (level with optic foramen (II)) (Coates, 1999; Giles et al., 2015b; Giles et al., 2017.)

0 absent

1 present

136. Anterodorsal myodome (Patterson 1973; Olsen & McCune 1991; Coates, 1999; Gardiner et al. 1996; Hurley et al. 2007; Xu & Gao, 2011; Xu et al., 2014, 2015; Giles et al., 2015b; Poyato-Ariza 2015; Xu & Zhao, 2016; Giles et al., 2017.)

0 paired

1 single

2 absent

137. Posterior myodome (Modified from Patterson 1973; Olsen & McCune 1991; Coates, 1999; Xu et al., 2014. Wiley 1976; Gardiner, 1984; Gardiner & Schaeffer, 1989; Gardiner et al. 1996; Hurley et al. 2007; López-Arbarello 2012; Xu & Gao, 2011; Bermúdez-Rochas & Poyato-Ariza 2015; Xu et al. 2014, 2015; Giles et al., 2015b; Thies & Waschkewitz, 2015; Gibson 2016; Xu & Zhao, 2016; Giles et al., 2017; López-Arbarello & Sferco 2018.)

0 absent

1 paired

2 median

138. Basicranial fenestra (Ahlberg & Johanson, 1998; Zhu et al., 2001; Zhu & Yu, 2002; Zhu & Ahlberg, 2004; Friedman, 2007; Zhu et al., 2009; Zhu et al., 2013; Giles et al., 2015b,c; Giles et al., 2017.)

0 absent

1 present

139. Endoskeletal spiracular canal (Modified from Patterson, 1982; Gardiner, 1984; Gardiner & Schaeffer, 1989; Taverne, 1997; Coates, 1999; Gardiner et al., 2005; Xu & Gao, 2011; Xu et al., 2014; Giles et al., 2015b; Giles et al., 2017; López-Arbarello & Sferco 2018. Taxa that lack a groove on the lateral commissure are coded as inapplicable for this character.)

0 open

1 partial closure or spiracular bar

2 complete enclosure in canal

140. Basipterygoid process (Gardiner et al., 2005; Xu & Gao, 2011; Xu et al., 2014, 2015; Giles et al., 2015b; Xu & Zhao, 2016; Giles et al., 2017; López-Arbarello & Sferco 2018.)

0 present

1 absent

141. Basipterygoid process with vertically oriented component (Ahlberg & Johanson, 1998; Zhu & Schultze, 2001; Zhu et al., 2001; Zhu & Yu, 2002; Zhu & Ahlberg, 2004; Zhu et al., 2006; Friedman, 2007; Zhu et al., 2009; Davis et al., 2012; Zhu et al., 2013; Giles et al., 2015b,c; Giles et al., 2017.)

0 absent

1 present

142. Dermal component to basipterygoid process (Gardiner, 1984; Gardiner & Schaeffer, 1989; Taverne, 1997; Coates, 1999; Giles et al., 2015b; Giles et al., 2017.)

0 absent

1 present

143. Hyoid facet (Gardiner et al. 2005; Gardiner et al. 1996; Hurley et al. 2007; Xu & Gao 2011; Xu et al. 2015; Giles et al., 2017; López-Arbarello & Sferco 2018.)

0 directed posteroventrally

1 horizontal

144. Fossa bridgei (Gardiner, 1984; Gardiner & Schaeffer, 1989; Taverne, 1997; Coates, 1999; Xu & Gao, 2011; Xu et al., 2014; Giles et al., 2015b; Giles et al., 2017.)

0 absent

1 present

145. Posttemporal fossae (Zhu & Yu, 2002; Friedman, 2007.)

0 absent

1 present

146. Vestibular fontanelle (Friedman, 2007; Brazeau, 2009; Zhu et al., 2009; Friedman & Brazeau, 2010; Davis et al., 2012; Zhu et al., 2013; Brazeau & Friedman, 2014; Giles et al., 2015b,c; Giles et al., 2017.)

0 absent

1 present

147. Ventral cranial fissure and vestibular fontanelle (Coates, 1999; Giles et al., 2015b; Giles et al., 2017. We follow Coates (1999) in coding Howqualepis as '0' on the basis of Long 1988 fig. 16 and AMF65495 (pers. obs. S.G.), rather than the braincase reconstruction (Long, 1988: fig. 18.)

0 separated by bridge of bone

1 confluent

148. Accessory fenestration in otic capsule (Friedman, 2007; Zhu et al., 2009; Giles et al., 2015b; Giles et al., 2017.)

0 absent

1 present

149. Otoccipital fissure (Friedman, 2007; Brazeau, 2009; Davis et al., 2012; Zhu et al., 2013; Giles et al., 2015b,c; Giles et al., 2017.)

0 absent

1 present

150. Median projection overhanging posterior part of posterior dorsal fontanelle (Giles et al., 2015b; Giles et al., 2017. Variable in *Boreosomus*: the posterior dorsal fontanelle is closed in the specimen figured in Nielsen (1942: plate 25F), but developed in the specimen figured in plate 28. This taxon is coded ‘0/1’ to reflect this polymorphism.)

0 absent

1 present

151. Median projection overhanging anterior part of posterior dorsal fontanelle (Giles et al., 2015b; Giles et al., 2017. This projection is

somewhat reduced in *Pteronisculus* (Nielsen, 1942), but is coded '1' here. Variable in *Boreosomus*: the posterior dorsal fontanelle is closed in the specimen figured in Nielsen 1942 plate 25F, but developed in the specimen figured in plate 28. This taxon is coded ‘0/1’ to reflect this polymorphism. *Cheirolepis trailli* is coded '0' (2015a).)

0 absent

1 present

152. Craniospinal processes

0 absent

1 present

153. Dorsal aorta (Coates & Sequeira, 1998; Coates & Sequeira, 2001a, b; Coates, 1999; Friedman, 2007; Zhu et al., 2009; Friedman & Brazeau, 2010; Zhu et al., 2013; Giles et al., 2015b,c; Giles et al., 2017; López-Arbarello & Sferco 2018. This character is coded as inapplicable in taxa that lack a canal for the dorsal aorta. *Cheirolepis trailli* is coded '0' (Giles et al., 2015a). The aortic canal of *Moythomasia* is not figured by Gardiner (1984), but a clear posterior notch in the aortic canal can be seen in Long & Trinajstic (2010:fig 5b). The neurocranium of *Gogosardina* is not yet described, but this character can be coded on the basis of Choo et al. (2009: fig. 9).)

0 open in groove

1 canal notched posteriorly

2 completely enclosed in canal

154. Dorsal aorta pierced by canal/s for exit of eff.a.2 (Giles et al., 2015b; Giles et al., 2017. In *Mimipiscis bartrami* and *M. toombsi*, a groove for one of the efferent branchial arteries branches off from the lateral dorsal aorta immediately before the articular area for the first infrapharyngobranchial. However, it is uncertain which, so both taxa coded as '?' for these characters. The neurocranium of *Gogosardina* is not yet described, but this character can be coded on the basis of Choo et al. (2009: fig. 9).)

0 absent

1 present

155. Dorsal aorta pierced by canal/s for exit of eff.a.1 (Giles et al., 2015b; Giles et al., 2017. In *Mimipiscis bartrami* and *M. toombsi*, a groove for one of the efferent branchial arteries branches off from the lateral dorsal aorta immediately before the articular area for the first infrapharyngobranchial. However, it is uncertain which, so both taxa coded as '?' for these characters. The neurocranium of *Gogosardina* is not yet described, but this character can be coded on the basis of Choo et al. (2009: fig. 9).)

0 absent

1 present

156. Bifurcation of dorsal aort (Coates & Sequeira, 1998; Coates & Sequeira, 2001a, b; Coates, 1999; Friedman, 2007; Zhu et al., 2009; Friedman & Brazeau, 2010; Zhu et al., 2013; Giles et al., 2015b,c; Giles et al., 2017.)

0 posterior to occiput

1 anterior to occiput

157. Bifurcation of dorsal aorta into lateral dorsal aortae (Coates, 1999; Giles et al., 2015b; Giles et al., 2017. This character is coded as inapplicable in taxa that lack a canal for the dorsal aorta. In *Mimipiscis toombsi*, the bifurcation point of the dorsal aorta can be open (Giles & Friedman, 2014: fig. 2) or closed (Gardiner 1984: fig. 15). This taxon is coded '0/1' to reflect this polymorphism. The aortic canal of *Moythomasia* is not figured by Gardiner (1984), but the bifucation into the lateral dorsal aortae can be seen in Long & Trinajstic (2010:fig 5b).)

0 open

1 enclosed in canal

158. Braincase ossifications differentiated (Giles et al., 2017.)

0 absent

1 present

159. Basisphenoid (Wiley 1976; López-Arbarello 2012; Bermúdez-Rochas & Poyato-Ariza 2015; Thies & Waschkewitz, 2015; Gibson 2016; Giles et al., 2017; López-Arbarello & Sferco 2018.)

0 present

1 absent or very reduced

160. Opisthotic-pterotic relationship (Gardiner et al. 1996; Hurley et al. 2007; Giles et al., 2017. This character can only be coded when separate braincase ossifications can be identified.)

0 opisthotic larger than subotic

1 opisthotic and pterotic equal in size

161. Epioccipital (Hurley et al. 2007; Giles et al., 2017. This character can only be coded when separate braincase ossifications can be identified.)

0 present

1 absent

162. Forward extension of the exoccipital around the vagus nerve (Olsen & McCune 1991; Gardiner et al. 1996; Cavin & Suteethorn 2006; Hurley et al. 2007; López-Arbarello 2012; Bermúdez-Rochas & Poyato-Ariza 2015; Thies & Waschkewitz, 2015; Gibson 2016; Giles et al. 2017; López-Arbarello & Sferco 2018. This character can only be coded when separate braincase ossifications can be identified.)

0 absent

1 present

163. Spenotic with small dermal component (Grande 2010; López-Arbarello 2012; Xu & Wu 2012; Xu et al. 2014, 2015; Arratia 2013; Bermúdez-Rochas & Poyato-Ariza 2015; Poyato-Ariza 2015; Thies & Waschkewitz, 2015; Gibson 2016; Xu & Zhao, 2016; Giles et al. 2017; López-Arbarello & Sferco 2018. This character can only be coded when separate braincase ossifications can be identified.)

0 absent

1 present

164. Pterotic (Gardiner et al. 1996; Grande & Bemis, 1998; Hurley et al. 2007; Xu et al. 2014; Poyato- Ariza 2015; Xu & Shen, 2015; Xu & Zhao, 2016; Giles et al. 2017; López-Arbarello & Sferco 2018. This character can only be coded when separate braincase ossifications can be identified.)

0 present

1 absent

165. Opisthotic bone (Wiley 1976; Olsen & McCune 1991; Grande & Bemis 1998; Cavin & Suteethorn 2006; Hurley et al. 2007; Grande 2010; López-Arbarello 2012; Bermúdez-Rochas & Poyato-Ariza 2015; Poyato-Ariza 2015; Thies & Waschkewitz, 2015; Xu et al., 2014, 2015; Gibson 2016; Xu & Zhao, 2016; Giles et al. 2017; López-Arbarello & Sferco 2018. This character can only be coded when separate braincase ossifications can be identified.)

0 present

1 absent

166. Intercalar (Olsen & McCune 1991; Olsen 1994; Gardiner et al. 1996; López-Arbarello 2012; Xu et al. 2014; Poyato-Ariza 2015; Xu & Shen, 2015; Thies & Waschkewitz, 2015; Gibson 2016; Xu & Zhao, 2016; Giles et al. 2017; López-Arbarello & Sferco 2018. This character can only be coded when separate braincase ossifications can be identified.)

0 present

1 absent

167. Occipital region ossification pattern

0 basioccipital and exoccipitals as separate ossifications

1 'co-mineralised'

168. Supraoccipital bone (Grande 2010; Poyato-Ariza 2015; Xu et al. 2014, 2015; Xu & Zhao, 2016; Giles et al. 2017; López-Arbarello & Sferco 2018. This character can only be coded when separate braincase ossifications can be identified.)

0 absent

1 present

169. Membranous outgrowth of intercalar

(Patterson 1973; Olsen & McCune 1991; Gardiner et al. 1996; Hurley et al. 2007; Giles et al. 2017; López-Arbarello & Sferco 2018. This character can only be coded when separate braincase ossifications can be identified.)

0 absent

1 present

170. Post-temporal fossa (Patterson 1973; Gardiner, 1984; Gardiner & Schaeffer, 1989; Olsen & McCune 1991; Coates, 1999; Hurley et al. 2007; López-Arbarello 2012; Xu & Gao, 2011; Xu et al. 2014, 2015; Bermúdez-Rochas & Poyato-Ariza 2015; Giles et al., 2015b; Poyato-Ariza 2015; Thies & Waschkewitz, 2015; Gibson 2016; Xu & Zhao, 2016; Giles et al. 2017.)

0 absent

1 present

171. Sub-temporal fossa (Gardiner, 1984; Gardiner & Schaeffer, 1989; Gardiner et al. 1996; Hurley et al. 2007; Xu & Gao, 2011; Xu et al. 2014, 2015; Xu & Zhao, 2016.)

0 absent

1 present

172. Dilatator fossa (Gardiner, 1984; Gardiner & Schaeffer, 1989; Coates, 1999; Gardiner et al. 1996; Hurley et al. 2007; Xu & Gao, 2011; Xu et al. 2014, 2015; Xu & Zhao, 2016; Giles et al. 2017.)

0 absent

1 present

173. Parasphenoid (Gardiner, 1984; Brazeau, 2009; Davis et al., 2012; Zhu et al., 2013; Giles et al., 2015b,c; Giles et al. 2017.)

0 absent

1 present

171. Parasphenoid (Coates, 1999; Zhu & Yu, 2002; Gardiner et al., 2005; Friedman, 2007, Xu & Gao, 2011; Xu et al., 2014, 2015; Giles et al., 2015b; Xu & Zhao, 2016; Giles et al. 2017; López-Arbarello & Sferco 2018.)

0 terminates at/anterior to ventral otic fissure

1 extends across ventral otic fissure

2 extends to basioccipital

175. Ascending process of the parasphenoid (Patterson, 1982; Coates, 1999; Dietze, 2000; Schultze & Cumbaa, 2001; Zhu & Schultze, 2001; Cloutier & Arratia, 2004; Gardiner et al., 2005; Friedman & Blom,

2006; Zhu et al., 2006; Zhu et al., 2009; Choo, 2011; Xu & Gao, 2011; Zhu et al., 2013; Xu et al., 2014; Giles et al., 2015b,c; Giles et al. 2017; López-Arbarello & Sferco 2018.)

0 absent

1 present

176. Parasphenoid with multifid anterior margin (Friedman & Blom, 2006; Friedman, 2007; Zhu et al., 2009; Choo, 2011; Zhu et al., 2013; Giles et al., 2015b,c; Giles et al. 2017.)

0 absent

1 present

177. Buccohypophyseal canal pierces parasphenoid (Giles et al., 2015b,c; Giles et al. 2017. The buccohypophyseal canal typically enters the dorsal surface of the parasphenoid, but whether it exits via the ventral surface is more variable, and this distribution is captured by this character.)

0 present

1 absent

178. Parasphenoid teeth (Arratia 2013; Giles et al. 2017; López-Arbarello & Sferco 2018.)

0 small

1 large

2 absent

179. Parasphenoid pierced by ascending common carotids

0 absent

1 present

180. Parasphenoid pierced by internal carotid artery (Gardiner et al. 1996; Hurley et al. 2007; Xu & Wu, 2012; Xu et al., 2015; Xu & Zhao, 2016; Giles et al. 2017.)

0 absent

1 present

181. Parasphenoid pierced by efferent pseudobranchial artery (Gardiner et al. 1996; Hurley et al. 2007; Xu & Wu, 2012; Xu et al., 2015; Xu & Zhao, 2016; Giles et al. 2017.)

0 absent

1 present

182. Aortic notch in parasphenoid (Modified from Gardiner et al. 2005; Giles et al. 2017.)

0 absent

1 present

183. Parabasal canal (Xu and Gao 2011; Xu et al. 2014; Giles et al. 2017.)

0 present

1 absent

Endocast

184. Anterolaterally divergent olfactory tracts (Coates, 1999; Giles & Friedman, 2014; Giles et al., 2015b; Giles et al. 2017.)

0 absent

1 present

185. Elongate olfactory tract(s) (Brazeau, 2009; Friedman & Brazeau 2010; Davis et al., 2012; Zhu et al., 2013; Brazeau & Friedman, 2014; Giles & Friedman, 2014; Giles et al., 2015b,c; Giles et al. 2017. The olfactory tracts of *Osorioichthys* are elongate (pers. obs. unpubl. scan data S.G.).)

0 absent

1 present

186. Olfactory nerves carried in a single tract (Coates, 1999; Giles & Friedman, 2014; Giles et al., 2015b; Giles et al. 2017. The olfactory nerves are carried in separate tracts in *Osorioichthys* (pers. obs. unpubl. scan data S.G.).)

0 present

1 absent

187 Arrangement of olfactory nerve in orbital region

0 enclosed in olfactory canal

1 'traversing the orbit lateral to the interorbital septum, at times leaving a groove on the latter'

188. Hypophyseal chamber (Coates, 1999; Xu & Gao, 2011; Xu et al., 2014; Giles et al., 2015b; Giles et al. 2017.)

0 projects posteroventrally

1 projects ventrally or anteroventrally

189. Optic lobes (Giles & Friedman, 2014; Giles et al., 2015b; Giles et al. 2017.)

0 narrower than cerebellum

1 same width or wider than cerebellum

190. Optic lobes (Coates 1999; Hurley et al. 2007; Xu et al. 2014; Giles et al. 2017.)

0 smaller than telencephalon

1 larger than telencephalon

191. Optic tectum divided into bilateral halves (Coates, 1999; Giles et al., 2015b; Giles et al. 2017.)

0 absent

1 present

192. Cerebellar corpus (Giles et al., 2015b,c; Giles et al. 2017. The region posterior to the cerebellar auricles in *Lawrenciella* was considered to be the area octavolateralis by Hamel & Poplin (2005). However, we interpret it as the corpus cerebellum, and this taxon is coded '1'.)

0 absent

1 present

193. Cerebellar corpus (Coates 1999; Hurley et al. 2007; Xu & Gao 2011; Xu et al. 2014; Giles et al. 2017.)

0 divided bilaterally

1 undivided

194. Position of cerebellar corpus (Coates 1999; Hurley et al. 2007; Xu & Gao 2011; Xu et al. 2014; Giles et al. 2017.)

0 enters fourth ventricle

1 arches above fourth ventricle

195. Cerebellar corpus with median anteriorly projecting portion (Coates 1999; Hurley et al. 2007; Xu & Gao 2011; Xu et al. 2014; Giles et al. 2017.)

0 absent

1 present

196. Horizontal semicircular canal (Davis et al., 2012; Zhu et al., 2013; Giles & Friedman, 2014; Giles et al., 2015b,c; Giles et al. 2017.)

0 joins vestibular region dorsal to ampulla for the posterior semicircular canal

1 joins vestibular region level with ampulla for the posterior semicircular canal

197. Junction between ampulla of posterior semicircular canal and cranial cavity (Giles et al., 2015b,c; Giles et al. 2017. In certain stem actinopterygians, such as *Mimipiscis* (Giles and Friedman, 2014), a short length of canal lies between the posterior ampulla and the remainder of the labyrinth.)

0 separated by short length of canal

1 confluent

198. Crus commune of anterior and posterior semicircular canal (Giles & Friedman, 2014; Giles et al., 2015b; Giles et al. 2017.) 0 dorsal to endocranial roof

1 ventral to endocranial roof

199. Lateral cranial canal (Gardiner, 1984; Gardiner & Schaeffer, 1989; Coates, 1999; Cloutier & Arratia, 2004; Gardiner et al., 2005; Zhu et

al., 2006; Zhu et al., 2009; Zhu et al., 2013; Giles & Friedman, 2014; Xu et al., 2014; Giles et al., 2015b,c; Giles et al. 2017. The presence of a lateral cranial canal in *Ligulalepis* and *Psarolepis* is uncertain, but its presence in *Meemannia* is confirmed following Lu et al. (2016). *Erpetoichthys* is conservatively coded as '?'.)

0 absent

1 present

200. Lateral cranial canal connects to cranial cavity anteriorly (Giles et al. 2017.)

0 absent

1 present

201. Lateral cranial canal connects to lateral wall of braincase

0 absent

1 present

202. Intramural diverticula opening in fossa bridgei

0 absent

1 present

Scales and histology

203. Enameloid on dermal bones and scales (Giles et al., 2015b,c, 2017. Characters 203-206 form part of an atomisation of the compound characters 'ganoine' (typically defined as a single or multilayer enamel covering) and 'cosmine' (typically defined as a single layer of enamel with a well-defined pore canal network) (e.g. Cloutier & Ahlberg, 1996; Ahlberg & Johanson, 1998; Zhu & Ahlberg, 2004; Schultze & Cumbaa, 2001; Zhu

& Schultze, 2001; Zhu et al., 2001; Zhu & Yu, 2002; Daeschler et al., 2006; Long et al., 2006; Zhu et al., 2006; Zhu et al., 2009; Davis et al., 2012; Zhu et al., 2013). A similar approach to atomization was taken by Friedman (2007), Brazeau & Friedman (2010) and Giles et al. (2015b). As detailed histological investigations have not been carried out for the majority of early actinopterygians (rather, they have simply been described as being covered in/bearing ridges of ganoine), many of these characters cannot be coded for a number of taxa.)

0 absent

1 present

204. Extensive pore-canal network (See notes ch. 203.)

0 absent

1 present

205. Enamel (See notes ch. 203.)

0 single-layered

1 multi-layered

206. Enamel layers (See notes ch. 203)

0 applied directly to one another

1 separated by layers of dentine

207. Scales on body (Giles et al. 2017.)

0 present

1 absent

208. Scales (Cloutier & Arratia, 2004; Friedman & Blom, 2006; Long et al., 2008; Swartz, 2009; Zhu et al., 2009; Choo, 2011; Giles et al., 2015b; Giles et al. 2017.)

0 micromeric

1 macromeric

209. Scales with ‘peg and socket articulation' (Maisey, 1986; Gardiner & Schaeffer, 1989; Cloutier & Ahlberg, 1996; Coates, 1999; Dietze, 2000; Poplin & Lund, 2000; Schultze & Cumbaa, 2001; Cloutier & Arratia, 2004; Friedman & Blom, 2006; Friedman, 2007; Long et al., 2008; Brazeau, 2009; Swartz, 2009; Zhu et al., 2009; Friedman & Brazeau, 2010; López-Arbarello 2012; Xu & Gao, 2011; Choo, 2011; Davis et al., 2012; Zhu et al., 2013; Xu et al., 2014; Giles et al., 2015b,c; Xu & Zhao, 2016; Giles et al. 2017; López-Arbarello & Sferco 2018. This character is coded only for taxa that possess rhombic scales.)

0 absent

1 present

210. Peg on rhomboid scale (Patterson, 1982; Cloutier & Ahlberg, 1996; Dietze, 2000; Schultze & Cumbaa, 2001; Zhu & Schultze, 2001; Zhu et al., 2001: Zhu & Yu, 2002; Cloutier & Arratia, 2004; Friedman & Blom, 2006; Zhu et al., 2006; Friedman, 2007; Zhu et al., 2009; Giles et al. 2017. Although peg-and-socket articulation of is present between the scales of *Limnomis* (Daeschler, 2000), the nature of the peg is not described. As such, this taxon is conservatively coded '?'.)

0 narrow

1 broad

211. Anterodorsal process on scale (Patterson, 1982; Gardiner, 1984; Gardiner & Schaeffer, 1989; Schultze & Cumbaa, 2001; Zhu & Schultze, 2001; Zhu et al., 2001; Zhu & Yu, 2002; Cloutier & Arratia, 2004; Friedman & Blom, 2006; Zhu et al., 2006; Friedman, 2007; Long et al., 2008; Swartz, 2009; Zhu et al., 2009; Choo, 2011; Zhu et al., 2013; Giles et al., 2015b,c; Giles et al. 2017.)

0 absent

1 present

212. Scales with well-developed pores on surface (Friedman & Blom 2006; Long et al., 2008; Swartz, 2009; Choo, 2011; Xu et al., 2014; Giles et al., 2015b; Giles et al. 2017. Scales from the posterior half of the flank in *Wendichthys* bear pores on the enamel surface, whereas those from the anterior part of the flank lack these pores (Lund & Poplin, 1997: fig. 6). This taxon is scored '1'.)

0 absent

1 present

213. Small scales below dorsal fin (Giles et al. 2017.)

0 absent

1 present

214. Lepidotrichia (Friedman, 2007; Brazeau, 2009; Zhu et al., 2009; Friedman & Brazeau, 2010; Davis et al., 2012; Zhu et al., 2013; Brazeau & Friedman, 2014; Giles et al., 2015b,c; Giles et al. 2017.)

0 absent

1 present

215. Fringing fulcra (Patterson, 1982; Gardiner & Schaeffer, 1989; Grande & Bemis 1998; Coates, 1999; Dietze, 2000; Schultze & Cumbaa, 2001; Poyato-Ariza & Wenz, 2002; Cloutier & Arratia, 2004; Friedman & Blom, 2006; Friedman, 2007; Long et al., 2008; Swartz, 2009; Zhu et al., 2009; Choo, 2011; Xu & Gao, 2011; López-Arbarello 2012; Zhu et al., 2013; Xu et al., 2014, 2015; Bermúdez-Rochas & Poyato-Ariza 2015; Poyato-Ariza 2015; Giles et al., 2015b; Thies & Waschkewitz, 2015; Gibson 2016; Xu & Zhao, 2016; Giles et al. 2017; Cawley & Kriwet 2018; López-Arbarello & Sferco 2018.)

0 absent

1 present

Hyoid arch

216. Double headed hyomandibular (Cloutier & Ahlberg, 1996; Zhu & Schultze, 2001; Schultze & Cumbaa, 2001; Zhu et al., 2001; Zhu & Yu, 2002; Zhu et al., 2006; Friedman, 2007; Zhu et al., 2009; Friedman & Brazeau, 2010; Zhu et al., 2013; Giles et al., 2015b,c; Giles et al. 2017; López-Arbarello & Sferco 2018.)

0 absent

1 present

217. Perforate hyomandibula (Friedman, 2007; Zhu et al., 2009; Friedman & Brazeau, 2010; Xu & Gao, 2011; Zhu et al., 2013; Brazeau & Friedman, 2014; Xu et al., 2014, 2015; Giles et al., 2015b; Xu & Zhao, 2016; Giles et al. 2017. Although Long (1988: p.24) mentions the presence

of a depression for the hyomandibular nerve in *Howqualepis*, it is unclear whether this perforated the hyomandibula. This taxon is conservatively coded as '?'.)

0 absent

1 present

218. Opercular process (Gardiner & Schaeffer, 1989 Poyato-Ariza & Wenz, 2002;; Giles et al., 2015b; Giles et al. 2017; Cawley & Kriwet 2018; López-Arbarello & Sferco 2018.)

0 absent

1 present

219. Ceratohyal (Gardiner et al., 2005; Xu & Gao, 2011; Giles et al., 2015b; Giles et al. 2017; Xu et al., 2014.)

0 single ossification

1 two ossifications

220. Anterior ossification of ceratohyal (Revised from Coates, 1999; Giles et al., 2015b; Giles et al. 2017; López-Arbarello & Sferco 2018.The character captures whether the ceratohyal (or the anterior ossification if an anterior and posterior ceratohyal are present) is medially constricted (hourglass-shaped) or plate-like in lateral view.)

0 no medial constriction

1 medial constriction (hourglass-shaped)

221. Anterior ceratohyal (Coates, 1999; Giles et al., 2015b; Giles et al. 2017. The groove for the afferent hyoidean artery in the ceratohyal of *Gogosardina* is visible in Choo 2009 (fig 6).)

0 no groove

1 groove for afferent hyoidean artery

222. Ossified accessory hyoid elements

0 absent

1 present

223. If present, number of accessory hyoid elements

0 one

1 two

224. Symplectic shape (Giles et al. 2017; López-Arbarello & Sferco 2018.)

0 tube/splint like

1 hatchet

2 l-shaped

225. Symplectic, position

0 posterior to posterior margin of quadrate

1 medial to posterior margin of the quadrate

226. Hypohyal (Friedman & Brazeau, 2010; Brazeau & Friedman, 2014; Giles et al., 2015b,c; Giles et al. 2017.)

0 absent

1 present

227. Basihyal (Davis et al., 2012; Zhu et al., 2013; Giles et al., 2015b,c; Giles et al. 2017; López-Arbarello & Sferco 2018.)

0 absent

1 present

Gill skeleton

228. Gill arches (Giles et al., 2015b,c; Giles et al. 2017.)

0 largely restricted to area under braincase

1 extend far posterior to braincase

229. Number of ceratobranchials (Giles et al. 2017.)

0 five

1 four

230. Number of hypobranchials (Grande, 2010; Xu & Wu, 2012; Xu et al., 2014, 2015; Xu & Zhao, 2016; Giles et al. 2017; López-Arbarello & Sferco 2018.)

0 three

1 four

231. Uncinate processes on epibranchials (Coates, 1999; Xu & Gao, 2011; Xu et al., 2014, 2015; Poyato-Ariza 2015; Xu & Zhao, 2016; Giles et al. 2017; López-Arbarello & Sferco 2018. An uncinate process is a dorsally- directed extension on the epibranchial that articulates with the pharyngobranchial skeleton.)

0 absent

1 present

232. Endoskeletal urohyal (Friedman, 2007; Friedman & Brazeau, 2010; Giles et al., 2015b,c; Poyato-Ariza 2015; Giles et al. 2017; López-Arbarello & Sferco 2018.)

0 absent

1 present

233. Urohyal formed as a tendon bone of the sternohyoideus muscle (Arratia 2013; Giles et al. 2017.)

0 absent

1 present

234. Presupracleithrum (Patterson, 1982; Gardiner, 1984; Gardiner & Schaeffer, 1989; Taverne, 1997; Lund, 2000; Schultze & Cumbaa, 2001; Zhu & Schultze, 2001; Zhu et al., 2001; Lund & Poplin, 2002; Zhu & Yu, 2002; Cloutier & Arratia, 2004; Gardiner et al., 2005; Friedman & Blom, 2006; Zhu et al., 2006; Friedman, 2007; Long et al., 2008; Swartz, 2009; Zhu et al., 2009; Choo,

2011; Xu & Gao, 2011; Zhu et al., 2013; Xu et al., 2014; Giles et al., 2015b; Giles et al. 2017; López-Arbarello & Sferco 2018. An elongate bone termed the 'anocleithrum' is variably present in *Wendichthys* (Lund & Poplin, 1997) in the position occupied by the presupracleithrum in other taxa. We regard this as a positional homologue, and code the taxon '0/1' to reflect this polymorphism. Coded as '?' in *C. trailli* following arguments in Friedman & Blom (2006).)

0 absent

1 present

Dermal shoulder girdle

235. Presupracleithrum (Xu et al. 2014; Giles et al. 2017.)

0 single

1 multiple

236. Dorsal margin of cleithrum (Cloutier & Ahlberg, 1996; Schultze & Cumbaa, 2001; Zhu & Schultze, 2001; Zhu et al., 2001; Zhu & Yu, 2002; Cloutier & Arratia, 2004; Zhu et al., 2006; Friedman, 2007; Zhu et al., 2009; Giles et al., 2015b,c; Giles et al. 2017.)

0 pointed

1 broad and rounded

237. Medial wing on cleithrum (Cavin & Suteethorn 2006; Poyato-Ariza 2015; Giles et al. 2017; López-Arbarello & Sferco 2018.)

0 absent

1 present

238. Anocleithrum (Gardiner & Schaeffer, 1989; Lund et al., 1995; Cloutier & Ahlberg, 1996; Dietze, 2000; Poplin & Lund, 2000; Schultze & Cumbaa, 2001; Zhu & Schultze, 2001; Zhu et al., 2001; Zhu & Yu, 2002; Cloutier & Arratia, 2004; Zhu et al., 2006; Friedman, 2007; Zhu et al., 2009; Zhu et al., 2013; Giles et al., 2015b; Giles et al. 2017; López-Arbarello & Sferco 2018.)

0 bone developed as postcleithrum

1 bone developed as anocleithrum sensu stricto

2 bone absent

239. Clavicle (Patterson 1973; Olsen & McCune 1991; Coates 1999; Xu & Gao 2011; Xu et al. 2014; Poyato-Ariza 2015; Xu & Zhao, 2016; Giles et al. 2017; López-Arbarello & Sferco 2018.)

0 present as a broad plate

1 much reduced or absent

240. Serrated organ (Arratia 2013; Giles et al. 2017; López-Arbarello & Sferco 2018. The serrated organ (or appendage) is a small, elongate element, typically ornamented with serrated ridges, present near the anterior margin of the cleithrum.)

0 absent

1 present

241. Interclavicle (Cloutier & Arratia, 2004; Giles et al. 2017; Xu et al., 2014.)

0 present

1 absent

Paired fins

242. Triradiate scapulocoracoid (Olsen & McCune 1991; Zhu & Schultze, 2001; Zhu et al., 2001; Zhu & Yu, 2002; Zhu et al., 2006; Friedman, 2007; Zhu et al., 2009; Xu & Gao, 2011; Zhu et al., 2013; Xu et al., 2014; Giles et al., 2015b; Giles et al. 2017.)

0 absent

1 present

243. Perforate propterygium (Patterson, 1982; Gardiner, 1984; Gardiner & Schaeffer, 1989; Rosen, 1989; Taverne, 1997; Coates, 1999; Zhu & Schultze, 2001; Zhu et al., 2001; Zhu & Yu, 2002; Zhu et al., 2006; Brazeau, 2009; Zhu et al., 2009; Friedman & Brazeau, 2010; Xu & Gao, 2011; Davis et al., 2012; Zhu et al., 2013; Xu et al., 2014; Giles et al., 2015b,c.)

0 absent

1 present

244. Anterior rays embrace propterygium (Patterson, 1982; Gardiner, 1984; Gardiner & Schaeffer, 1989; Taverne, 1997; Coates, 1999; Schultze & Cumbaa, 2001; Zhu & Schultze, 2001; Friedman & Blom, 2006; Long et al., 2008; Swartz, 2009; Choo, 2011; Xu & Gao, 2011; Giles et al., 2015b; Giles et al. 2017.)

0 absent

1 present

2 fused

245. Propterygium fused to first ray (Giles et al. 2017; López-Arbarello & Sferco 2018.)

0 absent

1 present

246. Pectoral fin endoskeleton (Taverne, 1997; Coates, 1999; Friedman & Blom, 2006; Long et al., 2008; Swartz, 2009; Xu & Gao, 2011; Xu et al., 2014; Giles et al., 2015b; Giles et al. 2017.)

0 extends far beyond body wall (fins lobate)

1 barely extends beyond body wall (fins not lobate)

247. Pectoral fin radials (Zhu & Yu, 2002; Friedman, 2007; Giles et al., 2015b; Giles et al. 2017. Two series of pectoral fin radials are described (but not figured) for *Cheirolepis candensis* (Arratia & Cloutier, 2004). Although we consider this arrangement to be unlikely, for now this taxon is coded '1'.)

0 unjointed

1 jointed

248. Fin articulation (Zhu & Schultze, 2001; Zhu et al., 2001; Zhu & Yu, 2002; Zhu et al., 2006; Friedman, 2007; Zhu et al., 2009; Friedman & Brazeau, 2010; Zhu et al., 2013; Giles et al., 2015b,c; Giles et al. 2017.)

0 monobasal

1 polybasal

249. Pectoral fin-ray segmentation (Coates, 1999; Friedman & Blom, 2006; Long et al., 2008; Choo, 2011; Xu & Gao, 2011; Xu et al., 2014; Giles et al., 2015b; Giles et al. 2017.)

0 roughly even segmentation to fin base

1 proximal segments elongate with terminal segmentation

2 no significant segmentation on pectoral fin

3 terminal segments elongate with proximal segmentation

250. Pectoral fin (Giles et al., 2015b; Giles et al. 2017.)

0 leaf-like

1 not leaf-like

251. Paired fin spines (Zhu et al., 2001; Zhu & Yu, 2002; Friedman, 2007; Zhu et al., 2009; Brazeau, 2009; Davis et al., 2012; Zhu et al., 2013; Giles et al., 2015b,c; Giles et al. 2017.)

0 absent

1 present

252. Pelvic fins (Friedman & Blom, 2006; Friedman, 2007; Brazeau, 2009; Choo, 2011; Davis et al., 2012; Zhu et al., 2013; Brazeau & Friedman, 2014; Giles et al., 2015b,c; Giles et al. 2017.)

0 absent

1 present

253. Pelvic fin insertion (Gardiner & Schaeffer, 1989; Coates, 1998; Coates, 1999; Lund, 2000; Schultze & Cumbaa, 2001; Cloutier & Arratia, 2004; Friedman & Blom, 2006; Zhu et al., 2006; Long et al., 2008; Swartz, 2009; Zhu et al., 2009; Choo, 2011; Xu et al., 2014; Giles et al., 2015b; Giles et al. 2017.)

0 shorter than fin depth (short based)

1 longer than fin depth (long based)

Median fins

254. Basal scutes on fins (Friedman, 2007; Zhu & Yu, 2002; López-Arbarello 2012; Bermúdez-Rochas & Poyato- Ariza 2015; Giles et al., 2015b; Thies & Waschkewitz, 2015; Gibson 2016; Giles et al. 2017; López-Arbarello & Sferco 2018.)

0 absent

1 present

255. Dorsal scutes anterior to dorsal fin (Olsen & McCune 1991; Lund, 2000; Poplin & Lund, 2000; Poyato-Ariza & Wenz, 2002; Cloutier & Arratia, 2004; Friedman & Blom, 2006; Long et al., 2008; Swartz, 2009; Choo, 2011; Giles et al., 2015b; Thies & Waschkewitz, 2015; Gibson 2016; Giles et al. 2017; Cawley & Kriwet 2018; López-Arbarello & Sferco 2018.)

0 absent

1 few limited to region immediately anterior to fin (basal fulcra only)

2 many, extending to posterior of skull roof (complete set of dorsal ridge scales)

256. Ventral scutes between hypochordal lobe of caudal fin and anal fin

(Patterson, 1982; Taverne, 1997; Friedman & Blom, 2006; Long et al., 2008; Choo, 2011; Giles et al., 2015b; Giles et al. 2017; López-Arbarello & Sferco 2018.)

0 absent

1 present

257. Ventral scutes anterior to anal fin (Cloutier & Arratia, 2004; Friedman & Blom, 2006; Long et al., 2008; Swartz, 2009; Choo, 2011; Giles et al., 2015b; Giles et al. 2017.)

0 absent

1 present

258. Dorsal fin(s) (Gardiner & Schaeffer, 1989; Schultze & Cumbaa, 2001; Zhu & Schultze, 2001; Zhu et al., 2001; Zhu & Yu, 2002; Cloutier & Arratia, 2004; Friedman & Blom, 2006; Zhu et al., 2006; Friedman, 2007; Long et al., 2008; Brazeau, 2009; Swartz, 2009; Zhu et al., 2009; Choo, 2011; Davis et al., 2012; Zhu et al., 2013; Giles et al., 2015b,c; Giles et al. 2017.)

0 two

1 one

259. Relative positions of anal and (second) dorsal fin (Poplin & Lund, 2000; Cloutier & Arratia, 2004; Friedman & Blom, 2006; Long et al.,

2008; Swartz, 2009; Choo, 2011; López-Arbarello 2012; Bermúdez-Rochas & Poyato-Ariza 2015; Giles et al., 2015b; Thies & Waschkewitz, 2015; Gibson 2016; Giles et al. 2017; López- Arbarello & Sferco 2018.)

0 anal shifted anteriorly relative to dorsal

1 fins opposite one another

2 anal shifted posteriorly relative to dorsal

260. Median fins (except caudal fin) (Gardiner et al., 2005; Xu & Gao, 2011; Xu et al., 2014, 2015; Xu & Zhao, 2016; Giles et al. 2017; López-Arbarello & Sferco 2018.)

0 rays more numerous than radials

1 rays and radials equal

261. Proximal and middle radials of dorsal fin (Giles et al. 2017.)

0 proximal and middle radials of similar size

1 proximal radials substantially enlarged

262. Posteriormost proximal radial of dorsal fin (Giles et al. 2017)

0 enlarged plate

1 smaller than more anterior radials

263. Epichordal lobe of caudal fin (Patterson, 1982; Cloutier & Ahlberg, 1996; Coates, 1999; Schultze & Cumbaa, 2001; Zhu & Schultze, 2001; Friedman & Blom, 2006; Long et al., 2008; Swartz, 2009; Choo, 2011; Giles et al., 2015b; Giles et al. 2017.)

0 present

1 absent

264. Fulcra along dorsal ridge of caudal fin (Patterson, 1982; Taverne, 1997; Gardiner & Schaeffer, 1989; Gardiner et al., 2005; Friedman & Blom, 2006; Long et al., 2008; Choo, 2011; López-Arbarello 2012; Bermúdez- Rochas & Poyato-Ariza 2015; Giles et al., 2015b; Giles et al. 2017; López-Arbarello & Sferco 2018.)

0 absent

1 present

265. Caudal fin geometry (Modified from Gardiner et al., 2005; Giles et al. 2017. A long chordal lobe is considered to be present when the notochord reaches the posterior margin of the caudal fin.)

0 long chordal lobe

1 short chordal lobe

266. Posterior margin of caudal fin (Grande & Bemis 1998; Xu & Gao 2011; Xu et al. 2014; Xu & Zhao, 2016; Giles et al. 2017; López-Arbarello & Sferco 2018.)

0 forked

1 unforked

267. Epineural processes

0 absent

1 present

268. Diplospondyly in mid-caudal region (Grande & Bemis 1998; Arratia 2013; Poyato-Ariza 2015; Giles et al. 2017; López- Arbarello & Sferco 2018.)

0 absent

1 present

269. Median neural spines in caudal region (Coates 1999; Hurley et al. 2007; Xu et al. 2014; Giles et al. 2017; López-Arbarello & Sferco 2018.)

0 absent

1 present

270. Uroneural (Pinna, 1996; Hurley et al., 2007; Xu & Wu, 2012, Xu et al., 2014; Xu & Zhao, 2016; Giles et al. 2017; López-Arbarello & Sferco 2018.)

0 absent

1 present

271. Division of hypurals into dorsal and ventral groups (Pinna, 1996, Xu & Wu, 2012, Xu et al., 2014; Xu & Zhao, 2016; Giles et al. 2017.)

0 absent

1 present

272. Number of caudal lepidotrichs borne per hypural (Giles et al. 2017; López-Arbarello & Sferco 2018.)

0 multiple

1 single

Axial skeleton

273. Opistocoelous vertebrae (Wiley, 1976; López-Arbarello 2012; Bermúdez-Rochas & Poyato-Ariza 2015; Thies & Waschkewitz, 2015; Poyato-Ariza 2015; Gibson 2016; Giles et al. 2017; López-Arbarello & Sferco 2018.)

0 absent

1 present

274. Ossified ribs (Giles et al. 2017.)

0 present

1 absent

275. Antorbital deeper than anteriormost infraorbital (López-Arbarello 2012; Thies & Waschkewitz, 2015; Gibson 2016; López-Arbarello & Sferco 2018.)

0 absent

1 present

276. Infraorbitals fragmented (The infraorbitals normally form as a single row partially surrounding the orbit. In some taxa, they may be fragmented into multiple irregular ossifications.)

0 absent

1 present

277. Suborbitals fragmented (Grande & Bemis 1998; López-Arbarello 2011; López-Arbarello & Sferco 2018. The suborbitals normally form as a single row partially surrounding the orbit, posterior and/or ventral to the infraorbitals. In some taxa, they may be fragmented into multiple irregular ossifications.)

0 absent

1 present

278. Suborbitals extend ventral to orbit (López-Arbarello 2011; López-Arbarello & Sferco 2018.)

0 absent

1 present

279. Coronoids contribute to lateral dentition field (Coronoids are normally restricted to the medial (lingual) surface of the jaw. In some dapediids, they may extend laterally to contribute to the labial tooth row.)

0 absent

1 present

280. Jaw articulation ventral or anterior to orbit (López-Arbarello 2012; Bermúdez-Rochas & Poyato-Ariza 2015; Poyato-Ariza 2015; Thies & Waschkewitz, 2015; Gibson 2016; López-Arbarello & Sferco 2018.)

0 absent

1 present

281. Parasphenoid wings around basiocciput (The parasphenoid is normally restricted to covering the ventral face of the braincase. In some taxa, extensions may extend dorsally and laterally to cloak the basiocciput.)

0 absent

1 present

282. Dorsal extension of parasphenoid between orbits (The parasphenoid extends dorsally between the orbits, contributing to the interorbital septum, in some taxa.)

0 absent

1 present

283. Ligament pit on posterior face of braincase (A deep ligament pit, dorsal to the foramen magnum, is found on the posterior face of the braincase in some taxa.)

0 absent

1 present

284. 'Hem-like' median fins (Gibson 2016.)

0 absent

1 present

285. Anal fin insertion

0 short based

1 long based

286. Denticulate ridge scales

0 absent

1 present

287. Ossified centra (Poyato-Ariza & Wenz, 2002; Cawley & Kriwet 2018.)

0 absent

1 present

288. Supratemporal commissure in parietal (Poyato-Ariza & Wenz, 2002; Thies & Waschkewitz, 2015; Gibson 2016; Cawley & Kriwet 2018; López-Arbarello & Sferco 2018. The supratemporal commissure is normally carried by the extrascapulars, but is sometimes borne in the parietal.)

0 absent

1 present

289. Enlarged vomerine teeth (Poyato-Ariza & Wenz, 2002; Cawley & Kriwet 2018; López-Arbarello & Sferco 2018.)

0 absent

1 present

290. Enlarged prearticular teeth (Poyato-Ariza & Wenz, 2002; Cawley & Kriwet 2018.)

0 absent

1 present

291. Prearticular symphysis (Nursall 2010.)

0 absent

1 present

292. Dermal supraoccipital (Poyato-Ariza & Wenz, 2002; Cawley & Kriwet 2018. A median bone, typically referred to as a dermal supraoccipital, is present between the parietals in some taxa.)

0 absent

1 present

293. Preoperculum taller than operculum

(Poyato-Ariza & Wenz, 2002; Cawley & Kriwet 2018.)

0 absent

1 present

294. Preoperculum wider than operculum (Poyato-Ariza & Wenz, 2002; Cawley & Kriwet 2018.)

0 narrower

1 wider

295. Branchiostegals contact next in sequence (Poyato-Ariza & Wenz, 2002; Cawley & Kriwet 2018.)

0 absent

1 present

296. Dorsal lateral line

0 absent

1 present

297. Parasphenoid inflected ventrally below orbit (Nursall 2010.)

0 absent

1 present

298. Sagittal flange on neural spine (Poyato-Ariza & Wenz, 2002; Cawley & Kriwet 2018.)

0 absent

1 present

299. Sagittal flange on haemal spine (Poyato-Ariza & Wenz, 2002; Cawley & Kriwet 2018.)

0 absent

1 present

300. Pleural ribs alate (Nursall 2010.)

0 absent

1 present

301. Lacrimal contributing to oral margin

0 absent

1 present

302. Teeth on lacrimal

0 absent

1 present

303. Dermosphenotic position

0 extending well below dermopterotic

1 located at same horizontal level than dermopterotic

A.4 Taxon list for phylogenetic analyses

Taxon	Source
Acanthodes bronni	Miles, 1973; Davis et al.,
Acipenser	Nieuwenhuys, 1982; Hilton
Aesopichthys	Poplin & Lund, 2000.
Aetholepis mirablis	Woodward 1895.
Amia calva	Grande & Bemis, 1998;
Amphicentrum	Traquair, 1875; Bradley-
Arduafrons prominoris	Nursall 1999.
Atractosteus spatula	Grande, 2010.
Australosomus kochi	Nielsen, 1949.
Beagiascus	Mickle et al., 2009.
Beishanichthys	Xu & Gao, 2011.
Birgeria groenlandica	Nielsen, 1949.
Bobasatrania	Stensiö, 1932.
Boreosomus	Nielsen, 1942.
Brembodus ridens	Tintori 1981.
Caturus furcatus	Patterson, 1975; Lambers, 1994; Grande
Cheirolepis	Arratia & Cloutier, 1996;
Cheirolepis schultzei	Arratia & Cloutier, 2004.

Cheirolepis trailli	Pearson & Westoll, 1979; Giles et al.,	
Chondrosteus acipenseroides	Hilton & Forey 2009; Hilton et al.,	
Cladodoides	Maisey, 2005.	
Coccocephalichthys	Poplin, 1974; Poplin &	
Cosmoptychius	Schaeffer, 1971; Coates,	
Cyranorhis bergeraci	Lund et al., 1997.	
Dandya ovalis	Tintori 1983.	
Dapedium caelatum	Thies & Hauff, 2008; Thies & Herzog,	
Dapedium punctatum	Thies & Herzog, 1999; Thies & Hauff,	
Dapedium noricum	Tintori 1983.	
Dapedium pholidotum	Patterson, 1975; Thies & Herzog, 1999;	
Dapedium stollorum	Thies & Herzog, 1999; Thies & Hauff,	
Dapedium sp.	Rayner 1948; Patterson	
Dialipina salguerioensis	Schultze, 1968; Schultze & Cumbaa,	
Diplocercides kayseri	Stensiö, 1922a,b; Forey,	
Dipteronotus ornatus	Bürgin, 1992.	
Discoserra	Lund, 2000; Hurley et al.,	
Donnrosenia	Long et al., 2008.	
Dorsetichthys bechei	Patterson, 1968; Patterson, 1973; Patterso	
Ebenaqua ritchei	Campbell & Le Duy Phuoc,	
Elops hawaiensis	Forey, 1973.	
Entelognathus	Zhu et al., 2013.	
Eomesodon liassicus	Gardiner 1960.	
Erpetoichthys calabaricus	Claeson et al., 2007; Claeson &	

Eusthenopteron	Jarvik, 1980.	
Evenkia eunoptera	Berg, 1942; Selenzneva, 1985;	
Fouldenia ischiptera	Sallan & Coates, 2013.	
Fukangichthys	Xu et al., 2014.	
Gibbodon cenensis	Tintori 1981.	
Glyptolepis	Jarvik, 1972; Jarvik, 1980.	
Gogonasus andrewsae	Long et al., 1997; Long et al., 2006;	
Gogosardina coatesi	Choo et al., 2009.	
Guiyu oneiros	Zhu et al., 2009; Qiao &	
Hemicalypterus weiri	Schaeffer, 1967; Gibson	
Heterostrophus	Woodward 1928, 1929.	
Hiodon alosoides	Hilton, 2002.	
Howqualepis	Long, 1988; Choo, 2009.	
Hulettia americana	Schaeffer & Patterson,	
Ichthyokentema	Griffith & Patterson, 1963.	
Kalops monophyrum	Poplin & Lund 2000.	
Kansasiella eatoni	Poplin, 1974.	
Kentuckia deani	Rayner, 1951; Giles &	
Lawrenciella	Poplin, 1984; Hamel &	
Lepisosteus osseus	Balfour & Parker, 1882; Mathiesen &	
Leptolepis bronni	Rayner, 1937.	
“Ligulalepis”	Basden et al., 2000; Basden & Young,	
Luederia kempi	Schaeffer &	
Luganoia lepidosteoides	Bürgin, 1992.	
Macrepistius arenatus	Schaeffer, 1960;	
Macrosemimimus lennieri	Jain & Robinson, 1963; Wenz, 1967;	
Macrosemius rostratus	Bartram, 1977.	
Meemannia eos	Zhu et al., 2006,	
Melanecta anneae	Coates, 1998.	

Mesturus sp.	Nursall 1999
Mesturus verrucosus	Nursall 1999
Mesopoma planti	Coates, 1999.
Miguashaia bureaui	Cloutier, 1996.
Mimipiscis bartrami	Gardiner, 1984;
Mimipiscis toombsi	Gardiner, 1984; Choo, 2011; Giles &
Moythomasia lineata	Jessen, 1968; Choo
Moythomasia nitida	Jessen, 1968; Choo
Moythomasia durgaringa	Gardiner, 1984; Long & Trinajstic, 2010;
Obaichthys decoratus	Grande, 2010.
Onychodus jandemarrai	Andrews et al., 2006.
Osorioichthys marginis	Taverne, 1997.
Osteolepis macrolepidotus	Jarvik 1948.
Ozarcus mapesae	Pradel et al., 2014.
Paradapedium egertoni	Jain 1973.
Peltopleurus lissocephalus	Bürgin, 1992.
Platysomus superbus	Moy-Thomas &
Polypterus bichir	Allis 1922; Jollie 1984; Bjerring 1991; Bartsch & Gemballa
Porolepis sp.	Jarvik, 1972; Jarvik,
Propterus elongatus	Bartram, 1977.
Psarolepis romeri	Yu, 1998; Zhu et al., 1999; Zhu & Yu,
Pteronisculus stensioi	Nielsen 1942;
Raynerius splendens	Giles et al., 2015b.
Sargodon tomicus	Tintori 1983.
Saurichthys madagascarensis	Kogan et al., 2016.
Scanilepis dubia	Aldinger, 1937;
Semionotus elegans	Olsen & McCune,
Styloichthys changae	Zhu & Yu, 2002; Zhu et al., 2006;

Styracopterus fulcratus	Sallan & Coates,
Tanaocrossus kalliokoskii	Schaeffer, 1967; Schaeffer & Donald,
Tegeolepis clarki	Gardiner, 1963; Dunkle & Schaeffer,
Tetragonolepis oldhami	Jain 1973.
Tetragonolepis semicincta	Thies, 1991.
Venusichthys comptus	Xu & Zhao, 2016.
Watsonulus eugnathoides	Olsen, 1984; Grande
Wendyichthys dicksoni	Lund & Poplin, 1997.
Woodichthys bearsdeni	Coates, 1998.
NHMD–73588	this work
Pteronisculus gunnari	Nielsen, 1942
Pteronisculus magnus	Nielsen, 1942
Pteronisculus changae	Ren & Xu, 2021
Pteronisculus nielseni	Xu et al., 2014
Pteronisculus cicatrosus	Lehman, 1952

A.5 Figures and Tables

Figure A.1: Strict consensus tree of 135 most parsimonious trees, implied weight analysis (K = 100) with outgroup topology constrained.

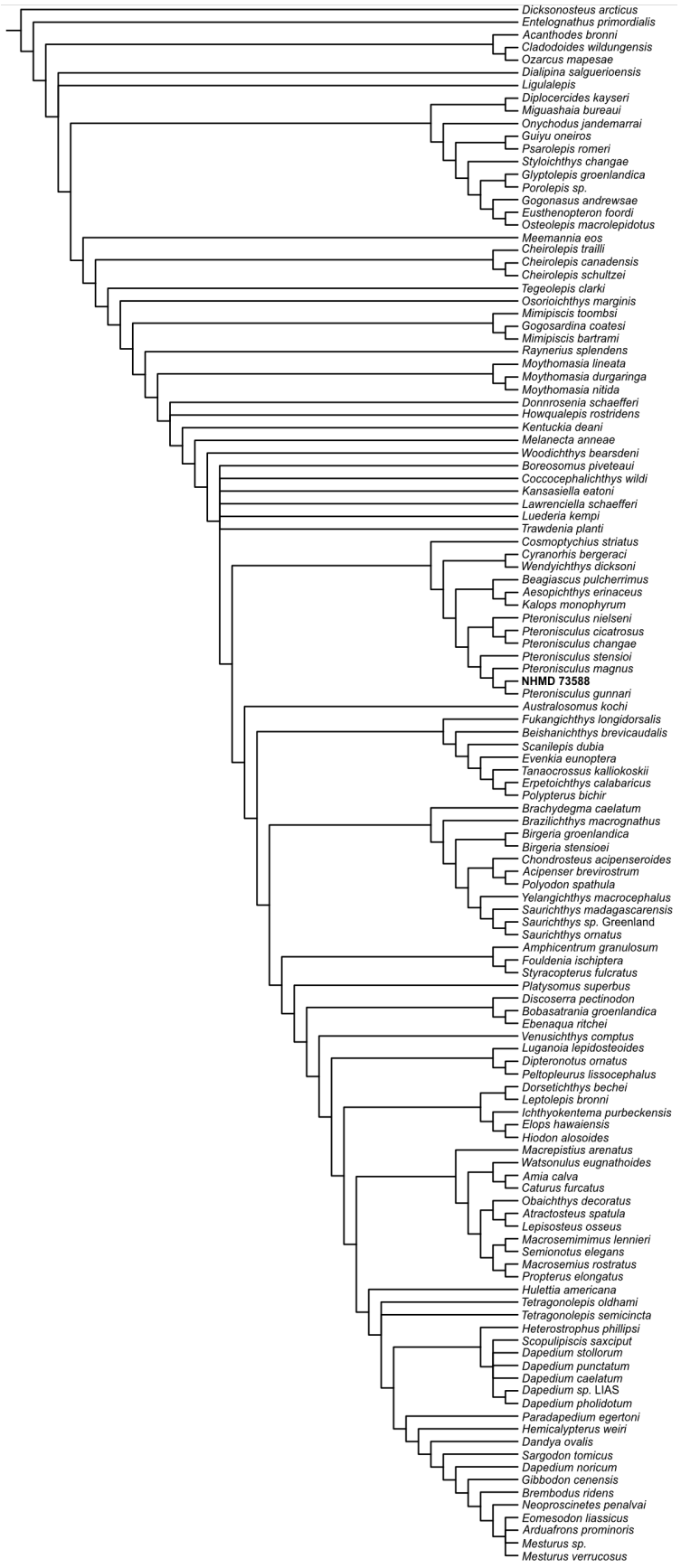
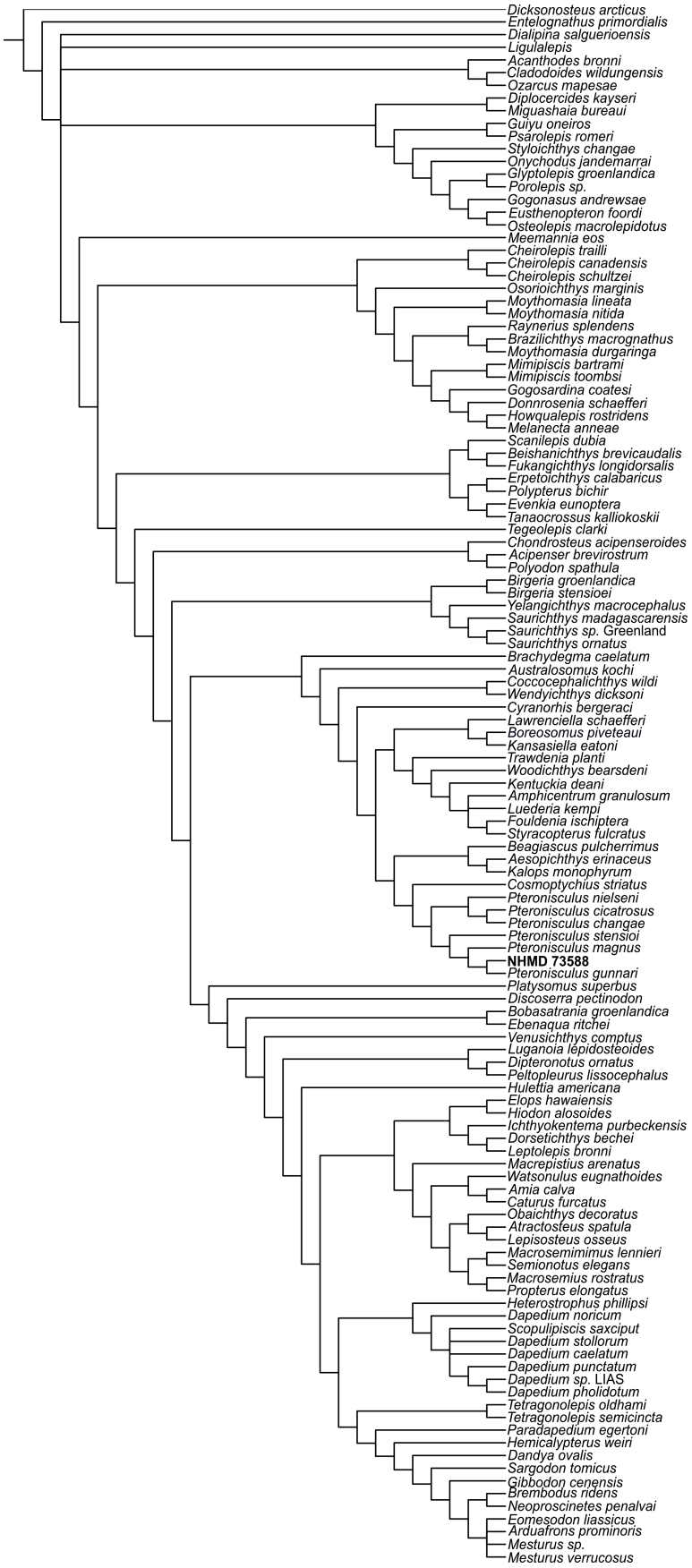

Dicksonosteus arcticus
Entelognathus primordialis
Acanthodes bronni
Cladodoides wildungensis
Ozarcus mapesae
Dialipina salguerioensis
Ligulalepis
Diplocercides kayseri
Miguashaia bureaui
Onychodus jandemarrai
Guiyu oneiros
Psarolepis romeri
Styloichthys changae
Glyptolepis groenlandica
Porolepis sp.
Gogonasus andrewsae
Eusthenopteron foordi
Osteolepis macrolepidotus
Meemannia eos
Cheirolepis trailli
Cheirolepis canadensis
Cheirolepis schultzei
Tegeolepis clarki
Osorioichthys marginis
Mimipiscis toombsi
Gogosardina coatesi
Mimipiscis bartrami
Raynerius splendens
Moythomasia lineata
Moythomasia durgaringa
Moythomasia nitida
Donnrosenia schaefferi
Howqualepis rostridens
Kentuckia deani
Melanecta anneae
Woodichthys bearsdeni
Boreosomus piveteaui
Coccocephalichthys wildi
Kansasiella eatoni
Lawrenciella schaefferi
Luederia kempi
Trawdenia planti
Cosmoptychius striatus
Cyranorhis bergeraci
Wendyichthys dicksoni
Beagiascus pulcherrimus
Aesopichthys erinaceus
Kalops monophyrum
Pteronisculus nielseni
Pteronisculus cicatrosus
Pteronisculus changae
Pteronisculus stensioi
Pteronisculus magnus
NHMD 73588
Pteronisculus gunnari
Australosomus kochi
Fukangichthys longidorsalis
Beishanichthys brevicaudalis
Scanilepis dubia
Evenkia eunoptera
Tanaocrossus kalliokoskii
Erpetoichthys calabaricus
Polypterus bichir
Brachydegma caelatum
Brazilichthys macrognathus
Birgeria groenlandica
Birgeria stensioei
Chondrosteus acipenseroides
Acipenser brevirostrum
Polyodon spathula
Yelangichthys macrocephalus
Saurichthys madagascarensis
Saurichthys sp. Greenland
Saurichthys ornatus
Amphicentrum granulosum
Fouldenia ischiptera
Styracopterus fulcratus
Platysomus superbus
Discoserra pectinodon
Bobasatrania groenlandica
Ebenaqua ritchei
Venusichthys comptus
Luganoia lepidosteoides
Dipteronotus ornatus
Peltopleurus lissocephalus
Dorsetichthys bechei
Leptolepis bronni
Ichthyokentema purbeckensis
Elops hawaiensis
Hiodon alosoides
Macrepistius arenatus
Watsonulus eugnathoides
Amia calva
Caturus furcatus
Obaichthys decoratus
Atractosteus spatula
Lepisosteus osseus
Macrosemimimus lennieri
Semionotus elegans
Macrosemius rostratus
Propterus elongatus
Hulettia americana
Tetragonolepis oldhami
Tetragonolepis semicincta
Heterostrophus phillipsi
Scopulipiscis saxciput
Dapedium stollorum
Dapedium punctatum
Dapedium caelatum
Dapedium sp. LIAS
Dapedium pholidotum
Paradapedium egertoni
Hemicalypterus weiri
Dandya ovalis
Sargodon tomicus
Dapedium noricum
Gibbodon cenensis
Brembodus ridens
Neoproscinetes penalvai
Eomesodon liassicus
Arduafrons prominoris
Mesturus sp.
Mesturus verrucosus

Figure A.2: Strict consensus tree of 135 most parsimonious trees, implied weight analysis (K = 100) with outgroup topology constrained.


Dicksonosteus arcticus
Entelognathus primordialis
Dialipina salguerioensis
Ligulalepis
Acanthodes bronni
Cladodoides wildungensis
Ozarcus mapesae
Diplocercides kayseri
Miguashaia bureaui
Guiyu oneiros
Psarolepis romeri
Styloichthys changae
Onychodus jandemarrai
Glyptolepis groenlandica
Porolepis sp.
Gogonasus andrewsae
Eusthenopteron foordi
Osteolepis macrolepidotus
Meemannia eos
Cheirolepis trailli
Cheirolepis canadensis
Cheirolepis schultzei
Osorioichthys marginis
Moythomasia lineata
Moythomasia nitida
Raynerius splendens
Brazilichthys macrognathus
Moythomasia durgaringa
Mimipiscis bartrami
Mimipiscis toombsi
Gogosardina coatesi
Donnrosenia schaefferi
Howqualepis rostridens
Melanecta anneae
Scanilepis dubia
Beishanichthys brevicaudalis
Fukangichthys longidorsalis
Erpetoichthys calabaricus
Polypterus bichir
Evenkia eunoptera
Tanaocrossus kalliokoskii
Tegeolepis clarki
Chondrosteus acipenseroides
Acipenser brevirostrum
Polyodon spathula
Birgeria groenlandica
Birgeria stensioei
Yelangichthys macrocephalus
Saurichthys madagascarensis
Saurichthys sp. Greenland
Saurichthys ornatus
Brachydegma caelatum
Australosomus kochi
Coccocephalichthys wildi
Wendyichthys dicksoni
Cyranorhis bergeraci
Lawrenciella schaefferi
Boreosomus piveteaui
Kansasiella eatoni
Trawdenia planti
Woodichthys bearsdeni
Kentuckia deani
Amphicentrum granulosum
Luederia kempi
Fouldenia ischiptera
Styracopterus fulcratus
Beagiascus pulcherrimus
Aesopichthys erinaceus
Kalops monophyrum
Cosmoptychius striatus
Pteronisculus nielseni
Pteronisculus cicatrosus
Pteronisculus changae
Pteronisculus stensioi
Pteronisculus magnus
NHMD 73588
Pteronisculus gunnari
Platysomus superbus
Discoserra pectinodon
Bobasatrania groenlandica
Ebenaqua ritchei
Venusichthys comptus
Luganoia lepidosteoides
Dipteronotus ornatus
Peltopleurus lissocephalus
Hulettia americana
Elops hawaiensis
Hiodon alosoides
Ichthyokentema purbeckensis
Dorsetichthys bechei
Leptolepis bronni
Macrepistius arenatus
Watsonulus eugnathoides
Amia calva
Caturus furcatus
Obaichthys decoratus
Atractosteus spatula
Lepisosteus osseus
Macrosemimimus lennieri
Semionotus elegans
Macrosemius rostratus
Propterus elongatus
Heterostrophus phillipsi
Dapedium noricum
Scopulipiscis saxciput
Dapedium stollorum
Dapedium caelatum
Dapedium punctatum
Dapedium sp. LIAS
Dapedium pholidotum
Tetragonolepis oldhami
Tetragonolepis semicincta
Paradapedium egertoni
Hemicalypterus weiri
Dandya ovalis
Sargodon tomicus
Gibbodon cenensis
Brembodus ridens
Neoproscinetes penalvai
Eomesodon liassicus
Arduafrons prominoris
Mesturus sp.
Mesturus verrucosus

B | Investigating the impact of X-rays on decay: X-ray computed tomography as a non-invasive visualisation technique for sediment-based decay experiments

B.1 Character matrix and decay data

Character matrix and experimental decay data for the CTRL and SNDCTRL experiments, as well as the data used for the statistical comparisons that were conducted, can be found and downloaded at: https://doi.org/10.25500/edata.bham.00001179.

B.2 Figures and Tables

Table B.1: Scoring and rankings of the Spearman's rank analysis between characters of the CTRL and SNDCTRL.

Characters	CTRL	CTRL ranks	SNDCTRL	SNDCTRL ranks
Anal fin, endoskeleton	51	35	15.5	32.5
Anal fin, spines	45	26.5	20	19
Anterior myomers	35.5	15.5	20.5	15
Brain	35.5	15.5	29	9.5
Caudal fin, endoskeleton	51	38	14.5	39
Caudal fin, spines	45.5	30	18.5	26.5
Dorsal fin, endoskeleton	51	38	15	36
Dorsal fin, spines	45.5	28.5	19.5	22
Eye	34	11	23	11
Gill filaments	35.5	6	29	9.5
Gill skeleton	41.5	22	19.5	22
Heart	37.5	3.5	30.5	5
Intestine, anterior	35.5	6	30	7
Intestine, bulb	38.5	9	30.5	5
Intestine, posterior	37	6	29.5	8
Kidney, mesonephros	39	19	19	24.5
Kidney, pronephros	39	19	19	24.5
Liver	37	1.5	35	2
Mouth	41.5	23	20	19
Opercle muscles	35.5	12.5	20.5	15
Operculum	41.5	21	20.5	15
Ovary/testis	38.5	10	21	12
Pancreas	37	1.5	34.5	3
Pectoral fin muscles	33	12.5	20.5	15
Pectoral fins, endoskeleton	48	33.5	14.5	39
Pectoral fins, spines	45	26.5	17.5	28
Pectoral girdle	45.5	28.5	16	29.5
Pelvic fins, endoskeleton	48	32	15	36
Pelvic fins, spines	43.5	25	20.5	15
Pigmentation	35.5	14	14.5	39
Posterior myomers	35.5	17	19.5	22
Ribs	48	31	16	29.5
Scales	39	19	18.5	26.5
Skull roof	43.5	24	20	19
Swim bladder, anterior	35.5	3.5	36	1
Swim bladder, posterior	37.5	8	30.5	5
Vertebrae, caudal	53.5	38	15	36
Vertebrae, hemal	53.5	38	15.5	32.5
Vertebrae, prehemal	53.5	38	15.5	32.5
Vertebrae, Weberian	48	33.5	15.5	32.5
Spearman's coefficient	0.878574135433662			
t stat	11.3396706386348			
p value	0.000000000000046185277824406 5			

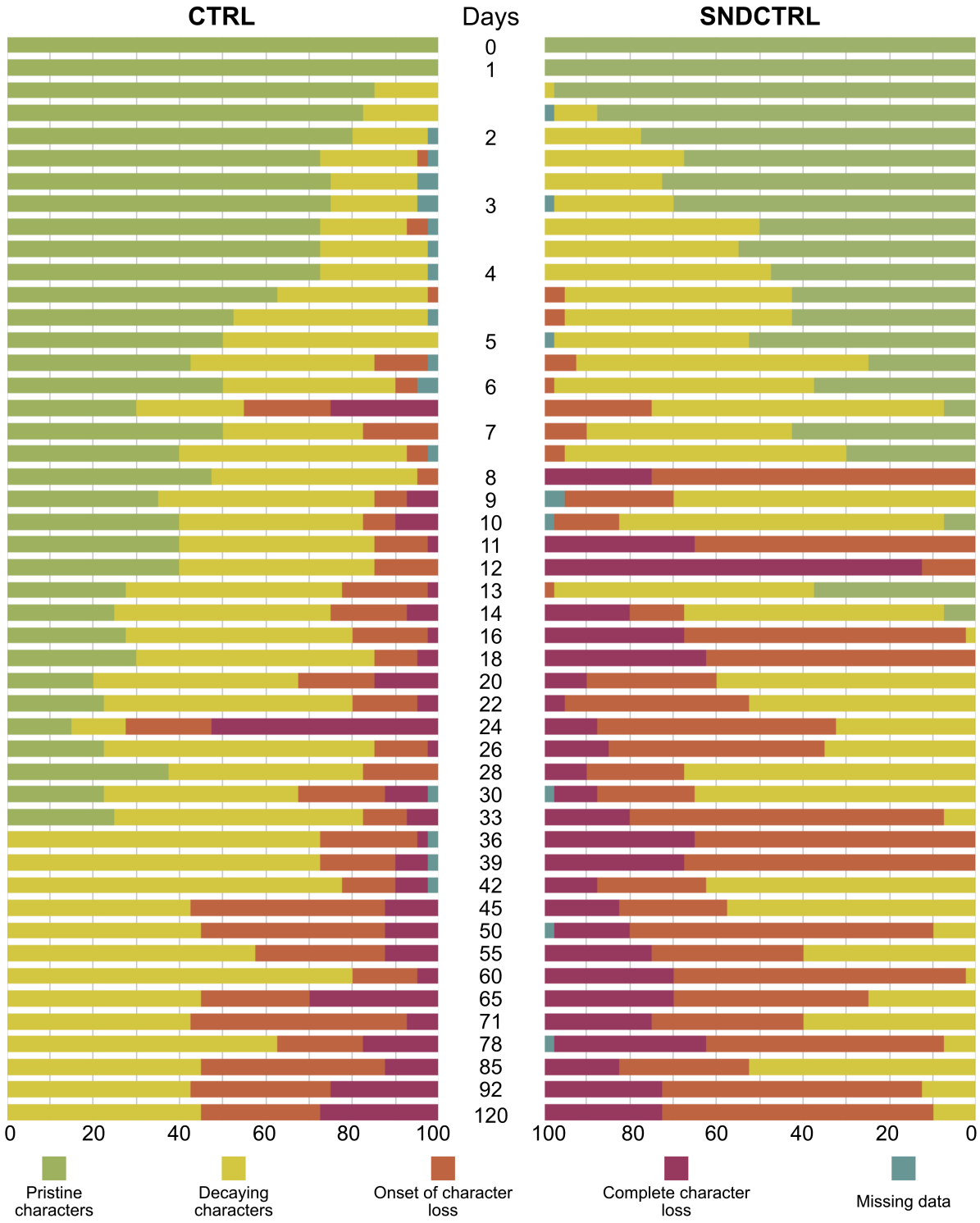


Figure B1: **Frequency of character state observation during traditional decay experiments.** Bar graphs showing the frequency of each character state in the codings from CTRL (decay experiment using water) (left) and SNDCTRL (decay experiment using water and sand) (right) as a percentage of the total coding for each specimen. Each bar represents decay states in one specimen. Experiment day number indicated in the centre.

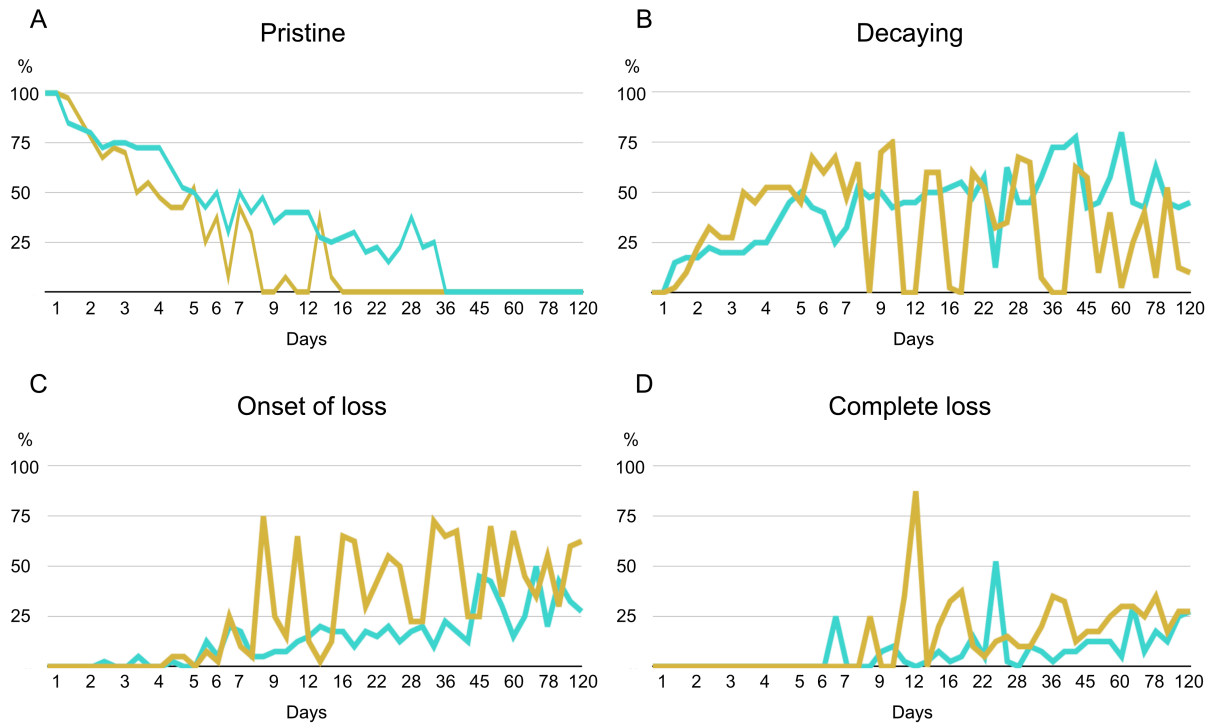


Figure B2: A Comparison of decay rates and decay through time in the CTRL and SNDCTRL experiments. Graphs for pristine percentages (A), decaying percentages (B), onset of loss percentages (C) and complete loss percentages (D). Graph of total decay through time (E). The blue lines indicate the CTRL experiment, the yellow lines the SNDCTRL. Percentages/scores indicated on the y axes, experiment days on the x axes.

C | Dicing with decay: diceCT scanning as a visualisation tool to aid decay experiments

C.1 Preliminary experiments

Calibration phase. We tested the optimal concentration of Lugol's with a trial experiment using 6 zebrafish carcasses in snap-on-lid, closed plastic jars. The specimens were prepared on day 3 of the experiment in the following way:

- *n* = 2 carcasses were stained with a 1% Lugol's solution in 100 mL deionised water; one of the carcasses was also buried in quartz sand.
- *n* = 2 carcasses were stained with a 2.5% Lugol's solution in 100 mL deionised water; one of the carcasses was also buried in quartz sand.
- *n* = 2 carcasses were stained with a 5% Lugol's solution in 100 mL deionised water; one of the carcasses was also buried in quartz sand.

After 14 days of staining time, in line with staining protocols present in the literature (Metscher 2009a), all the specimens were XCT scanned. The specimens in water and sand mixture were scanned *in situ* at 180 kV energy, 45 W current and using a 1.5 mm tin (Sn) filter. Two frames per projection were acquired, with an exposure time of 350 ms and an effective voxel size of 45 µm. Water was not removed prior to the scans, as the sediment was enough to keep the specimens from floating.

The specimens in water were scanned at 40 kV energy, 20 W current and using no filtration. Two frames per projection were acquired with an exposure time of 95 ms and an effective voxel size of 45 µm. The water was gently removed prior to the scans using a syringe, to keep the carcasses from floating.

In presence of sediment, the staining agent remained suspended above the water-sediment interface and did not penetrate the substrate or the buried carcasses. For the specimens prepared in water, there was no visible X-ray attenuation for the soft tissues during XCT scanning in the 1% and 2.5% Lugol's solutions.

The specimen treated with a 5% Lugol's solution was partially stained, but the staining agent did not penetrate deep enough to visualise the entirety of the internal anatomy. These intermediate results informed our experimental designs and standard staining protocol choice for the rest of the experiments: 20% Lugol's solution in deionised water, for 2 weeks staining time.

C.2 Character matrix and decay data

Character matrix and experimental decay data for the W-diceCT and S-diceCT experiments, as well as the data used for the statistical comparisons that were conducted, can be found and downloaded at: https://doi.org/10.25500/edata.bham.00001180